Università degli Studi di Ferrara

DOTTORATO DI RICERCA IN SCIENZE CHIMICHE

CICLO XXVIII

COORDINATORE Prof. Carlo Alberto Bignozzi

PREPARATION AND CHARACTERIZATION OF PHOTOELECTROACTIVE SUBSTRATES FOR WATER SPLITTING AND HYDROGEN PRODUCTION

Settore Scientifico Disciplinare CHIM/03

Dottorando
Dott. Ronconi Federico
(firma)

Tutore
Prof. Caramori Stefano
(firma)

Anni 2013/2015

"In the desert regions, unadapted to any kind of cultivation, photochemistry will artificially put their solar energy to practical uses."

"forests of glass tubes will extend over the plants and glass buildings will rise everywhere; inside of these will take place the photochemical processes that hitherto have been the guarded secret of the plants, but that will have been mastered by human industry which will know how to make them bear even more abundant fruit than nature"

"if in a distant future the supply of coal becomes completely exhausted, civilization will not be checked by that, for life and civilization will continue as long as the sun shines!"

Giacomo Ciamician, **1912**, *The Photochemistry of the Future*

"And what will they burn instead of coal?" "Water," replied Harding. "Water!" cried Pencroft, "water as fuel for steamers and engines!"

"I believe that water will one day be employed as fuel, that hydrogen and oxygen which constitute it, used singly or together, will furnish an inexhaustible source of heat and light, of an intensity of which coal is not capable."

"Water will be the coal of the future."

Jules Verne, **1875**, *The Mysterious Island*

"Perché aspettare che finisca il petrolio? L'età della pietra non è mica finita per mancanza di pietre."

Beppe Grillo, **2005**, *beppegrillo.it*

Dedicated to Mom and Dad, always ready to support me in every difficult moment and encourage me to do the best. I love you.

THESIS INDEX

THESIS ABSTRACT

Meeting the demand of a global energy thirst, while avoiding environmental damages, poses a major scientific and societal challenge for our future. Hydrocarbons energy sources will continue to play the major role on the next few decades, but their costs are doomed to increase and their availability decrease. Besides fossil fuels, there are many other power sources like nuclear fission, wind, biomass and geothermal, but in the long term the most appealing and widely distributed is solar, providing ~10000 times the energy currently consumed worldwide. In order to serve as a primary energy source, solar must be stored, with appropriate processes, into high-energy chemicals, for its utilization in power plants or in secondary chemical processes. This leads to the concepts of "artificial photosynthesis" and "solar fuels", having, as a main target, the photoinduced water splitting for hydrogen production.

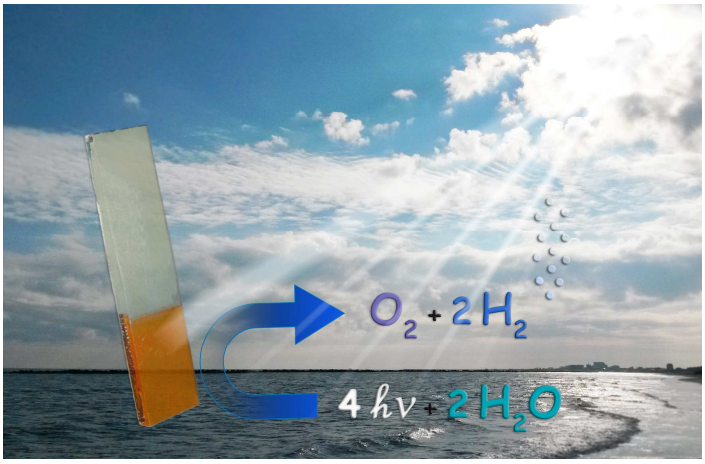

Schematic semiconductor based hybrid interface for photoinduced water splitting.

In principle, semiconductor based devices provide the most straightforward route to a cheap and tunable process for the direct conversion of sunlight into solar fuels, but, in order to obtain significant efficiencies, they must satisfy a number of kinetic and thermodynamic constraints, which pose a great chemical challenge. Scope of this Ph.D. work was the preparation of photoelectroactive substrates, based on wide band-gap semiconductor electrodes, functionalized with molecular sensitizers and catalysts, where both species operate in a concerted way to carry out the electron transfer events at the basis of the artificial photosynthetic process, thus driving water oxidation while hydrogen is simply evolved at a dark catalytic counter electrode. Several functionalization approaches

of semiconductor electrodes were explored, and the resulting devices were fully characterized by spectroscopic, electrochemical and photoelectrochemical experiments.

After discussing some general notions about the exploitation of artificial photosynthetic processes (**Chapter 1**) and on the main experimental techniques applied during this Ph.D. thesis (**Chapter 2**), the study of the photoelectroactive systems is described.

In **Chapter 3** it is reported the modification of TiO_2 photoanodes with a new ruthenium based assembly, constituted by a sensitizer and catalyst units linked together. The photoelectrochemical results demonstrated that the binuclear complex was able to inject electrons into the semiconductor, but was not able to drive photoinduced water oxidation with a significant improvement with respect to sensitizer unit alone. This was attributed to the unfavourable competition of the charge separation with recombination processes and to the demanding thermodynamics for generating the high-valent Ru(V), which was individuated as the active catalytic intermediate for water oxidation.

The unsatisfactory results obtained with the binuclear complex, lead us to consider the co-adsorption of independent sensitizing and catalytic species which represents a simpler and potentially more profitable approach. In **Chapter 4** it is reported the modification of nanocrystalline WO_3 photoanodes with an organic sensitizer (perylene bisimide). Under visible irradiation, the dye excited state underwent oxidative quenching by electron injection into WO_3, leaving a strongly positive hole (1.7 V vs. SCE), which allows to drive demanding photo-oxidation reactions in photoelectrochemical cells. The co-adsorption of IrO_2 nanoparticles, acting as water oxidation catalysts on the sensitized electrodes, led to a four fold enhancement in photoanodic current, consistent with hole transfer from oxidized dye to IrO_2. Interesting results were also achieved by using an anionic molecular catalyst (tetra-ruthenium polyoxometalate), producing performances comparable to some of the best literature results obtained in the heterogeneous phase with identical or similar catalysts.

In **Chapter 5**, the charge transfer dynamics on TiO_2 substrates, involving a new phosphonated Ru(II) polypiridine sensitizer, developed to generate highly oxidizing photoholes for water oxidation, were studied. Under illumination, in presence of LiI as a sacrificial electron donor, an anodic photocurrent of 0.2 mA/cm^2 was achieved, with correspondingly low IPCEs. Interestingly, the photoanodic response were largely increased in the presence of sodium ascorbate, with photocurrent undergoing a four to six fold enhancement, depending on the ascorbate concentration, explainable with a modification of the charge injection mechanism. For the first time in heterogeneous phase, a non

ambiguous evidence for the occurrence of dye excited state reductive quenching (anti-biomimetic pathway) was provided, and the possibility of exploiting such charge transfer process is discussed. Lastly, experiments performed with sensitized SnO_2 photoanodes, where the Ru(II) dye undergoes the usual oxidative quenching, allowed to verify the interaction with co-adsorbed IrO_2 nanoparticles, capable to drive photoinduced water oxidation.

Finally, in **Chapter 6** the pulsed-laser deposition (PLD) was considered as valuable tool for the preparation of nanostructured amorphous Fe_2O_3 catalyst, for the functionalization of conductive surface. The resulting electrodes, based on earth-abundant and non-hazardous iron metal, was able to sustain high current densities (up to 20 mA/cm^2), at reasonably low applied potential bias, for more than 1 hour when employed as anodes for electrochemical water oxidation at pH 11.8. The good catalytic performance achieved proves the validity of PLD as a method to prepare nanostructured materials with good control over surface coverage and morphology. The methodology lends itself to the exploration of other metal oxide catalysts and to functionalization of other surfaces, among which the ohmic contact of multi-junction photovoltaic cells provide the most attractive example.

CHAPTER 1. GENERAL INTRODUCTION

1.1 Chapter 1 - Abstract

Figure 1.1 Representation of "artificial photosynthesis" for the production of H_2 and O_2 from water.

In the first chapter of this Ph.D. thesis will be given general notions and principles about the exploitation of artificial photosynthetic processes, in the context of conversion and storage of solar energy (**Figure 1.1**). In principle, semiconductor based devices provide the most straightforward route to a cheap and tunable process for the direct conversion of sunlight into solar fuels, in the form of highly valuable chemicals that can be easily stored and utilized, when needed, in existing power plants, or by secondary electricity generation, in fuel cells.

The heterogeneous approach to molecular artificial photosynthesis is mostly concerned with the realization of semiconductor based hybrid interfaces, where molecular chromophores and catalysts operate in a concerted way to carry out the electron transfer events at the basis of the photosynthetic process, which is usually the splitting of the water in molecular oxygen and hydrogen. In order to obtain significant fuel forming efficiencies, these hybrid interfaces must satisfy a number of kinetic and thermodynamic constraints that pose a great chemical challenge. Nevertheless, this molecular approach, holds a great potential with plenty of room for optimization, and is currently actively pursued by the scientific community.

1.2 About actual energy sources and challenges for the future

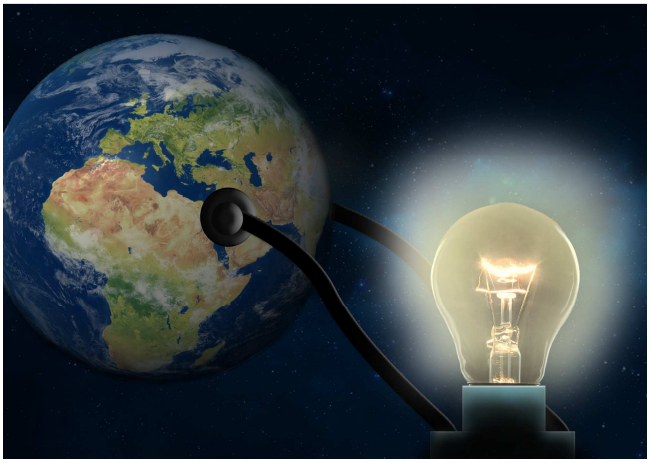

Figure 1.2 Representation of global energy dependence by fossil fuels.

Meeting the demand of a global energy thirst, while avoiding environmental damages, poses a major scientific and societal challenge for our future. The technological development of our society will be driven by increasing energy needs, cost and environmental impact. At the global scale, the combination of various hydrocarbons energy sources will continue to play the major role on the next few decades (**Figure 1.2**), but their costs are doomed to increase, due to issues related to pollution, impact on human health and geo-political instability connected to the inhomogeneous distribution of fossil resources. Besides fossil fuels, there are many power sources like nuclear fission, wind, biomass and geothermal, but in the long term the most appealing and widely distributed is solar.

The Sun is the ultimate sustainable energy source, providing ~10000 times the energy currently consumed worldwide. Solar energy is free of greenhouse gases and pollutants, is secure and without geo-political constraints. The classification of solar energy converters fall in three categories, according to their primary product: solar electricity, solar fuels and solar thermal systems. Chemistry has played a fundamental role in the design of materials and molecular systems for solar energy conversion to electricity. The technological development of single-crystal solar cells demonstrates the practicality of photovoltaics (PV), while novel approaches, exploiting thin films, organic semiconductors and dye sensitisation, offer new opportunities for cheaper and long lasting systems. However, it must be considered that,

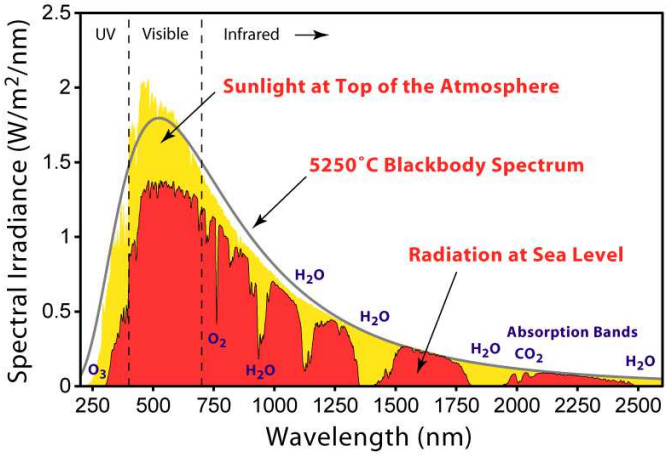

Figure 1.3 Spectral distribution of solar irradiance.

although the radiation is widely distributed, it is low in intensity, and large surface areas are required for its collection. Sunlight contains photons (*hν*) with energies between 3.5 eV and 0.5 eV (electron volts), which reflect the Sun's surface temperature (**Figure 1.3**). The visible region goes from 3.0 eV (violet) to 1.8 eV (red), with a peak power in the yellow at about 2.5 eV. At high noon on a cloudless day, the surface of the Earth at average latitudes receives 1000 watts of solar power per square meter (1 kW/m^2); such standard irradiance is expressed as "air mass 1.5" (AM 1.5) condition. To achieve the level of power consumption in the United States of ~3 TW (terawatts) at 10% efficiency, would require ~140000 km^2 for collection, roughly half the area of Italy. The materials costs with current solar photovoltaic technology would be enormous, 60 trillion dollars for 140000 km^2 based on silicon solar cell technology at 400 $\$/m^2$.[1]

There is an even greater drawback to solar energy. It is intermittent, depending on the day/night cycles, seasonal and local weather conditions. Thus in order to serve as a primary energy source, solar has to be coupled with large-scale energy storage capabilities. Only the energy density in chemical bonds is adequate for storage at the levels required for our current technology. The energy stored in C-H bonds of hydrocarbon sources has indeed its origin in photosynthetic processes occurred millions of years ago. With an appropriate process, excess solar electrical power could be stored as high-energy chemicals and utilized in existing power plants, or by secondary electricity generation in fuel cells. This leads to the concept of "solar fuels", main topic of this Ph.D. thesis, with targets including water splitting into hydrogen and oxygen, and carbon dioxide reduction into almost any form of reduced carbon (carbon monoxide, formaldehyde, methanol, methane) with liquid hydrocarbons as ultimate goal. Natural gas and liquid fuels are especially appealing since they would utilize our existing energy infrastructure.

The chemical reactions for water and carbon dioxide reduction (**Table 1.1**) require the multiple transfer of electrons (e^-) and protons (H^+) to occur. Efficient and selective catalysts, able to exchange quickly these H^+/e^- in a controlled way, will play an important role in electrochemical and photoelectrochemical production of H_2 and CO_2 derivatives. Probably, the first solar fuel available in a large amount will be hydrogen because routes to water splitting are more straightforward than reduction of carbon dioxide. Although the use of H_2 as primary energy vector may be limited, due to difficult storage and under-developed transportation networks, it could be used for on-site power generation or, reacted with CO_2, will represent a valuable feedstock for carbon dioxide sequestration and conversion into fuels using well-known and consolidated technologies.

Table 1.1 Half-reaction, with relative thermodynamic potential and number of electrons and protons exchanged, in water splitting and carbon dioxide reduction.

Half-reaction	*Potential (V vs. NHE at pH 0)*	*Number of H^+/e^- exchanged*
WATER SPLITTING		
$2H^+ + 2e^- \rightarrow H_2$	0.00 V	2
$2H_2O \rightarrow O_2 + 4H^+ + 4e^-$	1.23 V	4
CO_2 REDUCTION		
$CO_2 + 2H^+ + 2e^- \rightarrow HCO_2H$	-0.20 V	2
$CO_2 + 2H^+ + 2e^- \rightarrow CO + H_2O$	-0.12 V	2
$CO_2 + 4H^+ + 4e^- \rightarrow HCHO + H_2O$	-0.07 V	4
$CO_2 + 6H^+ + 6e^- \rightarrow CH_3OH + H_2O$	0.03 V	6
$CO_2 + 8H^+ + 8e^- \rightarrow CH_4 + 2H_2O$	0.17 V	8

At present, the use of biomass strategies (natural photosynthesis) for CO_2 capture and conversion, does not appear efficient enough if consideration is made for the current carbon dioxide production rate, as conversion efficiencies ≈10% are often considered as a minimum for an economically viable solar fuel device. Thus, the search for molecular based high-tech strategies for realizing an efficient artificial photosynthetic device represents a challenging multidisciplinary task, which, at present, is still in its infancy. However, semiconductor/liquid junctions provide the best known wet chemical method of converting solar energy into electrical energy or chemical fuels.[2-4] Semiconductor devices typically operate with a quantum yield close to unity for all electromagnetic frequencies, from the near infrared throughout the visible region of the spectrum, depending on their band-gaps. Before discussing their applications in this research field, the main properties of semiconductor materials will be briefly introduced.

1.3 Basics on semiconductor materials and their photovoltaic applications

Due to the essentially infinite number of atoms that must be considered, the electronic structure of solids is typically discussed in terms of energy bands, which are made up of atomic orbitals of the individual atoms.[5] As a result of the large numbers of interacting orbitals, the spacing of electronic energies within a band, arising from a given quantum state, becomes so small that the band can be effectively considered a continuum of energy levels. However, the energy gap between the groups of levels, corresponding to different atomic quantum states, is preserved. Thus, the allowed electronic energies fall into energy bands of closely spaced levels, with forbidden band-gaps. As with molecular orbitals, the energy levels of interest (**Figure 1.4**) are the "Highest Occupied" (the valence band, VB) and the "Lowest Unoccupied" (the conduction band CB).

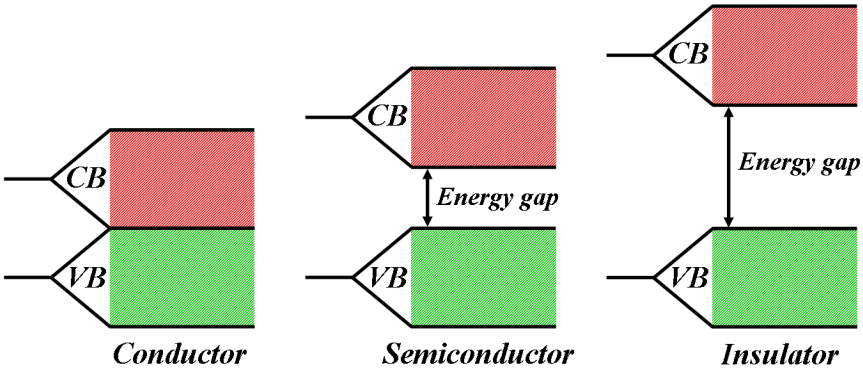

Figure 1.4 Representation of CB and VB in terms of band theory for a conductor (metal), a semiconductor and an insulator.

It is the energy gap (Eg), or band-gap (i.e., the difference in energy between the upper edge of the VB and the lower edge of the CB), that determines the properties of the material. In insulators the valence band is full, the conduction band is empty and no net motion of charge results from application of an electric field. In a conductor the uppermost energy band containing electrons (e^-) is only partially filled, or a filled band overlaps an empty band. These e^- are free to move, and they result in very high conductivities (10^4 - 10^6 $\Omega^{-1}cm^{-1}$), since they are present in large numbers. In semiconductors the situation is similar to that in insulators, except that the band-gap is smaller and e^- can be thermally or optically promoted to the conduction band, resulting in an electrical conductivity which is smaller than that of metals, because of the smaller number of current carriers. The promotion of e^- from the VB to the CB leaves a positively charged vacancy in the VB, which is referred to as a "hole" (h^+). These holes can be moved through space by the transfer of one e^- to the vacancy, therefore h^+ are considered to be mobile.

Another important concept in the discussion of solid-state materials is the Fermi Level. The Fermi-Dirac distribution is given by **Equation 1.1**:

$$f(E) = \frac{1}{1 + e^{\frac{(E - E_F)}{kT}}} \qquad \textbf{Equation 1.1}$$

where $f(E)$ is the probability that a state of energy E is occupied, E_F is a parameter called the "Fermi energy", k is the Boltzmann's constant and T is the absolute temperature. It can be seen that E_F is the energy level for which $f(E) = \frac{1}{2}$, therefore the "Fermi level" is a virtual energy level that has the 50% of probability to be occupied by the electrons.

The Fermi energy is just the electrochemical potential,[5] or partial molar free energy per electron. This result is physically understandable considering two equilibrating systems: thermodynamically we expect them to exchange particles (e^- in this case) until their electrochemical potentials are equal; from the point of view of Fermi statistics, the transfer of particles fills states of lower energy in one system, emptying higher lying filled states in the other system and proceeds until the distributions over energy match (i.e. E_F are equal). For an intrinsic semiconductor the Fermi level lies at the midpoint of the band-gap.

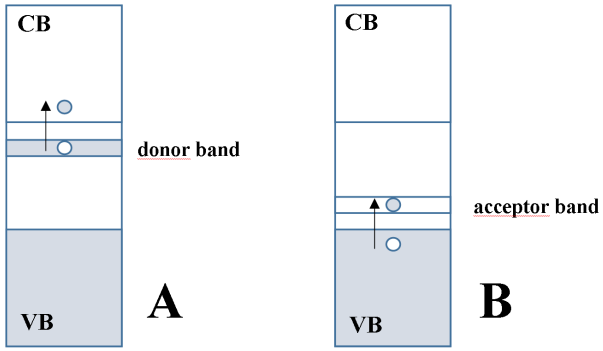

Figure 1.5 Band structure of an n-type semiconductor (A) and a p-type semiconductor (B).

Silicon and germanium are prototypical examples for clarifying the basic principles of semiconductor energetics and conduction mechanism. The introduction of electron rich or electron deficient impurities into the silicon lattice (doping) has a profound influence on the resulting electronic properties of the semiconductor. For example, a small level of arsenic in a silicon semiconductor introduces an extra e^- per As atom. Since the occupied molecular orbitals of Si are filled, these excess e^- fill new electronic states constituting the so called donor band (**Figure 1.5A**) energetically close to the CB. Thermal excitation from the donor band to the CB, results in improved conductivity due to the presence of an excess of negative charge carriers (e^-). Such material is known as "n-type" (negative) semiconductor. Similarly, impurities of gallium in a Si semiconductor lead to the formation of band of electron acceptors in the proximity of the VB. The excitation of an e^- from the VB to the acceptor band leaves an h^+, into the VB (**Figure 1.5B**). Thus, electronic conduction takes place by movement of holes and these

materials are referred to as “p-type” (positive) semiconductors. For many solid-state electronic devices, impurities such as Ga or As are deliberately introduced at controlled levels (at ratios of 1 to 10^9) into ultrapure Si or Ge to produce n-type and p-type extrinsic semiconductors, which are very important for their properties in solar devices.

Photovoltaic cells generally consist of a semiconductor material that can absorb solar photons only above a certain minimum energy, greater than or equal to the band-gap. Electrons and holes, formed upon absorption of light, separate and move to opposite sides of the cell structure, following electrochemical potential gradients, where they are collected by the ohmic contacts. The net effect of this process is the generation of a photovoltage and a photocurrent which translates into the production of electrical power.

A French physicist, Edmund Becquerel, discovered the photovoltaic effect in 1839,[6] when observing the production of a voltage and a current during the illumination of a silver chloride electrode, immersed in an electrolytic solution and connected to a metal counter electrode. However, the birth of the modern era of PV solar cells occurred in 1954, when D. Chapin, C. Fuller, and G. Pearson at Bell Labs demonstrated solar cells based on p-n junctions in single crystal Si with efficiencies of 5-6%. From the mid-1950s to the early 1970s, PV research and development was directed primarily toward space applications and satellite power. Total global PV (or solar) cell production increased from less than 10 MW_p/yr (Megawatt peak per year) in 1980 to about 1200 MW_p/yr in 2004; the current total global PV installed capacity is about 200 GW with a further increase foreseen for the next years.

Other interesting and cheaper approaches in the solar technology involve the use of wide band-gap semiconductor materials, such as TiO_2, ZnO, WO_3 and SnO_2. They have an Eg of the order of 3.0 eV, which means that e^--h^+ pairs can be generated, upon photoexcitation, by a radiation of wavelength below 400 nm, at the limit between the visible and the UV spectra. In order to increase the spectral sensitivity of these materials towards low energy photons, two general approaches have been devised: doping and “molecular sensitization”. As reported previously, through a suitable choice of doping elements, the bulk properties of a semiconductor material can be modified in such a way that donor levels are created just below the CB (n-type doping) or acceptor levels are created just beyond the VB (p-type doping). These intermediate levels reduce the amount of energy required to promote electrons to the conduction band, or holes to the valence band, by means of photon absorption, shifting towards red the useful range for light action. Although this approach is the preferred choice for conventional p-n photovoltaic devices, in the case of wide band-gap semiconductors it has been extensively applied in the field of

photocatalysis. Instead, molecular sensitization is obtained when a "sensitizer" or "dye", an organic or metallorganic molecule with high molar extinction coefficient ε (**Section 2.2**), in its electronically excited state (i.e. an energetic state of the molecular system generated after the absorption of photons) is capable of promoting a heterogeneous charge transfer process with the semiconductor. The sensitizer can be freely diffusing in solution, or firmly attached to the surface of the semiconductor by virtue of suitable anchoring groups. This latter case is preferred since it can ensure a better donor-acceptor interaction between dye molecules and semiconductor substrate, increasing the electron transfer efficiency.

When the excited state of the sensitizer is higher with respect to the bottom of the CB, an e^- can be injected with no thermal activation barrier in the semiconductor, leaving the sensitizer in its one electron oxidized form (**Figure 1.6A**). When the excited state is lower in energy with respect to the top of the VB, an electron transfer (formally an hole transfer) between the semiconductor and the sensitizer can take place leaving the molecule in its one electron reduced form (**Figure 1.6B**).[7]

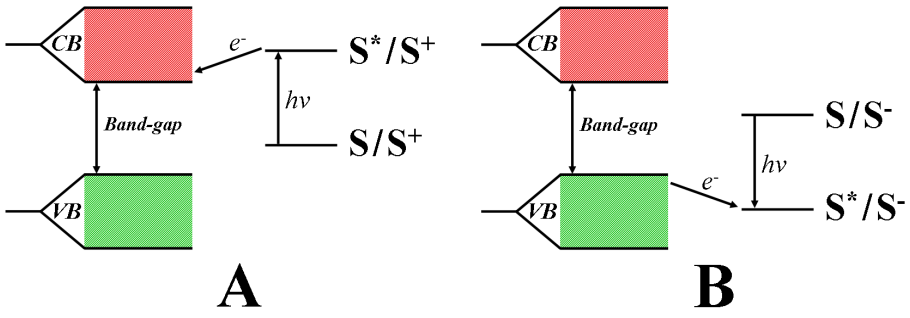

Figure 1.6 Sensitized charge injection: A) electron injection (oxidative quenching); B) hole injection (reductive quenching).

The principle of dye sensitization of semiconductors can be traced back to the end of 1960s,[8] however the efficiencies obtained with single crystal substrates were too low due to the poor light absorption of the adsorbed monolayer of dye molecules. The breakthrough in the field was brought by the introduction of mesoscopic films made of sintered nanoparticles of a semiconductor metal oxide with a large surface area which allowed the adsorption, at monolayer coverage, of a much larger number of sensitizer molecules leading to absorbance values, of thin films of a few microns, well above unity.[9]

Since their appearance in the early 1990s by the work of Grätzel,[10] photoelectrochemical solar cells based on the principle of sensitization of wide band-gap mesoporous semiconductors, called "dye-sensitized solar cells" (DSSCs or DSCs), have attracted the interest of the scientific community due to their outstanding performances which started the envision of a promising alternative to conventional junction-based photovoltaic devices. For the first time a solar energy device operating at a molecular level

showed the stability and the efficiency required for potential practical applications, in a strongly multidisciplinary research field involving several areas such as nanotechnology, materials science, molecular engineering, photochemistry and electrochemistry.

As already reported in **Section 1.2**, the most challenging aspects in solar energy conversion involves the production of interesting chemical fuels, but its progress is still in infancy. Scientists have always been fascinated by the way in which nature, through plants, can convert water and CO_2 into carbohydrates using the sunlight. The recent discoveries, of protein structures and isolation of catalyst sites, have allowed the understanding of the reaction paths that occur in natural photosynthesis. Inspired by these mechanisms, the research moved to the development of systems and devices able to mimic the fundamentals of photosynthetic process, leading to the so called "artificial photosynthesis" (**Figure 1.1**), which is aimed at the conversion of ubiquitous substrates, like water or carbon dioxide, into energy rich species, like hydrogen or reduced carbon species. The realization of hybrid interfaces, based on molecular chromophores and catalysts adsorbed on semiconductor electrodes, holds a great potential with plenty of room for optimization, and is, at present days, actively pursued. Such approach, clearly inspired by DSSC, will be described in detail in **Section 1.4**.

1.4 Artificial photosynthesis with dye-sensitized photoelectrochemical cells

As the fundamental knowledge about the functioning of natural photosynthetic structures and processes progresses,[11-19] the requirements for artificial photosynthesis become more clear. In fact, the key elements for a molecular approach should be tasked with the following functions:

1) Light absorption resulting in the formation of a molecular excited state with appropriate energetics.
2) Electron-transfer quenching of the excited state.
3) Spatially directed electron/proton transfer driven by free energy gradients, in order to give transiently stored oxidative and reductive equivalents.
4) Catalysis of water oxidation and $H_2O/H^+/CO_2$ reduction, in order to compete successfully with energy wasting charge recombination.

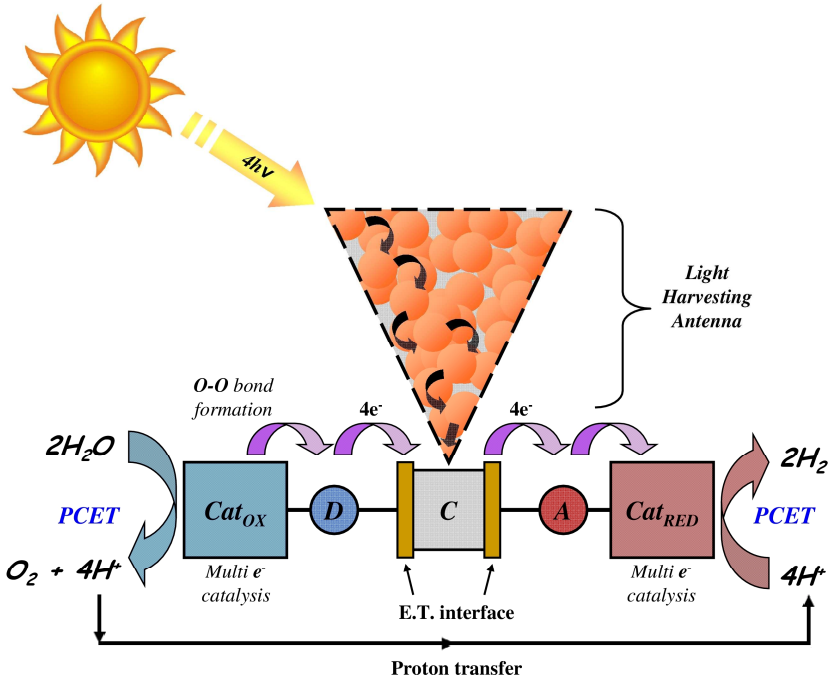

Figure 1.7 Schematic molecular assembly for water splitting.

The incorporation and integration, into appropriate configurations, of the elements able to perform functions 1-4 for practical devices, is one of the major challenges in artificial photosynthesis. The key modules are represented, in the case of a photochemical water splitting assembly, in **Figure 1.7**. It includes an antenna array for light collection, funnelling energy to a chromophore (C), whose excited state initiates a sequence of electron transfers to chemically linked electron-transfer donors (D) and acceptors (A), in order to activate redox catalysts for water oxidation (Cat_{OX}) or hydrogen evolution

(Cat_{RED}). The interfacing of a molecular system with solid electrodes in contact with an electrolytic solution offers the possibility to achieve a better organization and control over the processes as well as a simplified molecular assembly, by separating the overall processes into half-reactions occurring at the separate compartments of a photoelectrosynthetic device called "dye-sensitized photoelectrochemical cell" (DSPEC, **Figure 1.8**).

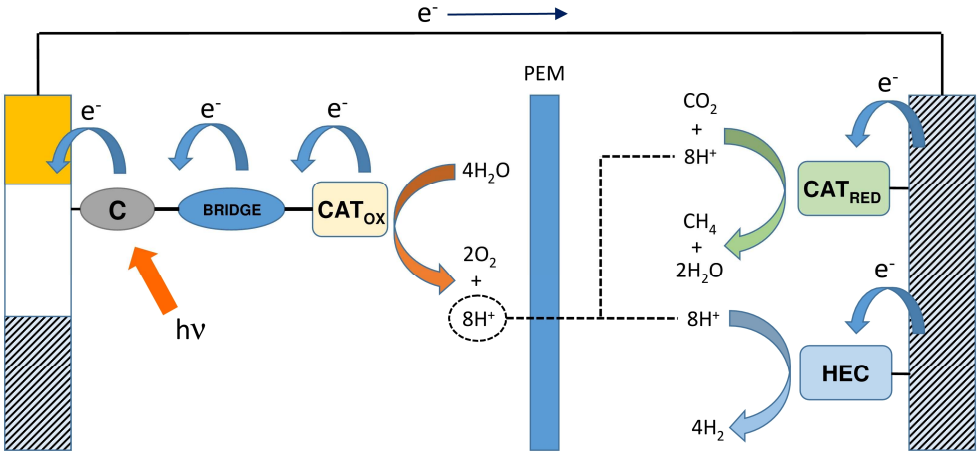

Figure 1.8 DSPEC for solar fuel production. C is the light absorber injecting electrons into the semiconductor, triggering a sequence of electron transfer events, which activate the water oxidation catalyst (Cat_{OX}). At the dark cathode either a water (HEC is the hydrogen evolving catalyst) or a CO_2 (Cat_{RED}) reduction catalyst drives the production of fuel (H_2 or CH_4 in the scheme). PEM is a proton exchange membrane.

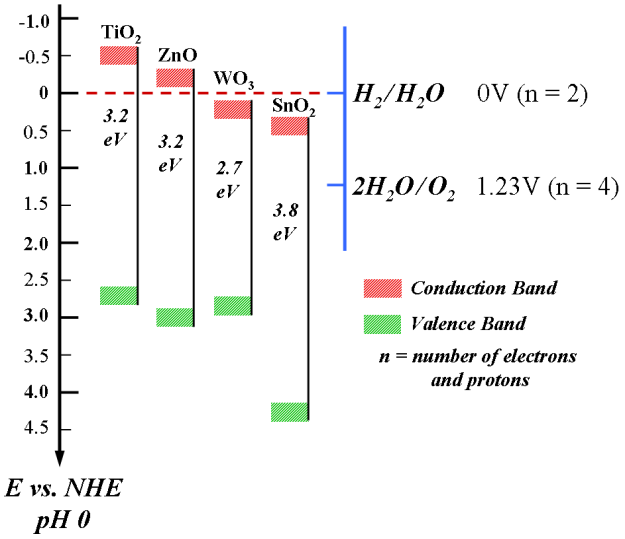

Figure 1.9 Typical wide band-gap n-type semiconductors used in DSPECs.

The essential features in the photoelectrochemical approach are the separation of the charge carriers (e^--h^+) to different phases. The solid phase that collects e^-, can also be controlled, via electrical connections, through the application of an external voltage. The oxidation and reduction intermediates, and products, are physically separated by an ion-permeable membrane (PEM in **Figure 1.8**), resulting in a further decreased probability of recombination by preventing the diffusional encounter of partly reduced and oxidised species in solution. The electronic characteristics of the semiconductor determines the direction of the electron flow through the cell. In their most common configuration DSPECs are built with transparent n-type semiconductors, like

TiO_2, ZnO, WO_3 and SnO_2 (**Figure 1.9**), as photoanodes, and e^- conduction results from charge injection into their empty CBs, while h^+ remain transiently confined on the molecular assembly bound at the surface of the material, before hole transfer to the final acceptor (H_2O) in the electrolyte solution occurs. Typically semiconductor thin films consisting of 20-40 nm nanoparticles and of the thickness of 3-5 μm, once covered with a monolayer of sensitizer having $\varepsilon \approx 10^4$ $M^{-1}cm^{-1}$, allow for the harvesting of large fractions of light (even >90% in the dye absorption maximum), making superfluous the use of antenna system as additional light capture approach and resulting in a further synthetic simplification.

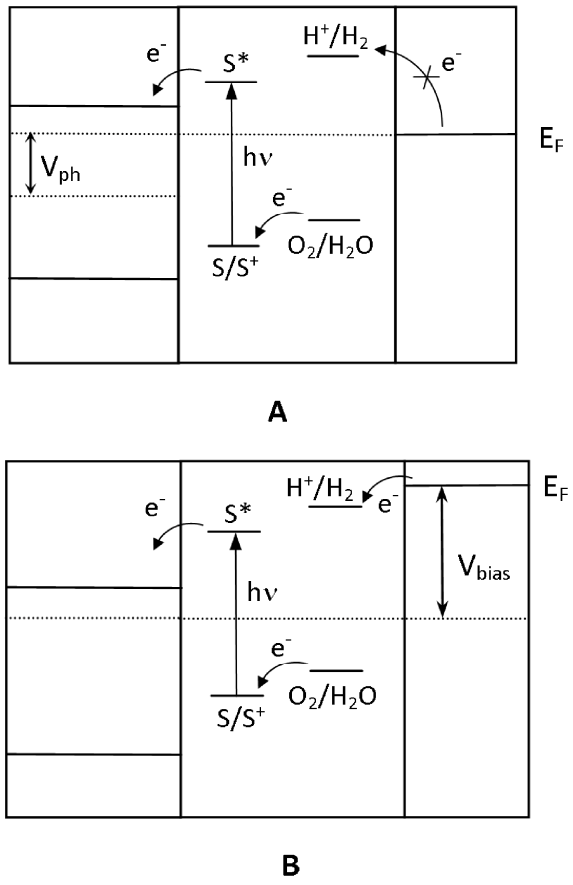

Figure 1.10 Energy level diagram for a sensitized n-type semiconductor used as a photoanode in DSPEC for water splitting with a single photoactive junction. S/S^+ represents the redox level of the oxidized sensitizer/catalyst assembly. Here the quasi-Fermi level (dotted line) of the n-type material is approximated with the flat band potential (V_{fb}) of the semiconductor, as commonly accepted.

The quasi-Fermi level of the semiconductors used to build the device determine the thermodynamics of the cell and the feasibility of the devised fuel forming process. For example, in order to observe hydrogen evolution without externally applied potential bias, the quasi-Fermi level of the semiconductor (which is in equilibrium with the Fermi level of the dark cathode) must be more negative than the formal potential for H_2 evolution (E° = 0 V vs. NHE at pH 0, **Table 1.1**). When this condition is not met, the application of an external potential is necessary to drive the reaction of interest. Referring to **Figure 1.10A**, for H_2 evolution to occur, since under illumination the Fermi level of the cathode is less negative than that of the H^+/H_2 couple, a positive bias must be applied to the semiconductor electrode, as shown in **Figure 1.10B**. The application of the voltage will raise the Fermi level of the dark cathode having opposite polarity, activating the charge transfer. This bias, which is usually provided by an external voltage source, should also account for the cathodic overvoltage to sustain the current flow. As a first approximation, the redox levels of the surface bound sensitizing species are not affected by the applied bias, and the photo-

produced oxidative equivalents must be capable to oxidize H_2O to O_2 ($E°$ = 1.23 V vs. NHE at pH 0, **Table 1.1**).

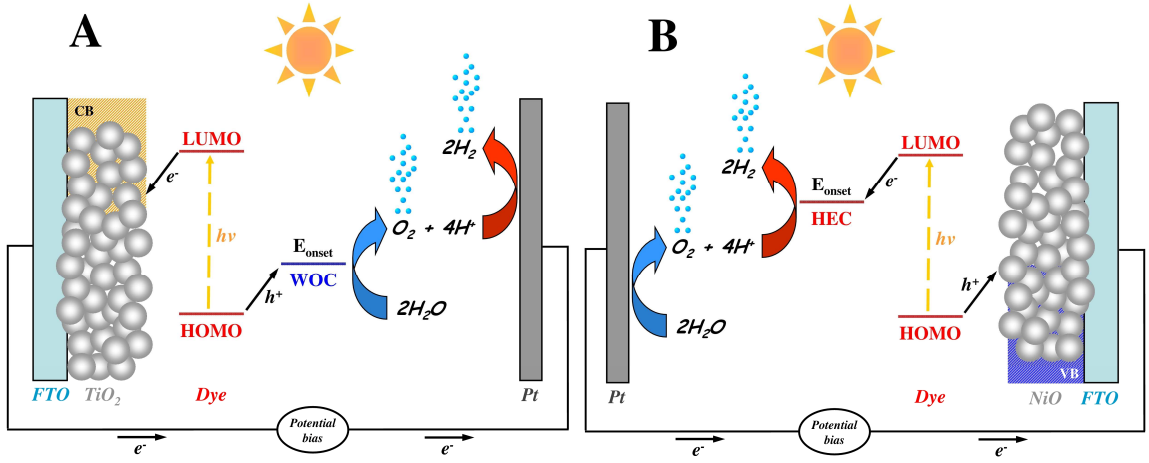

Figure 1.11 Principles of operation of n-type (A) and p-type (B) DSPECs for water splitting. TiO_2 and NiO are taken here as common examples of n- and p-type semiconductors respectively. Semiconductor electrodes are connected to a catalytic dark counter electrode (platinum wire in the example). In this configuration the application of a potential bias is often necessary to drive hydrogen (for n-type) or oxygen (for p-type) evolution at the counter electrode of the cell.

Other DSPEC configurations are possible with photoelectrochemical events driven at a photocathode by hole rather than electron injection. A p-type DSPEC (**Figure 1.11B**) operate in an inverse fashion compared to the more common n-type DSPECs (**Figure 1.11A**): the excited state of a dye molecule adsorbed on the semiconductor surface injects a hole into the VB of the p-type material (typically NiO). The h^+ diffuses to the back contact of the conducting substrate while the reduced dye is restored to its ground state by delivering an e^- to the oxidized component (for example H^+) in the electrolyte, resulting in hydrogen evolution. Clearly, also in this case the coupling of the dye with a catalyst (HEC in the case of the p-type water splitting DSPEC) may be necessary to boost the efficiency of the faradic reaction relevant to the production of solar fuel.

$$ABPE = \frac{J[mA/cm^2] \cdot (E^0{}_{fuel} - V_{bias})[V] \cdot \eta_F}{P[mW/cm^2]} \qquad \textbf{Equation 1.2}$$

When the application of an additional potential is required, the efficiency of the fuel forming solar cell must consider the energy loss due to the need of applying the bias voltage (referred to the counter electrode of the cell) according to **Equation 1.2**, where the photocurrent density (J) produced at a given voltage (V_{bias}) under the incident solar power (P) appear. $E°_{fuel}$ is the standard potential for the fuel forming reaction ($E°_{fuel}$ = 1.23 V, in the case of water splitting into O_2 and H_2) having a faradic efficiency η_F, which should ideally approach 100%. The quantity at the left side of **Equation 1.2** is rigorously called ABPE (applied bias photon-to-current efficiency).[20] In order to avoid the need of the

applied bias, a DSPEC cell architecture with separate n-p junctions, which sum their respective photovoltages, can be devised as reminiscent of photochemical diode (tandem solar cell).[21] The first reports of sensitized photoelectrosynthetic devices operating without external bias are beginning to appear in the recent literature (2014-2015).[22]

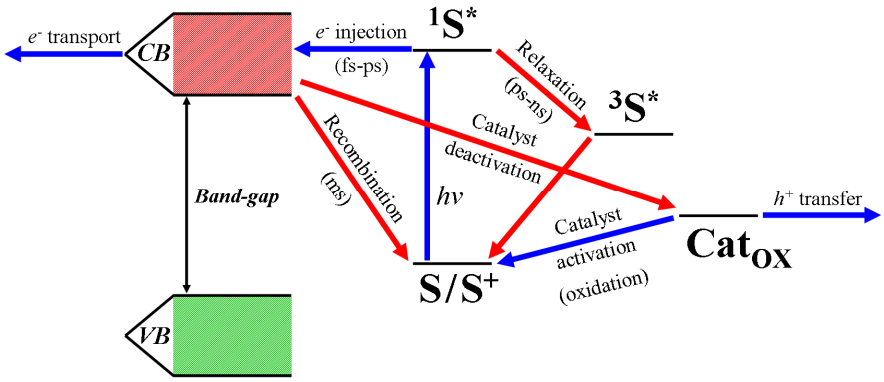

Figure 1.12 Examples of physical processes relevant for the dye-sensitized fuel forming reactions at an n-type interface. Blue arrows indicate the desired electron flow, red arrows energy wasting deactivation and recombination events.

Solar fuel production is a complex matter, resulting from the minimization of many recombination events (**Figure 1.12**).[23] The current approach is to try to optimize the separate interfaces, which can be later assembled together in an unassisted photoelectrochemical device. It is clear the importance of the identification and study of appropriate sensitizers, compatible band-gap semiconductors, and efficient catalysts able to drive the fuel forming reaction. The properties of these elements will be described in the following paragraphs.

1.5 Sensitizers for DSPECs: base structures and concepts

The dye is clearly an essential part of DSPECs and should fulfil some general requirements:

1) it should have strong visible absorption bands, in order to harvest a large fraction of the solar spectrum;
2) for n-type sensitization, the excited state oxidation potential ($^{*}E_{OX}$, **Section 2.4**), representing the electron donating capability of the dye at the excited state, should be more negative than the Fermi level of the semiconductor. In the case of p-type sensitization, the excited state reduction potential of the dye ($^{*}E_{RED}$, **Section 2.4**) should be more positive than the Fermi level of the p-type material;
3) in water photo-oxidation processes, the first oxidation potential of the ground state must be positive enough to drive hole transfer to the water oxidation catalyst (WOC); a similar statement holds for reductive conversion schemes at p-type interfaces, where the first reduction potential of the dye should be negative enough to activate HEC or CRC (CO_2 reduction catalyst);
4) it should possess stable anchoring group in hydrolytic and oxidative conditions;
5) chemical and electrochemical stability in operational conditions is a desirable quality for species supposed to resist several redox turnovers without degrading (at present real long term water splitting stability with molecular systems is not yet demonstrated).

Ruthenium-polypyridine complexes were the first species to be considered for light-driven water splitting photoanodes,[24-26] because of their broad spectral coverage and high molar absorptivity of metal-to-ligand charge transfer (MLCT) transitions ($\varepsilon \approx 1\text{-}2 \times 10^4$ $M^{-1}cm^{-1}$) in the blue-green portion of the visible region. They also show long-lived excited state lifetimes and good electrochemical stability with acceptable ground and excited state redox potentials. Spectroscopic and electrochemical properties can be optimized for the intended task by substituting the chromophoric ligands, typically bipyridines or terpyridines, with different electron donating or electron withdrawing functional groups. Electron injection into the most common wide band-gap semiconductors (TiO_2, SnO_2 and ZnO) is thermodynamically feasible for most ruthenium-polypyridine dyes from both the lowest singlet (^{1}MLCT) and triplet (^{3}MLCT) states, but, in order to maximize the charge injection rate, the electronic coupling of the sensitizer with the

substrate should be established through the formation of covalent bonds. For the attachment of molecular species to metal oxides, the most used anchoring groups are carboxylic (-COOH) and phosphonic ($-PO_3H_2$), owing also to their synthetic accessibility. Phosphonic groups were found to bind more strongly to the TiO_2 surface than carboxylates, resulting in greater stability. Desorption studies of ruthenium sensitizers in aqueous pH 5.7 solutions showed 90% desorption with a carboxylate anchor, compared to only 30% desorption for the phosphonate under the same conditions,[27] indicating that phosphonic anchors should be preferred to carboxylic groups to enhance the stability of water splitting cells, despite the less efficient electron injection of the former with respect to the latter, due to the interruption of π conjugation with the organic ligand. An interesting sensitizer, Ru-bis-terpyridine with a phosphonic anchor group, and its application will be described in detail in **Chapter 5**.

Organic dyes are a viable alternative to metal complexes in order to avoid the use of rare metals, at least in the light harvesting part of the electrode assembly. Organic species can exhibit π-π^* transitions with very high extinction coefficients ε, even on the order of 10^5 M^{-1} cm^{-1}. Among these species, the perylene bisimide are simple molecules possessing high ε and good thermal and photochemical stability. Most importantly, they show high oxidation potentials (E_{OX}), resulting compatible with the activation of many WOCs reported in literature, including ruthenium, cobalt, iridium, nickel and iron based catalysts, but are limited by a low $^*E_{OX}$. This fact precludes charge injection into many semiconductors and, in general, their use in energy conversion schemes relying on the oxidative quenching of their excited state. Detailed properties and application of this sensitizer will be described in **Chapter 4**.

1.6 Water oxidation catalysts: properties and mechanism of action

As stated before, the water oxidation part of the DSPEC has attracted the large majority of the research work, while, very commonly, hydrogen is simply evolved at a dark catalytic counter electrode under applied bias. This predominant interest about the photoanodic assembly is largely justified by the fact that the water oxidation is considered to be the ubiquitous part in sustainable fuel forming reactions and by the convenience of having a wider arsenal of optimized materials at our disposal as well.

The catalyst plays a fundamental role, since the complex kinetics, imposed by multi-electron water oxidation, would result in exceedingly high activation barriers for the direct hole transfer from the photo-oxidized dye, immobilized at the semiconductor surface, to water molecules, resulting in predominant recombination events. The most used WOCs are metal complexes or simply oxides, which display, as a general requirement, the production of stable high-valent metal-oxo species at low redox potentials, to be able to initiate the multielectron oxidation of water. To enable the rational design of molecular complexes that can fulfill this requirement, extensive research has been directed toward the elucidation of the fundamental steps of H_2O oxidation. Despite the experimental difficulties in determining the exact reaction mechanisms, the current view proposes two major mechanistic pathways for H_2O oxidation (**Figure 1.13**): the solvent water nucleophilic attack (WNA) and the interaction of two M-O units (I2M).[28]

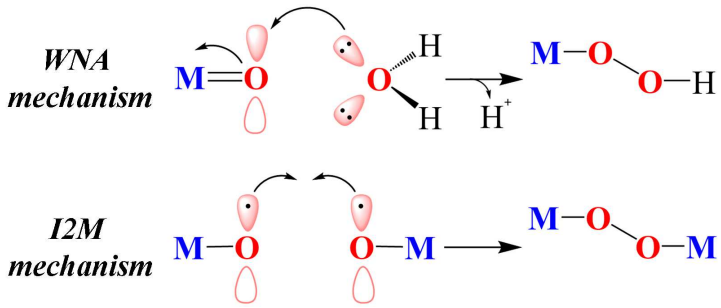

Figure 1.13 Representation of the two main pathways for oxygen evolution in WOC.

In the WNA mechanism, H_2O acts as the nucleophile by attacking the electrophilic high-valent metal-oxo species, which leads to cleavage of the metal-oxo π-bond and the concomitant generation of the crucial O–O bond. This results in the formal two-electron reduction of the metal center to form a metal hydroperoxide species (M-OOH), which can subsequently undergo further oxidation to liberate O_2.

The other mechanistic pathway (I2M) involves the radical coupling of two metal-oxo species that hold significant radical character, generating a [M-O–O-M] intermediate that may undergo further oxidation to ultimately release of O_2. Generally, systems proceeding via the I2M pathway contain flexible ligand scaffolds with large bite angles (>90°) that can promote the O–O bond formation.

Up-to-date excellent reviews about molecular water oxidation catalyst exist,[28,29] so the exhaustive and detailed description of a wide class of WOC, based on coordination compounds incorporating different metals, is beyond the scope of this Ph.D. thesis. The works reported in the next chapters will describe the use of some molecular catalysts and metal oxide applied to photoanodes for DSPEC.

1.7 Chapter 1 - Figures index

1.8 Chapter 1 - References

(1) Song, W.; Chen, Z.; Brennaman, M. K.; Concepcion, J. J.; Patrocinio, A. O. T.; Iha, N. Y. M.; Meyer, T. J. *Pure and Applied Chemistry* **2011**, *83*, 749.

(2) Tan, M. X.; Laibnis, P. E.; Nguyen, S. T.; Kesselman, J. M.; Stanton, C. E.; Lewis, N. S. In *Progress in Inorganic Chemistry*; John Wiley & Sons: New York, **1994**; Vol. 41, p 21.

(3) Gerischer, H. *Pure and Applied Chemistry* **1980**, *52*, 2649.

(4) Fujishima, A.; Honda, K. *Nature* **1972**, *238*, 37.

(5) Hannay, N. B. *Semiconductors*; Reinhold Publishing Corporation: New York, **1959**.

(6) Becquerel, E. *Comptes Rendus* **1839**, *9*, 561.

(7) Memming, R. *Progress in Surface Science* **1984**, *17*, 7.

(8) Gerischer, H.; Tributsch, H. *Berichte der Bunsengesellschaft für physikalische Chemie* **1968**, *72*, 437.

(9) Desilvestro, J.; Graetzel, M.; Kavan, L.; Moser, J.; Augustynski, J. *Journal of the American Chemical Society* **1985**, *107*, 2988.

(10) O'Regan, B.; Gratzel, M. *Nature* **1991**, *353*, 737.

(11) Yachandra, V. K.; Sauer, K.; Klein, M. P. *Chemical Reviews* **1996**, *96*, 2927.

(12) Kern, J.; Renger, G. *Photosynthesis Research* **2007**, *94*, 183.

(13) Renger, G.; Renger, T. *Photosynthesis Research* **2008**, *98*, 53.

(14) Meyer, T. J.; Huynh, M. H. V.; Thorp, H. H. *Angewandte Chemie International Edition* **2007**, *46*, 5284.

(15) McEvoy, J. P.; Brudvig, G. W. *Chemical Reviews* **2006**, *106*, 4455.

(16) Dau, H.; Zaharieva, I. *Accounts of Chemical Research* **2009**, *42*, 1861.

(17) Brudvig, G. W. *Philosophical Transactions of the Royal Society of London B: Biological Sciences* **2008**, *363*, 1211.

(18) Barber, J.; Andersson, B. *Nature* **1994**, *370*, 31.

(19) Barber, J. *Biochemical Society Transactions* **2006**, *34*, 619.

(20) Chen, Z.; Jaramillo, T. F.; Deutsch, T. G.; Kleiman-Shwarsctein, A.; Forman, A. J.; Gaillard, N.; Garland, R.; Takanabe, K.; Heske, C.; Sunkara, M.; McFarland, E. W.; Domen, K.; Miller, E. L.; Turner, J. A.; Dinh, H. N. *Journal of Materials Research* **2010**, *25*, 3.

(21) Hammarström, L. *Accounts of Chemical Research* **2015**, *48*, 840.

(22) Li, F.; Fan, K.; Xu, B.; Gabrielsson, E.; Daniel, Q.; Li, L.; Sun, L. *Journal of the American Chemical Society* **2015**, *137*, 9153.

(23) Young, K. J.; Martini, L. A.; Milot, R. L.; Snoeberger III, R. C.; Batista, V. S.; Schmuttenmaer, C. A.; Crabtree, R. H.; Brudvig, G. W. *Coordination Chemistry Reviews* **2012**, *256*, 2503.

(24) Youngblood, W. J.; Lee, S.-H. A.; Kobayashi, Y.; Hernandez-Pagan, E. A.; Hoertz, P. G.; Moore, T. A.; Moore, A. L.; Gust, D.; Mallouk, T. E. *Journal of the American Chemical Society* **2009**, *131*, 926.

(25) Li, L.; Duan, L.; Xu, Y.; Gorlov, M.; Hagfeldt, A.; Sun, L. *Chemical Communications* **2010**, *46*, 7307.

(26) Brimblecombe, R.; Koo, A.; Dismukes, G. C.; Swiegers, G. F.; Spiccia, L. *Journal of the American Chemical Society* **2010**, *132*, 2892.

(27) Gillaizeau-Gauthier, I.; Odobel, F.; Alebbi, M.; Argazzi, R.; Costa, E.; Bignozzi, C. A.; Qu, P.; Meyer, G. J. *Inorganic Chemistry* **2001**, *40*, 6073.

(28) Kärkäs, M. D.; Verho, O.; Johnston, E. V.; Åkermark, B. *Chemical Reviews* **2014**, *114*, 11863.

(29) Blakemore, J. D.; Crabtree, R. H.; Brudvig, G. W. *Chemical Reviews* **2015**, *115*, 12974.

CHAPTER 2. EXPERIMENTAL TECHNIQUES

2.1 Chapter 2 - Abstract

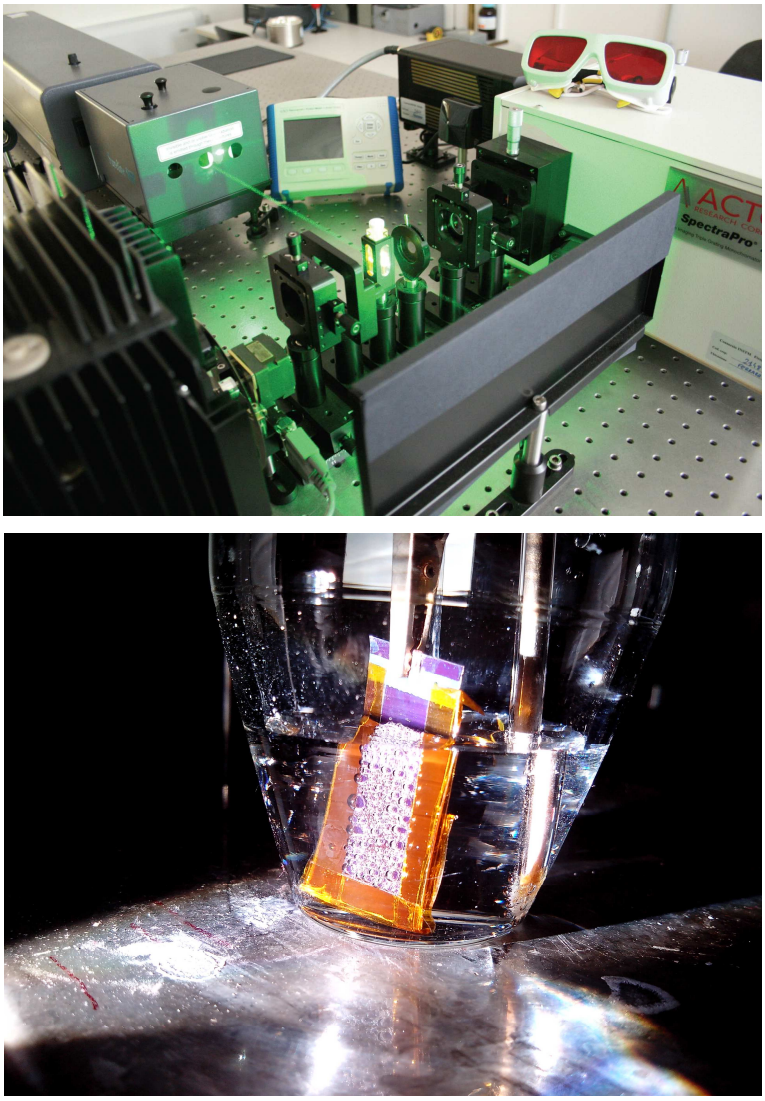

Figure 2.1 Photographs taken in our laboratories: on the top the nanosecond laser apparatus (shoot of Dr. Roberto Argazzi) and below an illuminated solar water splitting cell (shoot of Dr. Vito Cristino).

In this chapter, the main experimental techniques applied during the study of the systems reported in this Ph.D. thesis will be described. All experiments achieved in the following chapters, conducted on sensitizers and catalysts, in solution or deposited on semiconductor electrodes, are based on steady state and time resolved absorption/emission techniques, (**Figure 2.1**, top), and electrochemical/photoelectrochemical measurements (**Figure 2.1**, below). The main parameters for evaluating the efficiency of photoelectrochemical cells, often recurring during the description and study of the water splitting systems, will be defined.

2.2 Stationary absorption/emission techniques

UV-vis absorption spectra were measured with a *JASCO V-570* and a *Varian Cary 300* spectrophotometers (**Figure 2.2**), bandwidth of 2 nm, equipped with a W/I_2 (for NIR/vis, from 2500 nm to 400 nm) and a H_2/D_2 (for UV, from 400 nm to 200 nm) lamps. For the molecules studied in this thesis, absorption measurements were achieved with standard quartz cuvettes of 1.0 cm optical path (dyes in solution), or with transparent sensitized electrodes (dyes adsorbed on semiconductor). In transmission mode, the measurement consists in the detection of the light transmitted by a sample, compared with a suitable blank (either pure solvent or a bare semiconductor thin film) in a given wavelength range. The result is a plot of the absorbance (A) vs. wavelength (λ), described by **Equation 2.1**, **Equation 2.2** and **Equation 2.3**:

$$A = \log\frac{1}{T} \qquad \textbf{Equation 2.1}$$

$$T = \frac{I}{I_0} \qquad \textbf{Equation 2.2}$$

$$A = \varepsilon \cdot l \cdot C \qquad \textbf{Equation 2.3}$$

where, T is the transmittance, I and I_0 are the light intensities transmitted by the sample and the reference (blank), respectively. For optical diluted solutions, the absorbance can be correlated to the concentration of the absorbing species through the Lambert-Beer law (**Equation 2.3**), where ε is the molar extinction coefficient, l is the optical path, and C is the concentration. The Lambert-Beer law can be applied also for species adsorbed on semiconductor thin film, through the **Equation 2.4**:

$$A = 1000 \cdot \Gamma \cdot \varepsilon \qquad \textbf{Equation 2.4}$$

where Γ is the adsorbed species surface concentration (mol/cm^2) and 1000 is the volume conversion factor.

Photoluminescence and excitation spectra were recorded on an *Edinburgh Instruments FLS 920* fluorescence spectrometer (**Figure 2.3**), equipped with a double emission monochromator, Xe lamp (450 W, excitation range from 230 nm to 1700 nm) as excitation source and a *R928P-Hamamatsu* photomultiplier tube as detector. Standard quartz cuvettes, with 1.0 cm optical path, or sensitized thin film electrodes were employed. A photoluminescence measurement consists in the detection of the intensity of the emitted light by a sample at different wavelengths (in general in the UV/visible range) upon excitation at a fixed wavelength. The emission intensity is strongly dependent on the

experimental conditions (excitation wavelength, absorbance of the emitter at that wavelength, integration time, slits of both excitation and emission monochromators); therefore care has to be taken in order to compare emission spectra. On the contrary, an excitation spectrum is measured by fixing the emission wavelength and measuring the intensity at that wavelength upon excitation at different wavelengths. Importantly, an excitation measurement is meaningful only after correction of the lamp output and in the case of optical diluted solutions, since, only in these conditions, the absorbance is linear with the emitted intensity. The result is a spectral profile resembling the absorption spectrum of the emitting species.

By the intersection of normalized absorption and emission spectra, of a generic molecule, it is possible to calculate the zero-to-zero spectroscopic energy ($E^{0\text{-}0}$), relative to the energy gap between the HOMO-LUMO molecular orbitals:

$$E^{0-0}[eV] = \frac{10^7}{\lambda^{0-0}[nm] \times 8066[cm^{-1}]} \qquad \textbf{Equation 2.5}$$

where $\lambda^{0\text{-}0}$ is the intersection wavelength and 8066 is the energy conversion factor.

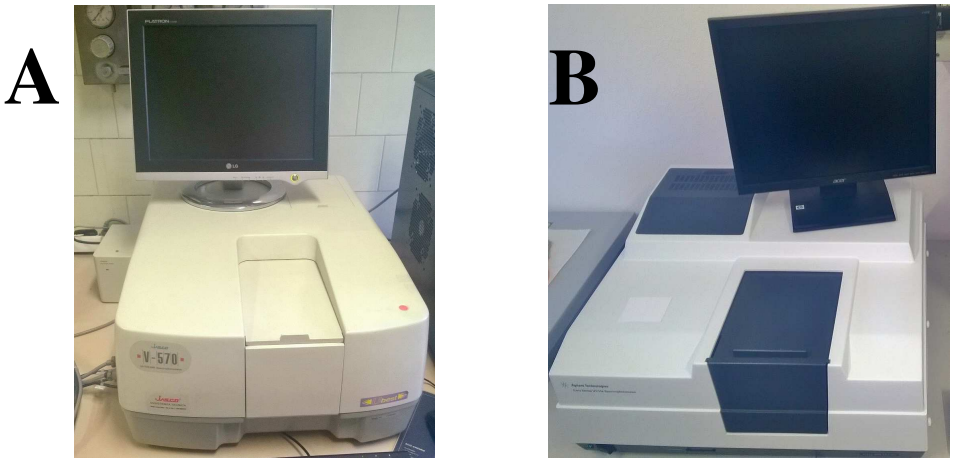

Figure 2.2 *JASCO V-570* (A) and *Varian Cary 300* (B) spectrophotometers, used during this Ph.D. thesis.

Figure 2.3 *Edinburgh Instruments FLS 920* fluorescence spectrometer apparatus, used during this Ph.D. thesis.

2.3 Time-resolved absorption/emission techniques

In order to unveil the complex mechanisms behind photochemical processes, time-resolved absorption/emission techniques are extremely useful. These techniques can be roughly distinguished based on the type of detection (emission or transient absorption) or the investigated time domain, even though the technical and physical concepts behind these powerful equipments can be completely different. As regarding transient absorption techniques, spectra and kinetics were measured in differential mode: the output is usually expressed as ΔOD (**Equation 2.6**) where A^* is the absorbance of the transient species and A_0 is that of the ground state.

$$\Delta OD(\lambda, t) = A^* - A_0 \qquad \textbf{Equation 2.6}$$

By combining **Equation 2.6** with the Lambert-Beer law in **Equation 2.3**, it is thus possible to calculate the concentration ΔC of the photogenerated transient species (**Equation 2.7**), if the molar extinction coefficient is known:

$$\Delta OD = \Delta\varepsilon \cdot l \cdot \Delta C \qquad \textbf{Equation 2.7}$$

$$\Delta C = C^* - C_0 = C_0 \cdot e^{-\frac{t}{\tau}} - C_0 \qquad \textbf{Equation 2.8}$$

where C^* is the molar concentration of excited molecules and C_0 is the concentration of molecules at ground state. From ΔOD, using the **Equation 2.8**, it is possible to determinate the life time (τ) of the light excited species. More importantly, in this case the parameter l, correlating ΔOD and ΔC, is not strictly the optical path of the cell, but rather the real fraction of the solution in the cell, which is pumped by the excitation source and analyzed by the light probe. As such, it could be better seen as an instrumental correction parameter that has to be known in order to perform the correlation reported in **Equation 2.7**.

Time-correlated single photon counting (TCSPC) is a time-resolved emission technique that is employed for the measurements of the lifetimes of emitting excited states. The basic principle of this instrument lies in the possibility of detecting single emitted photons and measure the delay time between excitation and emission. Experiments were recorded using a *PicoQuant Picoharp 300* apparatus (**Figure 2.4A**) equipped with subnanosecond LED sources (280, 380, 460, and 600 nm, 500-700 ps pulsewidth) powered by a *PicoQuant PDL 800-B* variable (2.5-40 MHz) pulsed power supply (a schematic representation is reported in **Figure 2.4B**). Detection is performed by a photomultiplier *Hamamatsu PMA 185* equipped with a monochromator. The decays were processed by an

integrated time-to-digital converter (TDC) and analyzed by means of *PicoQuant FluoFit Global Fluorescence Decay Analysis* software.

The time window of the experiment, dependent on the repetition rate, can arrive up to microseconds while the time resolution is strictly related to the pulse-width value, and is ca. 250 picoseconds. In a typical experiment the excitation pulse produces a "start signal", while the first photon emitted by the sample that is detected by the PMT yields the "stop signal"; the delay time between start/stop signals is measured. This experiment is repeated a certain number of times at a defined repetition rate until a sufficient number of counts is acquired to define a histogram of the decay probability. It is demonstrated that the decay probability histogram matches the decay of the emission of the excited state involved in the analysis. It is important to figure out that beside the emission from the sample there is a probability that photons of the excitation source are scattered by the sample solution and hit the detector, thus contributing to the probability histogram. The result is a convolution of the emission of the sample with the time profile of the laser source. From a practice viewpoint, when emission lifetimes are so short as to be comparable with the time profile of the excitation source (in general few nanoseconds) it is important to record, beside the experiment with the sample, the instrumental response factor (IRF), by repeating the experiment in the presence of a scatterer. Under this condition, the interpretation of the probability histogram is only possible after deconvolution and exponential fitting.

Figure 2.4 A) *PicoQuant Picoharp 300* TCSPC apparatus, used during this Ph.D. thesis. B) General scheme of a TCSPC apparatus: green line is the excitation beam; red line is the emission light; LH, laser head; F, filter; S, sample; MC, monochromator; PMT, photomultiplier tube; TDC, time-to-digital converter; LD, laser driver; PC, personal computer.

Nanosecond laser flash photolysis is a spectroscopic technique used for time-resolved absorption/emission measurements in a time window from 6-8 nanoseconds up to 0.1-1 seconds. Transient measurements were performed with a custom laser spectrometer (**Figure 2.5A**, a schematic representation is given in **Figure 2.5B**) comprised of a *Continuum Surelite II Nd:YAG* laser (1064 nm, FWHM = 6-8 ns), equipped with frequency doubled (532 nm), tripled (355 nm), or quadrupled (266 nm) options, an *Applied Photophysics* Xe light source, including a mod.720 150 W lamp housing, a mod. 620 power controlled lamp supply, and a mod. 03-102 arc lamp pulser. Laser excitation is

provided at 90° with respect to the white light probe beam. This latter is controlled by means of an *Oriel 71445* shutter, which opens only for ca. 100 milliseconds during the measurements, thus preventing continuous irradiation of the sample. Light transmitted (transient absorption measurements) or emitted (time-resolved emission measurements) by the sample is focused onto the entrance slit of a 300 mm focal length *Acton SpectraPro 2300i* triple grating, flat field, double exit monochromator equipped with a photomultiplier tube detector *Hamamatsu R3896*, used for kinetic studies at fixed wavelength, and a *Princeton Instruments PIMAX II* gated intensified CCD camera, used for spectral detection at fixed time-delays, employing a *RB Gen II* intensifier, a *ST133* controller and a *PTG* pulser. Signal from the photomultiplier is processed by means of a *LeCroy 9360* (600 MHz, 5 Gs/s). The switch between the two types of detection is obtained by means of a mirror comprised in the monochromator unit. Excitation source, lamp and shutter are computer-controlled by a LabVIEW (National Instruments) software routine (courtesy from Dr. Roberto Argazzi).

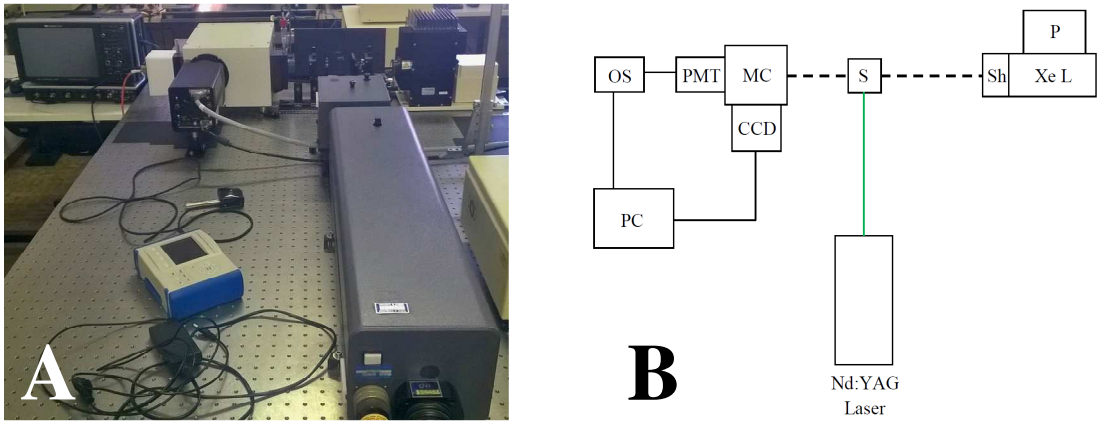

Figure 2.5 A) *Continuum Surelite II Nd:YAG* laser apparatus, used during this Ph.D. thesis. B) Schematic layout of the Nanosecond Laser Flash Photolysis setup: green line, excitation beam; black dashed line, white light probe beam; Xe L, xenon arc lamp; P, Xe lamp pulser; Sh, shutter; S, sample; MC, monochromator, PMT, photomultiplier tube; CCD, CCD camera; OS, oscilloscope; PC, personal computer.

2.4 Potentiodynamic electrochemical/photoelectrochemical techniques

In order to obtain experimental information on the redox properties of the investigated systems, potentiodynamic electrochemical techniques, such as cyclic voltammetry (CV), linear sweep (LS) and differential pulse voltammetry (DPV), have been used. These techniques are based on the possibility of studying electron transfer reactions between an electrode and a molecule in solution. By applying a variable external voltage it is possible to tune the virtual Fermi level of the electrode (a metal or more generally a conductor) thus allowing a "communication" with the electronic levels of the molecules in solution. This communication consists in a chemical reaction of the molecules in solution undergoing either oxidation (anodic process) or reduction (cathodic process) which is detected as a current. Considering a general reduction reaction ($A_{OX} + ne^- \rightarrow A_{RED}$) occurring at the interface between the electrode and the solution, in order to measure a current it is necessary that A_{OX} reaches the electrode and accepts electrons (e^-) from it. Therefore, the electron transfer process at the interface is controlled by two kinetic factors: *a)* the rate of diffusion (v_d) of A_{OX} to the electrode/solution interface and *b)* the rate of electron exchange (v_e) between the electrode and A_{OX}. For simple electron transfer reactions is often encountered the situation $v_e >> v_d$, therefore the observed current is only dependent on the diffusion process of the analyte to the electrode. In a typical reduction experiment, the supporting electrolyte (typically 0.1 M in water or organic solvent) is purged for 10 minutes with N_2. In both CV and DPV a voltage (E) is applied between the working electrode and the counter electrode (measured with respect to the reference electrode) and varied as a function of time (**Figure 2.6A**). A current is achieved at each potential value: the result is a cyclic voltammogram, plot of i vs. E (**Figure 2.6B**).

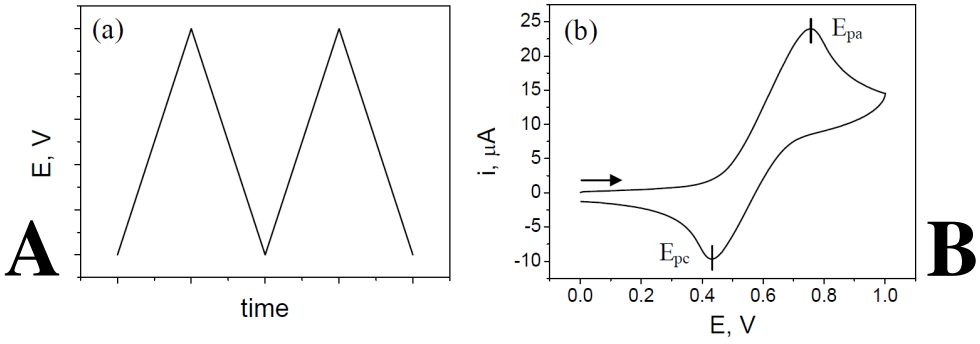

Figure 2.6 Cyclic voltammetry: (A) variation of the potential E as a function of time (two cycles); (B) example of the resulting cyclic voltammogram.

In CV the voltage is varied linearly with time (t), without illumination by a solar source (electrochemical measurements), from an initial potential to a final potential

followed by the opposite path (**Figure 2.6A**), with scan rate preset at the beginning of the experiment. Instead, in LS the potential variation is performed only in one way (anodic or cathodic), representing half of the total CV, and if is registered under illumination by Sun simulator, the change of *i* switching from light to dark is achieved.

In **Figure 2.6B** a typical CV behavior is reported representing the plot of the current *i* vs. *E*, in which two main features can be distinguished. Upon anodic scan (*i.e.* from negative to positive potentials) a positive wave is observed, ascribable to the oxidation of the analyte at the electrode/solution interface, featuring an anodic peak potential E_{pa}. Upon reversed scan (cathodic scan) a negative wave with a cathodic peak potential E_{pc} is detected, due to the reduction process. Important information can be obtained by CV about thermodynamic properties of the investigated system. In fact, if the redox process is reversible the cathodic and anodic peak potentials should follow the **Equation 2.9** (true for monoeletronic processes, $n = 1$).

$$E_{pa} - E_{pc} = 0.059 \text{ V} \qquad \textbf{Equation 2.9}$$

$$E^0 \approx E_{1/2} = \frac{E_{pa} + E_{pc}}{2} \qquad \textbf{Equation 2.10}$$

When these conditions are matched, according to **Equation 2.10** it is possible to calculate, with reasonably good approximation, the formal redox potential E^0 of the redox couple in analysis. Once determined the $E_{1/2}$ of a photoactive species, it is possible to calculate, through $E^{0\text{-}0}$ (**Equation 2.5**), the excited state redox potentials, ${}^*E_{OX}$ (**Equation 2.11**) and ${}^*E_{RED}$ (**Equation 2.12**), very important in the study of charge transfer dynamics between photoexcited sensitizers and semiconductor based photoelectrodes (**Section 1.5**).

$${}^*E_{OX} = E_{OX} - E^{0-0} \qquad \textbf{Equation 2.11}$$

$${}^*E_{RED} = E_{RED} + E^{0-0} \qquad \textbf{Equation 2.12}$$

As regarding DPV, potential pulses with fixed width are superimposed to a linear sweep potential scan (**Figure 2.7A**). The current values, before and after the pulses (black dots in **Figure 2.7A**), are taken and their difference is plotted versus the potential, yielding the voltammogram (**Figure 2.7B**) consisting in a wave featuring a peak potential E_p. Reversible processes display symmetric peaks in DPV, and, from the E_p value, the formal redox potential can also be calculated according to **Equation 2.13** (true for monoeletronic processes, $n = 1$), where ΔE is the potential pulse-width.

$$E^0 \approx E_{1/2} = E_p + \frac{\Delta E}{2}$$ **Equation 2.13**

While the reversibility of a process can be better discerned by means of CV, the very great advantage in the use of DPV is that it permits, comparing to CV, a better resolution of redox processes occurring at similar potentials, with lower intensity values of achieved current as drawback.

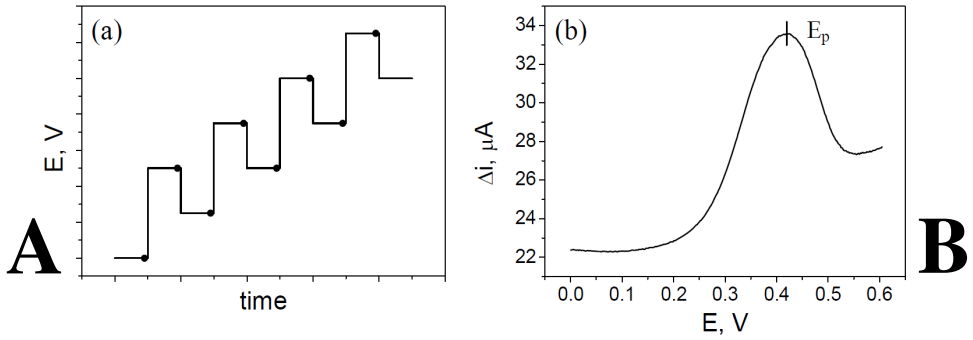

Figure 2.7 Differential pulse voltammetry: (A) variation of the potential *E* as a function of time (black dots, sampling time); (B) example of the resulting voltammogram.

Potentiodynamic electrochemical measurements were carried out with a PC interfaced *Eco Chemie Autolab/Pgstat 30* potentiostat workstation (**Figure 2.8a**) controlled by *GPES*. A conventional three-electrode cell assembly was adopted, with a saturated calomel electrode (SCE from Amel) as reference, a platinum bead (Pt from Amel) as counter and a glassy carbon (GC), or functionalized semiconductor based photoanodes, as the working electrode. For photoelectrochemical experiments (only LS) the same apparatus was coupled with a *LOT-Oriel* solar simulator (AM 1.5 G illumination, **Figure 2.8b**), and as the working electrode were used functionalized semiconductor photoanodes.

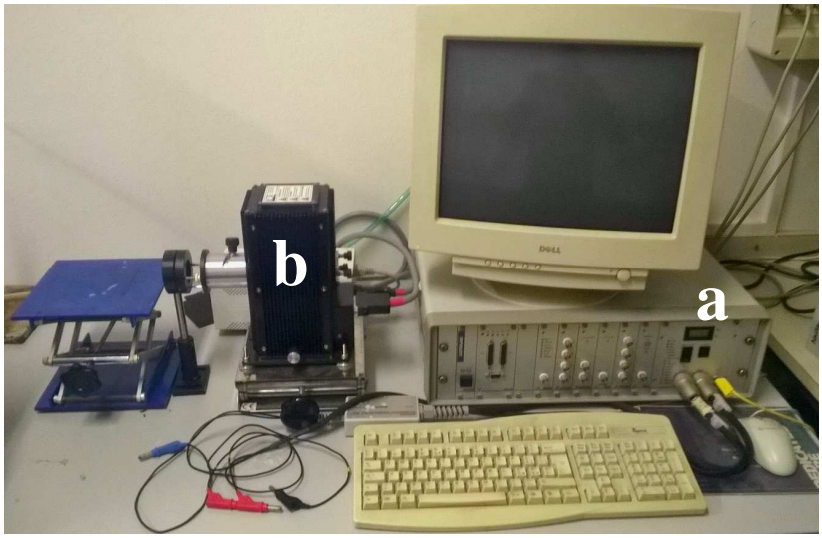

Figure 2.8 *Eco Chemie Autolab/Pgstat 30* potentiostat workstation (a) coupled with a *LOT-Oriel* solar simulator (b), used during this Ph.D. thesis.

2.5 Potentiostatic photoelectrochemical techniques

In potentiostatic techniques a constant external voltage is applied, while is recorded the variation of *i* under illumination by Sun simulator. In chronoamperometry the photocurrent (under illumination) or simply the current (in dark conditions), developed by faradaic processes caused by the imposed stepped potential at working electrode, is monitored as a function of time (*i* vs. *t*). Usually chronoamperometry generates high charging currents (**Figure 2.9**), which decay exponentially with time, as any RC circuit. Integrating the current, over relatively longer time intervals, gives a better signal to noise ratio (chronocoulometry). This technique was applied without solar illumination for the work reported in Errore. L'origine riferimento non è stata trovata., and the experiments were carried out on the *Eco Chemie Autolab/Pgstat 30* potentiostat workstation (**Figure 2.8**) used also for potentiodynamic measurements.

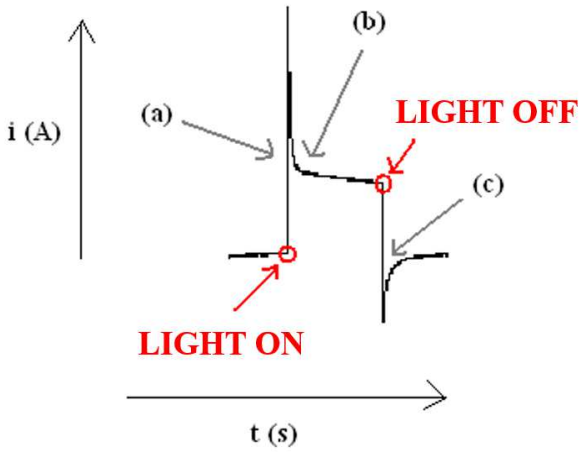

Figure 2.9 Example of photocurrent chronoamperometry decay of a typical sensitized semiconductor based photoanodes. After the illumination (a) the photocurrent sudden increase, due to electron transfer processes (charge injection) from all sensitizer molecules to semiconductor, achieving a maximum that subsequently drop exponentially (b), because of recombination processes that compete with charge injection, reaching stable values of photocurrent when the charge transfers are equilibrated. After turning off the light (c) the current drop to negative values, due to recombination that occur at oxidized sensitizer (back electron transfer from the semiconductor to dye molecules). After achieving a minimum negative value, the current raise exponentially to zero, restoring the initial equilibrium situation, before the light perturbation.

Incident photon-to-current conversion efficiency (IPCE) represents the quantum yield of generic solar converters, expressed in terms of the ratio between the number of e^-, collected in the external circuit, and the number of incident photons, at a particular wavelength, that striking the photoanode. In terms of measurable quantities, the IPCE value is given by **Equation 2.14**:

$$IPCE(\lambda) = \frac{n_e}{n_{h\nu}} = \frac{h \cdot c}{e} \frac{J}{\lambda \cdot P} = 1.24 \times 10^{-3} \frac{J}{\lambda \cdot P} \qquad \textbf{Equation 2.14}$$

where h is the Planck's constant [J s], c is the speed of light in vacuo [m s^{-1}], e is the electron charge [C] and their product give 1.24×10^{-3} [V m], J is the photocurrent density [A m^{-2}], λ is the photon wavelength [m] and P is the radiant power density [W m^{-2}] at the wavelength λ. The plot of IPCE as function of λ is called "action spectrum".

In the case of sensitized semiconductor based photoanodes, this quantum efficiency can be expressed as the product of three terms related to the key steps of the device working principle (**Equation 2.15**):

$$IPCE(\lambda) = LHE(\lambda) \cdot \phi_{inj} \cdot \eta \qquad \textbf{Equation 2.15}$$

where LHE is the light harvesting efficiency, ϕ_{inj} is the electron injection (from sensitizer to semiconductor) quantum yield and η is the efficiency of e^- collected at the photoanode. Light harvesting efficiency is the fraction of incident light that is absorbed by the dye-coated mesoporous film. Due to the small size of semiconductor nanoparticles (~20 nm), light scattering from a thin film (10 μm or lower) is almost negligible, so the transparency is sufficiently high that Lambert-Beer law can be successfully applied (**Equation 2.16**):

$$LHE = \frac{P_0}{P} = 1 - 10^{-A(\lambda)} \qquad \textbf{Equation 2.16}$$

where A is the absorbance of the sensitizer, obtained subtracting the background bare semiconductor absorption. The absorbance could be expressed also as (**Equation 2.17**):

$$A = 1000 \cdot \varepsilon \cdot C \cdot t \qquad \textbf{Equation 2.17}$$

with ε molar absorptivity of the dye [M^{-1} cm^{-1}], C dye concentration [M], t film thickness [cm] and 1000 is the volume conversion factor. From IPCE and LHE values is possible to determinate (**Equation 2.18**) the Absorbed Photon-to-Current Efficiency (APCE):

$$APCE = \frac{IPCE(\lambda)}{1 - 10^{-A(\lambda)}} \qquad \textbf{Equation 2.18}$$

The photocurrent in IPCE experiments was acquired on an *Amel mod.552* potentiostat (**Figure 2.10a**), under the illumination generated by an air cooled *Luxtel* 175 W Xe lamp (**Figure 2.10b**), coupled to an *Applied Photophysics* monochromator (**Figure 2.10c**). Incident irradiance was measured with a calibrated silicon photodiode (**Figure 2.10d**). A conventional three-electrode cell assembly was adopted, with a saturated calomel electrode (SCE from Amel) as reference, a platinum bead (Pt from Amel) as counter and functionalized semiconductor based photoanodes, as the working electrode.

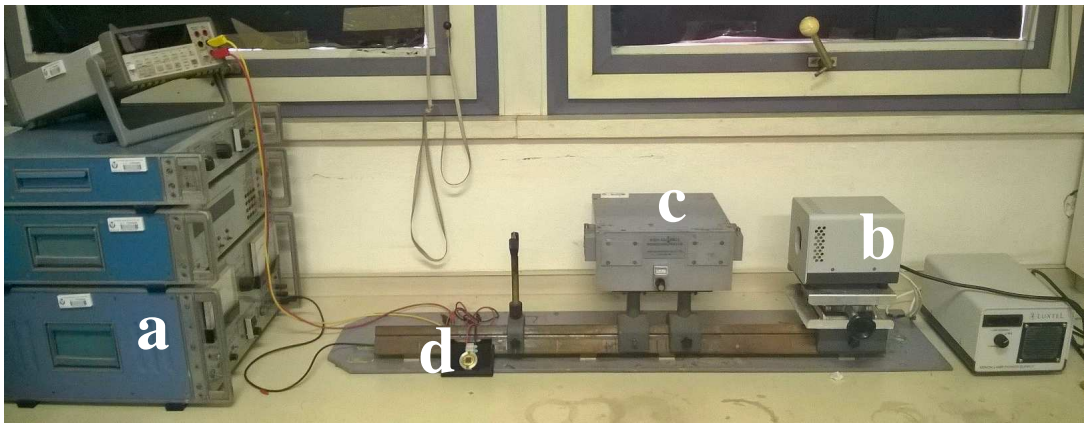

Figure 2.10 *Amel mod.552* potentiostat workstation (a) coupled with a *Luxtel* 175 W Xe lamp (b) and an *Applied Photophysics* monochromator (c), used during this Ph.D. thesis. Silicon photodiode (d) was employed in order to measure the incident irradiance.

Electrochemical impedance spectroscopy (EIS) measurements provide data on both electrode capacitance and charge transfer kinetic, giving valuable mechanistic information. The main advantage of EIS is the possibility to use a simple electronic model to represents an electrochemical cell, due to the analogy between electrode interfaces, where electrochemical reactions occur, and electric equivalent circuits, consisting in specific combination of resistors and capacitors. It is possible to use the alternate current (AC) circuit theory to characterize the electrochemical system (e.g. reaction mechanisms, charge transfer kinetics, physical properties), due to the correlation of its impedance behaviour with one or more equivalent circuits, simply extracting numerical values by fitting the experimental data from the circuit model.

During EIS experiments, a time-dependant signal, usually a sinusoidal perturbation of the constant bias potential (E) with frequency f (0.01 Hz < f < 100 MHz), is applied to the working electrode and the photocurrent (under illumination), or simply the current (in dark conditions), is registered. The excitation signal, imposed to the electrochemical cell, is typically a small potential (1 mV - 10 mV), so the response will be pseudo-linear, resulting in a sinusoidal i behaviour at the same frequency of the sinusoidal E applied, but shifted in phase (**Equation 2.21**). By varying the excitation frequency, processes with different time constants can be resolved. It should be noted that electrochemical cells are in general not linear: in fact, doubling the voltage will not necessarily double the current, but they can be considered pseudo-linear focusing on a small portion of the J-V characteristics (**Figure 2.11A**). The further analysis of the frequency dependant response, using an electronic model, can separate the different aspects of charge transport, charge trapping and charge transfer at the interface with electrolyte.

The excitation signal, expressed as function of time, has the form **Equation 2.19**:

$$E_t = E_0 \sin(\omega t) \qquad \textbf{Equation 2.19}$$

where E_t is the potential at time t, E_0 is the amplitude of the signal and ω is the radial frequency, related to the frequency expressed in hertz (f) by **Equation 2.20**.

$$\omega = 2\pi f \qquad \textbf{Equation 2.20}$$

$$I_t = I_0 \sin(\omega t + \phi) \qquad \textbf{Equation 2.21}$$

In a linear system, the response signal, I_t is shifted in phase (φ) and has a different amplitude than I_0 (**Equation 2.21**). The impedance (Z) denote the opposition to the flow of e^- and so, in analogous to Ohm laws, it can be written as reported in **Equation 2.22**:

$$Z = \frac{E_t}{I} = \frac{E_0 \sin(\omega t)}{I_0 \sin(\omega t + \phi)} = Z_0 \frac{\sin(\omega t)}{\sin(\omega t + \phi)} \qquad \textbf{Equation 2.22}$$

Reporting the sinusoidal signal E_t, on the x-axis of the J-V plot, vs. the sinusoidal response I_t, on the y-axis, the result is an oval shape known as "Lissajous figure" (**Figure 2.11B**), the first accepted method for impedance measurement.

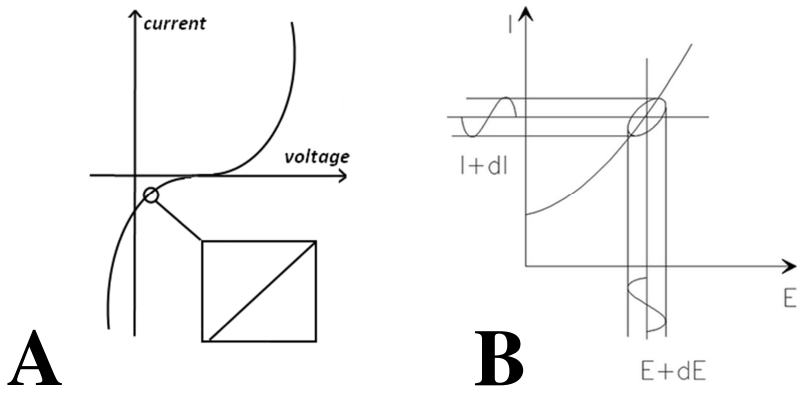

Figure 2.11 (A) E_t vs. I_t curve showing pseudo-linearity for little potential perturbation. (B) Graphical interpretation of the "Lissajous figure".

With the Euler relationship (**Equation 2.23**), Z can be also represented as a complex number (**Equation 2.24**), considering $j = \sqrt{-1}$ to avoid confusion with the electric current i.

$$e^{j\phi} = \cos\phi + j\sin\phi \qquad \textbf{Equation 2.23}$$

$$Z(\omega) = Z_0 e^{j\phi} = Z_0(\cos\phi + j\sin\phi) \qquad \textbf{Equation 2.24}$$

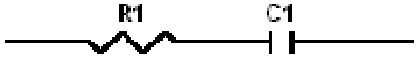

Figure 2.12 Simple electrical circuit composed by a resistor (**R**) in series with a capacitor (**C**).

Impedance represents a more general concept of the resistance defined by the classical Ohm law. In AC circuits, also capacitors and inductors impede the flow of e^- rather than resistors. Let consider for example a simple circuit composed by a resistor (**R**) in series with a capacitor (**C**) represented in **Figure 2.12**. The total impedance of the circuit

(Z_{tot}) is given by the sum of the single contributions, Z_R and Z_C for the resistor and the capacitor respectively (**Figure 2.13a**) according to **Equation 2.25**. Instead, for elements in parallel the Z_{tot} is the inverse of the sum of the inverse of singles Z (**Equation 2.26**).

$$Z_{tot} = Z_R + Z_C = R - jX_C \qquad \textbf{Equation 2.25}$$

$$\frac{1}{Z_{tot}} = \frac{1}{Z_R} + \frac{1}{Z_C} \qquad \textbf{Equation 2.26}$$

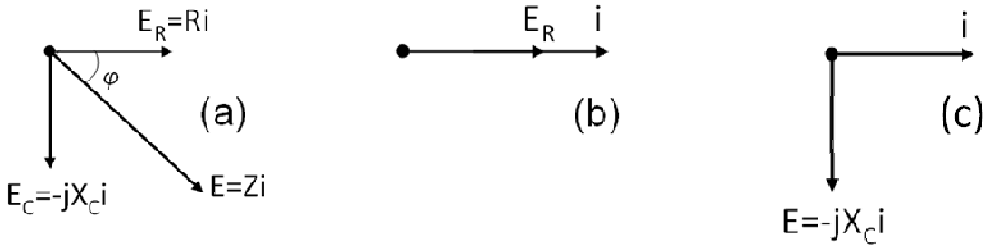

Figure 2.13 Vector representation of the relation between the *E* applied and the flowing *i* (a) in the circuit represent in **Figure 2.12**, (b) in only a resistor **R** and (c) in only a capacitor **C**. In **R**, the phase angle between *E* and *i* is 0°, so the two vectors are superimposed. In **C** the phase angle is 90° and, reporting *i* on the x-axis, the capacitive vector has an imaginary part for convention because coincident with the y-axis.

In **Equation 2.25**, R is the classic Ohm resistance and X_C is the capacitive reactance. It is evident that the impedance of a resistor (Z_R) is equal to the resistance value (R), due to its independency by f and so without imaginary component, because there is no phase angle shift between the voltage and the current flowing through the **R** (**Figure 2.13b**). With only a real Z component, i through **R** remain in phase with the E across the resistor. Capacitors instead, have only an imaginary component, because i through a **C** is 90° phase shifted in respect to E (**Figure 2.13c**), as can be demonstrated from **Equation 2.27**. In addition, Z_C is inversely proportional to f.

$$i = C\frac{dE}{dt} = C\frac{d(E_0 \sin(\omega t))}{dt} = \omega C \cos(\omega t) = \frac{E}{X_C}\sin(\omega t + \frac{\pi}{2}) \qquad \textbf{Equation 2.27}$$

A common way to represent Z data is the Nyquist plot, where the real part of impedance (Z') is reported on the x-axis, while the imaginary part (Z'') on the y-axis. In this characteristic, the y-axis is negative and each point corresponds to the impedance at one frequency. The main limitation in the Nyquist plot regards the impossibility to know at which f corresponds a single data point. The Bode plots allow to gain these additional information, by representing the logarithm of f, on the x-axis, vs. the absolute values of the impedance ($|Z| = Z_0$) and the phase shift angle (φ), both on the y-axis. In **Figure 2.14** are reported Nyquist and Bode plots for a circuit composed of parallel **R** and **C** elements (**Equation 2.26**).

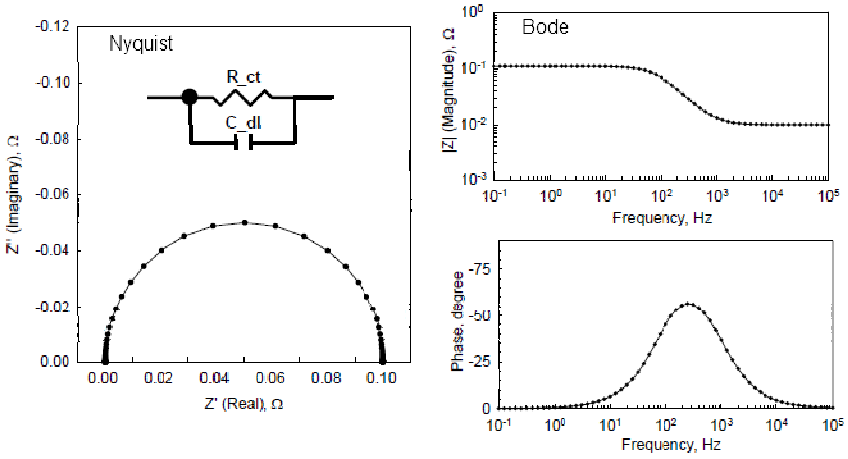

Figure 2.14 Nyquist (left) and Bode (right) plots for the reported RC circuit.

Once an experiment is complete, the raw data, at each measured *f*, consists in the real and imaginary component of both *E* applied and *i* achieved. These data are then processed and result possible to obtain φ and Z_{tot}, for each *f*, as well as many other impedance functions. An important step, in the elaboration process, is the choice of the correct equivalent circuital model, which well fit the experimental data. From this model, it is possible to extrapolate the values related to the physical and chemical properties of the investigated system. EIS measurements are repeated for different *E* values, in order to describe the system in the full potential range and to determine the active charge transfer processes, both under dark and illumination condition. Although the circuital elements have a detailed mathematical description, its physical interpretation, and so their association at the different electrode interfaces, is probably the most challenging part of the experiment. The physical descriptions of the most common circuital elements are reported in **Table 2.1**.

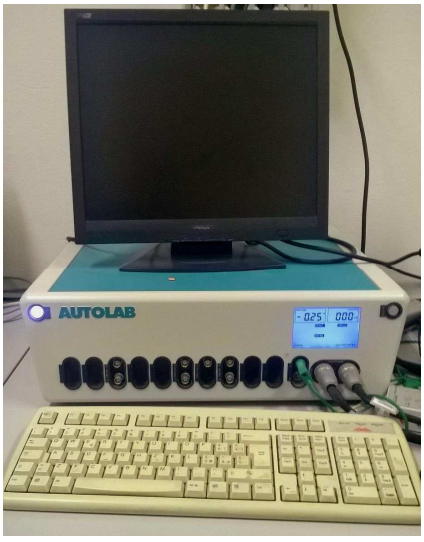

Figure 2.15 *Autolab PGSTAT 302/N* workstation, used during this Ph.D. thesis.

EIS experiments were performed on an *Autolab PGSTAT 302/N* workstation equipped with *FRA2.v10* frequency response analyzer (**Figure 2.15**), controlled by *Nova*

1.10. A conventional three-electrode cell assembly was adopted, with a saturated calomel electrode (SCE from Amel) as reference, a platinum bead (Pt from Amel) as counter and semiconductor based anodes, as the working electrode. The impedance responses were then fitted using *ZView* software by using combinations of the following circuital elements.

Table 2.1 Summary physical description of the most common circuital elements, which are used in equivalent circuits to approximate the investigated systems during EIS measurements.

Circuital element	***Symbol***	***Physical meaning***
Resistor	**R**	Used to estimate: limitation in electronic conductivity inside the material bulk; resistance to the polarization at values different to the open circuit voltage; charge transfer processes through interfaces; resistance due to the solution or to the cell setup, employed for the measurements.
Capacitor	**C**	Used to explain the charge accumulation at interfaces, where a double layer is formed.
Constant phase element	**CPE**	Used to approximate an interface that act as a non-ideal capacitor, showing a frequency strong dependence. This behaviour is probably due to high porosity, or non-homogeneity, of a surface that can generate charge dissipation process, which are no describe by an ideal capacitor.
Warburg element	**W**	Used to describe diffusive phenomena, inside the solution, of redox species that are generated at working electrode.

2.6 Chapter 2 - Figures index

CHAPTER 3. SYNTHESIS AND CHARACTERIZATION OF A NEW RU-BASED POLYPYRIDINE BINUCLEAR ASSEMBLY DEPOSITED ON TiO_2 ELECTRODES FOR PHOTOINDUCED WATER OXIDATION

3.1 Chapter 3 - Abstract

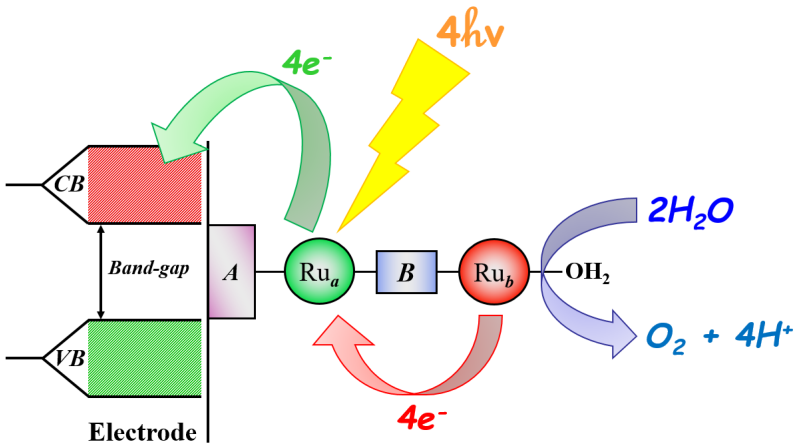

Figure 3.1 Schematization of the synthesized binuclear assembly constituted by two Ru-based polypyridine complexes, the sensitizer (green Ru_a) and the single-site catalyst (red Ru_b), bound to each other via the bridging ligand (blue *B*) and grafted to the semiconductor surface through the anchor group (purple *A*).

Molecular photoinduced water splitting, with ruthenium based sensitizer-catalyst assembly, represents an attractive and pursued research field, offering the possibility to organize and control the cascade of electron transfer events leading water oxidation.

Herein we report the synthesis and the characterization of a new binuclear compound (**3**), constituted by two distinct Ru-based polypyridine complexes, the sensitizer (**2**) and the single-site catalyst (**1**), linked together in order to obtain a supramolecular assembly able to achieve solar water splitting (**Figure 3.1**). The photoelectrochemical results obtained on sensitized **3**/TiO_2 photoanodes, demonstrated that the binuclear complex is able to inject electrons into the semiconductor, reaching a stable photoanodic response on the order of ~300 μA/cm^2, under AM 1.5 G illumination (420 nm cut-off filter) and 0.3 V vs. SCE applied potential bias, in the presence of ascorbic acid as sacrificial hole scavenger.

Unfortunately, the dyad was not able to drive photoinduced water oxidation, with a significant improvement with respect to the sensitizer unit alone. This is ostensibly due to unfavourable competition of the charge separation with recombination processes, and to the demanding thermodynamics for generating the active Ru(V), which was electrochemically individuated as the active catalytic intermediate for water oxidation. Therefore, a better tuning of the redox properties of the catalyst, to lower the oxidation potential of the high-valent redox active centre will be required.

3.2 Chapter 3 - Introduction

The heterogenization of molecular systems for solar water splitting has intrigued many scientists, due to the possibility of achieving a better organization and control, by separating the overall processes into half reactions occurring at the separate compartments of a photoelectrochemical cell. Most of the research work, conducted in this field, concerns the design and the optimization of the water oxidation part, while, very commonly, hydrogen is simply evolved at a dark catalytic counter electrode under applied bias. This predominant interest about the photoanodic assembly is largely justified by the fact that the water oxidation is considered the ubiquitous part in sustainable fuel forming reactions and by the convenience of having a wider arsenal of optimized materials at disposal as well.

The water oxidation catalyst (WOC) plays a fundamental role in "dye sensitized photoelectrochemical cells" (DSPEC) photoanode, since the complex kinetics, imposed by multi-electron oxygen evolution, would result in exceedingly high activation barriers for the direct hole transfer from the photo-oxidized dye to water molecules, resulting in predominant recombination events. In order to enable the rational design of molecular complexes that can fulfill this requirement, extensive research has been directed toward the elucidation of the fundamental steps of H_2O oxidation.

The first WOC, studied for water splitting in the homogeneous phase, was the ruthenium polypyridine binuclear complex (blue dimer) reported by Meyer and co-workers in 1982,[1,2] characterized by the presence of a Ru-O-Ru bridge and of two adjacent water molecules coordinating each Ru centre (**Figure 3.2**).

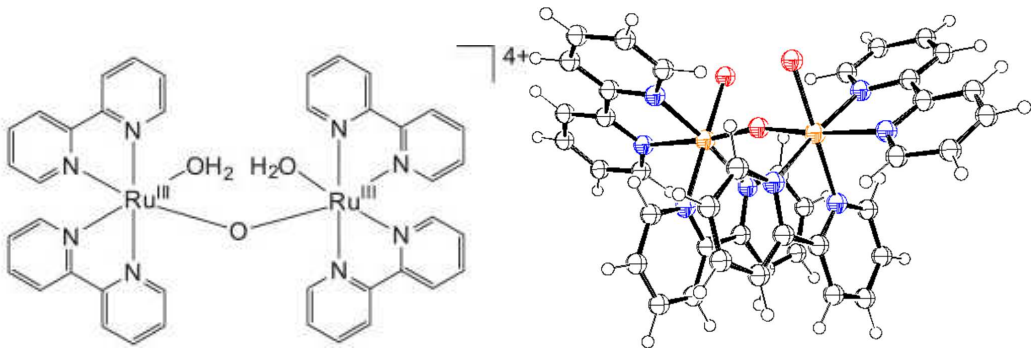

Figure 3.2 Schematic and X-ray structures of the blue dimer reported by Meyer and co-workers. Ruthenium atoms are indicated in orange, oxygen atoms in red and nitrogen atoms in blue. Hydrogens bound to the water molecules are removed for clarity.[3]

The presence of the μ-oxo bridge in the blue dimer promotes a strong electronic coupling between the two metal centres that facilitates the stabilization of the complex at high oxidation states by electronic delocalization. The mechanism proposed by Meyer and

co-workers (**Figure 3.3**) involved four proton-coupled electron transfer steps, which give access to a high-valent Ru(V,V) intermediate (***2***, **Figure 3.3**), subsequently attacked by H_2O generating a hydroperoxo species (***4***, **Figure 3.3**) that is intra-molecularly oxidized by the second Ru centre, ultimately resulting in the release of O_2.

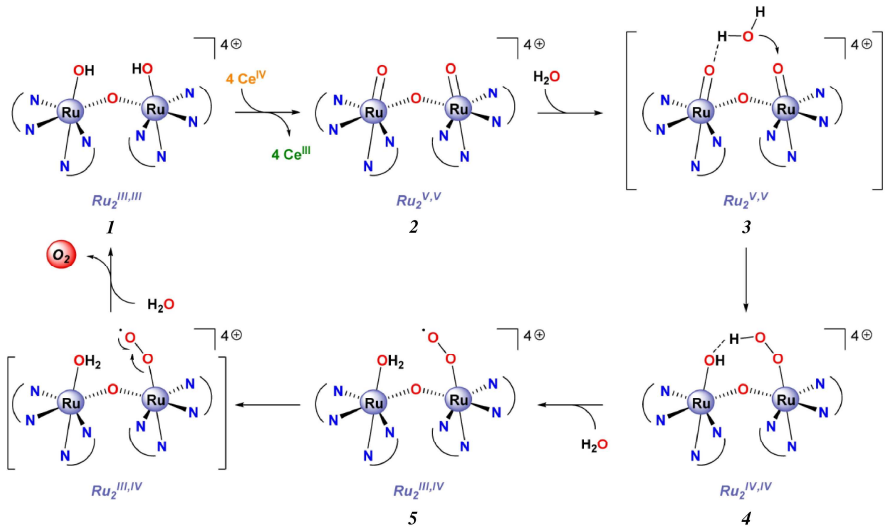

Figure 3.3 Proposed mechanism of oxygen evolution in μ-oxo bridged blue dimer-type Ru(II) complexes.[4]

Generally ruthenium blue dimers were characterized by moderate-to-low water oxidation activities, believed to be related to the instability of the μ-oxo bridge, which upon cleavage results in the breakdown of the dimeric structure into non-active monomeric ruthenium complexes. Research therefore focused on finding more stable organic ligands capable of bringing two ruthenium centres together in close proximity, which would enable more efficient oxygen evolution.

Because of the multi-metallic core of the natural oxygen evolving complex (OEC) in photosynthetic organisms,[5] it was long envisioned that artificial molecular WOCs must accommodate multiple metal centres to cope with the accumulation of the four oxidizing equivalents needed for water oxidation. The initial lack of reports on single-site WOCs led to the creation of a paradigm, which claimed that at least two metal centres were required for H_2O oxidation to occur. However, this early belief has now been disproved, and today there exists a variety of single-site catalysts that can mediate the four-electron oxidation of water. Molecular single-site catalysts offer the possibility of straightforward ligand design, synthesis and characterization. The relative ease, with which the ligand environment can be tuned in these molecular systems, both electronically and sterically, makes them amenable for structure-activity relationship studies. More importantly, the incorporation and/or attachment of these catalysts to viable supramolecular assemblies for H_2O photosplitting, resulting from the linkage to a chromophore, is also greatly facilitated.

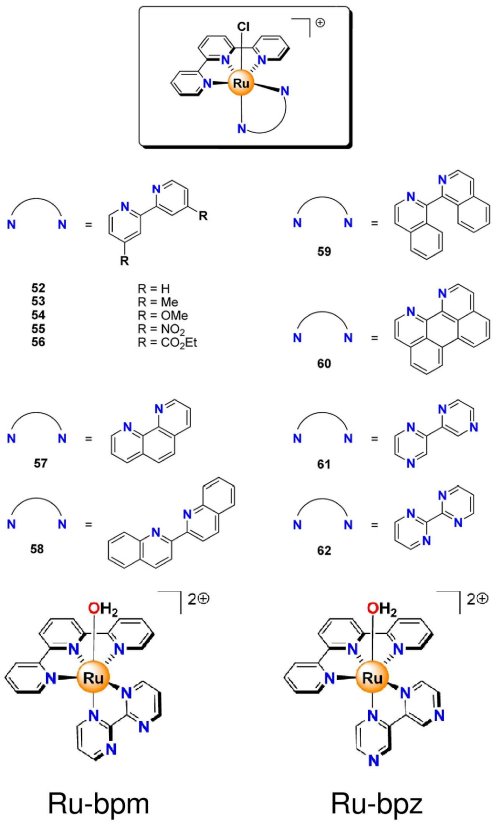

Figure 3.4 Family of precursor complexes based on different polypyridine ligand and single-site WOC based on bipyrimidine (bpm, Ru-bpm) and bipirazine (bpz, Ru-bpz) ligands investigated by Meyer et. al.[4]

The first proofs that the four-electron oxidation of H_2O could occur on single-site metal complexes was provided by the group of Thummel in 2005.[6] Solid evidence that water oxidation proceeded through single-site catalysis was provided by Meyer and co-workers in 2008[7,8] during the study of complexes obtained by substituting Cl^- with H_2O in the family reported in **Figure 3.4**. It was proposed that these single-site ruthenium WOCs catalysed the oxidation of water through a seven-coordinated ruthenium centre, involving a peroxide intermediate, $[Ru^{IV}–OO]^{2+}$. Starting from $[Ru^{II}–OH_2]^{2+}$, the addition of 3 equivalents of Ce^{IV} resulted in the formation of the key intermediate $[Ru^{V}=O]^{3+}$, which undergoes nucleophilic attack by H_2O molecule to generate a peroxide intermediate $[Ru^{III}–OOH]^{2+}$ via the WNA mechanism (**Section 1.6**). Further oxidation of this species through proton-coupled oxidation, formed the $[Ru^{IV}–OO]^{2+}$, finally leading to O_2 evolution (**Table 3.1** and **Figure 3.5**).

Table 3.1 Summary reactions of Meyer Ru single-site catalyst cycle, with relative rate constant where indicated.

Reaction	***Rate constant***	
$[Ru^{II}–OH_2]^{2+} + Ce^{4+} \rightarrow [Ru^{III}–OH]^{2+} + Ce^{3+} + H^+$	2.4×10^{2} $M^{-1}s^{-1}$	**Equation 3.1**
$[Ru^{III}–OH]^{2+} + Ce^{4+} \rightarrow [Ru^{IV}=O]^{2+} + Ce^{3+} + H^+$	rapid	**Equation 3.2**
$[Ru^{IV}=O]^{2+} + Ce^{4+} \rightarrow [Ru^{V}=O]^{3+} + Ce^{3+}$	5.0 $M^{-1}s^{-1}$	**Equation 3.3**
$[Ru^{V}=O]^{3+} + H_2O \rightarrow [Ru^{III}–OOH]^{2+} + H^+$	9.6×10^{-3} s^{-1}	**Equation 3.4**
$[Ru^{III}–OOH]^{2+} + Ce^{4+} \rightarrow [Ru^{IV}–OO]^{2+} + Ce^{3+} + H^+$	-	**Equation 3.5**
$[Ru^{IV}–OO]^{2+} + H_2O \rightarrow [Ru^{II}–OH_2]^{2+} + O_2$	7.5×10^{-4} s^{-1}	**Equation 3.6**
$[Ru^{IV}–OO]^{2+} + Ce^{4+} \rightarrow [Ru^{V}–OO]^{3+} + Ce^{3+}$	13 $M^{-1}s^{-1}$	**Equation 3.7**
$[Ru^{V}–OO]^{3+} + H_2O \rightarrow [Ru^{III}–OH]^{2+} + O_2 + H^+$	-	**Equation 3.8**
$[Ru^{III}–OH]^{2+} + Ce^{4+} \rightarrow [Ru^{IV}=O]^{2+} + Ce^{3+} + H^+$	-	**Equation 3.9**

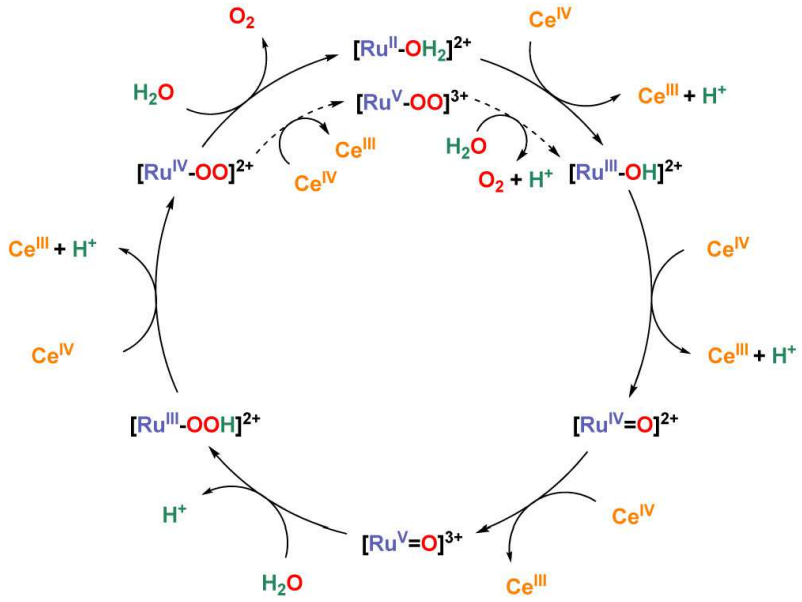

Figure 3.5 Mechanism of water oxidation by single-site Ru catalysts proposed by Meyer et al. for Ru-bpm and Ru-bpz type complexes.[4] Detailed reactions are reported in **Table 3.1**.

The catalytic studies, carried out with these complexes, were successively extended to the entire family of compounds, varying the polypyridine ligands.[9] For each, the catalytic activity in water oxidation was maintained, with mechanism similar to what reported in **Figure 3.5**, and was observed that a modification of electronic density on Ru^{II} centre occurs changing the coordination environment. Due to this fact, it is possible, with the proper ligand, to lower the redox properties of the metal, decreasing the overpotential (η) toward water oxidation.

In order to drive water splitting in heterogeneous phase single-site catalyst must be modified with anchoring groups for modification of semiconductor electrodes.[9,10] Electrochemical measurements showed that the catalysts, anchored on bare ITO or FTO/TiO_2, preserved its properties. Looking forward to the realization of photoanodes for water splitting in DSPEC, a further step involves the design of covalently linked sensitizer-WOC assemblies, where the loading ratio, between the chromophore and the catalyst, is optimized and the intramolecular electron transfer kinetics are facilitated by the close proximity of the two units. Meyer and co-workers have carried out several attempts to immobilize supramolecular assemblies, composed of Ru polypyridine sensitizers and Ru based single-site WOCs, onto the surface of nanoporous semiconductive metal oxides. In **Figure 3.6** it is shown a recent example (2013) of the chromophore-catalyst binuclear assembly $[(PO_3H_2)_2bpy)_2Ru_a^{II}(4\text{-Mebpy-}4'\text{-bimpy})Ru_b^{II}(tpy)(OH_2)]^{4+}$ where Ru_a (green) and Ru_b (red) identify the ruthenium cores of the dye and of the single catalyst respectively.[11]

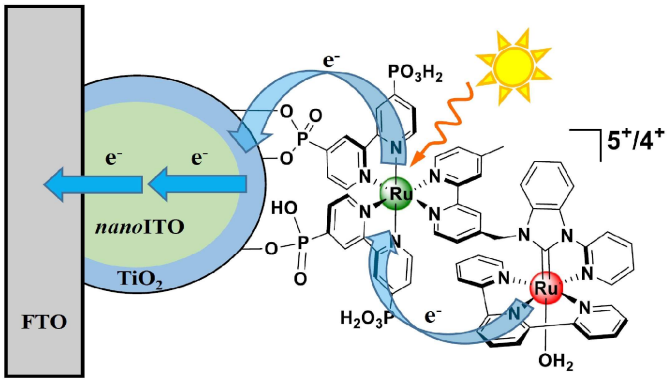

Figure 3.6 Schematic operational principles of the binuclear chromophore-catalyst supramolecular assembly developed by Meyer, attached on core-shell (ITO/TiO2) particles.[11]

As illustrated in **Section 1.5**, the metal-to-ligand charge transfer (MLCT) excitation of the chromophore results in excited state formation (*S) and electron (e^{-}) injection into the conduction band (CB) of the semiconductor, triggering the sequence of multi-hole (h^{+}) transfers from Ru_a to Ru_b, then, at last, to H_2O. In order to underline the difficulties of artificial photosynthesis, three sequential single-photon-single-electron excitation events are required for a single oxidative activation cycle to reach the key precursor intermediate $[Ru_a^{III}–Ru_b^{IV}=O]^{5+}$ which undergoes attack by water.[11] Given that, back electron transfer occurs on a timescale of micro- to milliseconds and three injection-oxidation cycles are required to activate the catalyst, its reactive form is present in trace amounts under ambient solar illumination and efficiencies for water splitting are negligible. Thus, the retardation of recombination events and the acceleration of electron transport across the semiconductor film acquire a paramount importance, for achieving success with covalent sensitizer-catalyst dyads.

Herein we report on the preparation and the characterization of a new binuclear compound (**3**), structured as $[Ru_a^{II}–Ru_b^{II}–OH_2]^{4+}$, which was prepared during the first Ph.D. period (2012-2013). In our design, two distinct units constitute this dyad: a Ru-based polypyridine sensitizer (**2**) and the cited above Ru-bpm (**1**, **Figure 3.4**) as single-site catalyst. The single units have been fully characterized before their linkage to constitute the supramolecular assembly **3**, intended to drive photoinduced solar water splitting.

3.3 Chapter 3 - Experimental section

3.3.1 Materials

Ruthenium(III) chloride hydrate ($Ru^{III}Cl_3 \times 3H_2O$) was from Alfa Aesar.

Dichloro(*p*-cymene)ruthenium(II) dimer (Ru^{II}*p*-cymene), 2,2'-bipyrimidine (*bpm*) 95% grade, 2,2'-bipyridyl-4,4'-dicarboxylic acid (*H_2bpy*) 98% grade, 2,2':6',2''-terpyridine (*tpy*) 98% grade, lithium chloride (LiCl) anhydrous 99%, lithium perchlorate ($LiClO_4$) ACS reagent ≥95.0%, ammonium hexafluorophosphate (NH_4PF_6) ≥95%, tetrabutylammonium hexafluorophosphate ($TBAPF_6$) purum ≥98.0%, silver nitrate ($AgNO_3$) ACS reagent ≥99.0%, silver trifluoromethanesulfonate (TfOAg) ≥99%, sodium hydroxide (NaOH) reagent grade ≥98.0% anhydrous pellets, sodium bicarbonate ($NaHCO_3$) ACS reagent ≥99.7%, anhydrous sodium sulfate (Na_2SO_4), absolute ethanol (EtOH) puriss. p.a. ACS reagent ≥99.8%, anhydrous diethyl ether (EtOEt) ACS reagent ≥99.0%, anhydrous acetonitrile (ACN) 99.8%, anhydrous methanol (MeOH) 99.8%, anhydrous toluene (TOL) 99.8%, ethyl acetate (EtAc) HPLC grade ≥99.7%, dimethyl sulfoxide (DMSO) ≥99.5%, anhydrous *N,N*-dimethylformamide (DMF) 99.8%, dichloromethane (CH_2Cl_2) HPLC grade ≥99.8%, 3-Methoxy-3-methyl-1-butanol (3-MeO-3-Me-1-ButOH) ≥98%, ascorbic acid 99% grade, trifluoromethanesulfonic acid (TfOH) reagent grade 98%, sulfuric acid (H_2SO_4) ACS reagent 95.0-98.0%, perchloric acid ($HClO_4$) ACS reagent 70%, nitric acid (HNO_3) ACS reagent puriss. p.a. ≥69%, triethylamine (Et_3N) ≥99%, sephadex LH-20, aluminum oxide (Al_2O_3) activated basic particle size ~150 mesh with 58 Å of pore size (surface area 155 m^2/g), celite, thin layer chromatography (TLC) silica gel on Al foils with fluorescent indicator and the deuterated solvents were from Sigma Aldrich.

18-NRT TiO_2 colloidal paste was purchased from Dyesol.

TEC 8 (8 Ω/□) fluorine tin oxide (FTO) 20×20 cm conductive glass slides were obtained from Pilkington.

All reagents, unless otherwise stated, were used as received.

3.3.2 Synthesis of [Ru^{III}(tpy)Cl$_3$]

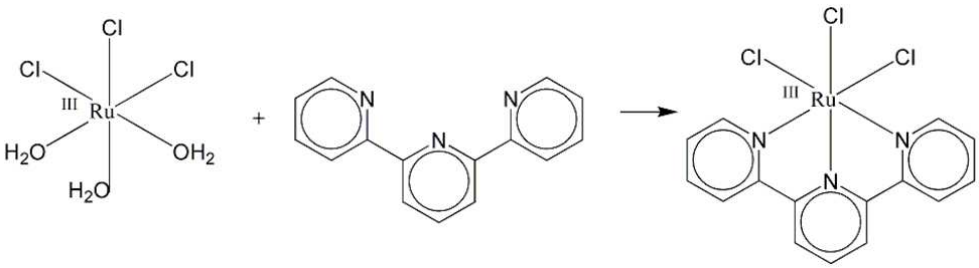

Figure 3.7 Reaction scheme of [Ru^{III}(*tpy*)Cl$_3$] synthesis.

This synthesis (**Figure 3.7**) was adapted from literature.[12] In a 250 ml round flask, 231.7 mg of Ru^{III}Cl$_3$×3H$_2$O (MW = 261.43 g/mol, 0.89 mmol), 178.3 mg of *tpy* (MW = 233.27 g/mol, 0.76 mmol) and 2.2 g of LiCl (42.39 g/mol, 52 mmol) were added to 125 ml of EtOH. The dark solution was refluxed for 3 hours, under vigorous magnetic stirring. The reaction was monitored with TLC (EtOH), by following the disappearance of the ligand. After that, the solution was cooled at room temperature and filtered. The brown-grey precipitate was washed in first with EtOH (3×30 ml) and then with EtOEt (3×30 ml), and finally dried at room temperature. 293.7 mg of [Ru^{III}(*tpy*)Cl$_3$] (MW = 440.70 g/mol, 0.67 mmol, 88% yield) were obtained. This compound was used without further purification and the characterization was not perform due to its paramagnetism.

3.3.3 Synthesis of [Ru^{II}(tpy)(bpm)Cl]PF$_6$

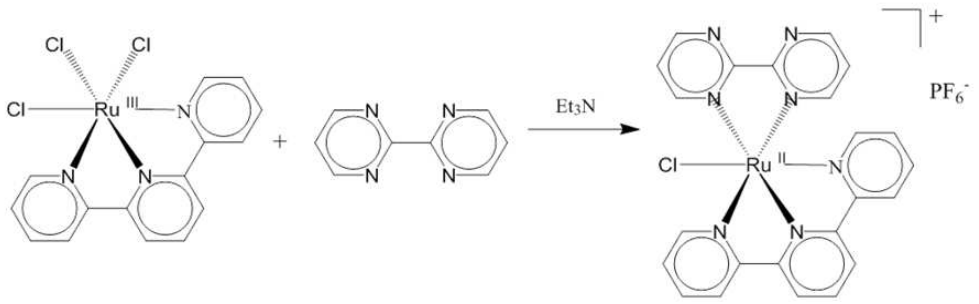

Figure 3.8 Reaction scheme of [Ru^{II}(*tpy*)(*bpm*)Cl]PF$_6$ synthesis.

This synthesis (**Figure 3.8**) was adapted from literature.[13] In a 100 ml round flask, 213.3 mg of [Ru^{III}(*tpy*)Cl$_3$] (MW = 440.70 g/mol, 0.48 mmol), 116.6 mg of *bpm* (MW = 158.16 g/mol, 0.74 mmol) and 2 ml of Et$_3$N (MW = 101.19 g/mol, ρ = 0.726 g/ml, 14 mmol) were added to 21 ml of 2:1 EtOH/H$_2$O solution. The dark solution was refluxed for 6 hours, under vigorous magnetic stirring. The reaction was monitored with TLC (EtOH), following the disappearance of the metal precursor and the formation of the red final product. After cooling at room temperature, 5 ml of an aqueous saturated NH$_4$PF$_6$ (~430 mg) were added to the dark red solution under magnetic stirring, resulting in the

precipitation of the raw final product. The dark brown-red precipitate was filtered, washed first with the NH_4PF_6 solution then with cold EtOH, and at last dried at 55 °C. A purification by chromatography (glass column, 15 cm length × 1.5 diameter) on basic Al_2O_3 was performed, using a 3:2 TOL/ACN. The first red fraction was collected and the solvent was removed by rotary evaporation. The product was solubilised in 5 ml of ACN and reprecipitated by adding 200 ml of EtOEt under magnetic stirring. After 30 minutes, the red-brown powder was filtered and washed with EtOEt. 172.8 mg of $[Ru^{II}(tpy)(bpm)Cl]PF_6$ (MW = 672.92 g/mol, 0.26 mmol, 54% yield) were obtained. This synthesis was repeated for 3 times, in order to accumulate enough product for the following steps.

^{1}H (Acetonitrile-d_3, 300 MHz) δH (ppm): 10.41 (dd, 1H), 9.32 (dd, 1H), 8.75 (dd, 1H), 8.53 (dd, 2H), 8.41 (d, 2H), 8.18 (t, 1H), 8.08 (t, 1H), 7.95 (td, 2H), 7.8 (d, 2H), 7.70 (dd, 1H), 7.32 (td, 2H), 7.10 (t, 1H).

*3.3.4 Synthesis of $[Ru^{II}(tpy)(bpm)OH_2](NO_3)(PF_6)$ (**1**)*

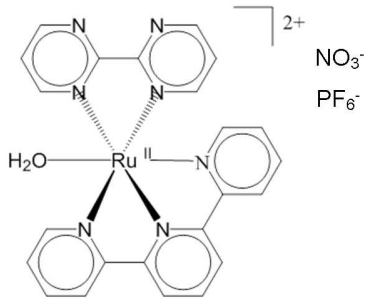

Figure 3.9 Single-site Ru-catalyst, named **1** for the sake of brevity.

This synthesis was adapted from literature.[7] In a 100 ml round flask 193.9 mg of $[Ru^{II}(tpy)(bpm)Cl]PF_6$ (MW = 672.92 g/mol, 0.29 mmol) and 197.4 mg of $AgNO_3$ (MW = 169.87 g/mol, 1.16 mmol) were added to 16 ml of 1:1 MeOH/H_2O solution. The red solution was refluxed for 2 hours, under vigorous magnetic stirring. After that, the mixture was cooled at room temperature, centrifuged in order to remove AgCl, and then filtered on celite. The solvent was dried by rotavapor, and the precipitate was rinsed with cold H_2O and filtered again. 121.8 mg of $[Ru^{II}(tpy)(bpm)OH_2](NO_3)(PF_6)$ (MW = 717.48 g/mol, 0.17 mmol, 59% yield, **Figure 3.9**) were obtained.

^{1}H (Water-d_2, 300 MHz) δH (ppm): 9.84 (dd, 1H), 9.22 (dd, 1H), 8.58 (dd, 1H), 8.48 (dd, 2H), 8.34 (d, 2H), 8.18 (m, 2H), 7.88 (m, 2H), 7.78 (dd, 1H), 7.70 (dd, 2H), 7.24 (m, 2H), 7.10 (t, 1H).

*3.3.5 Synthesis of [Ru^{II}(H_2bpy)$_2$(bpm)](ClO$_4$)$_2$ (**2**)*

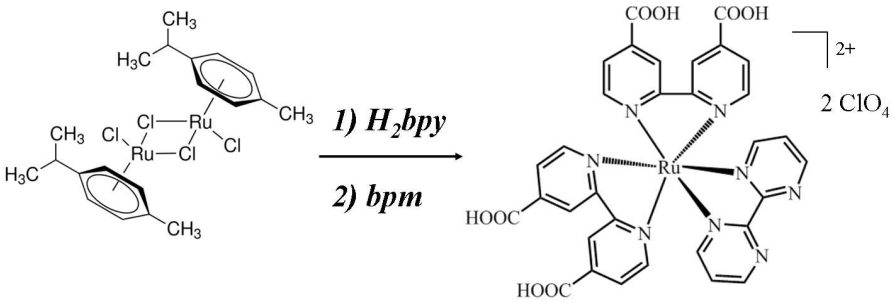

Figure 3.10 One-pot reaction scheme of [Ru^{II}(*H_2bpy*)$_2$(*bpm*)](ClO$_4$)$_2$ synthesis, named **2** for the sake of brevity.

This one-pot synthesis was adapted from literature.[14] In a 100 ml round flask 204.6 mg of Ru^{II}*p*-cymene (MW = 612.39 g/mol, 0.33 mmol of dimer) were dissolved in 20 ml of DMF, and the solution was stirred for 15 minutes. After that, 281.9 mg of *H_2bpy* (MW = 244.20 g/mol, 1.15 mmol, 87% of 4 equiv) were added and the solution was refluxed, under magnetic stirring, in dark conditions for 7 hours, during which the complete disappearance of the ligand, from the reaction mixture, was observed in TLC (EtOH). After this time, 127.7 mg of *bpm* (MW = 158.16 g/mol, 0.81 mmol) were added to the hot solution, which was refluxed for further 4 hours in the dark, under stirring. After that, the solution was cooled at room temperature and the solvent was removed under vacuum. The solid was dissolved in the minimal volume of H_2O and repeatedly extracted with CH_2Cl_2 in order to remove the unreacted compounds. The aqueous fraction was concentrated and $HClO_4$ was added dropwise until reaching pH 2. The acidic solution was stirred overnight; the precipitate was collected by centrifugation and washed with diluted $HClO_4$ at pH 2. The resulting solid was solubilised in 5 ml of MeOH and reprecipitated by adding 200 ml of EtOEt under magnetic stirring. The dark-orange solid was purified on LH-20, using H_2O as eluent. The pure fraction were concentrated and H_2O was removed by rotavapor. 539.57 mg of [Ru^{II}(*H_2bpy*)$_2$(*bpm*)](ClO$_4$)$_2$ (MW = 946,54 g/mol, 0.57 mmol, 99% yield, **Figure 3.10**) were obtained.

^{1}H (Methanol-d$_4$, 300 MHz) δH (ppm): 9.16 (dd, 2H), 9.05 (d, 4H), 8.21 (dd, 2H), 8.05 (d, 2H), 7.88 (dd, 2H), 7.81 (d, 4H), 7.65 (t, 2H).

3.3.6 Synthesis of diethyl 2,2'-bipyridine-4,4'-dicarboxylate (Et_2bpy)

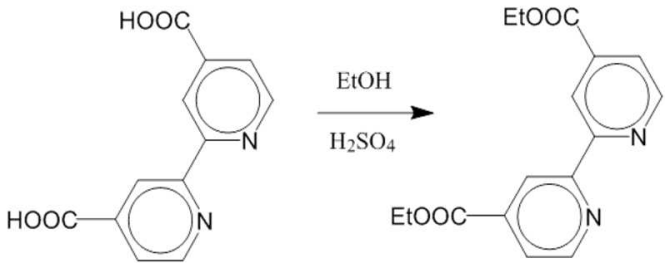

Figure 3.11 Reaction scheme of *Et_2bpy* synthesis.

This synthesis (**Figure 3.11**) is a simple Fischer esterification.[15] In a 250 ml round flask, 2 g of *H_2bpy* (MW = 244.20 g/mol, 8.2 mmol) and 2 ml of H_2SO_4 (MW = 98.08 g/mol, ρ = 1.840 g/ml, 37.5 mmol) were added to 160 ml of EtOH. The cloudy white suspension was refluxed for 72 hours, under vigorous magnetic stirring, until becoming transparent. After that, the solution, cooled at room temperature, was transferred in a 500 ml beacker in ice bath. 1.35 g of NaOH (MW = 40 g/mol, 33.7 mmol), dissolved in 10 ml of water, were added very carefully to the resulting ethanolic solution, followed by dropwise addition of satured $NaHCO_3$ in achieve neutrality. The product was extracted in EtAc, anhydrous with Na_2SO_4, and the solvent was removed by rotavapor. 2.28 g of *Et_2bpy* (MW = 300.31 g/mol, 7.6 mmol, 93% yield) were obtained.

^{1}H (Chloroform-d_1, 300 MHz) δH (ppm): 8.90 (s, 2H), 8.80 (d, 2H), 7.90 (d, 2H), 4.50 (q, 4H), 1.50 (t, 6H).

3.3.7 Synthesis of [$Ru^{II}(Et_2bpy)_2Cl_2$]

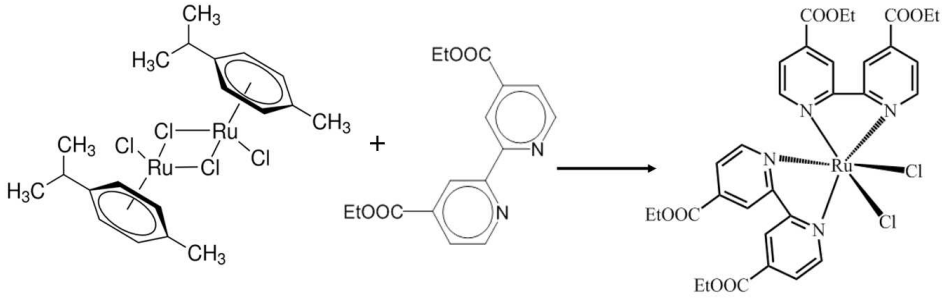

Figure 3.12 Reaction scheme of [$Ru^{II}(Et_2bpy)_2Cl_2$] synthesis.

This synthesis (**Figure 3.12**) was adapted from literature.[14] In a 100 ml round flask 300 mg of Ru^{II}*p*-cymene (MW = 612.39 g/mol, 0.49 mmol of dimer) were dissolved in 15 ml of DMF, and the solution was magnetic stirred for 15 minutes. After that, 472 mg of *Et_2bpy* (MW = 300.31 g/mol, 1.57 mmol, 80% of 4 equiv) dissolved in 15 ml of DMF were added and the resulting solution was refluxed, under stirring in dark conditions for 3 hours. The reaction was monitored both by TLC (95:5 MeOH/$CHCl_3$), following the

disappearance of the ligand, and by cyclic voltammetry (ACN/0.1 M $LiClO_4$), by observing the appearance of a reversible redox wave with $E_{1/2}$ = 1.0 V vs. SCE. After completion of the reaction, the solution was cooled at room temperature and the solvent was removed under vacuum. The solid was dissolved in the minimal volume of H_2O, and CH_2Cl_2 was used to extract the product. The solvent was first anhydrificated with Na_2SO_4 and then removed by rotary evaporation. 612 mg of $[Ru^{II}(Et_2bpy)_2Cl_2]$ (MW = 772,59 g/mol, 0.79 mmol, 81% yield) were obtained.

^{1}H (Methanol-d_4, 300 MHz) δH (ppm): 10.15 (d, 2H), 9.05 (d, 2H), 8.88 (d, 2H), 8.25 (dd, 2H), 7.85 (d, 2H), 7.55 (dd, 2H), 4.50 (m, 6H), 4.40 (q, 2H), 1.50 (m, 8H), 1.40 (t, 4H).

3.3.8 Synthesis of $[Ru^{II}(Et_2bpy)_2(bpm)Ru^{II}(tpy)Cl]Cl_3$

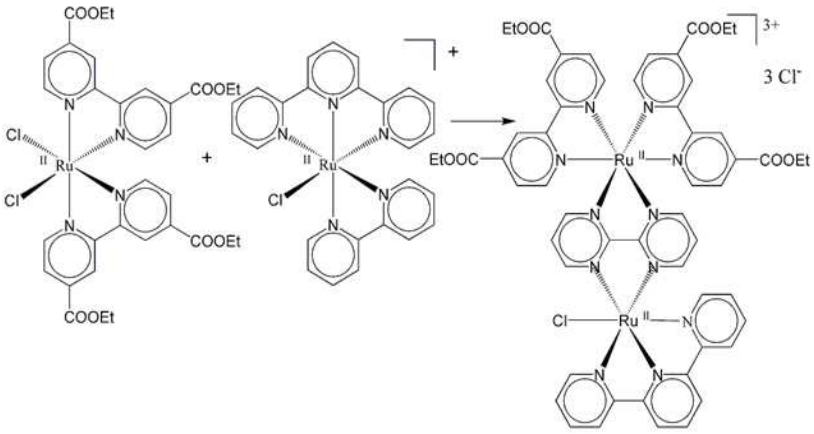

Figure 3.13 Reaction scheme of $[Ru^{II}(Et_2bpy)_2(bpm)Ru^{II}(tpy)Cl]Cl_3$ synthesis.

In a 100 ml round flask, 100 mg of $[Ru^{II}(Et_2bpy)_2Cl_2]$ (MW = 772,59 g/mol, 0.13 mmol) and 69 mg of $[Ru^{II}(tpy)(bpm)Cl]PF_6$ (MW = 672.92 g/mol, 0.10 mmol) were added to 20 ml of 1:1 H_2O/3-MeO-3-Me-1-ButOH solution. The red-brown solution was refluxed for 60 hours, under vigorous magnetic stirring, monitoring the reaction with TLC (MeOH + NH_4PF_6) and with UV-vis spectra, following the formation of the dark green product. The solvent was then removed by rotavapor, and the resulting solid was dissolved in the minimal volume of H_2O and repeatedly extracted with CH_2Cl_2, in order to remove the unreacted compounds. The aqueous residue was concentrated and purified on LH-20, using H_2O as eluent, collecting only the core of the band. The pure dark green fractions, were evaporated to dryness. 72 mg of $[Ru^{II}(Et_2bpy)_2(bpm)Ru^{II}(tpy)Cl]Cl_3$ (MW = 1336,00 g/mol, 0.05 mmol, 50% yield, **Figure 3.13**) were obtained.

^{1}H (Acetonitrile-d_3, 300 MHz) δH (ppm): 9.8 (d, 1H), 9.15 (s, 2H), 9.05 (d, 2H), 8.75 (q, 3H), 8.58 (q, 2H), 8.45 (d, 1H), 8.38 (m, 2H), 8 (m, 13H), 7.59 (t, 1H), 7.41 (t, 1H), 7.18(t, 1H), 5.45 (m, 8H), 3.30 (m, 12H).

3.3.9 Synthesis of [$Ru^{II}(H_2bpy)_2(bpm)Ru^{II}(tpy)Cl](TfO)_3$

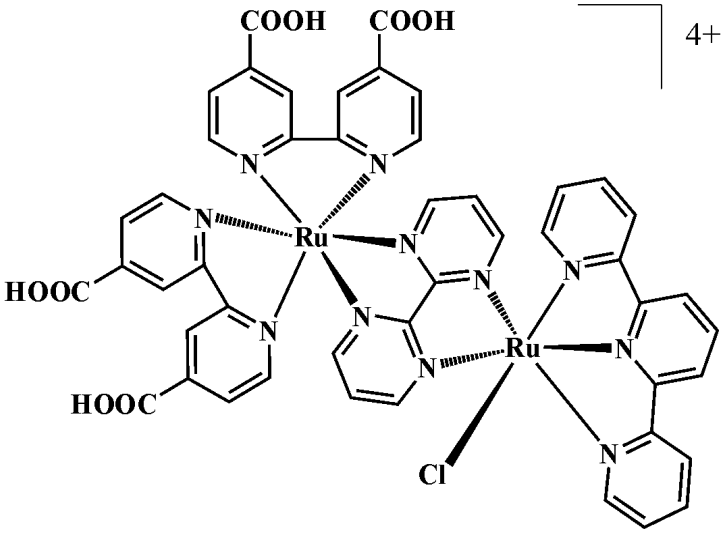

Figure 3.14 Reaction scheme of $[Ru^{II}(H_2bpy)_2(bpm)Ru^{II}(tpy)Cl]Cl_3$ synthesis.

In a 100 ml round flask, 72 mg of $[Ru^{II}(Et_2bpy)_2(bpm)Ru^{II}(tpy)Cl]Cl_3$ (MW = 1336,00 g/mol, 0.05 mmol) were added to 24 ml of 6:1:1 DMF/H_2O/Et_3N solution. The dark green solution was refluxed for 3 hours, under vigorous magnetic stirring, monitoring the reaction by TLC (MeOH + NH_4PF_6). The solvent was removed by rotavapor and the product was dissolved in the minimal volume of H_2O. The solution was first neutralized with 1.0 M TfOH, then concentrated and purified on LH-20, using H_2O as eluent. 58 mg of $[Ru^{II}(H_2bpy)_2(bpm)Ru^{II}(tpy)Cl](TfO)_3$ (MW = 1564,64 g/mol, 0.04 mmol, 80% yield, **Figure 3.14**) were obtained.

^{1}H (Acetonitrile-d_3, 300 MHz) δH (ppm): 9.88 (dd, 2H), 9.38 (dd, 2H), 9.05 (d, 2H), 8.86 (dd, 2H), 8.60 (d, 4H), 8.46 (d, 2H), 8.36 (t, 2H), 8.12 (t, 1H), 8.06 (td, 2H), 7.84 (d, 2H), 7.66 (dd, 2H), 7.40 (td, 4H), 7.24 (t, 2H).

*3.3.10 Synthesis of $[Ru^{II}(H_2bpy)_2(bpm)Ru^{II}(tpy)OH_2](ClO_4)_4$ (**3**)*

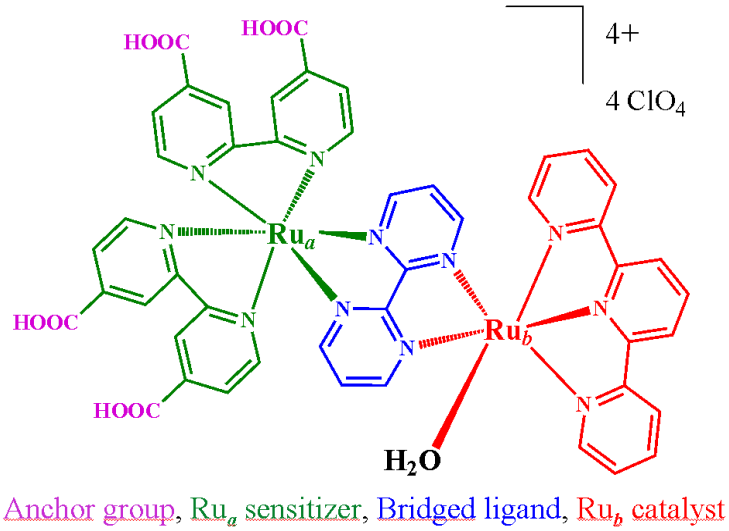

Figure 3.15 Binuclear assembly $[Ru^{II}(H_2bpy)_2(bpm)Ru^{II}(tpy)OH_2](ClO_4)_4$, named **3** for the sake of brevity.

In a 100 ml round flask 58 mg of $[Ru^{II}(H_2bpy)_2(bpm)Ru^{II}(tpy)Cl](TfO)_3$ (MW = 1564,64 g/mol, 0.04 mmol) were dissolved in 20 ml of 3:1 EtOH/H_2O solution. Then 134 mg of TfOAg (MW = 256.94 g/mol, 0.52 mmol) were added and the solution was refluxed for 2 hours. The AgCl precipitate was removed by centrifugation and the solution was evaporated to dryness. The product was dissolved in the minimal volume of H_2O and aqueous $NaHCO_3$ 0.1 M was added dropwise to reach pH 9, in order to precipitate the residual excess of Ag^+ as Ag_2O, which was removed by centrifugation. The solution was concentrated and purified on LH-20 using H_2O as eluent. The fraction of interest was brought to dryness and redissolved in the minimum volume of H_2O, and $HClO_4$ was added dropwise until reaching pH 2. The precipitate was centrifuged and washed first with diluted $HClO_4$ at pH 2 followed by EtOEt and dried in oven. 48 mg of $[Ru^{II}(H_2bpy)_2(bpm)Ru^{II}(tpy)OH_2](ClO_4)_4$ (MW = 1497,79 g/mol, 0.03 mmol, 75% yield, **Figure 3.15**) were obtained.

^{1}H (Acetonitrile-d_3, 300 MHz) δH (ppm): 9.86 (dd, 2H), 9.78 (dd, 2H), 9.40 (m, 2H), 8.86 (dd, 2H), 8.75 (dd, 4H), 8.60 (d, 2H), 8.45 (t, 2H), 8.32 (t, 1H), 8.06 (td, 2H), 7.90 (d, 2H), 7.64 (td, 2H), 7.40 (m, 4H), 7.12 (t, 2H).

3.3.11 Preparation of photoanodes

FTO glass slides 6×8 cm^2 were first cleaned by sonication in Alconox® solution (1 tablespoon in 250 ml of deionized water) for 10 minutes, followed by rinsing with water and by further sonication in 2-propanol for 10 minutes. The slides were finally rinsed with EtOH and dried with warm air. The TiO_2 semiconductor paste was blade cast (**Figure 3.16**) onto the active area of the glass (6×4 cm^2) and dried with a warm air stream, before the high temperature sintering at 450 °C for 30 minutes. The slides were cut to obtain single photoanodes having size of 4×1 cm^2 with active area of 2 cm^2; these were directly used for the sensitization with **2** (10^{-4} M in EtOH) and **3** (10^{-4} M in DMSO/EtOH 1:1). The electrodes were dipped for a couple of hours, in the **2** and **3** solutions, until saturation of the respective surfaces.

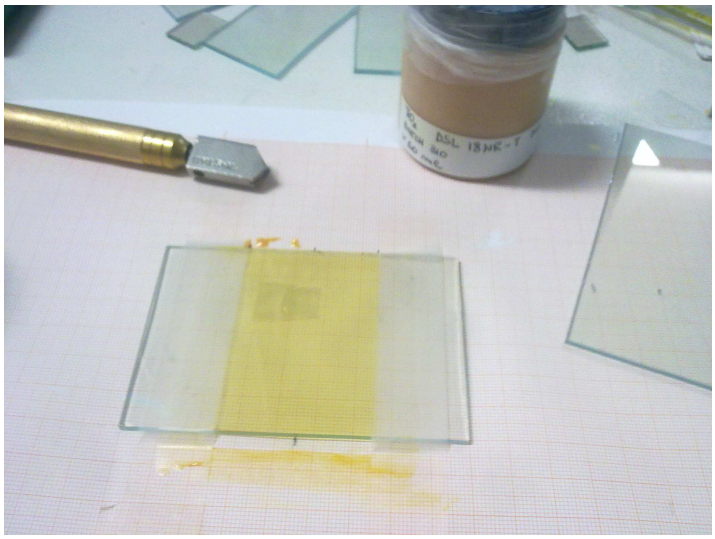

Figure 3.16 TiO_2 photoanodes preparation with FTO conductive glass (shoot by Dr.ssa Laura Casarin).

3.3.12 Electrochemistry and photoelectrochemistry

Electrochemical measurements were carried out on an *Autolab PGSTAT 302/N* workstation (**Figure 2.15**) in a three electrodes configuration using SCE as reference and a Pt bead as counter. Cyclic voltammetry experiments were carried out at glassy carbon (GC, geometrical area 0.07 cm^2) as working electrodes. Constant potential photoelectrochemical experiments, carried out on sensitized electrodes, were performed under 1 sun AM 1.5 G illumination generated by *ABET Technologies* solar simulator equipped with a 420 nm cut-off filter, in order to prevent significant direct bandgap excitation of the TiO_2. Different organic or aqueous electrolytes were used, depending on the experiment performed.

3.3.13 Steady state UV-vis spectroscopy

Absorption spectra in aqueous solution were measured between 800 and 300 nm or starting from 400 nm (on TiO_2) with a *JASCO V-570* spectrophotometer (**Figure 2.2A**) bandwidth of 2 nm.

3.3.14 Computational studies

Ground state equilibrium geometry of the complexes were computed at the DFT B3LYP level by using a 6-31G* basis set in vacuo. Calculations, structure and surface generation were carried out with *Wavefunction Spartan '08*, by using an i3-2100 processor (3.10 GHz) 32-bit PC running under Windows XP.

3.4 Chapter 3 - Results and discussions

The binuclear complex **3** was characterized by spectroscopic, computational, electrochemical and photoelectrochemical measurements. These properties were compared to those of the respective single-site catalysts (**1**) and sensitizer (**2**) in order to determine the differences between the dyad and its constituent components.

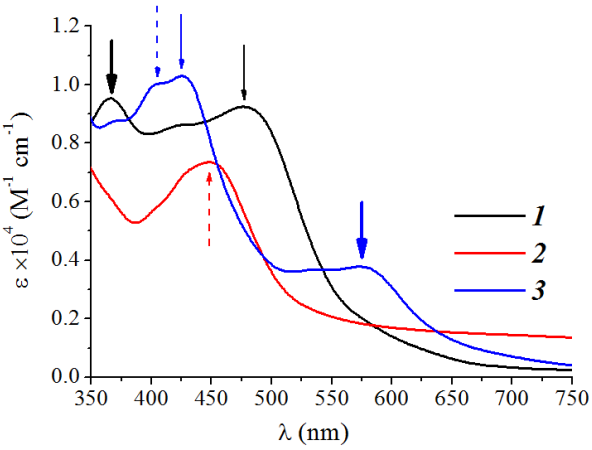

	λ_{max} (nm) [ε (×10⁴ M^{-1} cm^{-1})]
1	367 nm [9.53]; 477 nm [9.25].
2	448 nm [7.35].
3	405 nm [10.03]; 425 nm [10.29]; 574 nm [3.78].

Figure 3.17 Absorption spectra, referred to ε, of compound **1** (black), **2** (red) and **3** (blue) in H_2O, with relative main peaks, indicated by colored arrows. A summary table of $\varepsilon(\lambda)$ is reported at the right of the figure.

Absorption spectra, registered in H_2O at various concentration of complexes, allowed to calculate the ε for each compound, as reported in **Figure 3.17**. The catalyst **1** (black line) shows two MLCT transitions at 367 nm and 477 nm, with more or less the same ε, relative to the formation of [Ru(III)–(*bpm*)$^-$] and [Ru(III)–(*tpy*)$^-$] species respectively.[9] The sensitizer **2** (red line) is characterized, in the visible, by one clear but broad band attributed to the [Ru(III)–(*H*$_2$*bpy*)$^-$] MLCT state. Contrary to **1**, in the spectra of **2**, the [Ru(III)–(*bpm*)$^-$] transition is not observed; probably the relative band is hidden under the tail of ligand-centered transitions in the UV region. The spectrum of **3** (blue line) is representative of the contribution of each component, which are shifted in energy, due to the strong interactions between the subunits bridged by conjugated ligand. Three appreciable MLCT transitions, peaking at 405 nm, 425 nm and 574 nm, are assigned following the literature:[8] both [Ru$_a^{III}$–(*H*$_2$*bpy*)$^-$] (red and blue dash arrow) and [Ru$_b^{III}$–(*tpy*)$^-$] (black and blue thin solid arrow) transitions are blue-shifted by 43 nm and 52 nm respectively, while [Ru$_b^{III}$–(*bpm*)$^-$] (black and blue thick solid arrows), and [Ru$_a^{III}$–(*bpm*)$^-$] are red shifted, resulting in the new 574 nm broad band.

Table 3.2 Calculated molecular orbitals associated to the most intense MLCT transitions.

	λ_{max} (nm) [E(eV)][a]	MLCT state	HOMO	LUMO
1	367 nm [3.38 eV]	[Ru(III)–(*bpm*)$^-$]	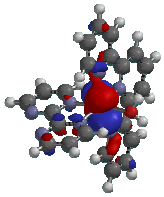 HOMO	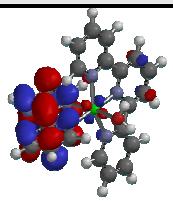 LUMO(+1)
	477 nm [2.60 eV]	[Ru(III)–(*tpy*)$^-$]		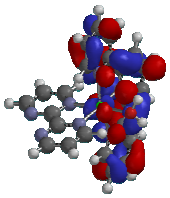 **LUMO**
2	448 nm [2.77 eV]	[Ru(III)–(*H$_2$bpy*)$^-$]	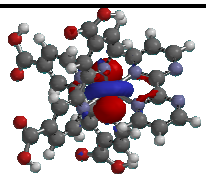 **HOMO**	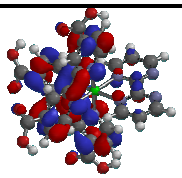 **LUMO**
3	405 nm [3.06 eV]	[Ru$_a^{III}$–(*H$_2$bpy*)$^-$]	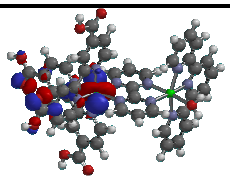 HOMO	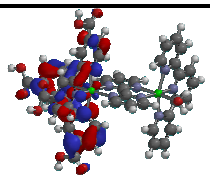 LUMO(+4)
	425 nm [2.92 eV]	[Ru$_b^{III}$–(*tpy*)$^-$]	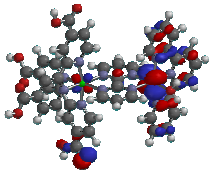 HOMO(-6)	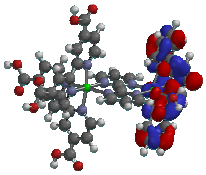 LUMO(+3)
	574 nm [2.16 eV]	[Ru$_b^{III}$–(*bpm*)$^-$]		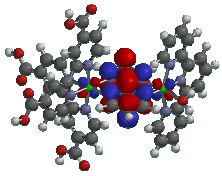 LUMO
		[Ru$_a^{III}$–(*bpm*)$^-$]	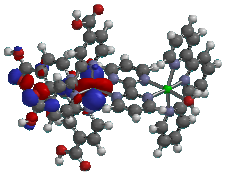 **HOMO**	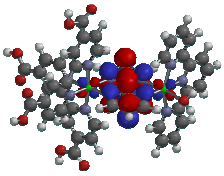 **LUMO**

(a) Calculated with **Equation 2.5** using λ_{max}.

Frontier orbitals of the dyad and the separate components, calculated according to DFT/B3LYP, are reported in **Table 3.2**, with the experimental energy of the assigned optical transition. Isodensity surfaces are consistent with the localization of the orbitals in well-defined molecular regions, either on the metal or on the ligands, coherent with the description of the resulting excited states, having a prevailing charge transfer character. While for the sensitizer **2** the LUMO orbital is localized on the *H_2bpy* ligands, the binuclear compound **3** displays the LUMO onto *bpm*, resulting in the HOMO-LUMO transition ([Ru_a^{III}–(*bpm*)$^-$]), peaking at 574 nm. The orbital localized on the *H_2bpy* is the LUMO(+4), leading to the population of the MLCT state at 405 nm ([Ru_a^{III}–(*H_2bpy*)$^-$]). Due to its high ε, the population of this MLCT excited state, having the best coupling with semiconductor, would lead to the fastest charge injection, assuming a favorable competition with thermalization to the lowest MLCT state ([Ru_a^{III}–(*bpm*)$^-$]). This latter does not display a good coupling, being the *bpm* ligand remote from the surface.

Considering the binuclear assembly adsorbed on a semiconductor electrode, the population of the [Ru_a^{III}–(*bpm*)$^-$] "trap" excited state may disadvantage the photoinduced charge injection, due to a localization of the electron density cloud in the middle of the molecule, away from the electrode surface. However, as reported in literature for similar complex,[8] the electron injection is still allowed, due to a bending of the molecular structure that bring the LUMO orbitals, centered onto the bridging ligand, close to the semiconductor surface, as reported in the model of **Figure 3.18**. Of course, the efficiency of a long-range (LUMO on bridged ligand) photoinduced electron transfer will be lower than a short-range one (LUMO on anchoring ligand).

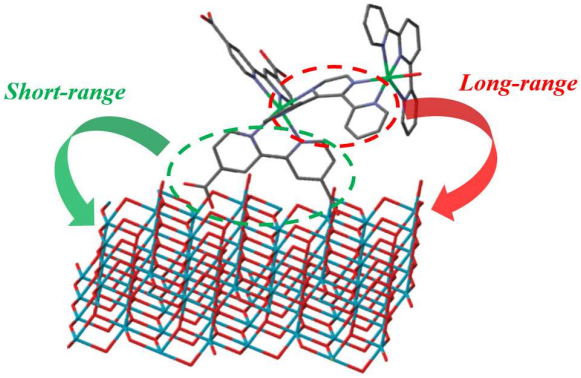

Figure 3.18 Structure of Meyer binuclear complex grafted on TiO_2 cluster surface.[8]

The electrochemical measurements were carried out in order to study the main redox processes of the component species in solution, and to relate them to the redox properties of the dyad. In addition, the catalytic performance of the binuclear complex **3** compared to **1** was evaluated. In **Figure 3.19A** is reported the CV of the catalyst **1** in aqueous 0.1 M HNO_3; consistent with reported literature results,[7] **1** reveals a bielectronic

reversible redox wave, attributed to the $[Ru^{II}–OH_2]^{2+}$ - $2e^-$ → $[Ru^{IV}=O]^{2+}$ + $2H^+$ process (**Equation 3.1** and **Equation 3.2**, reported in **Table 3.1**). The multielectronic wave is evident in a comparison with equimolar solution of the single-site catalyst and $[Fe(phen)_3]^{2+}$ (**Figure 3.19B**), which is known to originate a simple monoelectronic process (Fe^{II}/Fe^{III}).

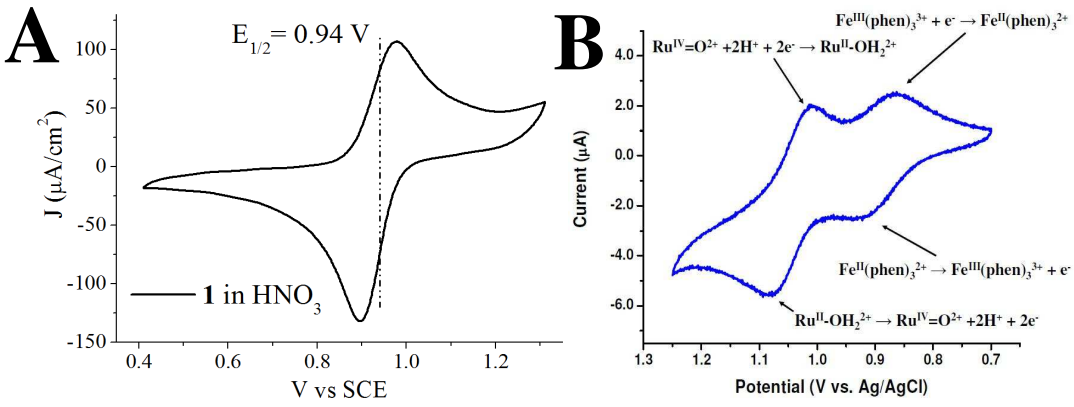

Figure 3.19 A) Cyclic voltammetry of **1** in aqueous 0.1 M HNO_3, at GC working electrode (SCE as reference and Pt bead as counter) achieved at 20 mV/s. B) Cyclic voltammetry of 1 mM Meyer $[Ru(tpy)(bpm)(OH_2)]^{2+}$ and 1mM $[Fe(phen)_3]^{2+}$ in aqueous 0.1 M HNO_3, achieved at 10 mV/s. The difference in redox wave intensity is due to the multielectronic process that occur for the single-site catalyst.[7]

In **Figure 3.20**, the sensitizer **2** show a reversible wave, with $E_{1/2}$ = 1.52 V vs. SCE, in the anodic range relative to Ru^{II}/Ru^{III} process (**Figure 3.20A**). This high oxidation potential should be positive enough to activate the single-site catalyst **1** ($E_{1/2}$ = 0.94 V vs. SCE) at least in the first charge transfer process, with a good driving force (580 mV), in order to obtain the important intermediate $[Ru_a^{III}–Ru_b^{IV}=O]^{5+}$ which will be photo-oxidized in order to achieve water splitting. At cathodic potentials (**Figure 3.20B**) two irreversible waves emerge, attributed to the ligands reduction, at -0.92 V (*bpm/bpm*$^-$) and -1.50 V (*H_2bpy/H_2bpy*$^-$) vs. SCE.

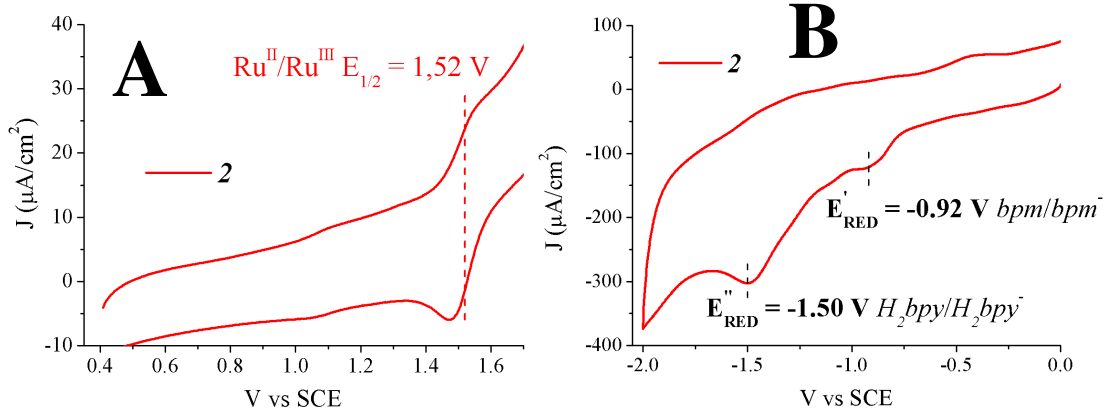

Figure 3.20 Cyclic voltammetry of **2** in A) aqueous 0.1 M HNO_3, B) N_2 purged DMF/0.1 M $LiClO_4$. Both collected at GC working electrode (SCE as reference and Pt bead as counter) at 50 mV/s.

In the binuclear assembly **3**, the anodic CV (**Figure 3.21A**) show two well-defined reversible waves at 1.04 V and 1.49 V vs. SCE, that can be assigned to the Ru^{II}/Ru^{III}

oxidation processes of catalyst (Ru_b) and sensitizer (Ru_a) units respectively, with another slight redox process in the middle at 1.22 V vs. SCE, attributed to Ru^{III}/Ru^{IV} process in Ru_b. This behavior is consistent with what is reported from Song and Meyer (**Figure 3.21B**).[16] This latter Ru^{III}/Ru^{IV} process has lower intensity with respect to the other two Ru^{II}/Ru^{III} waves, probably due to a slower electron transfer kinetic as pointed out by varying the scan rate (**Figure 3.22**). While at 20 mV/s the first Ru^{II}/Ru^{III} and Ru^{III}/Ru^{IV} have almost the same intensity, the latter peak becomes broader and less reversible at scan speed > 500 mV/s.

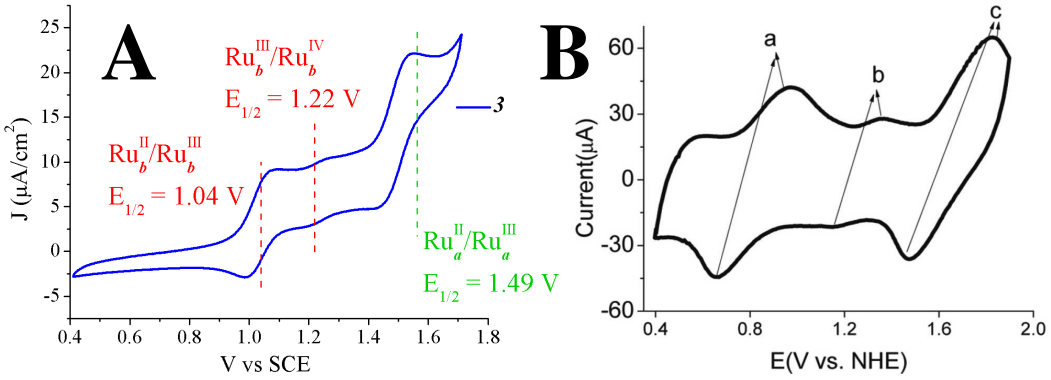

Figure 3.21 Cyclic voltammetry of A) **3** in ACN/0.1 M $TBAPF_6$ at GC working electrode (SCE as reference and Pt bead as counter); B) $[(dcb)_2Ru(bpy\text{-}Mebim_2py)Ru(bpy)(OH_2)]^{4+}$ adsorbed on *nano*ITO, in PC/0.1 M KPF_6 + 2% H_2O.[16] Both achieved at 10 mV/s.

Thus, the bielectronic wave of the single-site catalyst **1** is, upon binding with sensitizing sub-unit, split into two monoelectronic processes in the binuclear complex **3**. In **Figure 3.23** it is reported a comparison with equimolar **1** (black line) and **3** (blue line), where it is possible to have a better appreciation of this effect: the amplitude of the redox wave of **1** (black dash arrow) is more or less the sum of the two distinct waves in **3** (blue dash arrows).

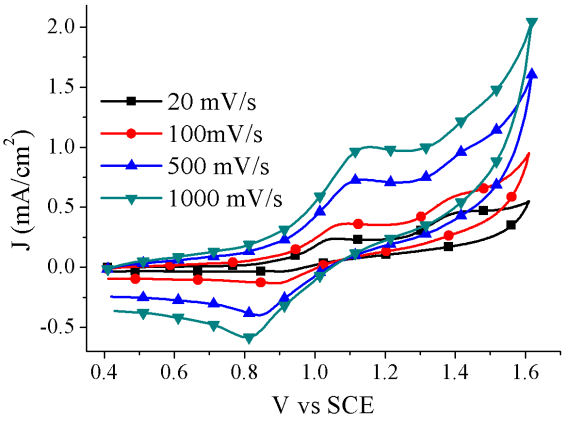

Figure 3.22 Cyclic voltammetry of **3** in aqueous 0.1 M HNO_3, at GC working electrode (SCE as reference and Pt bead as counter) achieved at different scan rate.

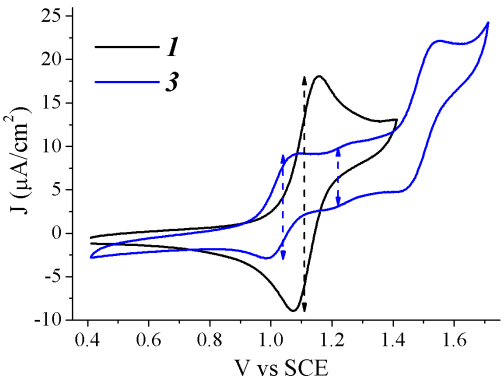

Figure 3.23 Comparison between equimolar **1** (black line) and **3** (blue line) in ACN/0.1 M $TBAPF_6$, at GC working electrode (SCE as reference and Pt bead as counter) achieved at 10 mV/s.

A clearer comparison in electrochemical behavior of these three compounds is better obtained in DPV mode (**Figure 3.24**), with the results summarized in **Table 3.3**. In the binuclear complex, due to the interaction of Ru_a and Ru_b through the bridged ligand *bpm*, the Ru_b^{III}/Ru_b^{IV} oxidation occur at higher potential (+430 mV) than in single-site catalysts, and this also affects the Ru^{IV}/Ru^{V} process that is shifted of 160 mV in passing from **1** to **3**. However, the Ru_a^{II}/Ru_a^{III} process is more positive than Ru_b^{III}/Ru_b^{IV} oxidation (130 mV of driving force), so the activation of the catalyst unit is still possible by the sensitizer, in order to obtaining the $[Ru_a^{III}–Ru_b^{IV}=O]^{5+}$ intermediate. However with our species we could observed the catalytic oxygen evolution only after formation of the Ru(V) intermediate, which, at an estimated peak potential of ~1.8 V vs SCE, would be thermodynamically out of reach of the sensitizing unit. The peak potential estimated by DPV is consistent with the onset of water oxidation observed in linear sweep voltammetry (**Figure 3.25**), where single-site catalyst **1** and binuclear dyad **3** were compared, in equimolar amount in aqueous 0.1 M HNO_3, in order to verify their electrocatalytic activity. It should be noted that a lower catalytic current is observed with the dyad. This effect cannot be explained only on the basis of the higher potential for Ru(V) oxidation, but also with a slower diffusion of larger binuclear species, and with a slower electron transfer kinetics, as can be appreciated by the much shallower slope of the anodic discharge in **3**.

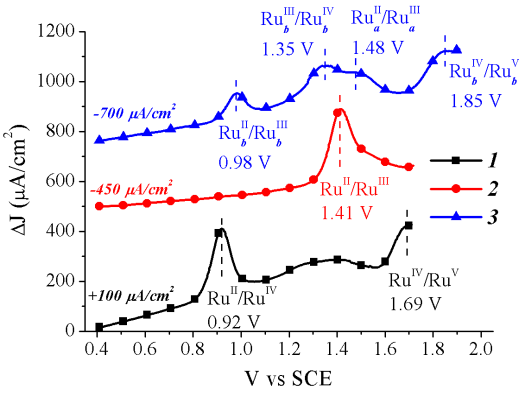

Figure 3.24 Differential pulse voltammetry (20 mV modulation potential), comparing equimolar (1 mM) **1**, **2** and **3**, in aqueous 0.1 M HNO_3 at GC working electrode (SCE as reference and Pt bead as counter) achieved at 50 mV/s.

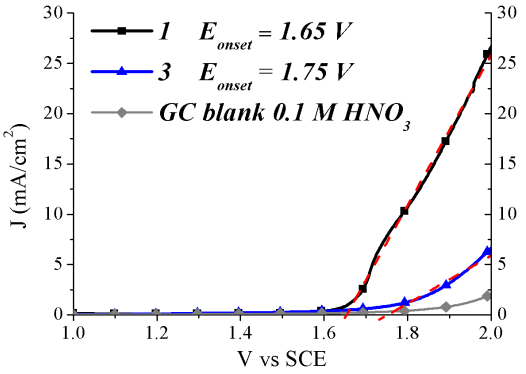

Figure 3.25 Linear sweep voltammetry of 1 mM **1** and **3**, in aqueous 0.1 M HNO_3 at GC working electrode (SCE as reference and Pt bead as counter) achieved at 50 mV/s.

Table 3.3 Summary of **1**, **2** and **3** oxidation processes.

Oxidation process	*1 (V vs. SCE)*	*2 (V vs. SCE)*	*3 (V vs. SCE)*
Ru^{II}/Ru^{III}	0.92 V	1.41 V	0.98 V (Ru_b), 1.48 V (Ru_a)
Ru^{III}/Ru^{IV}	0.92 V	-	1.35 V (Ru_b)
Ru^{IV}/Ru^{V}	1.69 V	-	1.85 V (Ru_b)

The photoelectrochemical experiments were carried out on mesoporous TiO_2 thin film photoanodes sensitized with the Ru-dye **2** and the dyad **3**, reaching on electrode absorbance value of ~0.9 and ~1.8 respectively (black lines in **Figure 3.26A** and **B**), in order to test the photoinjection properties in the presence of a sacrificial hole scavenger (ascorbic acid). Despite the same carboxylic anchoring groups for both complexes, which are known to be a less then optimal choice for long term stability in aqueous phase, **3**/TiO_2 reaches ca. twice absorbance values with respect to **2**/TiO_2, probably due to a better packing of the binuclear species on the semiconductor surface, and to lower solubility in the electrolyte, showing, upon irradiation cycles, a superior long term stability.

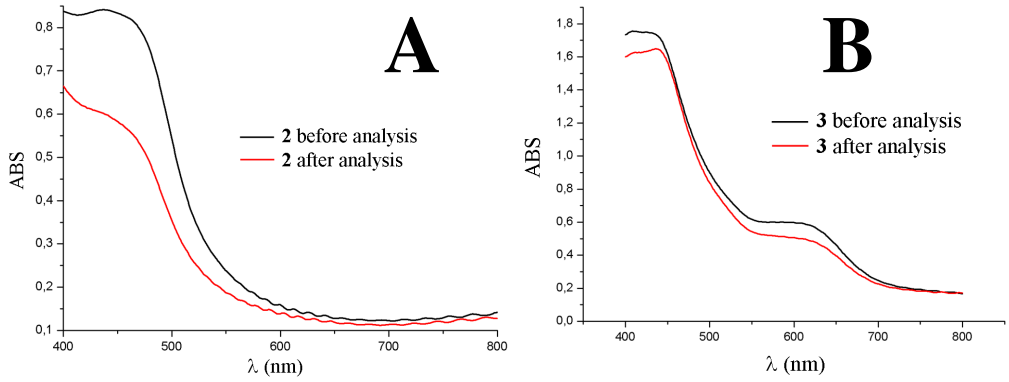

Figure 3.26 Absorption spectra of **2** (A) and **3** (B), adsorbed on TiO_2 thin films, before (black line) and after (red line) the photoelectrochemical measurements in aqueous 0.1 M HNO_3.

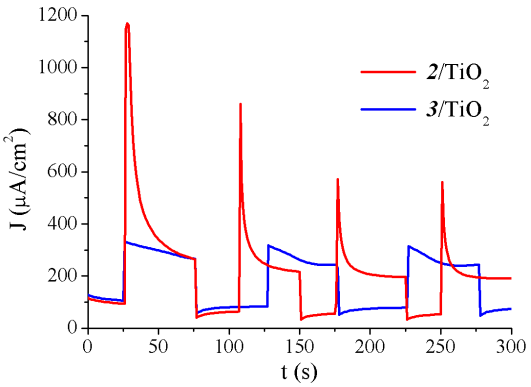

Figure 3.27 Constant potential (0.30 V vs. SCE) chronoamperometry of **2**/TiO_2 and **3**/TiO_2, achieved in aqueous 0.1 M HNO_3 + 0.1 M ascorbic acid 20:1 (v/v).

A constant potential (0.3 V vs. SCE) chronoamperometry was registered for **2**/TiO_2 (red line) and **3**/TiO_2 (blue line) photoanodes, in 20 ml aqueous 0.1 M HNO_3 and 1 ml aqueous 0.1 M ascorbic acid (20:1 v/v) mixture. Upon AM 1.5 G illumination, in the presence of a 420 nm cut-off filter, a photoanodic current was achieved, consistent with charge injection into TiO_2 and hole transfer to the sacrificial scavenger. In the case of **2**/TiO_2 (red line, **Figure 3.27**) a transient overshooting was observed, reaching 1200 μA/cm^2 and followed by a rapid photocurrent decrease, due to fast recombination processes, between the photogenerated h^+ (on **2**) and the photoinjected e^- (trapped in TiO_2), in competition with the hole transfer to the electrolyte. Another reason for the unstable photocurrent was dye desorption, which mainly occurs in the first seconds of immersion and illumination. After ~30 seconds of illumination, a stable photoanodic current, in the

order of 300 μA/cm^2, was registered, resulting from the attainment of a steady state under illumination, No large overshootings are observed for **3**, indicating a slower charge injection, probably occurring from remote sites (*bpm* orbitals). A stationary photocurrent value, equivalent to that achieved for **2**, is however reached during the first 50 seconds of illumination cycle (blue line, **Figure 3.27**) and maintained during the following cycles.

The chronoamperometry without sacrificial electron donor (**Figure 3.28**), to test the photoinduced capability of **3**, was carried out with an increased constant potential bias (0.7 V vs. SCE) in order to help the overcoming of the recombination processes. It can be observed that the photoanodic current is very low, with steady state values of the order of few microampere, and strong photoanodic spikes testifying fast recombination processes. Despite the absence of the catalytic unit that could dispose efficiently the photogenerated h^+, the response for **2**/TiO_2 (red line, **Figure 3.28**) is higher than **3**/TiO_2 (blue line, **Figure 3.28**), indicating that the very positive ground state oxidation potential of the dye can intercept with a low efficiency water oxidation. The lower response of **3**/TiO_2 can be assigned to formation of the Ru^{III}/Ru^{IV} states, which, consistently with the electrochemical results, transiently store h^+ without being able, by further hole transfer from the catalyst, to lead to the active Ru(V) intermediate. This highly valent state thus behave mostly as recombination centre on the surface of the semiconductor. In order to avoid this limitation, single-sites catalysts having a reduced oxidation potential should be developed. The assembly of these species in molecular dyads could be in any case problematic, due to significant changes in the ground state oxidation potential of the catalytic unit occurring upon interaction with the sensitizing species. The exact amount of these changes are difficult to predict, even with help of powerful computational tools, and may make, like in this case, the generation of states, active toward water oxidation, energetically unreachable by the photo-oxidized sensitizer.

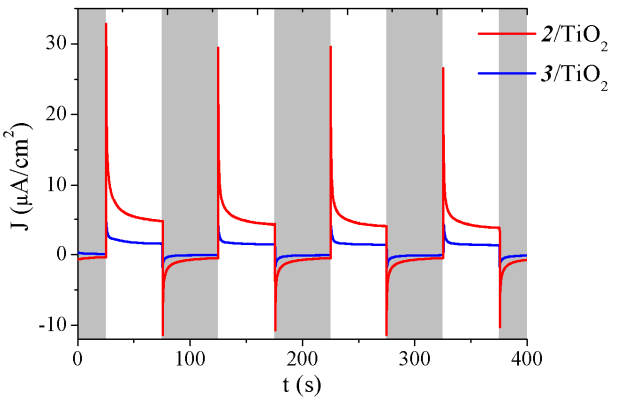

Figure 3.28 Constant potential (0.70 V vs. SCE) chronoamperometry of **2**/TiO_2 and **3**/TiO_2, achieved in aqueous 0.1 M HNO_3. 50 s of illumination cycles (white rectangles) were followed by 50 s dark cycles (little grey rectangles).

3.5 Chapter 3 - Conclusions

A dyad having in principle the correct frontier levels for photoinduced water splitting was designed by combining Ru(II) sensitizer with a single-site ruthenium catalyst. This dyad was shown to adsorb on TiO_2 leading to photoanodes having a strong light harvesting and a decent stability in aqueous electrolytes, despite the use of relatively labile carboxylic anchors. The main problem found with this approach was a substantial shift, in the oxidation potential, of highly valent species, of which only the Ru(V) state was found to be active in the catalytic water oxidation. This state was energetically out of reach of the sensitizing unit, and h^+ could be transiently stored up to the Ru(IV) state. This oxidized state, behaved as recombination centre on the surface of TiO_2, leading to photoanodic current lower than the sensitizing unit taken alone. Although better single-site species, having less demanding thermodynamics could be designed; the assembly of these species in a molecular dyads is a rather complex approach, let aside synthetic complexity, due to the difficulty of predicting changes in the ground state oxidation potential of the catalytic unit, occurring upon interaction with the sensitizing species which may make, like in the reported case, the generation of states, active toward water oxidation, energetically unreachable by the photo-oxidized sensitizer.

The co-grafting[17] of independent, or weakly interacting, sensitizing and catalytic species on the semiconductor surface, exploiting surface e^-/h^+ hopping, could be a simpler and more profitable approach, where the properties of both species will be kept well-defined, in the limit of their interaction with surface. Clearly, a fine tuning of the relative concentration of the absorber and of the catalyst should achieved, in order to realize optimal efficiency.

This approach will be explored in the next chapters, where different metal oxide semiconductors will be considered with the aim of optimizing the charge injection by poorly reducing excited state.

3.6 Chapter 3 - Figures index

3.7 Chapter 3 - References

(1) Gersten, S. W.; Samuels, G. J.; Meyer, T. J. *Journal of the American Chemical Society* **1982**, *104*, 4029.

(2) Gilbert, J. A.; Eggleston, D. S.; Murphy, W. R.; Geselowitz, D. A.; Gersten, S. W.; Hodgson, D. J.; Meyer, T. J. *Journal of the American Chemical Society* **1985**, *107*, 3855.

(3) Blakemore, J. D.; Crabtree, R. H.; Brudvig, G. W. *Chemical Reviews* **2015**, *115*, 12974.

(4) Kärkäs, M. D.; Verho, O.; Johnston, E. V.; Åkermark, B. *Chemical Reviews* **2014**, *114*, 11863.

(5) McEvoy, J. P.; Brudvig, G. W. *Chemical Reviews* **2006**, *106*, 4455.

(6) Zong, R.; Thummel, R. P. *Journal of the American Chemical Society* **2005**, *127*, 12802.

(7) Concepcion, J. J.; Jurss, J. W.; Templeton, J. L.; Meyer, T. J. *Journal of the American Chemical Society* **2008**, *130*, 16462.

(8) Concepcion, J. J.; Jurss, J. W.; Brennaman, M. K.; Hoertz, P. G.; Patrocinio, A. O. T.; Murakami Iha, N. Y.; Templeton, J. L.; Meyer, T. J. *Accounts of Chemical Research* **2009**, *42*, 1954.

(9) Concepcion, J. J.; Tsai, M.-K.; Muckerman, J. T.; Meyer, T. J. *Journal of the American Chemical Society* **2010**, *132*, 1545.

(10) Chen, Z.; Concepcion, J. J.; Jurss, J. W.; Meyer, T. J. *Journal of the American Chemical Society* **2009**, *131*, 15580.

(11) Alibabaei, L.; Brennaman, M. K.; Norris, M. R.; Kalanyan, B.; Song, W.; Losego, M. D.; Concepcion, J. J.; Binstead, R. A.; Parsons, G. N.; Meyer, T. J. *Proceedings of the National Academy of Sciences* **2013**, *110*, 20008.

(12) Sullivan, B. P.; Calvert, J. M.; Meyer, T. J. *Inorganic Chemistry* **1980**, *19*, 1404.

(13) Swavey, S.; Fang, Z.; Brewer, K. J. *Inorganic Chemistry* **2002**, *41*, 2598.

(14) Liska, P.; Vlachopoulos, N.; Nazeeruddin, M. K.; Comte, P.; Graetzel, M. *Journal of the American Chemical Society* **1988**, *110*, 3686.

(15) Fischer, E.; Speier, A. *Berichte der deutschen chemischen Gesellschaft* **1895**, *28*, 3252.

(16) Song, W.; Glasson, C. R. K.; Luo, H.; Hanson, K.; Brennaman, M. K.; Concepcion, J. J.; Meyer, T. J. *The Journal of Physical Chemistry Letters* **2011**, *2*, 1808.

(17) Gao, Y.; Ding, X.; Liu, J.; Wang, L.; Lu, Z.; Li, L.; Sun, L. *Journal of the American Chemical Society* **2013**, *135*, 4219.

CHAPTER 4. MODIFICATION OF NANOCRYSTALLINE WO_3 WITH A DICATIONIC PERYLENE BISIMIDE: APPLICATIONS TO MOLECULAR LEVEL SOLAR WATER SPLITTING

4.1 Chapter 4 - Abstract

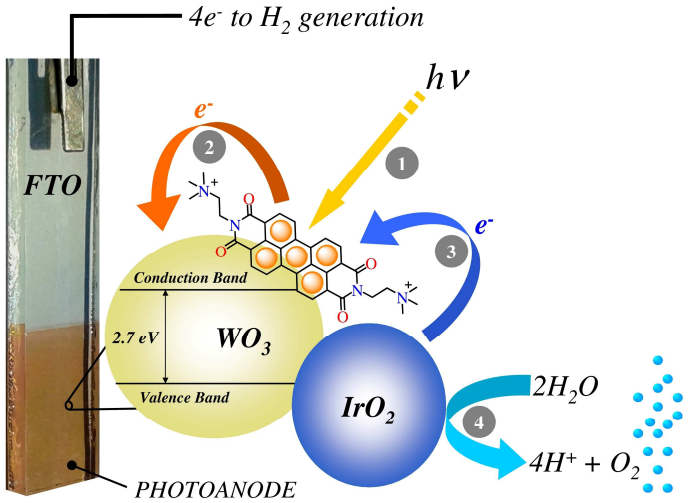

Figure 4.1 Schematic representation of the IrO_2/perylene/WO_3 photoanode, for water oxidation.

[(N,N′-Bis(2-(trimethylammonium)-ethylene) perylene 3,4,9,10-tetracarboxylic acid bisimide)-$(PF_6)_2$] (**1**) was observed to spontaneously adsorb on nanocrystalline WO_3 surfaces via aggregation/hydrophobic forces. Under visible irradiation (λ > 435 nm), the excited state of **1** underwent oxidative quenching by electron injection ($k_{inj} > 10^8$ s^{-1}) to WO_3, leaving a strongly positive hole ($E_{OX} \approx 1.7$ V vs. SCE), which allows to drive demanding photo-oxidation reactions in photoelectrochemical cells (PECs). The casting of IrO_2 nanoparticles (NPs), acting as water oxidation catalysts on the sensitized electrodes, led to a 4-fold enhancement in photoanodic current, consistent with hole transfer from oxidized dye to IrO_2 occurring on the microsecond time scale (**Figure 4.1**). Interesting results were also achieved using an anionic molecular catalyst (tetra-ruthenium polyoxometalate), producing photoelectrochemical performances comparable to some of the best literature results reported for such catalyst in the heterogeneous phase. Once the interaction of the sensitizer with suitable WOCs is optimized, **1**/WO_3 photoanodes may hold potentialities for the straightforward building of molecular level devices for solar fuel production.

4.2 Chapter 4 - Introduction

The exploitation of molecular level sensitized photoelectrodes in water splitting reactions, requiring careful dye and surface engineering,[1-4] is generally less successful due to the lack of stability of the molecular assemblies on the semiconductor surface and to efficient charge recombination processes. The main problem in the molecular approach is the development of visible absorbing sensitizers, having sufficient driving force to carry out both charge injection into the semiconductor and hole (h^+) transfer to a catalyst, achieving the primary charge separated state.

The catalyst should be able to promote, either in a stepwise or concerted way, water oxidation without recombining with electrons injected in the semiconductor, according to the following general reaction scheme:

$$S + h\nu \rightarrow {}^*S \qquad \text{(photoexcitation)} \qquad (1)$$

$${}^*S \rightarrow S^+ + e^-_{CB} \qquad \text{(electron injection)} \qquad (2)$$

$$S^+ + C \rightarrow S + C^+ \qquad \text{(electron transfer)} \qquad (3)$$

$$4C^+ + 2H_2O \rightarrow 4C + 4H^+ + O_2 \qquad \text{(hole transfer)} \qquad (4)$$

where S is the sensitizer, C is the catalyst, and CB is the semiconductor conduction band.

Recently Finke et al.[5] focused the attention on the assembly of a modified perylene bisimide (PBI) dye onto ITO electrodes in combination with Co-Pi.[6] In this configuration the main limitation, to achieve efficient photoelectrochemical water splitting, is the low light harvesting of the nonporous electrodes. Perylenes are simple organic molecules possessing high molar extinction coefficient and good thermal and photochemical stability.[7-9] Most importantly, they show high oxidation potentials, resulting compatible with the activation of many water oxidation catalysts (WOCs) reported in literature, including ruthenium,[10,11] iridium,[12] nickel,[13] and iron[14,15] based catalysts, but are limited by a low excited state oxidation potential. This fact precludes charge injection into many semiconductors and, in general, their use in energy conversion schemes relying on the oxidative quenching of their excited state, a problem that can be solved using semiconductors with appropriate CB energetics.

The high oxidation potential of perylenes can activate molecular catalysts such as Meyer's single-site Ru-complexes (Errore. L'origine riferimento non è stata trovata.) or other variants developed by Sun,[2,4,16,17] having a first oxidation potential at around at 1.30 V vs. SCE. Polyoxometalates (POMs) can represent another promising class of water oxidation catalyst, due to their chemical stability in highly oxidizing conditions. Stabilization of adjacent metal centres through multiple μ-hydroxo/oxo bridging units is one of the most powerful strategies adopted by natural enzymes to effect multiple or cascade charge transfer reactions. POMs are polyanionic clusters consisting of early transition metals (e.g. V, W, Nb, Mo, Ta) and oxygen. Moreover, the electron-withdrawing nature of the POM ligand is predicted to stabilize high-valent intermediates and assist deprotonation equilibria in proton-coupled electron transfer (PCET) reactions. Their synthesis is relatively simple and can usually be performed in one pot, where several parameters can be modulated for the fine-tuning of the synthetic protocol.[17]

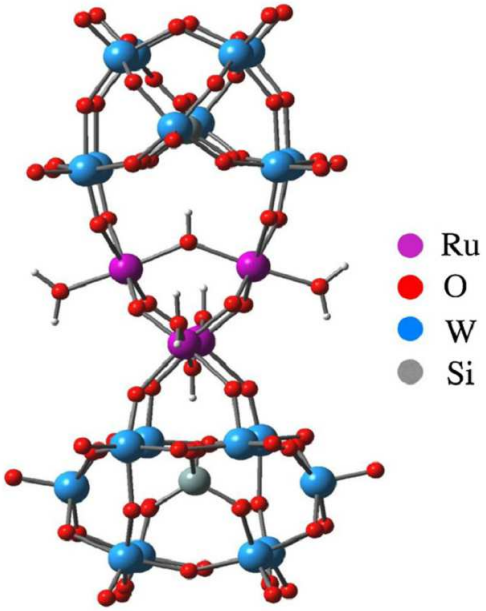

Figure 4.2 Structure of $[Ru_4POM]^{10-}$.

In 2008 a major breakthrough was made by the groups of Hill[18] and Bonchio,[19] who independently reported that the $[Ru_4(\mu\text{-}O)_4(\mu\text{-}OH)_2(H_2O)_4\ (\gamma\text{-}SiW_{10}O_{36})_2]^{10-}$ (Ru_4POM, **Figure 4.2**), was oxidatively and hydrolytically stable enough to carry out the O_2 evolution in homogeneous phase, under different conditions: with $[Ru(bpy)_3]^{3+}$ as chemical oxidant at pH 7,[18] and with a Ce(IV) salt at pH 0.6.[19] Both groups demonstrated that the Ru_4POM was stable under these catalytic conditions, maintaining its structure, electrochemical reversibility and fast kinetics.[19,20]

Herein we report on the sensitization of nanocrystalline WO_3 with the dicationic dye **1** (showed in **Figure 4.1**, **Figure 4.3** and **Figure 4.8**, synthesis described in **Section 4.3.2**), which was demonstrated capable to transfer photogenerated h^+ to sacrificial species in solution, and to co-deposited IrO_2 NPs or Ru_4POM, acting as WOCs.

4.3 Chapter 4 - Experimental section

4.3.1 Materials

15% SnO_2 colloidal solution in water and 99.999% LiI were from Alfa Aesar.

Polyethyleneglycol bisphenol A epichlorohydrin copolymer 15000 - 20000 Dalton, Triton-X 100, >99% $Na_2WO_4 \times 6H_2O$, 97% sulphuric acid, 70% perchloric acid, ≥99% glacial acetic acid, 37% hydrochloric acid, 99% ascorbic acid, 98% NaOH flakes, absolute ethanol, spectroscopic grade acetonitrile (ACN), ACS grade ≥99.8% 2-propanol, perylene-3,4,9,10-tetracarboxyldiimide, quinoline, N,N'-dimethylethylenediamine, methyl iodide, NH_4PF_6 and Alconox® were from Sigma Aldrich.

Dihydrate oxalic acid >99.8% was from Carlo Erba.

18-NRT TiO_2 colloidal paste was purchased from Dyesol.

TEC 8 (8 Ω/□) fluorine tin oxide (FTO) 20×20 cm conductive glass slides were obtained from Pilkington.

ZrO_2 and WO_3 colloidal pastes were prepared according to previously reported procedures.[21,22]

Colloidal IrO_2 NPs solution was prepared by following literature routes.[23]

$Na_{10}[Ru_4POM]$ (MW = 5689.28 g/mol) powder was prepared and supplied by M. Bonchio group.[19]

All reagents, unless otherwise stated, were used as received.

*4.3.2 Synthesis of [(N,N'-bis(2-(trimethylammonium)ethylene) perylene 3,4,9,10-tetracarboxylic acid bisimide)(PF_6)$_2$] (**1**)*

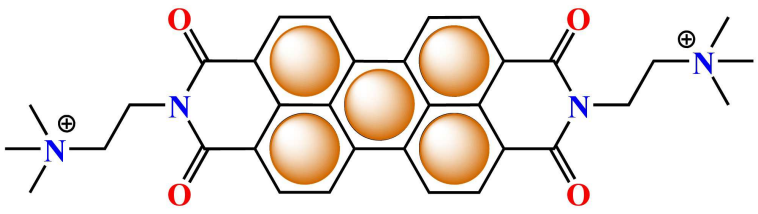

Figure 4.3 Image of the dicationic dye.

The molecule has been synthesized starting from the corresponding bis-iodide salt, described in the literature.[24,25] For the exchange of the counterion, the precursor was solubilized in H_2O and saturated aqueous solution of NH_4PF_6 was added. The required material was precipitated after stirring for 1 hour and collected by filtration, followed by washing with water and MeOH. The resulting solid was dried under vacuum to afford **1** as red powder (MW = 852.59 g/mol, 84% yield).

^{1}H (Acetone-d_6, 400 MHz) δH (ppm): 9.036 (d, J = 8.00 Hz, 4H), 8.73 (d, J = 8.40 Hz, 4H), 4.78 (bt, 4H), 3.96 (bt, 4H), 3.60 (s, 12H).

^{13}C (Acetone-d_6, 270 MHz) δC (ppm): 36.4, 55.6, 64.6, 123.5, 126.7, 128.7, 131.6, 135.5, 138.6, 167.

FT-IR (KBr powder, ν cm^{-1}): 1694, 1657 (>CO), 1593 (–C=C–), 1439, 1403, 1343 (>C-N-R).

ESI-MS, m/z: 852.60 $[PBI\cdot(PF_6)_2]^-$, 281.5 $[PBI]^{2-}$.

$\varepsilon(\lambda)$ [M^{-1} cm^{-1}]: 9650 (465 nm), 25750 (485 nm), 40450 (521 nm).

4.3.3 Preparation of SnO_2 colloidal paste

2.1 ml of glacial acetic acid were added to 50 ml of SnO_2 colloidal solution in order to favour nucleation and growth of larger SnO_2 particles. The mixture was vigorously stirred for 2 hours to avoid an early gelation and excessive thickening of the gel. The colloidal suspension was autoclaved in oven at 220 °C for 12 hours. After cooling at room temperature, 3.5 g of polyethyleneglycol bisphenol A epichlorohydrin copolymer (Carbowax) were added to the resulting white paste, followed by magnetic stirring for 6 hours, to allow a complete dissolution of the copolymer and homogenization with the SnO_2 colloid.

4.3.4 Electrochemistry and photoelectochemistry

Electrochemical and photoelectrochemical measurements were carried out on a *Eco Chemie Autolab/Pgstat 30* potentiostat workstation (**Figure 2.8**), in a three electrodes configuration using SCE as reference and a Pt bead as counter. Different electrolytes were employed, containing either sacrificial agents (ACN/0.1 M LiI; aqueous pH 3 0.1 M ascorbic acid) or neat supporting electrolyte (aqueous pH 3 0.1 M $NaClO_4$) for water splitting experiments. The choice of the acidic medium (pH < 5) was necessary to ensure the chemical stability of WO_3. Cyclic voltammetry of **1** was recorded in N_2 purged ACN/0.1 M $TBAPF_6$ solution, scan rate 100 mV/s, at a glassy carbon (GC, geometrical area 0.07 cm^2) working electrode.

Photoelectrochemical experiments on sensitized photoanodes were performed at a scan rate of 20 mV/s under AM 1.5 G illumination generated by *LOT-Oriel* solar simulator equipped with a 435 nm cut-off filter, in order to prevent significant direct bandgap excitation of the semiconductor substrates.

J-V curves were collected by repeated cycling of the potential between 0.5 V vs. SCE, or 0.35 V vs. SCE, and the open circuit potential (V_{OC}) until an overlapping response upon subsequent scans was achieved, indicating the attainment of a stationary state under illumination. Where indicated, the photocurrent density *J* was obtained by subtraction of the respective electrode dark current. J-V curves under shuttered illumination were acquired by manually chopping the excitation source.

Constant potential (0.35 V vs. SCE) chronocoulometry was obtained by integrating the J-t curves recorded in a time interval of 325 s, alternating 50 s of light to 50 s of dark.

IPCE (**Equation 2.14**) was measured in a three electrode configuration (type ***a*** or ***c*** photoelectrode/Pt/SCE in aqueous pH 3 0.1 M $NaClO_4$) under the monochromatic illumination generated by an air cooled *Luxtel* 175 W Xe lamp coupled to an *Applied Photophysics* monochromator. The photocurrent, recorded at the constant potential of 0.5 V vs. SCE, was acquired on an *Amel mod.552* potentiostat (**Figure 2.10**). Incident irradiance was measured with a calibrated silicon photodiode.

APCE (**Equation 2.18**) was calculated from IPCE data and from the background subtracted absorption spectrum of the dye.

4.3.5 Preparation of semiconductor photoanodes

FTO glass slides 10×8 cm^2 were first cleaned by sonication in Alconox® solution (1 tablespoon in 250 ml of deionized water) for 10 minutes, followed by rinsing with water and by further sonication in 2-propanol for 10 minutes. The slides were finally rinsed with EtOH and dried with warm air.

The semiconductor paste was blade cast (BC) onto the active area of the glass (10×3 cm^2) and dried with a warm air stream before high temperature sintering. In the case of TiO_2, ZrO_2 and SnO_2 the sintering temperature was set at 450 °C for 30 minutes, whereas WO_3 was heated at 550 °C for 45 minutes, in order to obtain the monoclinic phase. A further surface activation step was carried out by soaking the WO_3 thin films in aqueous 1 M H_2SO_4 for 2 hours at room temperature, followed by rinsing with EtOH, drying under warm air stream, and sintering at 550 °C for 45 minutes. The slides were cut to obtain single photoanodes having size of 4×1 cm^2 with active area of 1.5 cm^2; these were directly used for the sensitization with **1**.

Thicker WO_3 (ca. 1.5 μm) electrodes were obtained by repeated spin coating (6 subsequent runs, SC6); at each run the WO_3 paste was spread over either bare FTO or over a pre-existing nanocrystalline WO_3 layer, in order to obtain a complete coverage of the masked active surface. The spin coating was carried out at 600 rpm for 6s followed by high speed spinning at 2000 rpm for 20s. After each coating run the film was sintered at 550 °C for 30 minutes. The annealing of the sixth final WO_3 layer was prolonged to 45 minutes, followed by activation in H_2SO_4 and finally by sintering for further 45 minutes, as previously described.

Spin coating of SnO_2 was carried out by using the colloidal paste described in **Section 4.3.3**, with same procedure above reported for WO_3, except that the annealing temperature was set at 450 °C. The casting of two SnO_2 layer (SC2) produced the best photoelectrochemical performance (**Figure 4.4**).

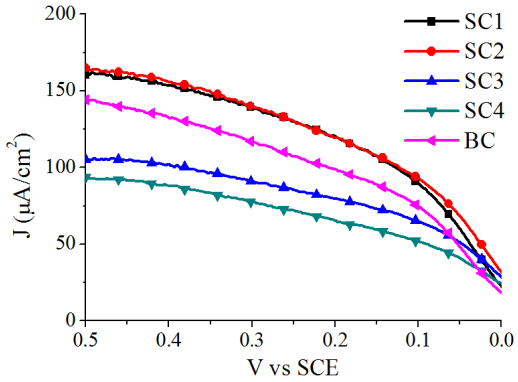

Figure 4.4 J-V characteristics of **1**/SnO_2 photoanodes, obtained by spin coating (SC1-SC4) and blade casting (BC), in aqueous pH 3 0.1 M ascorbic acid under AM 1.5 G with 435 nm cut-off filter. The photocurrent density *J* was obtained by subtraction of the respective electrode dark current.

4.3.6 Sensitization of photoanodes

Electrodes were dipped in a 10^{-3} M ACN solution of **1** (**Figure 4.5A**). WO_3 electrodes were shown to reach surface saturation after 6 hours at 50°C, resulting in optical densities of 0.25. With SnO_2, TiO_2 and ZrO_2 the adsorption was much faster.

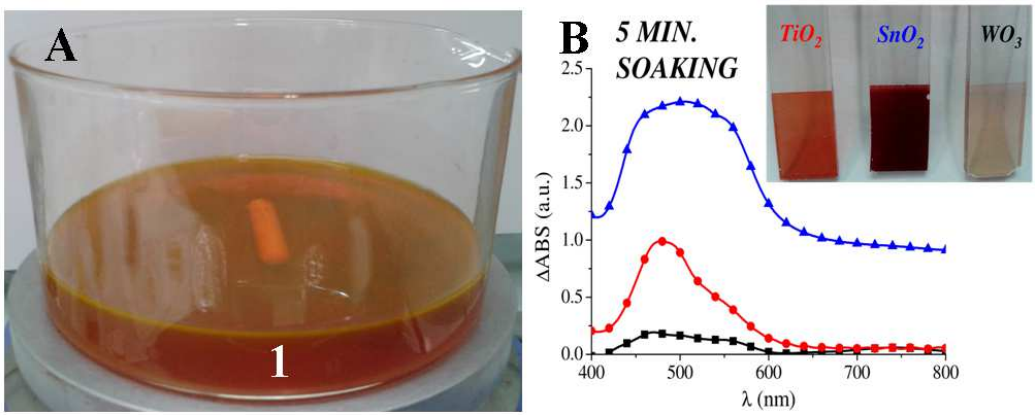

Figure 4.5 *(A)* 10^{-3} M ACN solution of **1**; *(B)* ABS between semiconductors after 5 minutes of soaking.

In order to obtain an optical density similar to WO_3, the dipping of these substrates was limited to few seconds in order to obtain electrodes where the dye loading and the associated bimolecular quenching events on the surface, like exciton annihilation or excimer formation, occurred, in principle, with comparable efficiencies. The **1** adsorption on spin coated SnO_2 (SC2) and WO_3 (SC6) electrodes was carried out till saturation of the respective surfaces (**Figure 4.16**).

4.3.7 Casting of catalysts on sensitized WO_3 photoanodes

Different functionalization methods of **1**/WO_3 BC substrates with IrO_2 NPs (**Figure 4.6**) were explored: drop casting, spin coating and soaking. For each method four treatments (1-4) were performed, in order to evaluate the conditions for optimal photoelectrochemical performances in aqueous pH 3 0.1 M $NaClO_4$, under AM 1.5 G + 435 nm cut-off filter. In every treatment, except soaking, 3 drops of colloidal IrO_2 were deposited on 1.5 cm^2 active area in different conditions, depending on deposition method. A short summary is reported in **Table 4.1** and a comparison of the four treatments, for each deposition methods, is reported in **Figure 4.7**.

Figure 4.6 Colloidal IrO_2 nanoparticles.

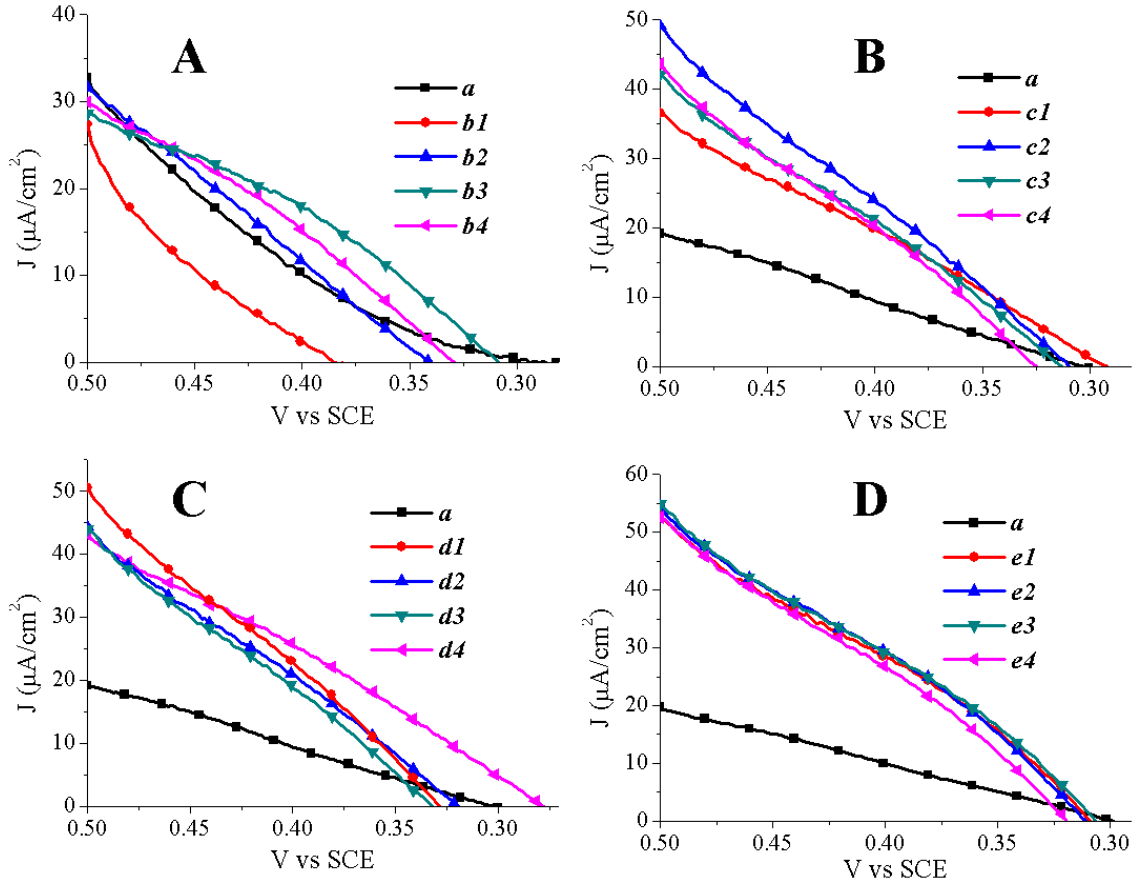

Figure 4.7 J-V characteristics of type ***a*** photoanodes (**1**/WO_3) functionalized with IrO_2 NPs: *(A)* drop casting; *(B)* spin coating; *(C)* spin coating + drying with warm air; *(D)* soaking for 15, 30, 60 and 180 minutes (1-4 numbers). For drop cast and spin coated electrodes, numbers 1-4 indicate the subsequent coating runs. The photocurrent density *J* was obtained by subtraction of the respective electrode dark current.

For sake of brevity the top performing electrodes, according to each different treatment, will be named ***b3* = *b***, ***c2* = *c***, ***d4* = *d*** and ***e3* = *e*** for the next discussions.

Table 4.1 Experimental procedures for sensitized electrodes modification with IrO_2 colloid.

Deposition method	*Electrode type*	*Treatments*
No IrO_2 NPs	***a***	Reference **1**/WO_3
drop casting	***b***	120°C, IrO_2 2×10^{-4} M
spin coating + drying at R.T.	***c***	1000 rpm/min 20s, R.T., IrO_2 2×10^{-3} M
spin coating + drying under warm air	***d***	1000 rpm/min 20s, R.T., IrO_2 2×10^{-3} M
soaking	***e***	R.T., IrO_2 2×10^{-3} M

For the comparison with polyoxometalate molecular catalyst, **1**/WO_3 SC6 substrates were functionalized with a fresh batch, of colloidal 10^{-3} M IrO_2 NPs (type ***c*** deposition method) or soaked (5 minutes) in 10^{-4} M Ru_4POM in aqueous pH 3 0.1 M $NaClO_4$ solution. A detailed summary is reported in **Table 4.4**.

4.3.8 Steady state UV-vis spectroscopy

UV-vis absorption spectra were measured with a *JASCO V-570* and *Varian Cary 300* spectrophotometers (**Figure 2.2**), with a bandwidth of 2 nm. Spectra, recorded between 800 and 400 nm, were subtracted from the contributions of the respective bare semiconductor thin films. For stationary emission experiments sensitized photoanodes were first soaked in aqueous pH 3 0.1 M $NaClO_4$ for several hours, in order to reproduce the local ionic environment of the PEC in aqueous conditions.

Stationary emission spectra were measured with an *Edinburgh Instruments FLS 920* spectrofluorimeter (**Figure 2.3**), equipped with a double emission monochromator. The photoanodes were placed in a dedicated film holder equipped with a micrometric mechanical regulation stage. In order to attain a good reproducibility, before collecting the whole spectrum, the maximum emission intensity was optimized by manually acting on the micrometric stage, to fine tune the angle between thin film, excitation beam and emitted light reaching the detector. The S/N ratio was optimized by summing 10 subsequent scans with 1 nm wavelength step and a bandwidth ($\Delta\lambda$) of 4 nm. Spectra were corrected for the photomultiplier (*R928P-Hamamatsu*) response by using a factory built calibration file. Excitation was into the absorption maximum of the sensitized thin films. Background subtracted spectra were corrected for the light harvesting efficiency (**Equation 2.16**) at the excitation wavelength λ_{ex}.

4.3.9 Transient emission and absorption spectroscopy

Emission lifetimes of the dye in ACN and loaded on semiconductor thin films, were recorded with a *PicoQuant Picoharp 300* time-correlated single photon counting apparatus (**Figure 2.4A**), by exciting at 460 nm with a nanoled driven by a *PDL 800 B* pulsing unit (40 MHz, FWHM 300 ps). Sensitized films were immersed in aqueous pH 3 0.1 M $NaClO_4$ solution and oriented at 45° respect to the excitation pulse. At 550 nm cut-off filter prevented scattered excitation light from reaching the phototube. The collected emission wavelength was at 680-700 nm, depending on the emission maximum on the different semiconductor substrates. In solution, the excited state decay followed a monoexponential kinetics, whereas the emission profile on the solid substrates immersed in aqueous pH 3 0.1 M $NaClO_4$ were deconvolved from excitation profile according to a biexponential function with $\chi^2 < 1.2$, by using the dedicated program *Fluofit*.

Transient absorption spectroscopy (TAS) was performed with a previously described apparatus (**Figure 2.5A**),[26] by using the 532 nm harmonic of a nanosecond *Nd:YAG* laser (*Continuum Surelite II*). Thin films under open circuit conditions, oriented at an angle of ca. 45° with respect to the laser beam, were excited with a pulse energy of ~4 mJ/cm^2/pulse, by defocusing with a plano concave lens and further attenuating with a 50% T neutral filter. A 532 nm notch filter prevented laser light from reaching the photomultiplier, while a 420 nm cut-off filter and a 25% T neutral filter attenuated the white light probe beam, preventing a substantial excitation of the exposed semiconductor substrate. In order to obtain a suitable amplification of the oscillographic traces, with reasonably good S/N ratio, an oscilloscope input resistance of 350 Ω was used. Single wavelength transient traces were further improved by averaging 10 to 30 laser shots at a frequency of 0.2 Hz, imported on a PC and refined by Savitzky-Golay smoothing before being used to construct the transient absorption spectra by means of *Origin 8*.

4.3.10 Computational studies

Ground state equilibrium geometry of **1**, pre-optimized at the semi-empirical PM3 level, were computed at the DFT B3LYP level by using a 6-31G* basis set by describing the solvent ACN with a continuum polarisable model (PCM). Structure and isodensity surfaces (isovalue = 0.02) generation was achieved with *Gaussview 5*. Calculations were carried out with *Gaussian 09 A.02*[27] by using a multiple core (2 X Intel quad core I7 processors) 64 bit PC running under Linux.

4.4 Chapter 4 - Results and discussions

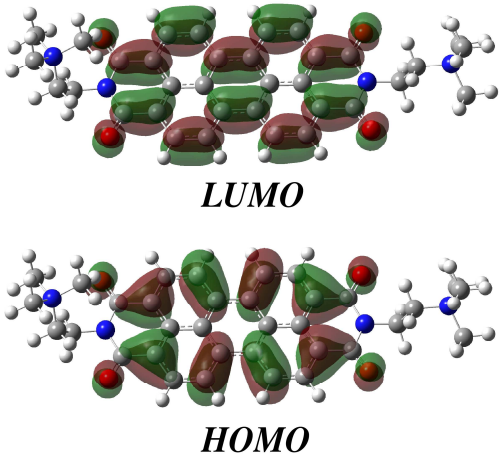

Figure 4.8 Optimized geometries and frontier molecular orbitals of **1** used in semiconductor sensitization, computed at DFT level in ACN.

Compound **1** is characterized by a planar geometry of the aromatic core, while the ethyl-tri-methyl-ammonium chains are bent over the π-plane with a dihedral angle close to 90°. The HOMO-LUMO (**Figure 4.8**) energy gap of 2.48 eV is in good agreement with both the electrochemical gap (2.5 eV, E_{OX} = 1.7 V vs. SCE and E_{RED} = -0.8 V vs. SCE, **Figure 4.9**) and with the spectroscopic energy gap of 2.36 eV evaluated in ACN solution (**Figure 4.10**). The resulting excited state oxidation potential ($^{*}E_{OX}$) is -0.66 V vs. SCE (**Equation 2.11**).

Despite the lack of specific anchoring groups, **1** was shown to functionalize porous semiconductors, including ZrO_2, TiO_2, SnO_2, and WO_3, probably due to aggregation-hydrophobic interactions demonstrated by the blue shift and by a substantial modification of the vibrational structure of the absorption spectrum on the surface, consistent with the probable formation of H-aggregates.[28] Similar spectral features, summarized by a main band in the 470-500 nm interval and by a shoulder at ~550 nm, are present with slight variations in all sensitized surfaces considered by this study (**Figure 4.11A**).

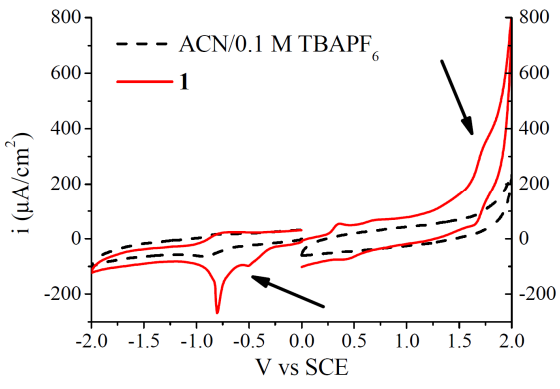

Figure 4.9 Cyclic voltammetry of **1** in ACN/0.1 M $TBAPF_6$ at GC working electrode (SCE as reference and Pt bead as counter). The arrows indicate the main redox waves in agreement with calculated and spectroscopic energy levels.

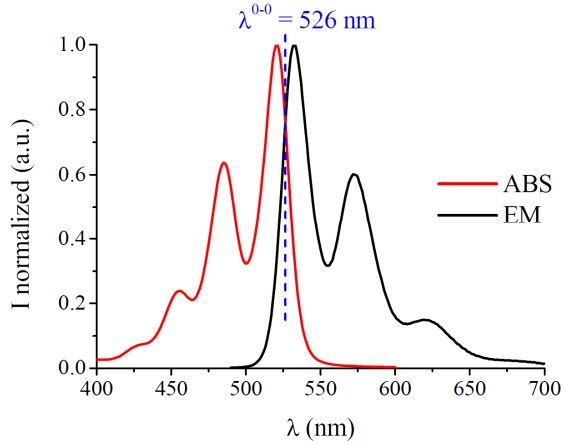

Figure 4.10 Zero-to-zero spectroscopic energy (E^{0-0}) of **1** evaluated by emission spectroscopy in fluid ACN solution. $E^{0-0} \approx 2.36$ eV (**Equation 2.5**).

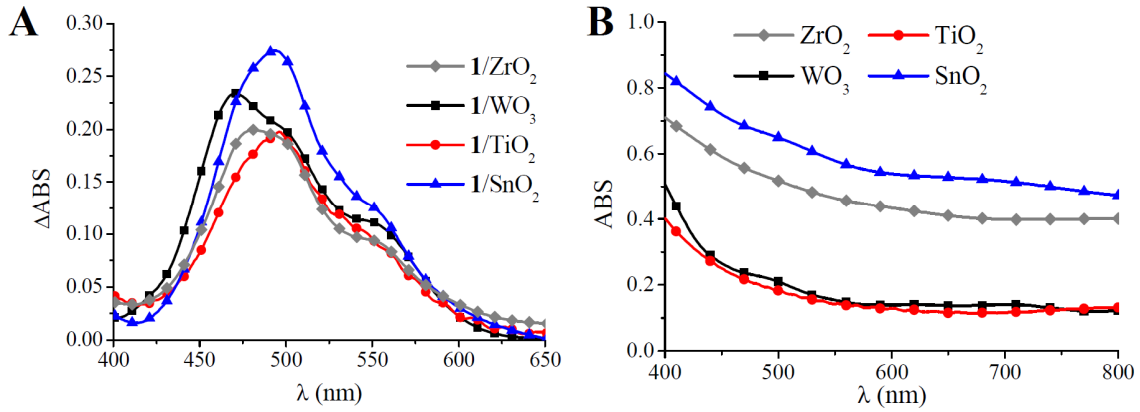

Figure 4.11 Absorption spectra of different porous semiconductors dyed with **1** *(A)*. Spectra in *(A)* were corrected from scattering and intrinsic semiconductor absorption by subtracting the related identical bare semiconductor thin films *(B)*.

Thin BC (**Section 4.3.5**) WO_3 films (~700 nm) reach a maximum optical density of ca. 0.25 at ~470 nm. On other semiconductor substrates the maximum absorbance was intentionally kept at comparable values. Upon illumination (AM 1.5 G + 435 nm cut-off filter) of the resulting photoanodes in the presence of sacrificial electron donors, including ACN/0.1M LiI (**Figure 4.12**) and aqueous pH 3 0.1 M ascorbic acid (**Figure 4.13**), a photoanodic current was observed, consistent with charge injection from **1** to WO_3 and hole transfer to the sacrificial hole scavenger.

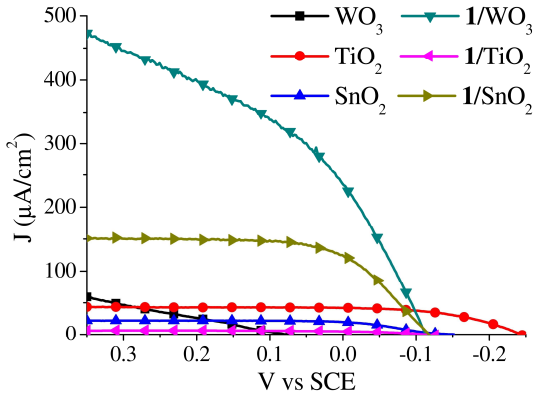

Figure 4.12 J-V characteristics of the **1** sensitized electrodes in the presence of ACN/0.1 M LiI. The photocurrent density *J* of each electrode was obtained by subtraction of the respective dark current.

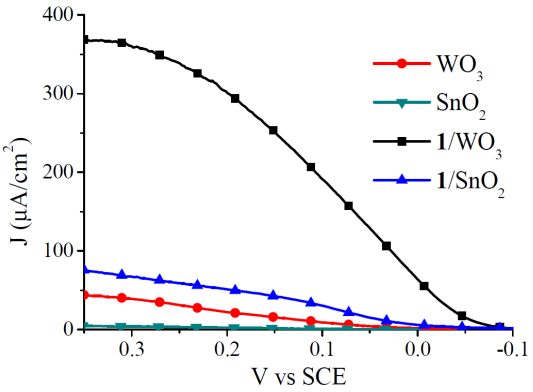

Figure 4.13 J-V characteristics of the different sensitized photoanodes in aqueous pH 3 0.1 M ascorbic acid at (AM 1.5 G + 435 nm cut-off filter). The photocurrent density *J* of each electrode was obtained by subtraction of the respective dark current.

The photoanodic current, reaching maximum values of ca. 0.5 mA/cm^2 in the case of WO_3 at a bias of 0.35 V vs. SCE, varies in the order WO_3>SnO_2>TiO_2. The same trend and similar photocurrent densities are found in ascorbic acid, where, however, TiO_2 was not considered due to the formation of Ti^{IV}ascorbate acting as photosensitizer.[29-31]

The poor performance observed with TiO_2 (magenta line **Figure 4.12**) was attributed to the inefficient injection by the excited state of **1**, having insufficient driving force for competing with its photophysical deactivation pathways. Indeed, the study of the

emission lifetimes of **1** loaded on semiconductor substrates (TiO_2, SnO_2 and WO_3) compared to inert ZrO_2 thin films, where charge transfer is thermodynamically forbidden, reveals that quenching increases in the order WO_3>TiO_2>SnO_2>ZrO_2 (**Figure 4.14**), providing a lower estimate to the injection rate constant $k_{inj}(WO_3) = 0.4\times10^9$ s^{-1}, which is 4 to 8 times larger than that found for SnO_2 ($k_{inj} = 0.1\times10^9$ s^{-1}) and TiO_2 ($k_{inj} = 0.05\times10^9$ s^{-1}) respectively, as reported in **Figure 4.15A-E** and **Table 4.2**.

Note that the injection rate constant measured by TCSPC (**Section 4.3.9**) has to be considered as an average lower limit to the rate constant, given that processes faster than 300 ps fall within the excitation profile of the pulsed led source and cannot be appropriately deconvolved.

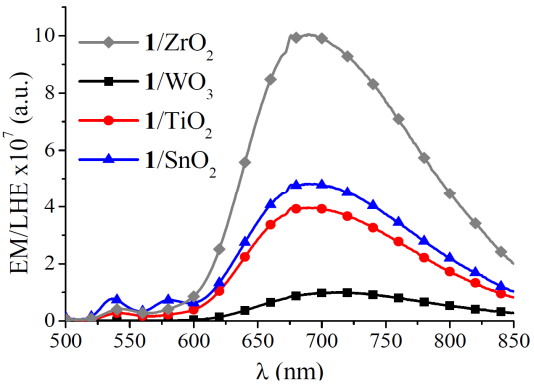

Figure 4.14 Emission spectra sensitized semiconductor thin films, in presence of aqueous pH 3 0.1 M $NaClO_4$. Spectra were normalized for *LHE* at the absorption maximum, chosen as excitation wavelength. The emission spectra recorded on thin films having different opacity and light scattering abilities can be used only for qualitative purposes. Nevertheless the emission intensity of **1** decreases in the order of ZrO_2>TiO_2~SnO_2>WO_3 is in reasonable qualitative agreement with the emission lifetimes measured by TCSPC (vide infra).

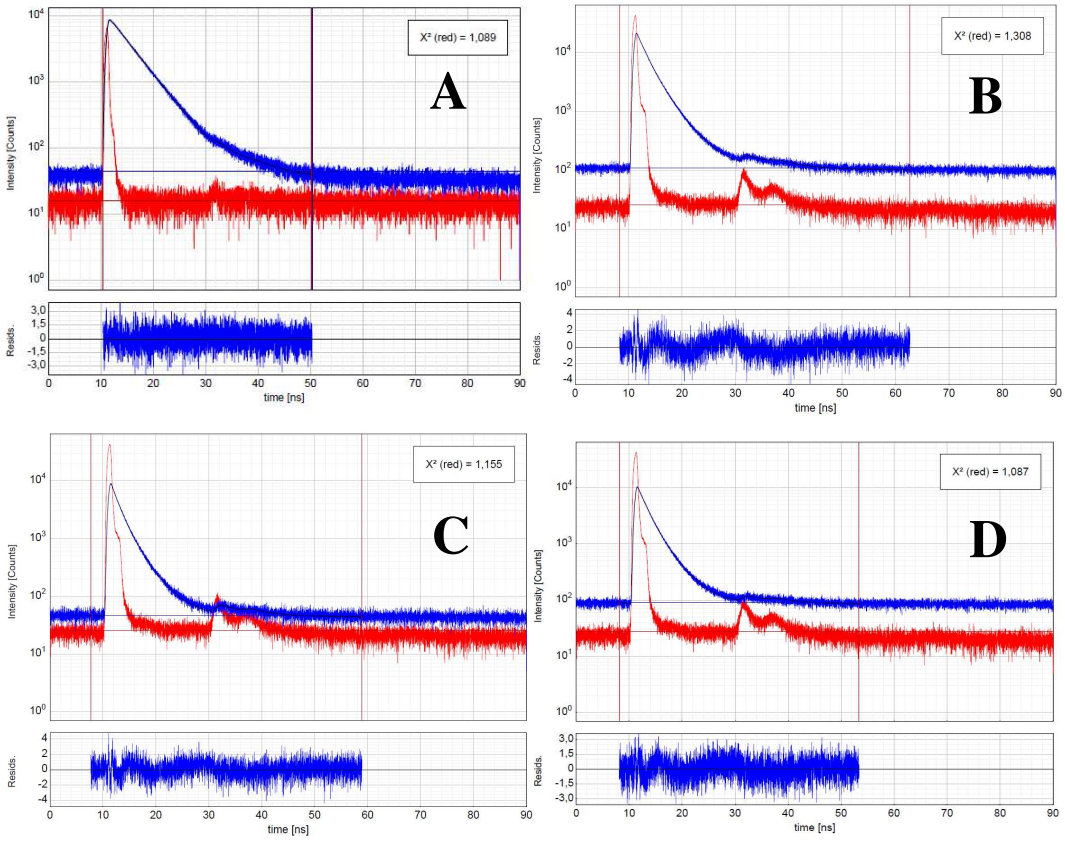

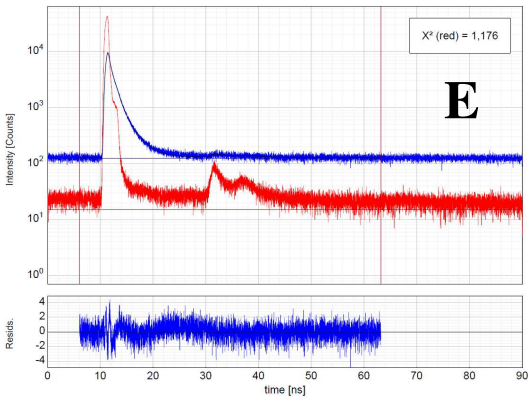

Figure 4.15 Fluorescence decay of **1** in *(A)* ACN solution, and on *(B)* ZrO_2, *(C)* SnO_2, *(D)* TiO_2, *(E)* WO_3 thin films, upon 460 nm excitation.

Table 4.2 Photophysical data from emission quenching on semiconductor substrates in aqueous pH 3 0.1 M $NaClO_4$.

Data	***Substrate***				
	ACN solution	*ZrO_2*	*SnO_2*	*TiO_2*	*WO_3*
$\tau^{(1)}$ (ns)	4.2	/	/	/	/
$A_1^{(2)}$	1924	11670	3723	5391	10140
$A_2^{(2)}$	/	18160	8700	9320	2743
τ_1 (ns)	/	3.3	3.1	3.1	0.7
τ_2 (ns)	/	1.3	1.1	1.2	2.2
τ_{AW} (ns)	/	2.1	1.7	1.9	1.1
τ_{IW} (ns)	/	2.5	2.2	2.4	1.4
$k_{inj}^{(AW)}$ ($\times 10^9$ s^{-1})$^{(3)}$	/	/	0.1	0.05	0.4
$k_{inj}^{(IW)}$ ($\times 10^9$ s^{-1})$^{(3)}$	/	/	0.05	0.02	0.3

AW: Amplitude weighted average lifetime. IW: Intensity weighted average lifetime.

$^{(1)}$ Monoexponential decay.

$^{(2)}$ Amplitudes of the biexponential fitting function $y = A_1 \exp(-\frac{t}{\tau_1}) + A_2 \exp(-\frac{t}{\tau_2})$.

$^{(3)}$ Rate constant calculated according to $k_{inj} = \frac{1}{\tau_{SC}} - \frac{1}{\tau_{ZrO_2}}$, where SC is either WO_3 or SnO_2.

Additional photoelectrochemical measurements, carried out in ACN/0.1 M LiI with optimized WO_3 (SC6) and SnO_2 (SC2) spin coated electrodes (**Figure 4.16** prepared as reported in **Section 4.3.5**), confirmed a superior performance of WO_3 (**Figure 4.17**) in generating higher photocurrent (~2.2 mA/cm^2), photovoltage (V_{OC}(WO_3) = −100 mV vs. SCE; V_{OC}(SnO_2) = −50 mV vs. SCE) and, more significantly, superior fill factor (28% vs. 23%). All these figures are consistent with a more effective charge separation on the WO_3 substrate with respect to SnO_2.

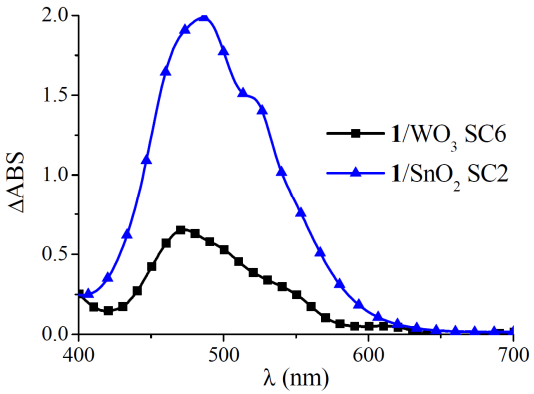

Figure 4.16 Absorption spectra of thicker WO_3 and SnO_2 porous films, obtained by repeated spin coating on FTO, dyed with **1**. Spectra were corrected from scattering and intrinsic semiconductor absorption by subtracting the related identical bare spin coated semiconductor films.

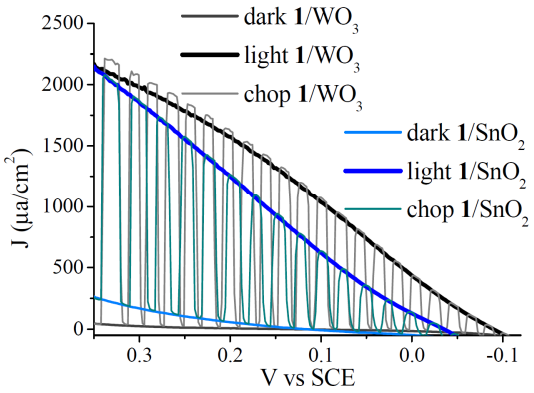

Figure 4.17 J-V characteristics of spin coated WO_3 (SC6) and SnO_2 (SC2) porous thicker films, dyed with **1**, in ACN/0.1 M LiI (AM 1.5 G + 435 nm cut-off filter). The limiting photocurrents recorded with SC2 SnO_2 are consistent with previously reported results obtained with carboxylated perylenes.[32]

Transient absorption measurements, in the ns/μs time scale, agree with the observation of a faster and more efficient formation of the charge separated state ($\mathbf{1}^+/e^-_{CB}$) on WO_3. The photophysical behaviour of **1** in solution, upon 532 nm nanosecond laser excitation, is dominated by the decay of the lowest singlet excited state, resulting in the bleaching of the ground state and in the appearance of the strong stimulated emission with a clear vibronic progression starting from 530 nm (**Figure 4.18**). Similar characteristics are found on ZrO_2 (**Figure 4.19**), where the longer lived ground state bleaching suggests population of the triplet state via spin-orbit coupling induced by heavy atom (Zr) effect in the proximities of the chromophore.

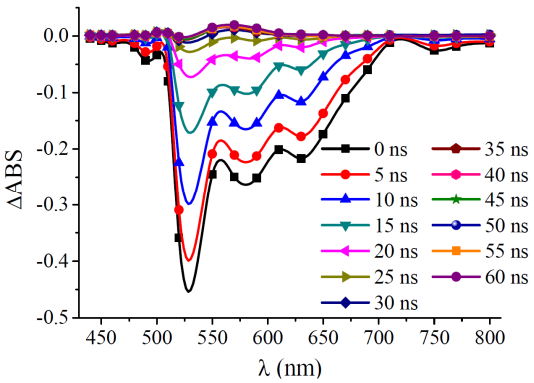

Figure 4.18 Transient differential absorption spectrum of **1** in ACN solution. 532 nm laser excitation, FWHM 7 ns, oscilloscope input resistance of 350 Ω.

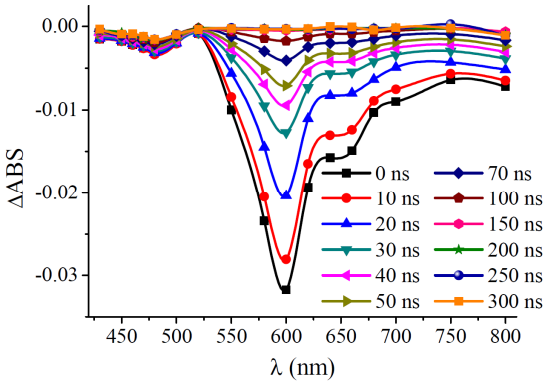

Figure 4.19 Transient differential absorption spectrum of **1**/ZrO_2 thin film, in presence of aqueous pH 3 0.1 M $NaClO_4$. 532 nm laser excitation, FWHM 7 ns, oscilloscope input resistance of 350 Ω.

By contrast on WO_3 (**Figure 4.20**) the magnitude of the residual emission of **1** is greatly reduced with respect to the ground state bleaching, and most importantly, the rise of a characteristic absorption in the blue region of the visible spectrum, between 400 and

450 nm, with maximum at ca. 430 nm can be observed, reaching the maximum intensity within 100 ns after excitation. At 300 ns after the laser pulse, a significant absorption is still evident, while the ground state bleaching at 470 nm undergoes a significant recovery. The transient absorption in the blue region was thus assigned to the formation of the photo-oxidized dye ($\mathbf{1}^+$) resulting from charge injection into WO_3. The electron recapture by the oxidized perylene derivative, occurring in the microsecond time scale, is at least 10^3 slower than injection, indicating a favourable kinetic competition for obtaining and storing a primary long-lived charge separated state ($\mathbf{1}^+/e^-(WO_3)$), which may constitute the basis for solar fuel production in a PEC. On SnO_2 electrodes (**Figure 4.21**), the signature of the charge separated state is much less evident, consistent with the slower charge injection observed in emission quenching experiments.

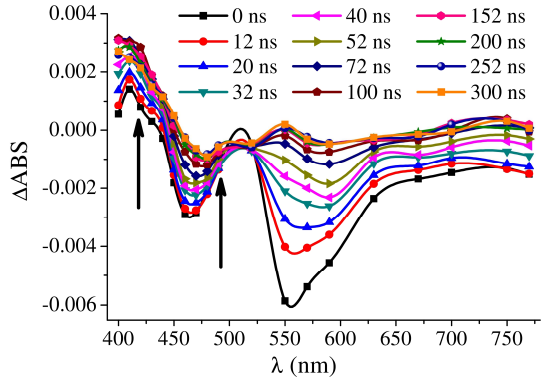

Figure 4.20 Transient differential absorption spectrum of **1**/WO_3 thin film, in presence of aqueous pH 3 0.1 M $NaClO_4$. 532 nm laser excitation, FWHM 7 ns, oscilloscope input resistance of 350 Ω.

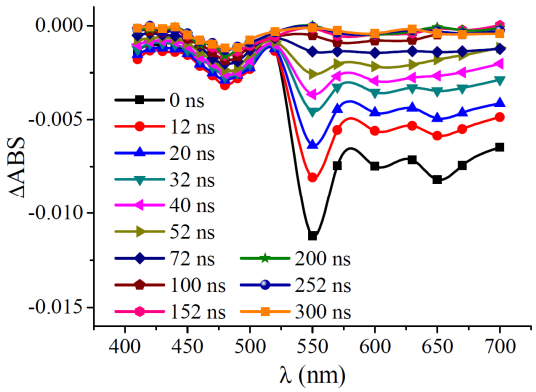

Figure 4.21 Transient differential absorption spectrum of **1**/SnO_2 thin film, in presence of aqueous pH 3 0.1 M $NaClO_4$. 532 nm laser excitation, FWHM 7 ns, oscilloscope input resistance of 350 Ω.

The ability to exploit relatively energetic photogenerated holes, located on surface adsorbed **1** in artificial photosynthetic processes, was tested in the presence of co-deposited IrO_2 NPs, prepared according to the directions of Mallouk et al.[23] Herein IrO_2 was chosen for convenience as an example of catalyst known for having stability and good activity[33] toward water oxidation in acidic media. The mechanism of action (**Figure 4.22**), at least for certain classes of Ir-catalysts, is proposed to follow the formation of high-valent intermediates, undergoing the nucleophilic attack of water (see **Section 1.6**) according to a mononuclear mechanism similar to that already seen for ruthenium single-site catalysts (**Figure 3.5**). Nevertheless the increased oxygen evolution rate and non linear effects at high Ir catalyst concentration suggest that speciation equilibrium and cooperative effects forming dimers or polymers may contribute to the mechanism of oxygen evolution.

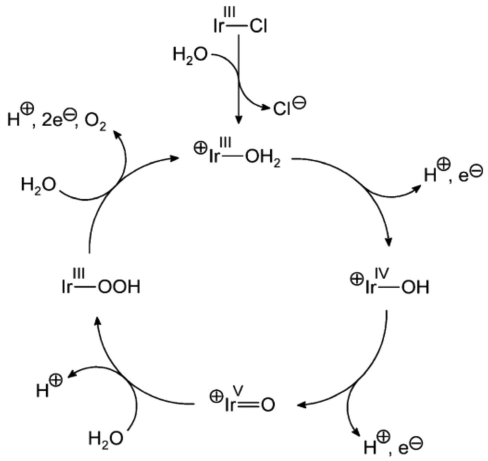

Figure 4.22 Proposed mechanism of action for oxygen evolution in iridium based catalysts.[34]

Different co-deposition methods of IrO_2 NPs on sensitized WO_3 films were explored (**Section 4.3.7**). The different photoanodes, named type ***a–e*** after the IrO_2 modification route, are briefly summarized in **Table 4.3**. Under AM 1.5 G illumination, with 435 nm cut-off filter, without sacrificial agents in aqueous pH 3 0.1 M $NaClO_4$, all IrO_2 co-deposited electrodes exhibit a photoanodic behaviour with photocurrent at 0.5 V vs. SCE decreasing in the order ***d*** > ***e*** > ***c*** > ***b*** > ***a***, reaching maximum values close to 70 μA/cm^2, with a good reproducibility, testified by the small amplitude of the error bars (**Figure 4.23A**), obtained for batches of three identical electrodes.

Table 4.3 Types of **1**/WO_3 photoanodes modified with IrO_2 nanoparticles.

electrode	*deposition method of IrO_2 NPs on **1**/WO_3*
a	without IrO_2 NPs
b	drop casting
c	spin coating
d	spin coating and drying with warm air
e	soaking

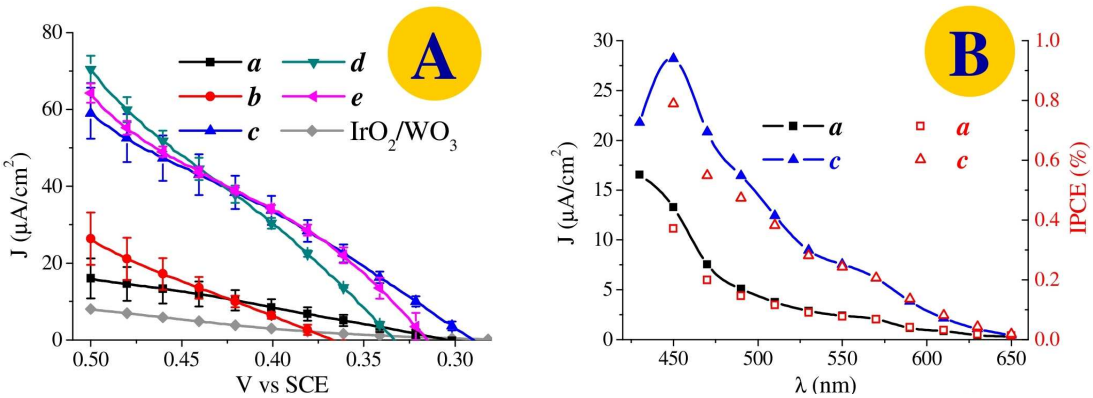

Figure 4.23 *(A)* J-V curves of five different batches of photoelectrodes **1**/WO_3, modified with IrO_2 (***b–e***) compared to the unmodified one (***a***). *(B)* Photocurrent spectra, recorded at constant 0.5 V vs. SCE, of type ***a*** (black squares) and ***c*** (blue triangles) photoanodes with their relative IPCE spectra (red empty squares and triangles). Both data were achieved in aqueous pH 3 0.1 M $NaClO_4$.

The lowest photocurrent onset, observed at ca. 0.3 V vs. SCE, is obtained with type ***c*** and ***d*** electrodes (spin coated IrO_2), which also produce a higher photocurrent density at voltages ranging from 0.28 to 0.43 V vs. SCE. It is clear that the presence of IrO_2 allows

for a ~6-fold enhancement of the photoanodic current density compared to the simple type **a** electrodes (**1**/WO_3) consistent with hole transfer from photogenerated $\mathbf{1}^+$ to IrO_2, which in turn catalyzes water oxidation. IPCE (**Figure 4.23B**) undergoes a doubling when moving from type ***a*** to type ***c*** electrodes, with a photocurrent response in good agreement with the absorption spectrum of the sensitizer. The corresponding APCE values, for the thicker SC6 **1**/WO_3 electrodes, increase from ca. 0.5% to ca. 1% in the IrO_2 treated photoanode (**Figure 4.24**).

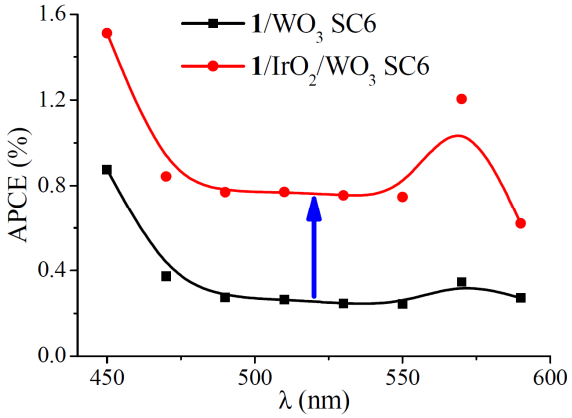

Figure 4.24 APCE spectra in aqueous pH 3 0.1 M $NaClO_4$ at 0.5 V vs. SCE in the presence of 435 nm cut-off filter.

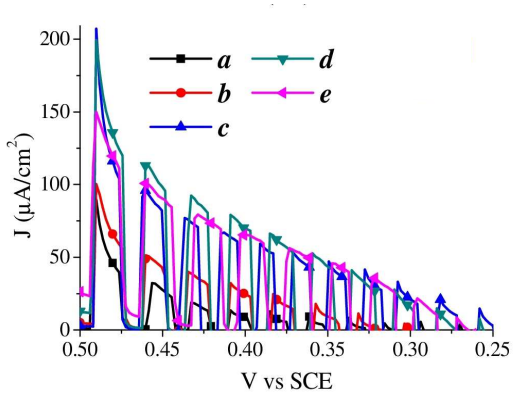

Figure 4.25 J-V curves of the type ***a-e*** electrodes under shuttered illumination. AM 1.5 G with 435 nm cut-off in aqueous pH 3 0.1 M $NaClO_4$.

The J-V curves collected under shuttered illumination (**Figure 4.25**) reveal photocurrent transients reaching ~200 μA/cm^2, at a potential close to 0.5 V vs. SCE (type ***c*** and ***d*** electrodes), which are clearly larger than the photoanodic current collected under steady state conditions (**Figure 4.23A**). The overshooting of the photocurrent transients and their shape, showing a rapidly decreasing photoanodic spike, are indicative of recombination processes in competition with hole transfer to the electrolyte. The charge transfer kinetics, probed at 430 nm (**Figure 4.26**), show that, in the presence of co-deposited IrO_2, a reduction in the lifetime (0.5 μs) of the photo-oxidized sensitizer on the WO_3 surface is observed, ostensibly due to hole transfer to randomly adjacent IrO_2 NPs. The hole transfer kinetics to IrO_2 thus occurs on the same time scale of electron recapture by $\mathbf{1}^+$, according to an apparent first order rate constant of 0.95×10^6 s^{-1}. Unfortunately the fate of the h^+ trapped on IrO_2 could not be directly monitored, due to the lack of significant spectroscopic signatures resulting from the oxidation of Ir(IV), as already pointed out by Wasielewski et al.[12] Nevertheless, even for prolonged illumination periods (hundreds of seconds) at constant potential (0.35 V vs. SCE), the best IrO_2/**1**/WO_3 assembly (***c***) is able to photogenerate a significantly higher anodic charge (up to 5 times) with respect to the unmodified photoelectrodes (***a***) (**Figure 4.27**).

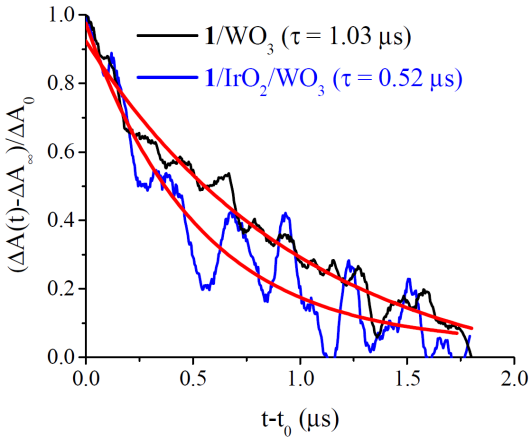

Figure 4.26 430 nm normalized decay kinetics of $\mathbf{1}^{+}/WO_3$, in absence (black) and in presence (blue) of spin coated IrO_2 NPs. The red lines are monoexponential fitting of the oscillographic traces. Thin films were immersed in aqueous pH 3 0.1 M $NaClO_4$ during the measurements. 532 nm laser excitation, FWHM 7 ns, oscilloscope input resistance of 350 Ω.

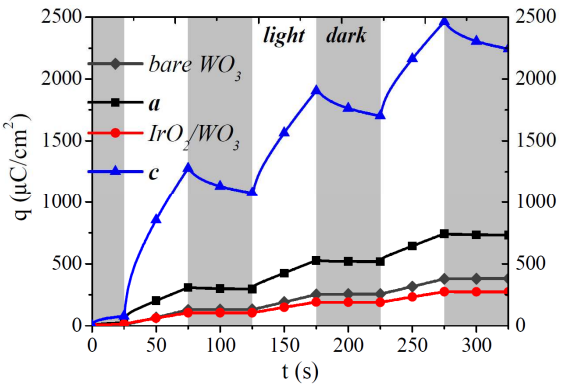

Figure 4.27 Constant potential (0.35 V vs. SCE) chronocoulometric plot of type ***c*** electrode (**1**/IrO_2/WO_3 - blue) compared to bare WO_3 (dark grey), type ***a*** electrode (**1**/WO_3 - black) and spin coated 2 times IrO_2 NPs on WO_3 (red). AM 1.5 G with 435 nm cut-off filter in aqueous pH 3 0.1 M $NaClO_4$. 50 s of illumination cycles (white rectangles) were followed by 50 s dark cycles (little grey rectangles).

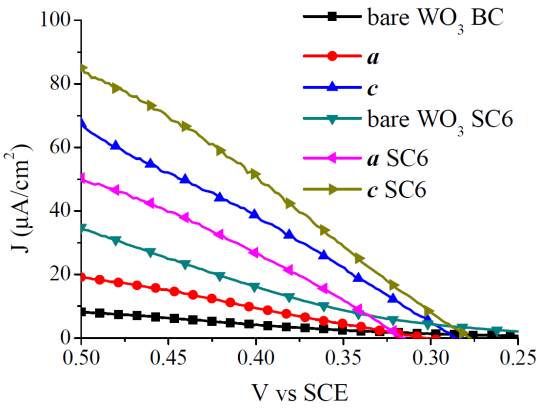

Figure 4.28 J-V characteristics of blade cast (BC) and spin coated (SC6) sensitized WO_3 films in aqueous pH 3 0.1 M $NaClO_4$ under AM 1.5 G with 435 nm cut-off filter: type ***a*** (red) and type ***c*** (blue) electrodes are compared to the equivalent SC6 type electrodes (magenta and gold). The photocurrent density *J* of each electrode was obtained by subtraction of the respective dark current. The performance on unmodified WO_3, blade cast (black) and SC6 (green), are reported for comparison.

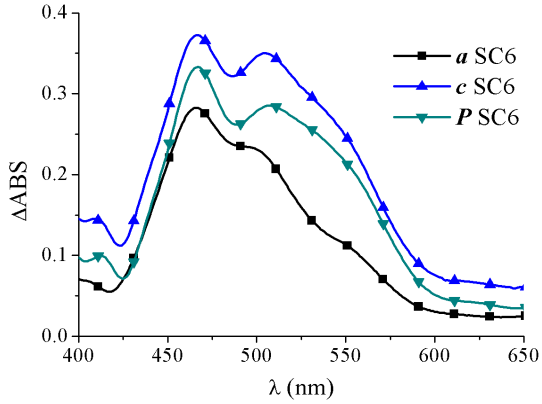

Figure 4.29 Absorption spectra of thicker **1**/WO_3 (***a***), obtained by 6 repeated spin coating on FTO, and decorated with IrO_2 NPs (***c***) or Ru_4POM (***P***). Spectra were corrected from scattering and intrinsic semiconductor absorption by subtracting the related identical bare spin coated semiconductor films.

Experiments carried out with thicker and more optically dense SC6 electrodes (**Figure 4.16**), which performed well in the presence of sacrificial agent (**Figure 4.17**) achieving a ~5 times increment of photocurrent in respect to BC **1**/WO_3 electrode (**Figure 4.12**), did not result in a substantially enhanced photoelectrochemical response in acidic $NaClO_4$, when consideration is made for the contribution of the improved bare WO_3 substrate, pointing out the kinetic bottleneck in the hole transfer to co-deposited IrO_2 NPs (**Figure 4.28**).

Well-optimized **1**/WO_3 SC6 electrode were also employed to photoactivate the known homogeneous phase catalyst Ru_4POM. It was recently published,[35] by Hill and co-workers an interesting application to heterogeneous phase where TiO_2 based photoanodes, functionalized with a series of novel crown ether Ru-dyes and Ru_4POM catalyst, can drive the oxygen evolution at near-neutral pH. Under a 455 nm LED lamp (33 mW/cm^2), in pH 5.8 Na_2SiF_6/$NaHCO_3$/$NaClO_4$ solution. For at least 50 seconds a stable photocurrent of 20 μA/cm^2, with transients reaching 80 μA/cm^2 (in the case of the best dye, trapping 2 Na^+ cation in crown ether), under 0 V vs. Ag/AgCl ~ -0.04 V vs. SCE) was achieved.

In our study, we employed the polyoxometalate molecular catalyst for decoration of **1**/WO_3 SC6 photoanodes, compared with same type of electrodes functionalized with a new batch of IrO_2 NPs, to outline the possibility of activating Ru_4POM loaded on WO_3 electrodes and preliminarily verify whether the tetra-metal core of POM could be more efficient in respect to metal oxide nanoparticles. In **Table 4.4** it is reported the detailed treatment of electrode functionalization, while the relevant absorption spectra are reported in **Figure 4.29**. It should be noted that the estimation of the hole transfer catalyst loading onto the photoelectrode has not been rigorously evaluated yet.

Table 4.4 Types of **1**/WO_3 SC6 photoanodes modified with catalyst.

Electrode	*Treatments*
a	Reference **1**/WO_3 SC6
c	spin coating, 2 times, 1000 rpm/min 20s, R.T., IrO_2 10^{-3} M fresh batch
P	soaking, 5 minutes, Ru_4POM 10^{-4} M in pH 3 0.1 M $NaClO_4$ solution

Under the same conditions previously reported (AM 1.5 G with 435 nm cut-off filter in aqueous pH 3 0.1 M $NaClO_4$), the electrodes exhibit a photoanodic behaviour with photocurrent at 0.5 V vs. SCE decreasing in the order ***c*** > ***P*** > ***a***, reported in **Figure 4.30A**. Type ***a*** and bare WO_3 SC6 (black squares and grey diamonds respectively) show more or less the same performances compared to the previous electrode batches, reported in **Figure 4.28** (magenta left-triangles and dark cyan down-triangles), whereas a good improvement occur for type ***c*** (blue up-triangles respect to gold right-triangles in **Figure 4.28**) at 0.5 V vs. SCE, with an increase in the photocurrent from 80 μA/cm^2 to 110 μA/cm^2, thanks probably to a new fresh batch of IrO_2 NPs having increased activity. ***P*** also shows an improved performance with respect to the unmodified electrode, reaching a photocurrent of ~100 μA/cm^2, that quickly drops to zero at 0.40 V vs. SCE, ostensibly due to comparatively increased recombination at lower potential bias. It is clear that ***c*** and ***P***

exhibit a sensible difference in global efficiency, which can be easily appreciated the different areas enclosed by their respective J-V characteristics (**Figure 4.30A**).

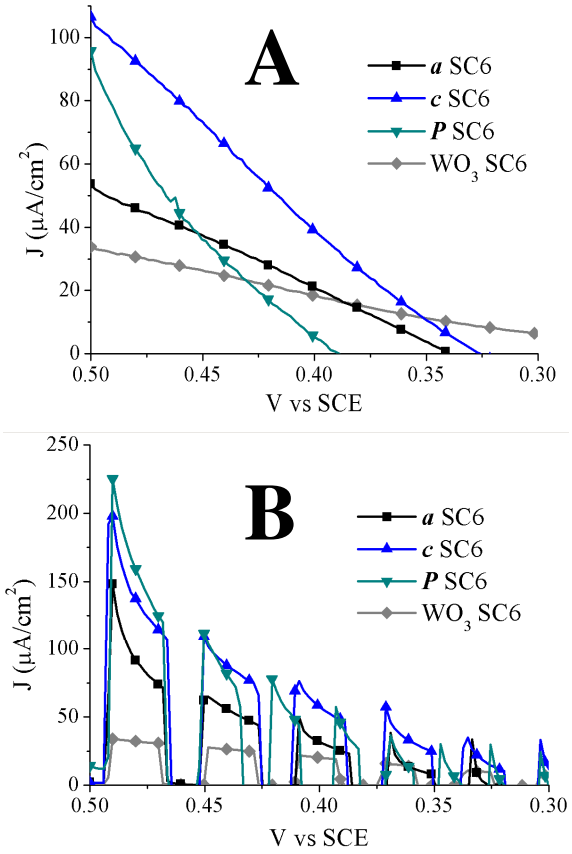

Figure 4.30 J-V characteristics (*A*) and under shuttered illumination (*B*) of **1**/WO_3 SC6 photoanodes, modified with IrO_2 (***c***) or Ru_4POM (***P***) compared to the unmodified one (***a***) and bare semiconductor (grey diamonds). AM 1.5 G with 435 nm cut-off in aqueous pH 3 0.1 M $NaClO_4$.

Photocurrent transient (**Figure 4.30B**) under potentiodynamic conditions are consistent with the results observed in J-V curves under steady state conditions. In both type ***c*** and ***P*** electrodes the overshooting of the transients reaching over 200 μA/cm^2, at ca. 0.5 V vs. SCE show the presence of recombination processes competitive with h^+ injection into the electrolyte, in agreement with the previously discussed results. Interestingly, the transients reveal that the ***P*** electrode generates photoanodic transients which are comparable, or even higher than the photoanodic current recorded in the presence of IrO_2, indicating that h^+ are effectively transferred from the sensitizer to the Ru_4POM. Unfortunately, the steeper decay of the transients and the smaller amplitude of the transients at lower applied bias, suggests that recombination involving oxidized POM or water oxidation intermediates on the surface with electrons trapped in WO_3 is kinetically more efficient than that observed in the presence of IrO_2. Appropriate surface passivation methods should be devised in order to exploit the full potentialities of the cationic perylene/Ru_4POM couples on the WO_3 surface. Another possibility for the increased recombination might involve the static reductive quenching in ionic couples or assemblies formed by the negative $[Ru_4POM]^{10-}$ and the positive PBI^{2+}.[36] On the other hand, this quenching mechanism could also represent an effective mean of charge separation on semiconductor surface (as described in **Chapter 5**), if the reduced state of the perylene is able to inject efficiently in the semiconductor, before back electron transfer occurs. Transient spectroscopic data will be needed to clarify the charge separation pathway effectively followed on these surfaces in order to rationally devise a strategy for suppressing the energy wasting processes.

Finally, APCE values recorded at constant 0.5 V vs SCE (**Figure 4.31**), are consistent with the steady state J-V results showing that ***c*** can generate an intrinsically superior photon-to-electron conversion with respect to ***P***, for which respectable mean values of the order of 2.5% with respect to ca. 4% in the IrO_2 catalyzed samples are recorded. These are among the best values for water splitting cells based on molecular processes and demonstrate the flexibility and suitability of robust cationic perylenes to photogenerate strongly oxidizing species for triggering water oxidation reactions at the molecular level.

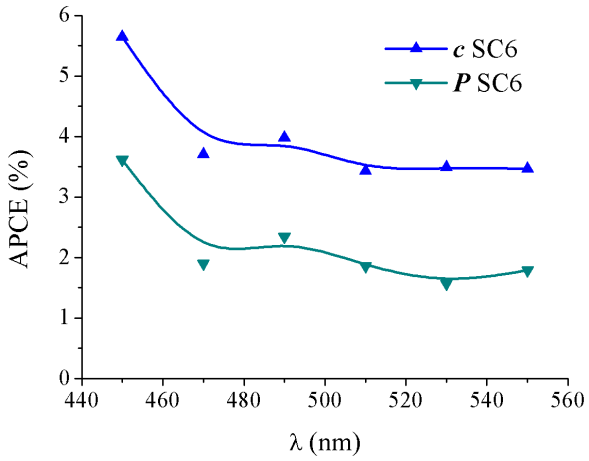

Figure 4.31 APCE spectra in aqueous pH 3 0.1 M $NaClO_4$ at 0.5 V vs. SCE in the presence of 435 nm cut-off filter.

4.5 Chapter 4 - Conclusions

In conclusion, we have demonstrated that the modification of WO_3 with simple PBI derivatives, by exploiting aggregation forces, leads to photoanodes where electron injection results in long-lived charge separated states in the heterogeneous phase, where the strong oxidizing power of photogenerated holes can be potentially employed to activate a wide array of catalysts, having $E_{OX} < 1.7$ V vs. SCE, to drive photo-oxidation reactions under visible illumination.

The fact that charge injection on WO_3 is more efficient than on SnO_2, which has a similar CB energetics, may underline the role of a stronger electronic coupling resulting either from a stronger electrostatic interaction with the negatively charged WO_3 surface at pH 3[37] or by a larger overlap between the *d* band and the π^* orbitals of **1**.

Clearly, the low WO_3 CB, while allowing an efficient quenching of the excited state of PBIs, requires the application of a positive potential to drive the hydrogen evolution reaction at the counter electrode of the PEC. Although this is disadvantageous for a self-standing cell operating without additional bias, it should be recalled that, even when using TiO_2 in sensitized PEC for water splitting, it is often necessary to apply a moderately positive bias, up to 0.3 V vs. NHE, to overcome, for both thermodynamic and kinetic reasons, recombination processes. In these cases, the sensitized electrode serves only as the photoanodic component of a cell, which will require the coupling to a photocathode, to achieve its independent operation without external potential.

Finally, these porous photoanodes may also constitute a convenient mean to explore and optimize the interaction of the PBI chromophores, immobilized on surfaces, with selected catalytic species, including amorphous metal oxides and molecular species, in order to increase the efficiency of the interfacial charge transfer over competitive carrier recombination, representing, at present, the most serious limitation to molecular level artificial photosynthetic processes. The preliminary but encouraging results obtained with the co-adsorption of **1** and Ru_4POM demonstrate with some generality that indeed, on suitable semiconductors, robust cationic perylenes can be exploited to photogenerate strongly oxidizing species for triggering water oxidation reactions at the molecular level.

4.6 Chapter 4 - Figures index

4.7 Chapter 4 - References

(1) Alibabaei, L.; Brennaman, M. K.; Norris, M. R.; Kalanyan, B.; Song, W.; Losego, M. D.; Concepcion, J. J.; Binstead, R. A.; Parsons, G. N.; Meyer, T. J. *Proceedings of the National Academy of Sciences* **2013**, *110*, 20008.

(2) Gao, Y.; Ding, X.; Liu, J.; Wang, L.; Lu, Z.; Li, L.; Sun, L. *Journal of the American Chemical Society* **2013**, *135*, 4219.

(3) Vannucci, A. K.; Alibabaei, L.; Losego, M. D.; Concepcion, J. J.; Kalanyan, B.; Parsons, G. N.; Meyer, T. J. *Proceedings of the National Academy of Sciences* **2013**, *110*, 20918.

(4) Gao, Y.; Zhang, L.; Ding, X.; Sun, L. *Physical Chemistry Chemical Physics* **2014**, *16*, 12008.

(5) Kirner, J. T.; Stracke, J. J.; Gregg, B. A.; Finke, R. G. *ACS Applied Materials & Interfaces* **2014**, *6*, 13367.

(6) Kanan, M. W.; Nocera, D. G. *Science* **2008**, *321*, 1072.

(7) Schmidt, C. D.; Hirsch, A. In *Ideas in Chemistry and Molecular Sciences: Advances in Synthetic Chemistry*; Pignataro, B., Ed.; Wiley WCH: New York, **2010**, p 283.

(8) Li, C.; Wonneberger, H. *Advanced Materials* **2012**, *24*, 613.

(9) Huang, C.; Barlow, S.; Marder, S. R. *The Journal of Organic Chemistry* **2011**, *76*, 2386.

(10) Concepcion, J. J.; Jurss, J. W.; Brennaman, M. K.; Hoertz, P. G.; Patrocinio, A. O. T.; Murakami Iha, N. Y.; Templeton, J. L.; Meyer, T. J. *Accounts of Chemical Research* **2009**, *42*, 1954.

(11) Kunz, V.; Stepanenko, V.; Wurthner, F. *Chemical Communications* **2015**, *51*, 290.

(12) Vagnini, M. T.; Smeigh, A. L.; Blakemore, J. D.; Eaton, S. W.; Schley, N. D.; D'Souza, F.; Crabtree, R. H.; Brudvig, G. W.; Co, D. T.; Wasielewski, M. R. *Proceedings of the National Academy of Sciences* **2012**, *109*, 15651.

(13) Weingarten, A. S.; Kazantsev, R. V.; Palmer, L. C.; McClendon, M.; Koltonow, A. R.; SamuelAmanda, P. S.; Kiebala, D. J.; Wasielewski, M. R.; Stupp, S. I. *Nature Chemistry* **2014**, *6*, 964.

(14) Fillol, J. L.; Codolà, Z.; Garcia-Bosch, I.; Gómez, L.; Pla, J. J.; Costas, M. *Nature Chemistry* **2011**, *3*, 807.

(15) Klepser, B. M.; Bartlett, B. M. *Journal of the American Chemical Society* **2014**, *136*, 1694.

(16) Ding, X.; Gao, Y.; Zhang, L.; Yu, Z.; Liu, J.; Sun, L. *ACS Catalysis* **2014**, *4*, 2347.

(17) Kärkäs, M. D.; Verho, O.; Johnston, E. V.; Åkermark, B. *Chemical Reviews* **2014**, *114*, 11863.

(18) Geletii, Y. V.; Botar, B.; Kögerler, P.; Hillesheim, D. A.; Musaev, D. G.; Hill, C. L. *Angewandte Chemie International Edition* **2008**, *47*, 3896.

(19) Sartorel, A.; Carraro, M.; Scorrano, G.; Zorzi, R. D.; Geremia, S.; McDaniel, N. D.; Bernhard, S.; Bonchio, M. *Journal of the American Chemical Society* **2008**, *130*, 5006.

(20) Sartorel, A.; Miró, P.; Salvadori, E.; Romain, S.; Carraro, M.; Scorrano, G.; Valentin, M. D.; Llobet, A.; Bo, C.; Bonchio, M. *Journal of the American Chemical Society* **2009**, *131*, 16051.

(21) Orbelli Biroli, A.; Tessore, F.; Pizzotti, M.; Biaggi, C.; Ugo, R.; Caramori, S.; Aliprandi, A.; Bignozzi, C. A.; De Angelis, F.; Giorgi, G.; Licandro, E.; Longhi, E. *The Journal of Physical Chemistry C* **2011**, *115*, 23170.

(22) Meda, L.; Tozzola, G.; Tacca, A.; Marra, G.; Caramori, S.; Cristino, V.; Alberto Bignozzi, C. *Solar Energy Materials and Solar Cells* **2010**, *94*, 788.

(23) Hara, M.; Waraksa, C. C.; Lean, J. T.; Lewis, B. A.; Mallouk, T. E. *The Journal of Physical Chemistry A* **2000**, *104*, 5275.

(24) Huang, Y.; Yan, Y.; Smarsly, B. M.; Wei, Z.; Faul, C. F. J. *Journal of Materials Chemistry* **2009**, *19*, 2356.

(25) Deligeorgiev, T.; Zaneva, D.; Petkov, I.; Timcheva, I.; Sabnis, R. *Dyes and Pigments* **1994**, *24*, 75.

(26) Mba, M.; D'Acunzo, M.; Salice, P.; Carofiglio, T.; Maggini, M.; Caramori, S.; Campana, A.; Aliprandi, A.; Argazzi, R.; Carli, S.; Bignozzi, C. A. *The Journal of Physical Chemistry C* **2013**, *117*, 19885.

(27) Frisch, M. J.; Trucks, G. W.; Schlegel, H. B.; Scuseria, G. E.; Robb, M. A.; Cheeseman, J. R.; Scalmani, G.; Barone, V.; Mennucci, B.; Petersson, G. A.; Nakatsuji, H.; Caricato, M.; Li, X.; Hratchian, H. P.; Izmaylov, A. F.; Bloino, J.; Zheng, G.; Sonnenberg, J. L.; Hada, M.; Ehara, M.; Toyota, K.; Fukuda, R.; Hasegawa, J.; Ishida, M.; Nakajima, T.; Honda, Y.; Kitao, O.; Nakai, H.; Vreven, T.; Montgomery Jr., J. A.; Peralta, J. E.; Ogliaro, F.; Bearpark, M. J.; Heyd, J.; Brothers, E. N.; Kudin, K. N.; Staroverov, V. N.; Kobayashi, R.; Normand, J.; Raghavachari, K.; Rendell, A. P.; Burant, J. C.; Iyengar, S. S.; Tomasi, J.; Cossi, M.; Rega, N.; Millam, N. J.; Klene, M.; Knox, J. E.; Cross, J. B.; Bakken, V.; Adamo, C.; Jaramillo, J.; Gomperts, R.; Stratmann, R. E.; Yazyev, O.; Austin, A. J.; Cammi, R.; Pomelli, C.; Ochterski, J. W.; Martin, R. L.; Morokuma, K.; Zakrzewski, V. G.; Voth, G. A.; Salvador, P.; Dannenberg, J. J.; Dapprich, S.; Daniels, A. D.; Farkas, Ö.; Foresman, J. B.; Ortiz, J. V.; Cioslowski, J.; Fox, D. J.; Gaussian, Inc.: Wallingford, CT, USA, **2009**.

(28) Gao, F.; Zhao, Y.; Liang, W. *The Journal of Physical Chemistry B* **2011**, *115*, 2699.

(29) Hines, E.; Boltz, D. F. *Analytical Chemistry* **1952**, *24*, 947.

(30) Rajh, T.; Nedeljkovic, J. M.; Chen, L. X.; Poluektov, O.; Thurnauer, M. C. *The Journal of Physical Chemistry B* **1999**, *103*, 3515.

(31) Sirimanne, P. M.; Soga, T. *Solar Energy Materials and Solar Cells* **2003**, *80*, 383.

(32) Ferrere, S.; Zaban, A.; Gregg, B. A. *The Journal of Physical Chemistry B* **1997**, *101*, 4490.

(33) Youngblood, W. J.; Lee, S.-H. A.; Kobayashi, Y.; Hernandez-Pagan, E. A.; Hoertz, P. G.; Moore, T. A.; Moore, A. L.; Gust, D.; Mallouk, T. E. *Journal of the American Chemical Society* **2009**, *131*, 926.

(34) Blakemore, J. D.; Crabtree, R. H.; Brudvig, G. W. *Chemical Reviews* **2015**, *115*, 12974.

(35) Fielden, J.; Sumliner, J. M.; Han, N.; Geletii, Y. V.; Xiang, X.; Musaev, D. G.; Lian, T.; Hill, C. L. *Chemical Science* **2015**, *6*, 5531.

(36) Natali, M.; Orlandi, M.; Berardi, S.; Campagna, S.; Bonchio, M.; Sartorel, A.; Scandola, F. *Inorganic Chemistry* **2012**, *51*, 7324.

(37) Kim, J.; Lee, C. W.; Choi, W. *Environmental Science & Technology* **2010**, *44*, 6849.

CHAPTER 5. CHARGE INJECTION FROM THE PHOTO-GENERATED REDUCED STATE OF A NEW RU(II) POLYPYRIDINE SENSITIZER INTO NANOSTRUCTURED TiO_2 ELECTRODES: THE "ANTI-BIOMIMETIC" MECHANISM AT WORK

5.1 Chapter 5 - Abstract

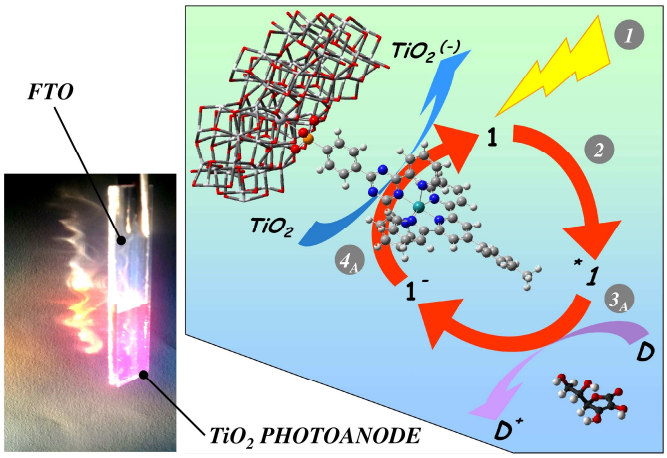

Figure 5.1 Representation of the anti-biomimetic effect that occur onto sensitized TiO_2 photoanodes, in presence of ascorbate.

The charge transfer dynamics involving a new Ru(II) polypiridine complex (**1**), developed to generate highly oxidizing photoholes for water oxidation, were studied by electrochemical, photoelectrochemical and spectroscopic means. Under 1 sun illumination (AM 1.5 G with a 420 nm cut-off filter) and a moderate potential bias (0.3 V vs. SCE), in ACN/0.1 M LiI as a sacrificial electron donor, can reach anodic photocurrent of ~0.2 mA/cm^2 and correspondingly low IPCEs. If aqueous pH 3 0.1 M sodium ascorbate is used instead of iodide, the photocurrent grows to ~0.8 mA/cm^2 and up to 1.2 mA/cm^2 if the concentration of ascorbate is increased to 0.5 M, explainable with a modification of the charge injection mechanism. This is the photoelectrochemical evidence of the so called "anti-biomimetic" pathway in heterogeneous phase, confirmed in transient differential absorption spectroscopy by a long lived sharp bleaching at 480 nm and a narrow absorption between 500-550 nm, characteristic fingerprints of the photogenerated reduced state (**1**$^-$). After the formation of ***1**/TiO_2, the reductive quenching occurs (**Figure 5.1**), carried out by ascorbate and not in LiI conditions, where the classic oxidative quenching take place. Due to the modest excited state oxidation potential, charge injection onto TiO_2 is thermodynamically more favorable from **1**$^-$ rather than ***1**. Lastly, experiments performed with sensitized SnO_2 photoanodes, where ***1** undergoes the usual oxidative quenching, by charge transfer to the conduction band of the metal oxide, allowed to verify the interaction between **1**$^+$ and IrO_2 nanoparticles, grafted on the surface, in order to drive photoinduced water oxidation.

5.2 Chapter 5 - Introduction

Visible light sensitization of semiconductor electrodes, by molecular dyes, is an attractive way to drive solar energy conversion. Indeed, this approach is well-explored in dye-sensitized solar cells (DSSCs) in order to obtain electric potential, particularly with n-type semiconductor such as mesoporous nanostructured TiO_2 electrodes.[1] Dye-sensitized photoelectrochemical cells (DSPECs) combine some principles of DSSC and of the Fujishima-Honda experiment[2] in light-to-fuels conversion schemes, in order to drive, for example, water splitting in heterogeneous phase.[3] Significant models of water oxidation DSPEC have been reported in recent years, starting from pioneering approaches,[4,5] and are now investigated by various research teams worldwide.[6-14]

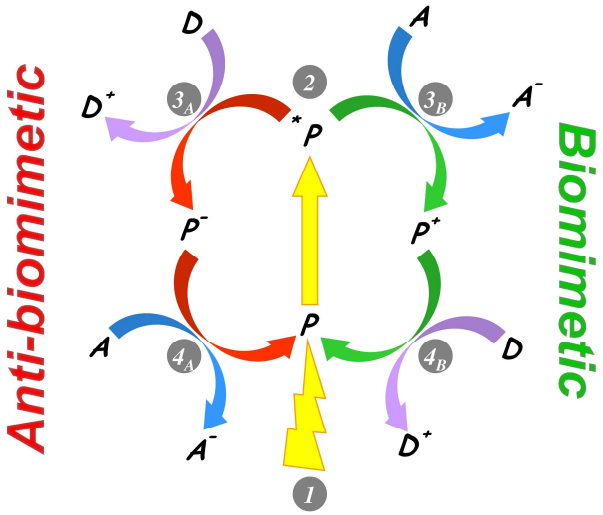

Figure 5.2 Schematization of the two processes that take place after light absorption by the photosensitizer (*P*). In the biomimetic pathway (green arrows, 1-2-3_B-4_B) $^*P$ undergoes an oxidative quenching by the electron acceptor (*A*, in our case the semiconductor CB), then the reductive quenching occurs by the electron donor (*D*, the electrolyte or the WOC) restoring *P* to the initial situation. In the anti-biomimetic pathway (red arrows, 1-2-3_A-4_A) the order of the quenchings is switched.

Usually in devices based on sensitized n-type semiconductor electrodes, the valuable process (photogenerated current in DSSC and photoinduced water splitting in DSPEC) can be developed and sustained by two different interfacial electron transfer mechanisms, which are schematized in **Figure 5.2**. In the conventional oxidative quenching of excited state, here termed "biomimetic" pathway (green arrows, 1-2-3_B-4_B), after the light absorption, the excited photosensitizer ($^*P$) inject one electron (e^-) in the conduction band (CB) of the semiconductor (the electron acceptor *A*). The oxidized dye (P^+) is finally reduced by the electron donor (*D*) present in solution, i.e. the iodide/triiodide reversible electrolytic couple for DSSC or the water oxidation catalyst (WOC) for DSPEC. The biomimetic pathway is a very simplified version of the natural photosynthesis,[15] where water oxidation in photosystem II (PSII) occurs by oxidative quenching of the photoexcited chromophore (special pair P680) by a primary pheophytin acceptor. Subsequently, the oxidated P680 is restored by a protein tyrosine residue that transfer the photogenerated hole (h^+) on the Mn_4OEC (oxygen evolving catalyst) for four

times. After that, the OEC is able to convert two molecules of water in one of oxygen and four protons.

The alternative mechanism, here termed the "anti-biomimetic" pathway (**Figure 5.2**, red arrows, 1-2-3_A-4_A), assumes that the excited sensitizer does not transfer an e^- to semiconductor, because of, for example, thermodynamically forbidden (or partially) charge injection, faster competitive deactivation processes, or both. Given that, $^*P$ could be reductively quenched by *D*, if the redox potential of both species are appropriately matched, generating P^- that successively undergoes charge injection into the semiconductor CB. The two mechanisms showed in **Figure 5.2** could seem to be qualitatively equivalent, but essentially all the reported systems, dealing with mesoporous TiO_2 electrodes – both in the well-studied DSSC and in DSPEC, which are still in their infancy – are based on the biomimetic one.

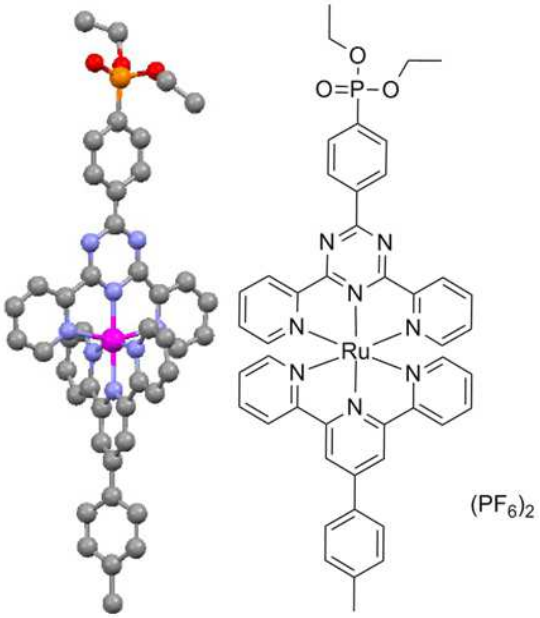

Figure 5.3 X-ray crystallographic structure (anions omitted) and structural formula of **P1**.

Herein we report on the synthesis of a new Ru(II) polypyridine compound, **P1** (**Figure 5.3**), designed for generating highly oxidizing holes in photoinduced water splitting processes. After the conversion of **P1** in **1** (**Figure 5.6**), by acid hydrolysis, the sensitization of semiconductor based photoanodes (TiO_2 and SnO_2) was carried out in order to assess its performance as charge transfer sensitizer. Interestingly, it was found that the excited state of the TiO_2-anchored species **1** has a poor ability to inject electrons into the CB, and therefore to produce a good photon-to-electron conversion, whereas a substantial increase in photoanodic current is observed when the electrode is exposed to ascorbate solutions. This effect, on the basis of photoelectrochemical and transient spectroscopic measurements, was attributed to the anti-biomimetic mechanism, where the main excited state deactivation pathway occurs via reductive photoinduced electron transfer by ascorbate salts, leading to the reduced species [Ru(II)–L^-] having enough potential to inject e^- onto TiO_2.

In literature, some works have been devoted to demonstrate that the anti-biomimetic mechanism can be effective on TiO_2[16,17] and SnO_2[18] thin films, but, to the best of our knowledge, up to now no conclusive evidence of the mechanism action in an

operational TiO_2 based photoelectrode was provided. Nevertheless, this pathway has been recently introduced in the homogeneous phase, in order to rationalize the machinery of a sacrificial system for photoinduced water oxidation.[19,20] The anti-biomimetic mechanism could reserve intriguing properties, for example allowing the use of dyes with interesting redox peculiarities, in order to drive solar water splitting in combination with suitable catalysts, which, for thermodynamic or kinetic reasons, cannot inject e^- from the excited state into semiconductor. This has the advantage of extending the range of potentially useful species for sensitization and of removing some limits to the designing principles of these devices. Moreover, the anti-biomimetic pathway avoids the formation of the oxidized form of the photosensitizer, so it could be profitably used when stability of P^+ is an issue.

5.3 Chapter 5 - Experimental section

5.3.1 Materials

15% SnO_2 colloidal solution in water and 99.999% LiI were from Alfa Aesar.

Polyethyleneglycol bisphenol A epichlorohydrin copolymer 15000 - 20000 Dalton, Triton-X 100, Alconox®, lithium perchlorate ($LiClO_4$) ACS reagent ≥95.0%, ammonium hexafluorophosphate (NH_4PF_6) ≥95%, tetrabutylammonium hexafluorophosphate ($TBAPF_6$) purum ≥98.0%, silver nitrate ($AgNO_3$) ACS reagent ≥99.0%, sodium hydroxide (NaOH) reagent grade ≥98.0% pellets anhydrous, absolute ethanol (EtOH) puriss. p.a. ACS reagent ≥99.8%, acetonitrile (ACN) anhydrous 99.8%, ACS grade ≥99.8% 2-propanol, toluene (TOL) anhydrous 99.8%, *N,N*-dimethylformamide (DMF) anhydrous 99.8%, ascorbic acid 99% grade, perchloric acid ($HClO_4$) ACS reagent 70%, 37% hydrochloric acid (HCl), ≥99% glacial acetic acid, triethylamine (Et_3N) ≥99%, pyridine-2-carbaldehyde, 4-bromobenzaldehyde, [1,1-bis-(di-phenyl-phosphino)ferrocene]di-chloropalladium(II), diethyl phosphite, 4-tolualdehyde, silica gel and the deuterated solvents were from Sigma Aldrich.

2,4-di(2'-pyridyl)-6-(*p*-bromophenyl)-1,3,5-triazine were synthesized according to previous literature reports,[21] as well as the ligand 4'-(tolyl)-2,2':6',2''-terpyridine (*Tol-tpy*)[22] and their $Ru(III)Cl_3$ complexes.[23]

18-NRT TiO_2 colloidal paste was purchased from Dyesol.

TEC 8 (8 Ω/□) fluorine tin oxide (FTO) 20×20 cm conductive glass slides were obtained from Pilkington.

SnO_2 and ZrO_2 colloidal pastes was prepared according to previously reported directions.[14,24]

Colloidal IrO_2 nanoparticles solution was prepared by following literature routes.[25]

All reagents, unless otherwise stated, were used as received.

*5.3.2 Synthesis of diethyl 4-(4,6-di(pyridin-2-yl)-1,3,5-triazin-2-yl) phenyl-phosphonate (**L**)*

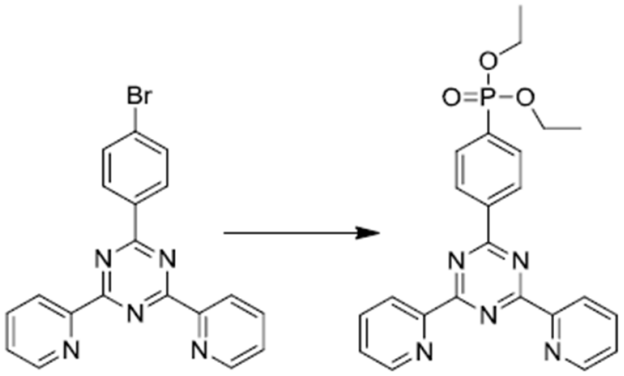

Figure 5.4 Reaction scheme of **L** synthesis.

The synthesis (**Figure 5.4**) was adapted from literature.[26] In a 50 ml round flask, 19 mg of [1,1-bis-(di-phenyl-phosphino)ferrocene]di-chloropalladium(II) (MW = 735.90 g/mol, 0.026 mmol) were suspended in 5 ml of dry TOL under N_2 and vigorous magnetic stirring. Successively 200 mg of 2,4-di(2'-pyridyl)-6-(*p*-bromophenyl)-1,3,5-triazine (MW = 390.24 g/mol, 0.51 mmol), 72 µl of diethyl phosphite (MW = 138.10 g/mol, ρ = 1.072 g/ml, 0.56 mmol) and 80 µl of NEt_3 (MW = 101.19 g/mol, ρ = 0.726 g/ml, 0.57 mmol) were added. The mixture was heated at 90 °C for 24 hours under N_2. The solution was cooled at room temperature and the solid was filtered off. The filtrate was evaporated to dryness, in order to give 206 mg of diethyl 4-(4,6-di(pyridin-2-yl)-1,3,5-triazin-2-yl) phenyl-phosphonate (MW = 447.43 g/mol, 0.46 mmol, 90% yield) as a yellow oil, which was used as obtained in the following step.

^{1}H (Chloroform-d_1, 300 MHz) δH (ppm): 8.97 (d, J = 6 Hz, 2H), 8.91-8.80 (m, 4H), 8.09-7.96 (m, 4H), 7.55 (m, 2H), 4.16 (m, 4H), 1.36 (m, 6H).

^{31}P (Chloroform-d_1, 121 MHz) δP (ppm): 17.6, 17.5.

ESI-MS, m/z: 448.15 [**L**+H]$^+$.

*5.3.3 Synthesis of [Ru^{II}(tol-tpy)**L**]$(PF_6)_2$ (**P1** and **1**)*

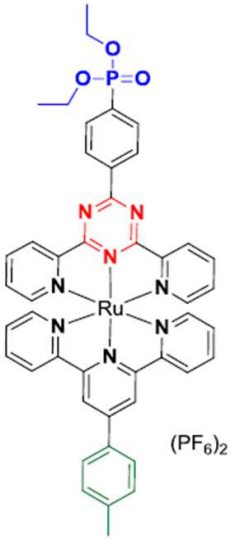

Figure 5.5 Complex [Ru^{II}(*tol-tpy*)**L**]$(PF_6)_2$ diethyl phosphonate, named **P1** for the sake of brevity.

In a 100 ml round flask, 239 mg of (4'-(tolyl)-2,2':6',2''-terpyridine)$Ru^{III}Cl_3$ (MW = 530.82 g/mol, 0.45 mmol) and 229 mg of $AgNO_3$ (MW = 169.87 g/mol, 1.35 mmol) were refluxed for 1 hour in 15 ml degassed absolute EtOH. The solvent was evaporated and the residue dissolved in 20 ml of DMF. 200 mg of **L** (MW = 447.43 g/mol, 0.45 mmol) were added and the mixture was refluxed under N_2 for 3 hours. SiO_2 column chromatography (gradient ACN/KNO_3 aq.) and salt metathesis with NH_4PF_6 afforded 128 mg of complex **P1** (MW = 1161.82 g/mol, 0.11 mmol, 24% yield) (**Figure 5.5**).

^{1}H (Acetonitrile-d_3, 300 MHz) δH (ppm): 9.17 (d, J = 6 Hz, 2H), 9.11 (d, J = 9 Hz, 2H), 9.04 (s, 2H), 8.67 (d, J = 6 Hz, 2H), 8.23-8.12 (m, 6H), 7.96 (d, J = 6 Hz, 2H), 7.68 (d, J = 6 Hz, 2H), 7.60 (d, J = 9 Hz, 2H), 7.44 (m, 4H), 7.14 (t, J = 6 Hz, 2H), 4.21 (t, J = 6 Hz, 4H), 1.38 (t, J = 6 Hz, 6H).

^{31}P (Acetonitrile-d_3, 121 MHz) δP (ppm): 16.0, -144.6 (sept, *J* = 705 Hz).

ESI-MS: 872.13 (55%) [**P1**]$^+$, 436.13 (100%) [**P1**]$^{2+}$.

The complex **P1** was refluxed in 4 M HCl for several days, in order to obtain **1**.

^{1}H (Chloroform-d_1, 300 MHz) δH (ppm): 9.11 (d, J = 6 Hz, 4H), 9.03 (s, 2H), 8.64 (d, J = 9 Hz, 2H), 8.10 (m, 6H), 7.92 (m, 2H), 7.60 (d, J = 6 Hz, 2H), 7.55 (d, J = 9 Hz, 2H), 7.42 (m, 4H), 7.13 (m, 2H).

^{13}C (Acetonitrile-d_3, 300 MHz) δC (ppm): 161.7, 161.0, 160.1, 158.4, 155.6, 154.6, 154.3, 153.3, 149.8, 145.8, 139.1, 138.9, 134.0, 132.0, 130.9, 130.7, 129.6, 129.4, 128.5, 128.0, 127.8, 125.0, 121.6, 119.3.

^{31}P (Chloroform-d_1, 121 MHz) δP (ppm): 10.2, -144.8 (sept, J = 702 Hz).

ESI-MS, m/z: 408.0653 [**1**]$^{2+}$.

5.3.4 Preparation of photoanodes

FTO glass slides 10×8 cm^2 were first cleaned by sonication in Alconox® solution (1 tablespoon in 250 ml of deionized water) for 10 minutes, followed by rinsing with water and by further sonication in 2-propanol for 10 minutes. The slides were finally rinsed with EtOH and dried with warm air. In the case of TiO_2 the semiconductor paste was blade cast (**Figure 3.16**) onto the active area of the glass (10×3 cm^2) and dried with a warm air stream before high temperature sintering. SnO_2 electrodes were prepared by spin coating the paste (prepared as reported in **Section 4.3.3**) at 600 rpm for 6s followed by high speed spinning at 2000 rpm for 20s and after each coating run the film was sintered. The casting of two SnO_2 layer produced the best photoelectrochemical performance.[14] For both TiO_2 and SnO_2 the sintering temperature was set at 450°C for 30 minutes. The slides were cut to obtain single photoanodes having size of 4×1 cm^2 with active area of 1.5 cm^2; these were directly used for the sensitization with **1**. Electrodes were dipped in 8×10^{-5}M ACN fluid solution of **1**, at 50°C for a couple of hours till saturation of the respective surfaces.

The functionalization of **1**/SnO_2 substrates, with an aqueous 2×10^{-3} M IrO_2 nanoparticles (NPs) solution, was performed with two different methods: spin coating 2 times (1000 rpm/min 20s, R.T.),[14] and soaking 15 minutes (R.T.).

5.3.5 Electrochemistry and photoelectochemistry

Electrochemical measurements in solution were carried out in dry and Ar purged solvents (ACN or DMF), at room temperature with an *Autolab* multipurpose equipment interfaced to a PC. The working electrode was an Amel glassy carbon (GC, geometrical area 0.08 cm^2) electrode. The counter electrode was a Pt wire, and the pseudo-reference electrode was a silver wire. The reference was set using the redox couple ferrocene/ferrocinium at 395 mV vs. SCE in ACN (internal reference). The concentration in analyte was about 1 mM, unless otherwise stated. 0.1 M $TBAPF_6$ was used as supporting electrolyte. Cyclic voltammograms were obtained at scan rates between 50-500 mV/s and were stated in each case. The criteria for reversibility were the separation of 60 mV between cathodic and anodic peaks, the close to unity ratio of the intensities of the cathodic and anodic currents, and the constancy of the peak potential on changing scan rate.

Electrochemical measurements of sensitized electrodes were carried out on a *Eco Chemie Autolab/Pgstat 30* potentiostat workstation (**Figure 2.8**), in a three electrodes configuration using SCE as reference and Pt bead as counter. Cyclic voltammetry of **1**

grafted on TiO_2 and SnO_2 was recorded in ACN/0.1 M $LiClO_4$ at 50 mV/s as scan rate. Photoelectrochemical experiments were performed at a scan rate of 20 mV/s under AM 1.5 G illumination generated by *LOT-Oriel* solar simulator equipped with a 420 nm cut-off filter, in order to prevent significant direct bandgap excitation of semiconductors. Different electrolytes were employed, containing sacrificial agents (ACN/LiI and aqueous pH 3 sodium ascorbate) at various concentration (0.1 M, 0.25 M and 0.5 M) for the photoinjection tests. The measurements of **1**/SnO_2 decorated with IrO_2 NPs were performed in aqueous pH 3 0.1 M $NaClO_4$. J-V curves were collected by repeated cycling of the potential between 0.3 V vs. SCE (in sacrificial agent) or 0.5 V vs. SCE (in aqueous $NaClO_4$) and the open circuit potential (V_{OC}) until an overlapping response upon subsequent scan was achieved, indicating the attainment of a stationary state under illumination. Where indicated, the photocurrent density *J* was obtained by subtraction of the respective electrode dark current. J-V curves under shuttered illumination were acquired by manually chopping the excitation source.

IPCE was measured in the same three electrode configuration, under the monochromatic illumination generated by an air cooled *Luxtel* 175 W Xe lamp coupled to an *Applied Photophysics LTD.* monochromator. The photocurrent, recorded at the constant potential of 0.3 V vs SCE, was acquired on an *Amel mod.552* potentiostat (**Figure 2.10**), in ACN/LiI or aqueous pH 3 ascorbate at various concentration. Incident irradiance was measured with a calibrated silicon photodiode.

5.3.6 Steady state UV-vis spectroscopy

For the complexes in solution, absorption spectra have been recorded with a *Jasco V-560* spectrophotometer. For steady-state luminescence measurements, a *Jobin Yvon-Spex Fluoromax P* spectrofluorimeter was used, equipped with a *Hamamatsu R3896* photomultiplier. The spectra were corrected for photomultiplier response by using a program purchased with the fluorimeter. For the luminescence lifetimes, an *Edinburgh OB 900* time-correlated single-photon-counting spectrometer was used. A *Hamamatsu PLP 2* laser diode (59 ps pulse width at 408 nm) and/or nitrogen discharge (pulse width 2 ns at 337 nm) were employed as excitation sources.

For the complex **1** grafted on semiconductor electrodes, absorption spectra were measured between 800 and 400 nm with a *JASCO V-570* and a *Varian Cary 300* spectrophotometers (**Figure 2.2**), with a bandwidth of 2 nm.

5.3.7 Transient emission and absorption spectroscopy

Transient absorption spectroscopy (TAS) was performed with a previously described apparatus (**Figure 2.5A**),[27] by using the 532 nm harmonic of a nanosecond *Nd:YAG* laser (*Continuum Surelite II*), with 1.3 kV of supply voltage. Thin films, under open circuit conditions, were oriented at an angle of ca. 45° with respect to the laser beam, defocusing with a plano concave lens and further attenuating with a 50% T neutral filter. Two 532 nm notch filters prevented laser light from reaching the photomultiplier, while a 420 nm cut-off filter and a 25% T neutral filter attenuated the white light probe beam, preventing a substantial excitation of the exposed semiconductor substrate. In order to obtain a suitable amplification of the oscillographic traces, with reasonably good S/N ratio, an oscilloscope input resistance of 50 Ω was used. Single wavelength transient traces were further improved by averaging 10 to 30 laser shots at a frequency of 0.2 Hz, imported on a PC and used to construct the transient absorption spectra by means of *Origin 8*.

5.3.8 Computational studies

Ground state equilibrium geometry of **1**, pre-optimized at the semi-empirical PM3 level, were computed at the DFT B3LYP level by using a LANL2DZ basis set. TDDFT/LANL2DZ calculations in the presence of solvent (ACN) described according to the continuum polarisable model (IEFCPM) afforded the ten lowest singlet vertical transitions. Structure and isodensity surfaces (isovalue = 0.004) generation was achieved with *Gaussview 5* and *Gaussssum 2.2*. Calculations were carried out with *Gaussian 09 A.02*[28] by using a multiple core (2 X Intel quad core I7 processors) 64 bit PC running under Linux.

5.4 Chapter 5 - Results and discussions

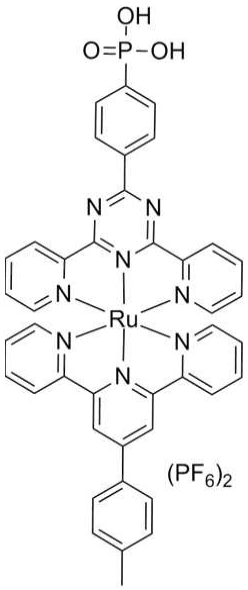

Figure 5.6 Image of the synthesized dye, called **1** for the sake of brevity.

In order to satisfy the tight requirements for sensitizers in molecular water splitting devices (**Section 1.5**),[29] our purpose was to synthesize a Ru(II) polypyridine complex, having both high molar extinction coefficient and oxidation potential, positive enough to activate a water oxidation catalyst at mild pH. On the basis of the former experience of some of us with bis-pyridyl triazine (**L**),[30] a strong electron withdrawing tridentate ligand, we imagined that compound **1** (**Figure 5.6**) would have been able to fulfil our requirements. The absorption spectra of **1** and **P1** (the ethyl-ester precursor) in ACN fluid solution are shown in **Figure 5.7** and the relevant data are gathered in **Table 5.1**, where also the luminescence properties of the two compounds are reported (in ACN at room temperature and in butyronitrile rigid matrix at 77 °K). The emission spectra of **P1** are also reported in the inset of **Figure 5.7**.

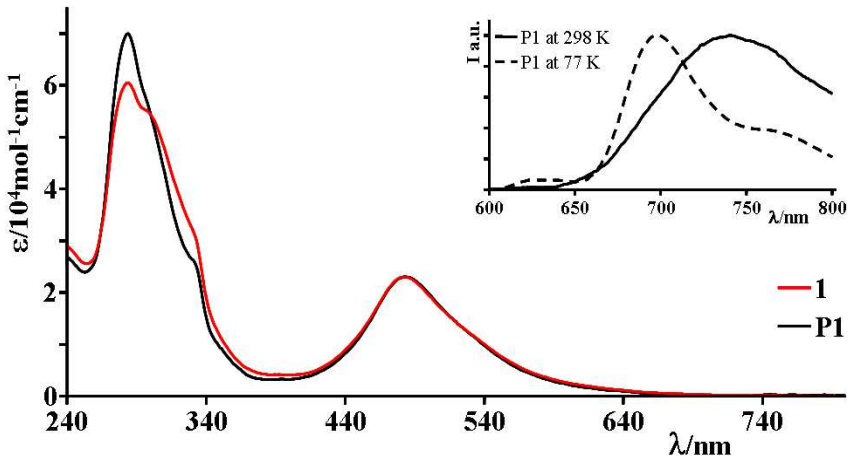

Figure 5.7 Absorption spectra of **1** and **P1** in ACN fluid solution. In the inset are shown the emission spectra of **P1**, in ACN at room temperature (black line) and in butyronitrile rigid matrix at 77 °K (black dash line).

Table 5.1 Absorption spectra and luminescence properties of **1** and **P1**.

	Absorption[a]	*Luminescence,*[a] *298 °K*			*Luminescence,*[b] *77 °K*	
	λ_{max} (nm), ε ($\times 10^4$ M^{-1} cm^{-1})	λ_{max} (nm)	τ (ns)	Φ	λ_{max} (nm)	τ (ns)
P1	483 nm, 2.28	738 nm	12 ns	$< 10^{-4}$	700 nm	630 ns
1	482 nm, 2.28	722 nm	7 ns	$< 10^{-4}$	715 nm	340 ns

(a) In ACN fluid solution. (b) In butyronitrile matrix.

From the data summarized in **Table 5.1**, it is possible to note a minimum difference between **P1** and **1**, for both absorption and luminescence. At room temperature, the very small emission quantum yield (< 10^{-4}) and short lifetime (~10 ns) could be attributed to the weak ligand field, induced by the triazine subunit in **L**,[30] and also to the tridentate nature of both ligands.[31] For what concern emission lifetime at 77 °K, a larger difference emerge: τ(**1**) results almost half than τ(**P1**) (340 ns vs. 630 ns respectively). Possible, radiationless pathways, involving peripheral phosphonic groups, can have a role in determining this difference.

By the maximum of **P1** in the emission spectra at 77 °K (700 nm) a zero-to-zero spectroscopic energy ($E^{0\text{-}0}$) of 1.77 eV is obtained (**Equation 2.5**), that is relative to the energy gap between the triplet state and the ground state. The absorption and luminescence of **1** and **P1** are in line with the properties of Ru(II) polypyridine molecules,[32-34] and in good agreement with those complexes containing bis-pyridyl triazine ligands.[30,31] The visible absorption spectrum and the luminescence, at 298 °K and 77 °K, are dominated by spin allowed metal-to-ligand charge transfer (MLCT) bands. In particular, in emission spectra are assigned to triplet MLCT states involving **L**, which is expected to have a lower lying π^* orbital than the terpyridine (*tpy*) ligand.[31]

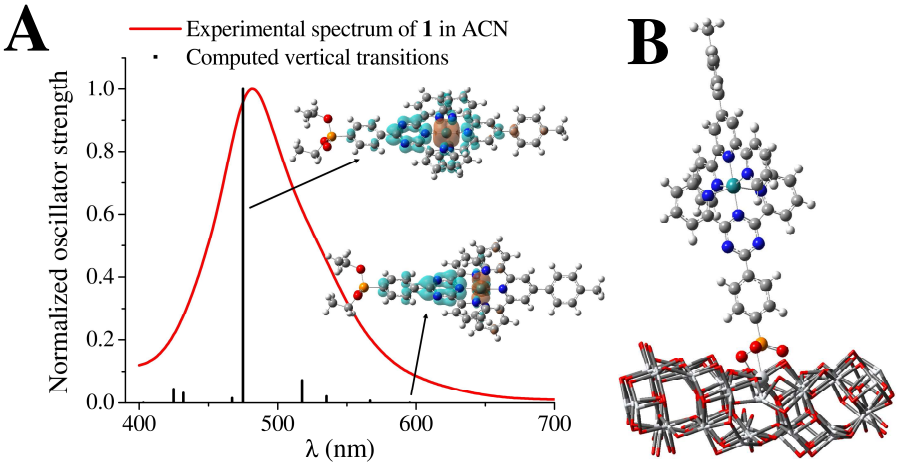

Figure 5.8 (A) Computed vertical transitions calculated at the TDDFT/LANL2DZ level, compared to the experimental spectrum of **P1** in fluid ACN solution. The most significant transitions (the lowest at 595 nm and the highest at 475 nm) are associated to EDDM depicting "hole" (orange) and "electron" (cyan). (B) Complex **1** attached to the TiO_2 surface slab, described at the MM level.

TDDFT calculations carried out on the optimized ground state structure of **P1** in the presence of ACN, according to the IEFCPM formalism, predict singlet vertical optical transitions which describe, in a very satisfactory fashion, the experimental spectrum measured in solution, showing a sharp absorption maximum at ~480 nm (**Figure 5.8A**). The computed transitions are generally characterized by a significant MLCT character, involving the transfer of electron density from prevailingly Ru(II) orbitals to **L**π orbital.

Interestingly, the aromatic ring bearing the phosphonic ester showed a dihedral angle close to 0°, in agreement with the X-ray results, due to electron conjugation with the strongly e^- withdrawing triazine ring. By contrast, the tilt angle of the tolyl- substituent, on the other *tpy* ligand, is ~48°. The electron density difference maps (EDDM) show a sizable e^- concentration on the ortho- and para-position of the phenyl-phosphonic ring, sites that should allow for an acceptable electronic coupling with the TiO_2 surface. However, contrary to carboxylic acid binding groups, no electron density is observed directly on the phosphonic units, in agreement with previous comparative studies.[35] The molecular mechanics (MM) model of **1** interacting with the 101 surface of a TiO_2 cluster (**Figure 5.8B**), computed by relaxing only the two P-O-Ti linkages while freezing the other internal coordinates (calculating within high level DFT framework), show that **1** binds to the surface with a tilt angle close to 80°. Given this geometry, the shortest pathway for the electron transfer, from the MLCT state to TiO_2, should involve a "trough bond" mechanism with the mediation of non-conjugating PO_3H_2 group.

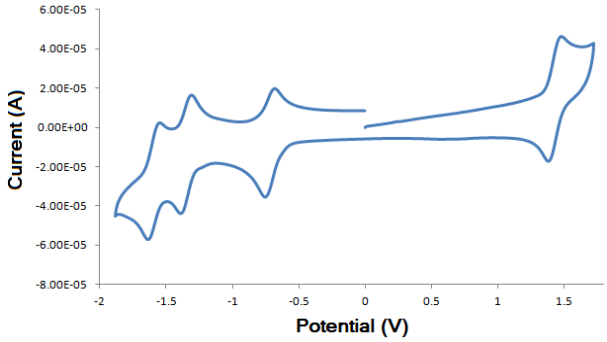

Figure 5.9 Cyclic voltammetry of **P1** in ACN/0.1 M $TBAPF_6$ at GC working electrode (SCE as reference and Pt bead as counter), scan rate = 100 mV/s. For cathodic measurements, the solution was previously purged with Ar for 10 minutes.

The redox behaviour of **P1** has been studied by cyclic voltammetry (**Figure 5.9**) in ACN/0.1 M $TBAPF_6$, at scan rate 100 mV/s from +1.70 V to -1.80 V vs. SCE. Complex **P1** undergoes a reversible monoelectronic anodic process at 1.41 V vs. SCE (E_{OX}), involving the ruthenium metal centre, and several reversible monoelectronic cathodic processes at -0.71 V (E_{RED}), -1.50 V and -1.61 V vs. SCE, doubtless assigned to first reduction of **L**, first reduction of the *tpy* and second reduction of **L**, respectively; these assignments are based on literature data of similar compounds.[30]

The experimental electrochemical gap ($E_{OX} - E_{RED}$ = 2.12 eV) resulting in very good agreement with the computational spectroscopic gap (2.08 eV, **Equation 2.5**), obtained from the lowest singlet transition energy at 595 nm (**Figure 5.8A**), confirms the identity between spectroscopic and redox orbitals and the presence of substantially localized redox states (i.e. states centred on distinct weakly interacting metal and ligand orbitals). The weak absorption tail, extending further to the red (up to 700 nm), could be thus originated by spin forbidden singlet-to-triplet absorption, consistent with the threshold (~640 nm) of the emission spectra from the lowest triplet state.

The electrochemical behaviour of **1** in fluid solution cannot be studied in detail, in fact, particularly upon reduction, **1** tends to be absorbed on the electrode and a clear determination of the redox processes becomes impossible. However, the absence of the **1** electrochemical data in fluid solution is not a real problem for our aims, since the properties of **P1** are more relevant, because it represent a better model for the dye when anchored on TiO_2, with ethyl groups mimicking the coupling with the metal oxide surface better than protons. For the same reason, also the **P1** photophysical data are probably more reliable than **1**.

Clear cyclic voltammetries in oxidative regime, of **1** adsorbed either on mesoporous TiO_2 (**Figure 5.10A**) or SnO_2 (**Figure 5.10B**) thin films, confirm the reversible oxidative behaviour observed in solution. However, the metal centred redox wave shown a slightly cathodic shift compared to the solution (1.37 V vs. SCE on TiO_2 and 1.32 V vs. SCE on SnO_2). Nevertheless the driving force is, in principle, still sufficient for the activation of a wide selection of WOC.[4,36-40]

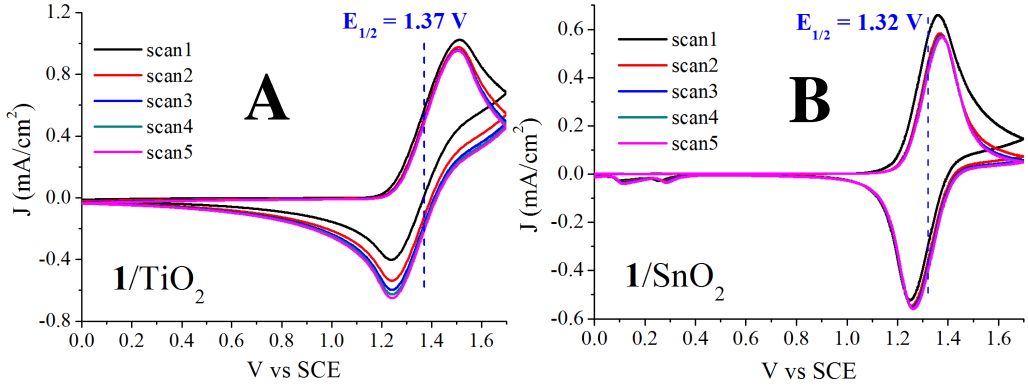

Figure 5.10 Cyclic voltammetry of **1** in ACN/0.1 M $LiClO_4$ on (A) TiO_2 and (B) SnO_2 thin films (SCE as reference and Pt bead as counter), at scan rate = 50 mV/s.

From the luminescence data in **Table 5.1** and the redox potential discussed above, results a triplet excited state oxidation potential (t-$^*E_{OX}$) for **P1** equal to -0.36 V vs. SCE (**Equation 2.11**), indicating that photoinjection, from the lowest excited state of **1** to the TiO_2 CB, should be thermodynamically forbidden. The singlet excited state oxidation potential (s-$^*E_{OX}$), instead, estimated by combining E_{OX} with the computed singlet $E^{0\text{-}0}$ (595 nm), results -0.67 V vs. SCE. This more reducing value is approximately isoergonic with the TiO_2 CB, in non-anhydrous ACN, and barely above the band edge in aqueous pH 3 solution, according to **Equation 5.1**,[41] allowing the charge injection into TiO_2.

$$V_{fb} = (-0.4) - 0.06 \times pH \qquad \text{(V vs. SCE)} \qquad \textbf{Equation 5.1}$$

However, once **1** singlet excited state (***1**) is generated, the intersystem crossing to triplet state could compete efficiently with electron transfer to TiO_2, reducing the photoinjection efficiency. This is probably the most representative case of complex **1**,

given both insufficient driving force and non-optimal coupling with the semiconductor surface, due to the presence of non-conjugating phosphonic binding groups. On the contrary, the **1** triplet excited state reduction potential (t-$^{*}E_{RED}$), calculated by using **Equation 2.12** considering $E^{0\text{-}0}$ = 1.77 eV, results +1.06 V vs. SCE, positive enough to undergo reductive quenching from ascorbate, forming **1** (or **P1**, with substantially analogous energetic) at its reduced state (**1**$^{-}$).[42]

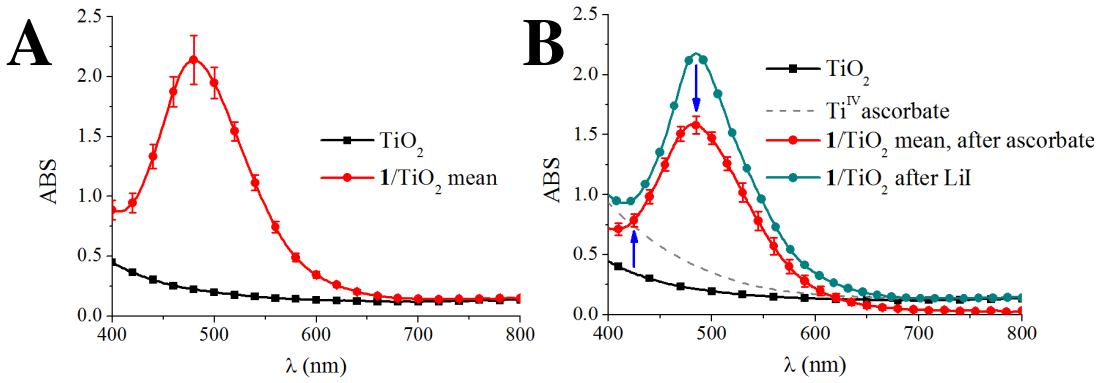

Figure 5.11 Averaged absorption spectra of **1**/TiO_2 photoanodes, with error bars calculated on a set of 3 equivalent electrodes. (A) Before measurements, **1**/TiO_2 (red line) in comparison with bare mesoporous TiO_2 (black line). (B) Bare TiO_2 (black line) compared to **1**/TiO_2 after 10 minutes of measurement cycle in aqueous pH 3 0.1 M sodium ascorbate (red line), and with **1**/TiO_2 after soaking and measurement in ACN/0.1 M LiI (dark cyan line). Also, is reported for reference the absorbance of the bare TiO_2 film, immersed in aqueous pH 3 0.1 M sodium ascorbate (dashed grey line).

The charge transfer dynamics of **1**, relevant to application in molecular artificial photosynthesis, were preliminarily studied by fabricating transparent TiO_2 photoanodes of the approximate thickness of 7 ± 1 μm, according to the procedure reported in the **Section 5.3.4**. Soaking TiO_2 electrodes in a 8×10^{-5} M ACN solution of complex **1**, at 50°C for a couple of hours, leads to a sensitization of the semiconductor, reaching maximum absorbance mean values of ~2 at 480 nm (**Figure 5.11A**), demonstrating efficient dye uptake. The stability of **1** is acceptable, in aqueous pH 3 0.1 M sodium ascorbate solution, although not optimal, since the maximum optical density drops by 32%, after ca. 10 minutes soaking (**Figure 5.11B**, red line), during which the electrode is subjected to several J-V cycles under illumination (typically from +0.35 V to -0.5 V vs. SCE) until reaching a stationary photoelectrochemical response. Instead, the bare TiO_2 film shows, after 10 minutes soaking under the same measurements conditions and electrolyte, an absorbance increase in the blue region of the visible spectrum, due to the formation of a charge transfer adduct between surface exposed Ti(IV) and ascorbate[43] (**Figure 5.11B** dash grey line) which was found to act as charge transfer sensitizer. By contrast, the stability of **1**/TiO_2 in organic solvents, under the same photoelectrochemical conditions, is optimal, with no appreciable changes in film absorbance during potential cycling (**Figure 5.11B**, dark cyan line).

As reported in **Figure 5.12A**, the J-V curves, obtained under AM 1.5 G illumination with a 420 nm cutoff filter, in ACN/0.1 M LiI indicate that **1**/TiO_2 (dark cyan line) generates a modest plateau photocurrent of ~0.2 mA/cm^2, with an open circuit potential of ca. -0.35 V vs. SCE. The blank TiO_2 electrode (dash blue line) generates the expected negligible photoresponse, in agreement with the insufficient light harvesting of unmodified TiO_2. By contrast, in aqueous pH 3 0.1 M sodium ascorbate, more than a 4-fold increase in photocurrent (0.9 mA/cm^2) and enhanced photovoltage (-0.45 V vs. SCE) are observed for **1**/TiO_2 (red line). The blank TiO_2 film (dash grey line) also generates a higher plateau photocurrent (0.3 mA/cm^2) due to the local formation of titanium ascorbate sensitizer.[43] Clearly, the formation of Ti^{IV}ascorbate cannot explain the enhanced photocurrent observed with **1**/TiO_2, even more so when consideration is made for the modest Ti^{IV}ascorbate formation on the **1**/TiO_2 surface, where most Ti(IV) is already coordinated to the Ru(II) sensitizer. Both photocurrent and photovoltage are improved by increasing the ascorbate concentration up to 0.5 M (**Figure 5.12B**), leading to rectangular shaped phototransients, reaching 1.4 mA/cm^2 and -0.55 V vs. SCE respectively, in good agreement with the estimation of the TiO_2 flat band potential (**Equation 2.1**).[41]

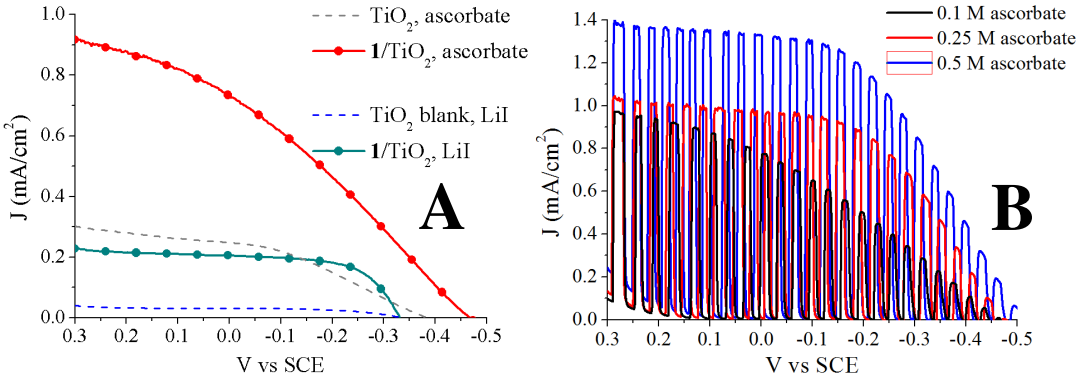

Figure 5.12 J-V characteristics of TiO_2 photoanodes in the presence of different sacrificial agents, obtained under AM 1.5 G illumination with a 420 nm cutoff filter. (A) In aqueous pH 3 0.1 M sodium ascorbate, **1**/TiO_2 (red line) and bare TiO_2 (dash grey line); in ACN/0.1 M LiI, **1**/TiO_2 (dark cyan line) and bare TiO_2 (dash blue line). (B) Shuttered J-V characteristics of **1**/TiO_2 in the presence of increasing aqueous pH 3 sodium ascorbate concentration: 0.1 M (black line), 0.25 M (red line) and 0.5 M (blue line).

These results are consistent with IPCE spectra reported in **Figure 5.13A**, where the best conversion efficiency (~10%, 500-550 nm) is observed, within the explored conditions, in aqueous pH 3 0.5 M sodium ascorbate. The IPCE spectrum of **1** in the presence of ascorbate is broader than expected on the basis of the absorption spectrum of the Ru(II) sensitizer, due to the direct contribution of Ti^{IV}ascorbate which becomes significant around and below 450 nm (**Figure 5.11B** dash grey line). Nevertheless, the increased IPCE at 550 nm, in a region where the Ti^{IV}ascorbate efficiency contribution becomes relatively unimportant, confirms that the ruthenium sensitizer originates most of

the photoconversion. Instead, the poor reducing ability of ***1**, discussed above, is confirmed in ACN/0.1 M LiI, due to a modest photoconversion behaviour. Combining these data to short lifetime and to less than ideal electronic coupling with TiO_2 surface, results ~1% in quantum yield of charge injection, under the reasonable assumption that regeneration of **1** by iodide occurs with nearly unitary efficiency.

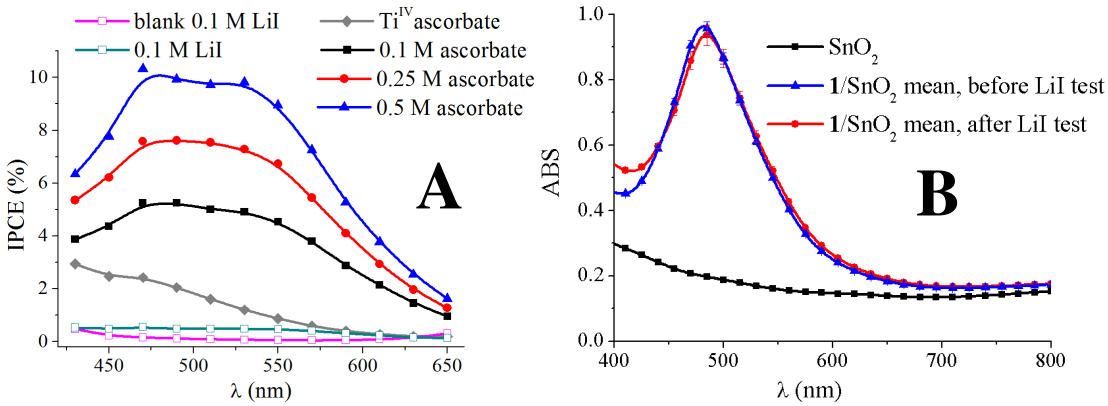

Figure 5.13 (A) Constant potential (0.3 V vs. SCE) incident photon-to-current efficiency spectra, under AM 1.5 G illumination with a 420 nm cutoff filter, of TiO_2 photoanodes, in the presence of different electrolytes: **1**/TiO_2 in various aqueous pH 3 sodium ascorbate concentration (0.1 M black line, 0.25 M red line, 0.5 M blue line) and bare TiO_2 in aqueous pH 3 0.1 M sodium ascorbate (grey line); **1**/TiO_2 (dark cyan line) and blank TiO_2 (magenta line) in ACN/0.1 M LiI. (B) Averaged absorption spectra of **1**/SnO_2 photoanodes, with error bars calculated on a set of 3 equivalent electrodes, before measurements (blue line) and after ACN/0.1 M LiI photoelectrochemical tests (red line) in comparison with bare mesoporous SnO_2 (black line).

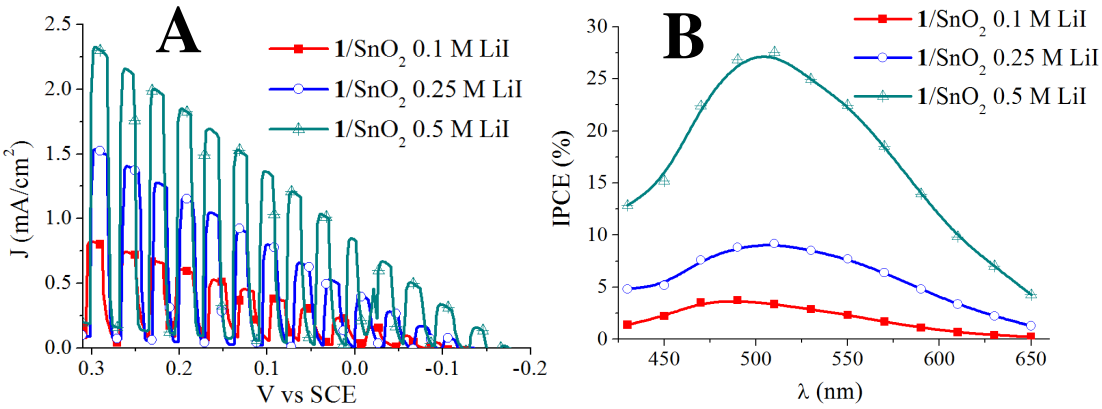

Figure 5.14 (A) J-V characteristics and (B) constant potential (0.3 V vs. SCE) IPCE, both under AM 1.5 G illumination with a 420 nm cutoff filter, of **1**/SnO_2 photoanodes in ACN solvent, containing increasing concentration of LiI: 0.1 M (red line), 0.25 M (blue line), 0.5 M (dark cyan line).

On the other hand, charge injection from ***1** in ACN/0.1 M LiI is clearly observed on mesoporous SnO_2 films (**Figure 5.13B**, thickness < 2 μm, maximum absorbance mean ~0.9 at 480 nm), prepared according to **Section 5.3.4**. The semiconductor flat potential (ca. -0.1 V vs. SCE) clearly allows the oxidative quenching of **1** excited states, in fact the photocurrent of **1**/SnO_2 electrodes, as well as the IPCE, raise by increasing the LiI concentration from 0.1 M to 0.5 M, with top values of 2.3 mA/cm^2 at 0.3 V vs. SCE (**Figure 5.14A**, dark cyan line), corresponding to a maximum IPCE of ~27% (**Figure**

5.14B, dark cyan line). The sharp slope of sensitized SnO_2 photocurrent transients (**Figure 5.14A**), in respect to **1**/TiO_2 (**Figure 5.12B**), is ostensibly due to recombination from SnO_2 and from the underlying FTO back contact, which is more exposed to the electrolyte, being covered by a thinner semiconductor layer (< 2 μm), if compared to the TiO_2 (7 ± 1 μm).

The ability to photogenerate and store highly oxidizing h^+, on SnO_2 photoanodes, has been preliminary confirmed in a water splitting cell, where **1** was coupled with IrO_2 NPs acting as WOC.[5,14,25] Although the coupling between the sensitizer and the catalyst was not optimized, it can be observed, in **Figure 5.15A** and **Figure 5.15B**, an increased photoanodic current density (from ca. ×2 to ×3, under steady state conditions) in the presence of the IrO_2, suggesting the activation of h^+ transfer pathways to co-adsorbed NPs.

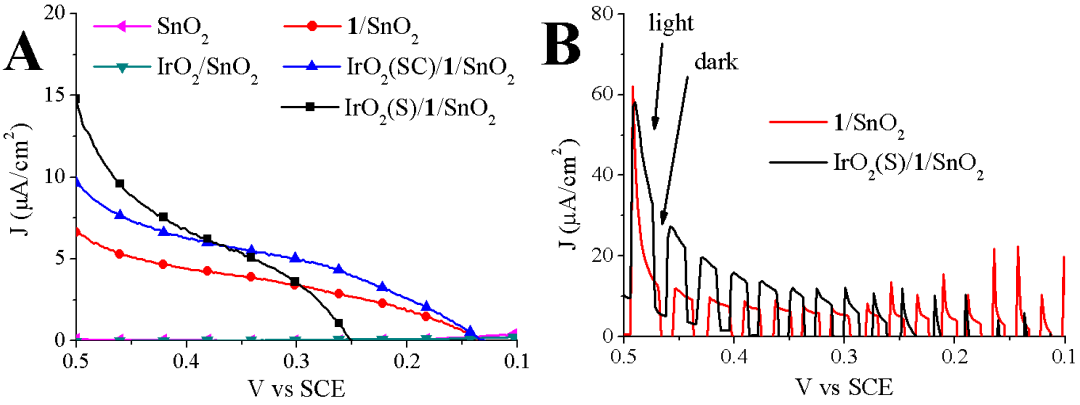

Figure 5.15 J-V characteristics, under continuous (A) and shuttered (B) AM 1.5 G illumination with a 420 nm cutoff filter, of **1**/SnO_2 photoanodes functionalized with IrO_2 NPs, in aqueous pH 3 0.1 M $NaClO_4$. In (A) the photocurrent density *J* of each electrode was obtained by subtraction of the respective dark current. Two different methods of IrO_2 casting were used: spin coating 2 times (SC, blue line), according to the results obtained in **Chapter 4**, and soaking 15 minutes (S, black line).

From the described results, and taking into account the thermodynamic and electronic considerations mentioned above, it appears that, in the presence of LiI electrolytes, charge injection into TiO_2 takes place directly from ***1**, following the usual oxidative quenching of the sensitizer excited state (biomimetic pathway 1-2-3_B-4_B, **Figure 5.2**), grafted on the semiconductor surface. Accordingly, it has a modest efficiency on TiO_2 (**Figure 5.13A**, dark cyan line) while undergoes a significant improvement on SnO_2 (**Figure 5.14B**), due to increased exoergonicity for such electron transfer pathway. Instead, in the presence of sodium ascorbate, the increased photon-to-electron conversion observed on TiO_2 (**Figure 5.13A**) could be explained by a change in the electron transfer mechanism. In our case, it consists in the reductive quenching of the MLCT excited state (anti-biomimetic pathway 1-2-3_A-4_A, **Figure 5.2**), because of bimolecular reaction with ascorbate that leads to the formation of $\mathbf{1}^-$. The reductive quenching is followed by the thermodynamically allowed electron injection into TiO_2, due to the $\mathbf{1}^-$ stronger reduction

potential, compared to $^{*}E_{OX}$ of the singlet and the triplet states. Transient optical spectroscopy in solution, carried out on various semiconductor substrates, was used to elucidate and confirm this crucial point.

Upon 532 nm laser excitation of **1** in ACN fluid solution, population of the triplet state occurs, which decays completely within 40 ns from the laser pulse, according to a monoexponential behaviour with a lifetime of ~9 ns (**Figure 5.16A**). This value appears to be in good agreement with that estimated by more accurate TCSPC techniques (10 ns in ACN fluid solution), resulting in a transient absorption partly convolved with the excitation profile of the *Nd-YAG* source (FWHM 7 ns). The short lived triplet state has the typical features of Ru(II) polypyridine MLCT excited states (**Figure 5.16B**), characterized by: a bleaching of the MLCT band, peaking at 480 nm; a relatively intense and narrow absorption in the blue region, peaking at ~400 nm; a weaker, but well defined, absorption band extending into the red, with a broad maximum between 600-700 nm.

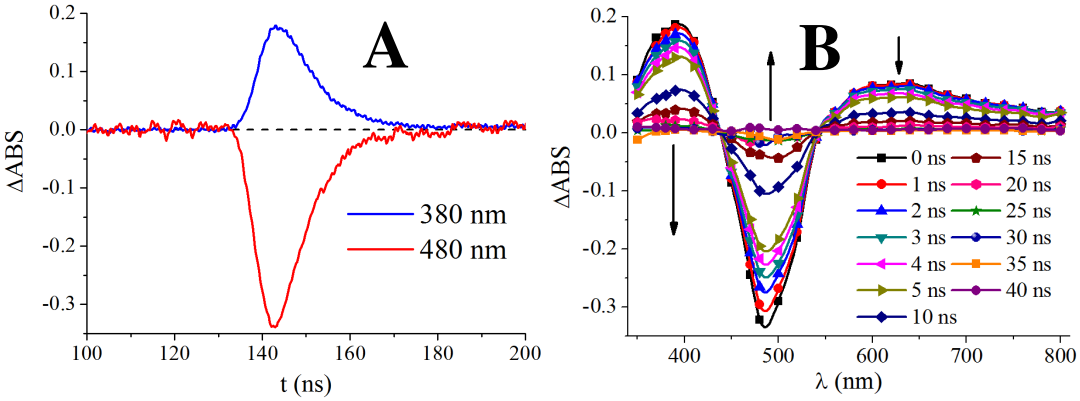

Figure 5.16 Excited state decay kinetics (A), observed in correspondence of the most intense transitions (480 nm bleaching and 380 nm absorption), and transient differential absorption spectrum (B) of **1** in ACN fluid solution, upon 532 nm laser excitation, FWHM 7 ns, oscilloscope input resistance of 50 Ω.

After the addition dropwise of aqueous pH 3 0.75 M sodium ascorbate, to the Ar purged ACN solution, in order to achieve a concentration ~0.3 M of ascorbate in the ACN/H_2O mixture, a significant change in excited state decay occurs. The kinetic behaviour, reported in **Figure 5.17B**, shows a pulse width limited decay (τ = 7.5 ns) to a long-lived signal, having at least 1/3 of the initial ΔABS amplitude, which remains essentially constant within a time interval of 500 ns. This behaviour is consistent with formation of $\mathbf{1}^{-}$, which is able to survive for long time, in the absence of oxygen and of other electron scavengers in the solvent medium. The transient absorption of $\mathbf{1}^{-}$ (at early delays **Figure 5.17A** and longer delays **Figure 5.17C**) shows some analogy with the triplet excited state spectrum (**Figure 5.16B**), but it is characterized by a narrower structured bleaching (peaking at 480 nm), preceded by a small shoulder (450 nm), and by a narrow absorption (500-550 nm), consisting in its own diagnostic fingerprints. The absorption at

longer wavelength (beyond 600 nm) is weak, flat and featureless. It is interesting to note that these spectral features are already present in the transients taken at 0 ns delay (**Figure 5.17A**, black line), and are very similar to those recorded after the establishment of the long lived state (**Figure 5.17C**) which follows the initial fast decay.

We thus conclude that, in the presence of a large excess of ascorbate, similar in concentration to that used in the electrolyte for photoelectrochemical tests, the reductive quenching in solution is nearly instantaneous for the temporal resolution of our spectrometer. Furthermore, the fast initial decay, occurring in few ns, is mostly due to the e^--h^+ recombination within the bimolecular adduct (i.e. **1**$^-$/ascorbate$^+$), of which only a fraction is able to separate, finally yielding the long-lived charge separated species. Similar spectral fingerprints and long-lived kinetics are found in **1** grafted on ZrO_2 film (**Figure 5.17D**), showing that **1**$^-$ can be accumulated also on inert (with respect to charge injection) sensitized semiconductor surfaces exposed to ascorbate solutions.

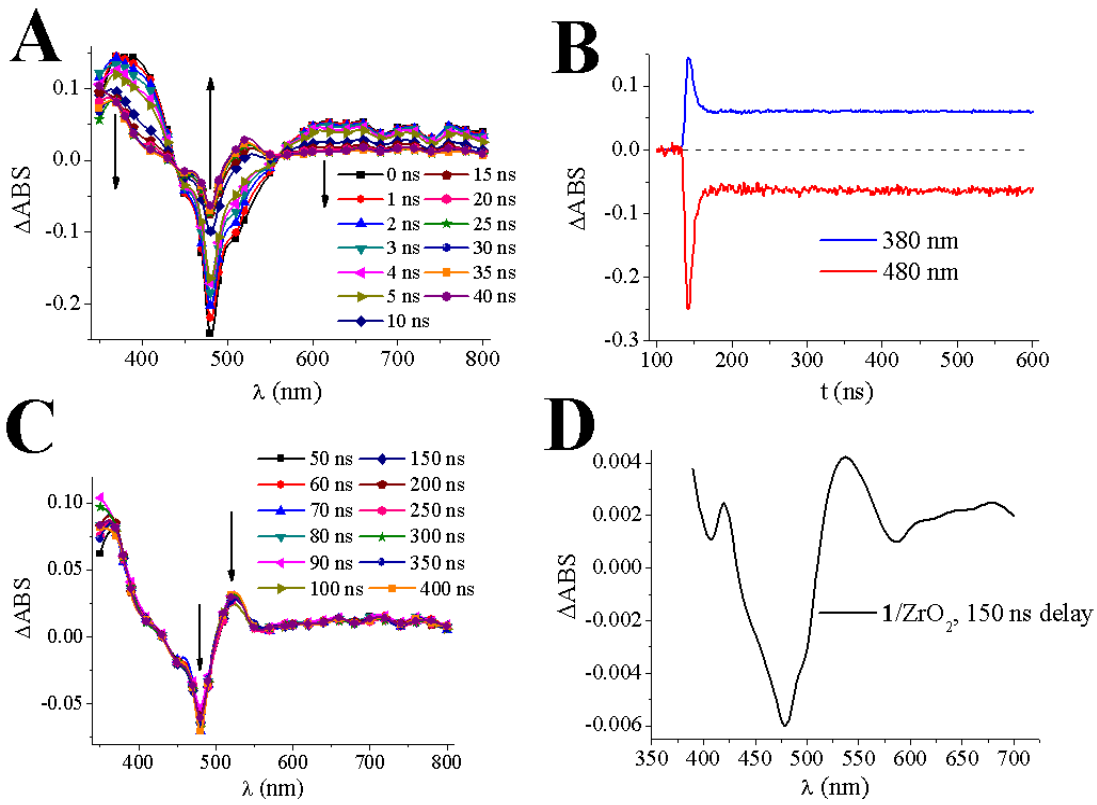

Figure 5.17 Transient differential absorption spectrum of **1** in ACN/H_2O mixture 0.3 M sodium ascorbate, upon 532 nm laser excitation (FWHM 7 ns, oscilloscope input resistance of 50 Ω), at (A) early delays (0-40 ns) and (C) longer delays (50-400 ns), showing the achievement of a long lived state. B) Excited state decay kinetics observed in correspondence of the most intense transitions (480 nm bleaching and 380 nm absorption). D) Transient differential absorption spectrum of **1**/ZrO_2, recorded in the same previous condition, at long delays (150 ns) in order to avoid interference from the excited state.

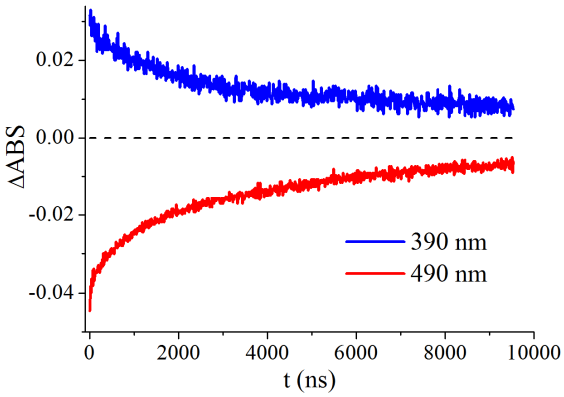

Figure 5.18 Excited state decay kinetics of **1**/SnO_2 in ACN/0.1 M $LiClO_4$, upon 532 nm laser excitation (FWHM 7 ns, oscilloscope input resistance of 50 Ω), observed in correspondence of the most intense transitions (490 nm bleaching and 390 nm absorption).

The transient spectra of **1** loaded on SnO_2, exposed to ACN/0.1 M $LiClO_4$, are consistent with the formation of Ru(III), following the ***1** oxidative quenching by charge injection into the SnO_2 CB (biomimetic pathway). The oxidized state (**1**$^+$) is characterized by long lived multiexponential kinetics, which do not recover completely on a time scale of 10000 ns (**Figure 5.18**), according to the comparatively slow **1**$^+$/e^-(SnO_2) electron recapture. The charge separated state characteristic spectral signature is summarized by the intense bleaching of the ground state, leading to a minimum at 480 nm followed by a 510 nm shoulder (**Figure 5.19A** and **Figure 5.19B**). Contrary to the signature of ***1**, the transient spectrum of **1**$^+$ lacks the broad but well defined band, having maximum between 650-700 nm, and only shows a featureless, weak, sloping absorption rising for $\lambda > 650$ nm, due to the sum of both LMCT transitions and optical contributions of photoinjected e^- trapped into SnO_2.

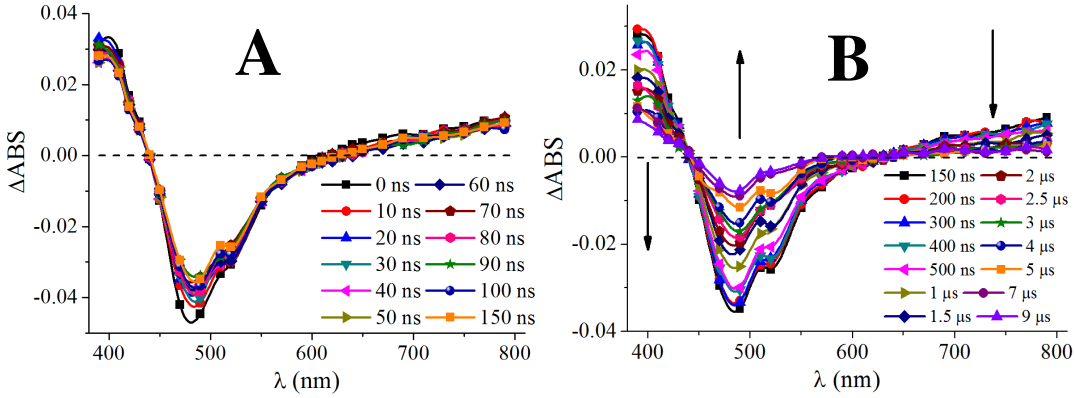

Figure 5.19 Transient differential absorption spectrum of **1**/SnO_2 in ACN/0.1 M $LiClO_4$, upon 532 nm laser excitation (FWHM 7 ns, oscilloscope input resistance of 50 Ω), at (A) early delays (0-150 ns) and (B) longer delays (150-9000 ns).

The transient spectrum of **1**/TiO_2 exposed to ACN/0.1 M $LiClO_4$ (**Figure 5.20A** and **C**) shows the dominating contribution of the triplet excited state of the sensitizer, decaying within few tens of nanoseconds, and having the characteristic 650-700 nm absorption hump, confirming that the excited state quenching by electron transfer into TiO_2 is largely inefficient. Nevertheless a small long-lived amplitude, having ~20% of the initial amplitude (**Figure 5.20B**, blue line) is detected and assigned to the formation of **1**$^+$, because of the spectral fingerprints observed at long delays (i.e. bleaching band with two shoulders and sloping absorption for $\lambda > 650$ nm, **Figure 5.20C**). This is consistent with

the small, but clearly detectable, photoanodic current of ~0.2 mA/cm^2 observed in ACN/0.1 M LiI (**Figure 5.12A**).

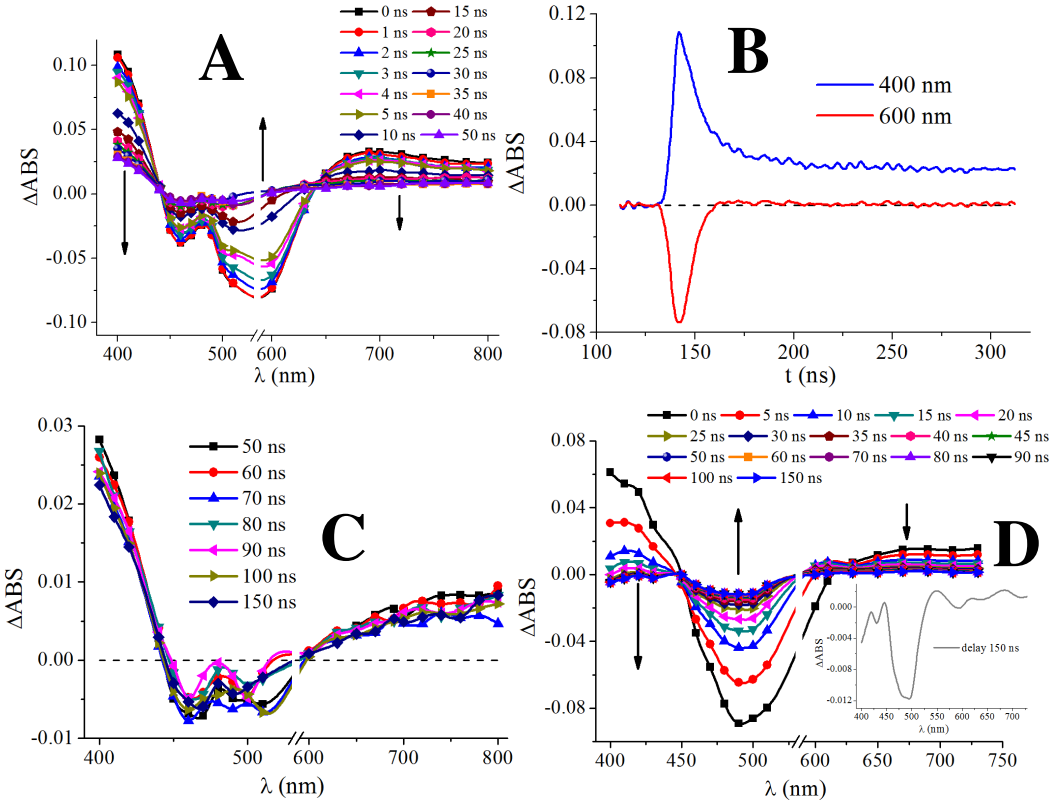

Figure 5.20 Transient differential absorption spectrum of **1**/TiO_2 in ACN/0.1 M $LiClO_4$, upon 532 nm laser excitation (FWHM 7 ns, oscilloscope input resistance of 50 Ω), at (A) early delays (0-50 ns) and (C) longer delays (50-150 ns). B) Excited state decay kinetics observed in correspondence of the most intense transitions (600 nm bleaching and 400 nm absorption), showing the formation of a long-lived state assigned to Ru(III). At 600 nm, the **1**$^+$ state has a negligible contribution and only the excited state decay is observed. D) Transient differential absorption spectrum of **1**/TiO_2, recorded in the same previous condition, in ACN/H_2O mixture 0.3 M sodium ascorbate. As inset the transient at long delays (150 ns), after the complete decay of the excited state.

In the presence of sodium ascorbate, the dynamics on TiO_2 become more complicated (**Figure 5.20D**), by the presence of at least three possible excited state deactivation processes. From ***1**, these pathways leading to three different transient species, all displaying a short lifetime:

i) the triplet excited state;

ii) the reduced state of the sensitizer (**1**$^-$), formed by reductive quenching of ***1**, which would be continuously depleted by charge transfer into TiO_2 without possibility of substantial accumulation;

iii) the oxidized dye (**1**$^+$), formed by electron injection from ***1** to TiO_2 CB, which would be short-lived due to regeneration by ascorbate, acting as sacrificial electron donor.

The possibility to discriminate these three photoproducts is related to the analysis of the transients at early delays. The spectral signature observed at 0-40 ns, after the laser

pulse, is consistent with the prevailing presence of the **1** triplet state (**Figure 5.20D** compared to **Figure 5.16B**), characterized by the structureless bleaching of the ground state followed by the diagnostic absorption band at 650-700 nm. Consistent with the excited state lifetime measured in solution and on ZrO_2, the 90% of the initial amplitude decays within 40 ns from the laser pulse. There is a small amplitude, ~10% of the initial ΔABS, which however survives well beyond the excited state decay. Despite the modest signal-to-noise ratio, the analysis of this residual component is consistent with the survival of a small population of $\mathbf{1}^-$, characterized by a narrow bleaching bland centred at 480 nm and by a flat long wavelength absorption (inset of **Figure 5.20D**), which, contrary to the $\mathbf{1}^+$, does not display the characteristic sloping feature for $\lambda > 700$ nm. Therefore, in the presence of ascorbate, the main quenching mechanism of $^*\mathbf{1}$ involves the reductive pathway. However, the observation of a prevailing population of the excited state is suggestive of the following possibilities:

a) a significant fraction of **1**, immobilized on the TiO_2 surface, is not able to form encounter complex with ascorbate contained in the electrolyte;

b) a large fraction of $\mathbf{1}^-$ is able to inject in TiO_2 CB within the instrumental response of the laser apparatus, therefore is not observed;

c) A large fraction of the $\mathbf{1}^-$/ascorbate$^+$ adducts recombines, reforming **1** at triplet state.

Based on the photoelectrochemical results reported in **Figure 5.13A**, from which maximum IPCEs of the order of 10% are observed, we can dismiss point *b)*, otherwise a much larger photon-to-electron conversion would be achieved. The possibility *c)* seems also unlikely, based on the results obtained for **1** in ascorbate ACN/H_2O solution (**Figure 5.17A** and **C**), considering that no prevailing triplet state is observed in those conditions, but rather the reduced state is the dominating species, clearly observable at very early delays after the excitation pulse. We can thus confirm that in the presence of ascorbate, on the TiO_2 surface, a fraction of **1** excited state is reductively intercepted by the sacrificial electron donor, forming $\mathbf{1}^-$ as the main charge injecting species. This process has on TiO_2 a rather low efficiency, probably due to surface sterical blocking as well as to screening by neighbouring sensitizer species on the surface, which limit the access of ascorbate to the majority of sites onto the semiconductor electrode, consistent with relatively modest IPCE. Nevertheless, in the case of the dye under investigation, it provides a significantly improved photon-to-electron conversion with respect to the conventional quenching mechanism, based on direct charge transfer to the TiO_2 CB.

5.5 Chapter 5 - Conclusions

In conclusion, we have designed and synthesized a new phosphonated Ru(II) polypyridine complex, characterized by electrochemical reversibility, strongly oxidizing Ru(III) state, and intense optical transitions in the visible region, in order to obtain an efficient and stable dye for the sensitization of semiconductor based photoanodes in DSPEC. Preliminary spectroscopic and electrochemical analysis have underlined the promising properties of **1** as sensitizer, both for the high ε values in the visible region and the redox potentials. From ab-initio results and MM modelling of **1** grafted on TiO_2 cluster surface, it was expected a less than ideal electronic communication between the dye MLCT state and TiO_2 acceptor states, due to a chemisorption geometry that constrains the charge transfer trough the non-conjugating PO_3H_2 groups.

The photoelectrochemical characteristics of **1**/TiO_2 electrodes, in ACN/0.1 M LiI, reflected the computational data, achieving an anodic photocurrent of ~0.2 mA/cm^2 with IPCE at 1%, consistent with the poorly reducing abilities of the lowest MLCT excited state of the dye. This limitation was circumvented by using SnO_2, where much larger photocurrents and IPCE were observed, thanks to the increased charge injection driving force in the low lying SnO_2 CB. The ability to photogenerate and transfer h^+ to co-adsorbed WOC was also confirmed, by the significantly enhanced photoanodic response in the presence of IrO_2 NPs. Interestingly, the photocurrent on TiO_2 substrates were largely increased, compared to ACN/LiI, in the presence of aqueous pH 3 sodium ascorbate, with photocurrent undergoing a four to six fold enhancement depending on the concentration of ascorbate, with corresponding photon-to-current conversion between 5-10%; we have attributed this behavior to a modification in the charge injection mechanism. The anti-biomimetic pathway, confirmed by transient differential absorption spectra, allows for a more efficient e^- transfer from **1**$^-$ to the TiO_2 CB, thanks to both a stronger reduction potential and a longer lifetime of the active state.

Besides the fact that, for the first time, a non ambiguous evidence for the occurrence of dye excited state reductive quenching on TiO_2 photoanodes was provided, the possibility of exploiting such charge transfer pathway may result in some intriguing consequences, like the exploitation of sensitizer-catalyst ionic couples/assemblies where the strong redox potential of the dye, necessary to activate the WOC, would impede injection of e^- from the excited state into semiconductor. Thus, the range of useful species

for sensitization could be extended resulting in the removal of some constraint for dye and device design for solar water splitting.

5.6 Chapter 5 - Figures index

5.7 Chapter 5 - References

(1) O'Regan, B.; Gratzel, M. *Nature* **1991**, *353*, 737.

(2) Fujishima, A.; Honda, K. *Nature* **1972**, *238*, 37.

(3) Vannucci, A. K.; Alibabaei, L.; Losego, M. D.; Concepcion, J. J.; Kalanyan, B.; Parsons, G. N.; Meyer, T. J. *Proceedings of the National Academy of Sciences* **2013**, *110*, 20918.

(4) Concepcion, J. J.; Jurss, J. W.; Brennaman, M. K.; Hoertz, P. G.; Patrocinio, A. O. T.; Murakami Iha, N. Y.; Templeton, J. L.; Meyer, T. J. *Accounts of Chemical Research* **2009**, *42*, 1954.

(5) Youngblood, W. J.; Lee, S.-H. A.; Kobayashi, Y.; Hernandez-Pagan, E. A.; Hoertz, P. G.; Moore, T. A.; Moore, A. L.; Gust, D.; Mallouk, T. E. *Journal of the American Chemical Society* **2009**, *131*, 926.

(6) Brimblecombe, R.; Koo, A.; Dismukes, G. C.; Swiegers, G. F.; Spiccia, L. *Journal of the American Chemical Society* **2010**, *132*, 2892.

(7) Caramori, S.; Cristino, V.; Argazzi, R.; Meda, L.; Bignozzi, C. A. *Inorganic Chemistry* **2010**, *49*, 3320.

(8) Moore, G. F.; Blakemore, J. D.; Milot, R. L.; Hull, J. F.; Song, H.-e.; Cai, L.; Schmuttenmaer, C. A.; Crabtree, R. H.; Brudvig, G. W. *Energy & Environmental Science* **2011**, *4*, 2389.

(9) Zhao, Y.; Swierk, J. R.; Megiatto, J. D.; Sherman, B.; Youngblood, W. J.; Qin, D.; Lentz, D. M.; Moore, A. L.; Moore, T. A.; Gust, D.; Mallouk, T. E. *Proceedings of the National Academy of Sciences of the United States of America* **2012**, *109*, 15612.

(10) Alibabaei, L.; Brennaman, M. K.; Norris, M. R.; Kalanyan, B.; Song, W.; Losego, M. D.; Concepcion, J. J.; Binstead, R. A.; Parsons, G. N.; Meyer, T. J. *Proceedings of the National Academy of Sciences* **2013**, *110*, 20008.

(11) Gao, Y.; Ding, X.; Liu, J.; Wang, L.; Lu, Z.; Li, L.; Sun, L. *Journal of the American Chemical Society* **2013**, *135*, 4219.

(12) Kirner, J. T.; Stracke, J. J.; Gregg, B. A.; Finke, R. G. *ACS Applied Materials & Interfaces* **2014**, *6*, 13367.

(13) Alibabaei, L.; Sherman, B. D.; Norris, M. R.; Brennaman, M. K.; Meyer, T. J. *Proceedings of the National Academy of Sciences* **2015**, *112*, 5899.

(14) Ronconi, F.; Syrgiannis, Z.; Bonasera, A.; Prato, M.; Argazzi, R.; Caramori, S.; Cristino, V.; Bignozzi, C. A. *Journal of the American Chemical Society* **2015**, *137*, 4630.

(15) Kärkäs, M. D.; Verho, O.; Johnston, E. V.; Åkermark, B. *Chemical Reviews* **2014**, *114*, 11863.

(16) Thompson, D. W.; Kelly, C. A.; Farzad, F.; Meyer, G. J. *Langmuir* **1999**, *15*, 650.

(17) Kleverlaan, C. J.; Indelli, M. T.; Bignozzi, C. A.; Pavanin, L.; Scandola, F.; Hasselman, G. M.; Meyer, G. J. *Journal of the American Chemical Society* **2000**, *122*, 2840.

(18) Kirsch-De Mesmaeker, A.; Rochus-Dewitt, M.; Nasielski, J. *The Journal of Physical Chemistry* **1986**, *90*, 6657.

(19) Puntoriero, F.; La Ganga, G.; Sartorel, A.; Carraro, M.; Scorrano, G.; Bonchio, M.; Campagna, S. *Chemical Communications* **2010**, *46*, 4725.

(20) Natali, M.; Puntoriero, F.; Chiorboli, C.; La Ganga, G.; Sartorel, A.; Bonchio, M.; Campagna, S.; Scandola, F. *The Journal of Physical Chemistry C* **2015**, *119*, 2371.

(21) Medlycott, E. A.; Theobald, I.; Hanan, G. S. *European Journal of Inorganic Chemistry* **2005**, *2005*, 1223.

(22) Wang, J.; Hanan, G. S. *Synlett* **2005**, *2005*, 1251.

(23) Sullivan, B. P.; Calvert, J. M.; Meyer, T. J. *Inorganic Chemistry* **1980**, *19*, 1404.

(24) Orbelli Biroli, A.; Tessore, F.; Pizzotti, M.; Biaggi, C.; Ugo, R.; Caramori, S.; Aliprandi, A.; Bignozzi, C. A.; De Angelis, F.; Giorgi, G.; Licandro, E.; Longhi, E. *The Journal of Physical Chemistry C* **2011**, *115*, 23170.

(25) Hara, M.; Waraksa, C. C.; Lean, J. T.; Lewis, B. A.; Mallouk, T. E. *The Journal of Physical Chemistry A* **2000**, *104*, 5275.

(26) Spampinato, V.; Tuccitto, N.; Quici, S.; Calabrese, V.; Marletta, G.; Torrisi, A.; Licciardello, A. *Langmuir* **2010**, *26*, 8400.

(27) Mba, M.; D'Acunzo, M.; Salice, P.; Carofiglio, T.; Maggini, M.; Caramori, S.; Campana, A.; Aliprandi, A.; Argazzi, R.; Carli, S.; Bignozzi, C. A. *The Journal of Physical Chemistry C* **2013**, *117*, 19885.

(28) Frisch, M. J.; Trucks, G. W.; Schlegel, H. B.; Scuseria, G. E.; Robb, M. A.; Cheeseman, J. R.; Scalmani, G.; Barone, V.; Mennucci, B.; Petersson, G. A.; Nakatsuji, H.; Caricato, M.; Li, X.; Hratchian, H. P.; Izmaylov, A. F.; Bloino, J.; Zheng, G.; Sonnenberg, J. L.; Hada, M.; Ehara, M.; Toyota, K.; Fukuda, R.; Hasegawa, J.; Ishida, M.; Nakajima, T.; Honda, Y.; Kitao, O.; Nakai, H.; Vreven, T.; Montgomery Jr., J. A.; Peralta, J. E.; Ogliaro, F.; Bearpark, M. J.; Heyd, J.; Brothers, E. N.; Kudin, K. N.; Staroverov, V. N.; Kobayashi, R.; Normand, J.; Raghavachari, K.; Rendell, A. P.; Burant, J. C.; Iyengar, S. S.; Tomasi, J.; Cossi, M.; Rega, N.; Millam, N. J.; Klene, M.; Knox, J. E.; Cross, J. B.; Bakken, V.; Adamo, C.; Jaramillo, J.; Gomperts, R.; Stratmann, R. E.; Yazyev, O.; Austin, A. J.; Cammi, R.; Pomelli, C.; Ochterski, J. W.; Martin, R. L.; Morokuma, K.; Zakrzewski, V. G.; Voth, G. A.; Salvador, P.; Dannenberg, J. J.; Dapprich, S.; Daniels, A. D.; Farkas, Ö.; Foresman, J. B.; Ortiz, J. V.; Cioslowski, J.; Fox, D. J.; Gaussian, Inc.: Wallingford, CT, USA, 2009.

(29) Puntoriero, F.; Sartorel, A.; Orlandi, M.; La Ganga, G.; Serroni, S.; Bonchio, M.; Scandola, F.; Campagna, S. *Coordination Chemistry Reviews* **2011**, *255*, 2594.

(30) Santoni, M.-P.; Hanan, G. S.; Hasenknopf, B.; Proust, A.; Nastasi, F.; Serroni, S.; Campagna, S. *Chemical Communications* **2011**, *47*, 3586.

(31) Medlycott, E. A.; Hanan, G. S. *Coordination Chemistry Reviews* **2006**, *250*, 1763.

(32) Juris, A.; Balzani, V.; Barigelletti, F.; Campagna, S.; Belser, P.; von Zelewsky, A. *Coordination Chemistry Reviews* **1988**, *84*, 85.

(33) Meyer, T. J. *Pure and Applied Chemistry* **1986**, *58*, 1193.

(34) Campagna, S.; Puntoriero, F.; Nastasi, F.; Bergamini, G.; Balzani, V. In *Photochemistry and Photophysics of Coordination Compounds I*; Balzani, V., Campagna, S., Eds.; Springer Berlin Heidelberg: Berlin, Heidelberg, 2007, p 117.

(35) Zabri, H.; Gillaizeau, I.; Bignozzi, C. A.; Caramori, S.; Charlot, M.-F.; Cano-Boquera, J.; Odobel, F. *Inorganic Chemistry* **2003**, *42*, 6655.

(36) Fillol, J. L.; Codolà, Z.; Garcia-Bosch, I.; Gómez, L.; Pla, J. J.; Costas, M. *Nature Chemistry* **2011**, *3*, 807.

(37) Vagnini, M. T.; Smeigh, A. L.; Blakemore, J. D.; Eaton, S. W.; Schley, N. D.; D'Souza, F.; Crabtree, R. H.; Brudvig, G. W.; Co, D. T.; Wasielewski, M. R. *Proceedings of the National Academy of Sciences* **2012**, *109*, 15651.

(38) Klepser, B. M.; Bartlett, B. M. *Journal of the American Chemical Society* **2014**, *136*, 1694.

(39) Weingarten, A. S.; Kazantsev, R. V.; Palmer, L. C.; McClendon, M.; Koltonow, A. R.; SamuelAmanda, P. S.; Kiebala, D. J.; Wasielewski, M. R.; Stupp, S. I. *Nature Chemistry* **2014**, *6*, 964.

(40) Kunz, V.; Stepanenko, V.; Wurthner, F. *Chemical Communications* **2015**, *51*, 290.

(41) Enright, B.; Redmond, G.; Fitzmaurice, D. *The Journal of Physical Chemistry* **1994**, *98*, 6195.

(42) Creutz, C. *Inorganic Chemistry* **1981**, *20*, 4449.

(43) Sirimanne, P. M.; Soga, T. *Solar Energy Materials and Solar Cells* **2003**, *80*, 383.

CHAPTER 6. PULSED-LASER DEPOSITION OF NANO-STRUCTURED IRON OXIDE CATALYSTS FOR EFFICIENT WATER OXIDATION

6.1 Chapter 6 - Abstract

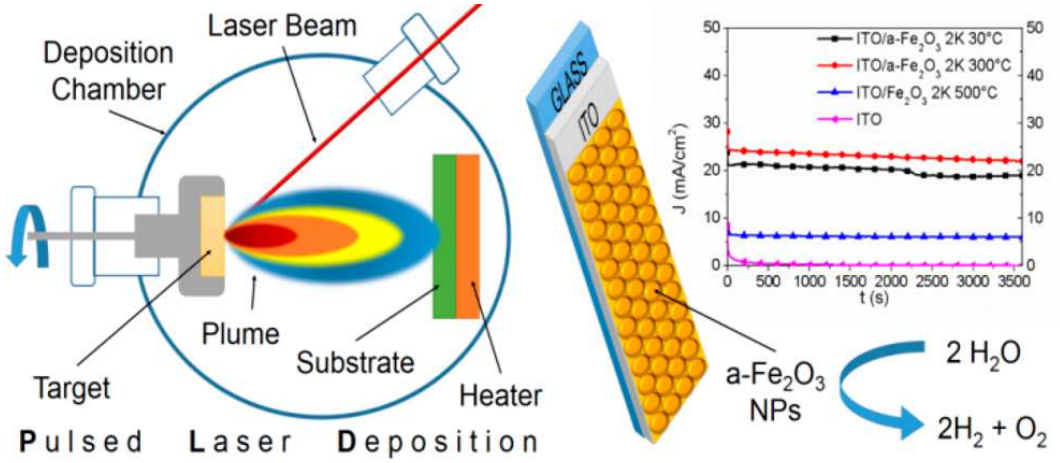

Figure 6.1 Schematization of PLD functionalization and constant potential (1.40 V vs. SCE) chronoamperometry of various a-Fe_2O_3/ITO electrodes, in aqueous pH 11.8 0.5 M sodium carbonate buffer.

Amorphous iron oxide nanoparticles were synthesized by pulsed-laser deposition (PLD) for the functionalization of indium tin oxide surfaces, resulting in electrodes capable of efficient electrocatalysis in water oxidation (**Figure 6.1**). These electrodes, based on earth-abundant and non-hazardous iron metal, are able to sustain high current densities (up to 20 mA/cm^2) at reasonably low applied potential (1.40 V at pH 11.8 vs. SCE) for more than 1 hour when employed as anodes for electrochemical water oxidation. The good catalytic performance proves the validity of PLD as a method to prepare nanostructured solid-state materials for catalysis, enabling control over critical properties such as surface coverage and morphology.

6.2 Chapter 6 - Introduction

Water splitting could unlock the use of hydrogen as a clean fuel from a renewable source.[1,2] Practical application of this reaction scheme on a large scale relies upon the development of catalysts able to meet the thermodynamically and kinetically challenging requirements[3,4] posed by the half-reactions reported in 1) and 2):

$$2H_2O + 4h^+ \rightarrow O_2 + 4H^+ \qquad E° = 1.23 \text{ V vs. NHE at pH 0 (}\mathbf{Table\ 1.1}\text{)} \qquad 1)$$

$$4H^+ + 4e^- \rightarrow 2H_2 \qquad E° = 0 \text{ V vs. NHE at pH 0 (}\mathbf{Table\ 1.1}\text{)} \qquad 2)$$

where h^+, H^+ and e^- are holes, protons and electrons, respectively. Water oxidation (1), in particular, requires a significant overpotential to overcome the kinetic barrier associated with the exchange of four H^+ and e^-. Amorphous iron oxide (a-Fe_2O_3) has been identified as a suitable water oxidation catalyst, conjugating an overall good catalytic performance[5,6] in both electrolysis[7] and solar water oxidation[8] to the advantage of being earth-abundant, nontoxic, and environmentally safe.

To our knowledge, three techniques are commonly employed for the preparation of a-Fe_2O_3: successive ionic layer adsorption and reaction (SILAR),[8] electrodeposition,[9,10] and photochemical metal-organic deposition (PMOD).[7] All three methods necessitate contact of the substrate with a solution phase. SILAR is the fastest and cheapest technique, requiring only common laboratory glassware, which leads, however, to incomplete surface coverage and poor adhesion, and it grants no control over morphology of the deposited catalyst. Electrodeposition, which could lead to nanostructured surfaces, suffers from similar problems. PMOD is a versatile technique to obtain amorphous metal and mixed metal oxides by spin coating solutions of metallorganic precursors followed by UV irradiation. However, the resulting films present smooth and featureless surfaces, whereas a high roughness is generally beneficial in catalysis.

Pulsed-laser deposition (PLD) of thin films is a technique that employs high energy density laser pulses to generate, in the regime of phase explosion, ablated material from a solid target, consisting of a mixture of vapor/liquid nanodroplets. PLD, over the methods listed above, could present some significant advantages: precise control of the quantity of the deposited material, enhanced adhesion due to the energetic nature of the process, and, most importantly, the possibility of nanostructuring the surface by the deposition of nanoparticles (NPs).[11-13] Additionally, being essentially a physical deposition method, it is

suitable to all kind of substrates; of course the main drawback is the necessity of specialized equipment, although this is already employed in industrial applications.[14]

We report here on the successful application of PLD to the synthesis of a-Fe_2O_3 NPs for functionalization of indium tin oxide (ITO) electrodes showing very good electrocatalytic activity toward water oxidation. As a model conductive substrate, ITO has been chosen for its transparency to visible light, in the perspective of extending the methodology to functionalization of silicon-based photovoltaic cells, following the approach to solar hydrogen generation proposed by Kanan and Nocera.[15,16] In such commercially available multijunction cells, ITO is commonly present as a protecting anodic conductive layer.

6.3 Chapter 6 - Experimental section

6.3.1 Materials

Sematrade indium tin oxide (ITO, purity 99.99%) conductive glass disk and iron foils (purity 99.9%) were from Sematrade.

Sodium carbonate anhydrous ≥99.0% was from Sigma Aldrich.

All reagents, unless otherwise stated, were used as received.

6.3.2 Synthesis of ITO by radio-frequency magnetron sputtering (RF-MS)

A commercial (Sematrade) ITO disk (purity 99.99%) was used as sputtering target and Ar (purity 99.99%) as working gas at a pressure of 0.8 Pa at room temperature in a custom built apparatus. Before deposition, a base pressure of about 2×10^{-5} Pa was attained and contaminations on the target surface were removed by pre-sputtering for 20 min. The sample-target distance was kept constant at 5.5 cm and the RF-MS power was maintained at 100 W throughout the deposition.

Each deposition was done on both silicon and glass substrates to allow a complete characterization of the catalysts: glass substrates are suitable for electrochemical and spectroscopic characterization and silicon substrates for electron microscopy and elemental analysis. Samples were annealed in air at 220 °C for 2 hours (heating ramp: 2 °C/min.).

6.3.3 Synthesis of a-Fe_2O_3 nanoparticles by PLD

NPs assembled iron oxide coatings were deposited by PLD using KrF excimer laser (*Lambda Physik LP 220i*) with an operating wavelength of 248 nm, pulse duration of 25 ns, repetition rate of 20 Hz, laser fluence of Ed = 6.2 J/cm^2 (energy density). Details of the deposition apparatus are reported in a previous publication.[17] Laser ablation was carried out by using a pure (99.9%, Sematrade) Fe target under oxygen gas atmosphere. The PLD chamber was evacuated up to a base pressure of 10^{-4} Pa prior to the deposition. NPs assembled coatings were deposited on Si and glass substrates by maintaining target to substrate distance at 5.5 cm, with substrate position parallel to the target, or normal to the flow velocity of the plume expansion. In the deposition chamber, the O_2 gas pressure was of about 4.5 Pa and substrate temperature of either 30 °C or 300 °C during the deposition.

6.3.4 Electrical properties measurement

Sheet resistance and resistivity measurements were carried out with I/V apparatus equipped with an in-line four-point probe.[18]

6.3.5 Grazing incidence X-ray diffraction (GIXD) analysis

GIXD analysis were carried out on a *Philips X'Pert θ/2θ* automatic diffractometer with grazing incidence geometry, with fixed incidence angle ω = 1.0°, employing Cu K_α (λ = 1.5416 Å, 1.6 kW) radiation. Angular range was 5°-90° (2θ), with 0.02° (2θ) steps and acquisition time 25 seconds per step. Inorganic phases identification was performed with the *Hanawalt method on PDF-2* (powder diffraction file, ICDD) data-set. Crystallite size, when indicated, was estimated by peak broadening with a method taken from fundamental parameter approach (*FPA-TOPAS* software).

6.3.6 X-ray photoelectron spectroscopy (XPS) analysis

XPS spectra were recorded using a *PHI-5500-Physical electronics* spectrometer, equipped with a monochromatized source with an Al anode (Kα = 1486.6 eV), operating at 200 W of applied power, 5.85 eV pass energy, and 0.05 eV energy-step. XPS spectra were collected at take-off angles of 45°. The analyzed area is around 0.5 mm^2 and the sampling depth is within 10 nm. During measurements, the vacuum level was around 10^{-9} Torr residue pressure. The spectrometer was calibrated assuming the $Ag(3d_{5/2})$ binding energy (BE) at 368.3 eV with respect to the Fermi-level and the measured full-width-half-maximum (FWHM) was 0.46 eV.

In order to neutralize the surface electrostatic charge of non-conductive samples, an electron gun was used. Furthermore, the charging effect on the analysis was also corrected considering the BE value of C(1s), due to adventitious carbon, at 284.8 eV. The BEs were measured at the maximum of the peaks without any baseline subtraction.

6.3.7 Scanning electron microscopy (SEM) analysis

SEM was used to analyze the morphology and thickness of films. The surface of the films was acquired by a *JEOL JSM-7001F* field effect gun (FEG-SEM) apparatus at 30 keV beam energy. SEM apparatus is equipped with an energy-dispersive X-ray spectroscopy detector (EDXS, *Oxford INCA PentaFETx3*). Working distance (WD) was maintained between 4 to 8 mm. Surface morphology images were acquired at 20° tilt angle whereas cross section analysis were performed putting the films on a 90° stub.

6.3.8 Optical properties measurement

UV-vis transmittance spectra were recorded on a *Cary 5000* spectrophotometer using a microscope glass slide as blank, while microRaman analysis was carried out on a *Horiba LabAramis* setup equipped with a HeNe 633 nm laser as source.

6.3.9 Electrochemical measurements

Electrochemical measurements were performed on a *PGSTAT 302/N* workstation equipped with *FRA2* frequency response analyzer (**Figure 2.15**). Electrochemical experiments were generally performed in a three-electrode configuration, by using either different types of catalytic Fe(III) electrodes or bare ITO as anodes, Pt as counter electrode and SCE as reference electrode, in a pH 11.8 0.5 M sodium carbonate buffer solution.

Linear sweep measurements were obtained between -0.04 V and 1.56 V vs. SCE with a scan rate of 50 mV/s, with and without dynamic iR-drop compensation.

Chronoamperometry was recorded by imposing a constant potential of 1.40 V vs. SCE, without dynamic iR-drop compensation.

Electrochemical impedance spectroscopy (**Section 2.5**) measurements were performed in the potential range between 0.80 V and 1.20 V vs. SCE with a sampling interval of 0.05 V and a sinusoidal perturbation amplitude of 10 mV (frequency range 100000 Hz - 0.05 Hz).

6.4 Chapter 6 - Results and discussions

As reported in **Section 6.3.2**, ITO films of thickness 350-450 nm were obtained by sputtering (RF-MS) of an ITO target in an Ar atmosphere (0.8 Pa working pressure) at room temperature over glass (for electrochemical and spectroscopic characterization) and silicon substrates (for electron microscopy and elemental analysis). Samples were then annealed in air at 220 °C for 2 hours, in order to increase transmittance and decrease the sheet resistance (*Rs*) and resistivity (ρ).

XPS analysis (**Table 6.1**) indicates the presence of indium(III) ($In(3d_4)$ peak; BE = 444.5 ± 0.5 eV) and tin(IV) ($Sn(3d_5)$ peak; BE = 486.5 ± 0.5 eV) with an In/Sn ratio of 9:1 (atomic %).

Table 6.1 XPS analysis of ITO surfaces. Si is included as a common contaminant and C is present both as an environmental contaminant and as adsorbed carbonate.

	Fe(2p)	***O(1s)***	***Sn($3d_5$)***	***In($3d_4$)***	***C(1s)***	***Si(2p)***
BE (eV)[a]		532.5-530.0	486.5	444.5	284.5	102.5
Conc. (atomic %)	---	32.2	0.6	5.4	42.8	19.0

a) Binding energies (BE) were measured with an approximation of 0.5 eV.

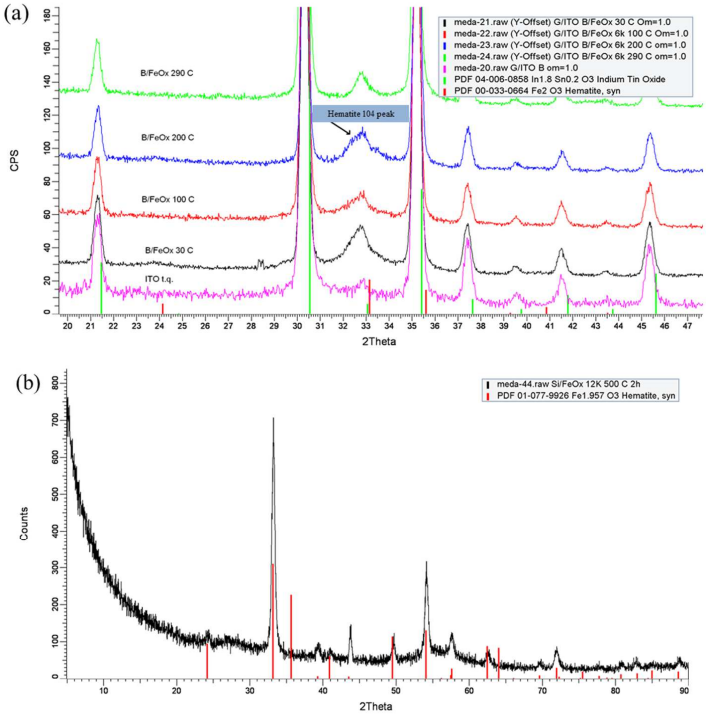

Figure 6.2 (a) GIXD analysis of Fe_2O_3 functionalized ITO electrodes at different deposition temperatures. Bare ITO is shown as reference. (b) GIXD analysis of hematite functionalized silicon substrates (room-temperature deposition followed by annealing at 500 °C for 2 h).

GIXD investigation reveals a crystalline phase with face-centered-cubic (fcc) structure and unit-cell parameter a = 10.16 Å (**Figure 6.2**). The combined results of these analyses are definitely compatible with ITO identification. SEM analysis, employed for thickness measurement via cross-sectional analysis and surface imaging, revealing compact films with a polycrystalline surface (**Figure 6.3**). Typical values for transmittance are between 70% and 80% (400-800 nm range; **Figure 6.4**) and 10-15 Ω/□ for resistance, corresponding to $\rho = (3.6\text{-}5.3)\times10^{-6}$ Ω.

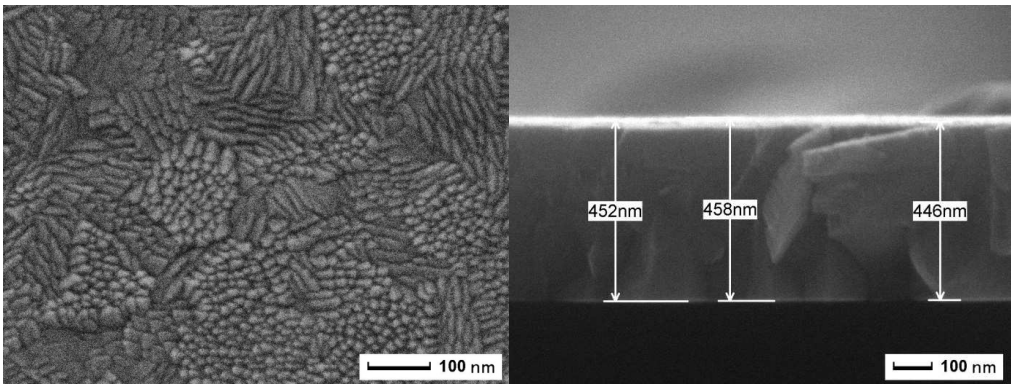

Figure 6.3 SEM top-down (above) and cross-sectional (below) analysis for a typical ITO film.

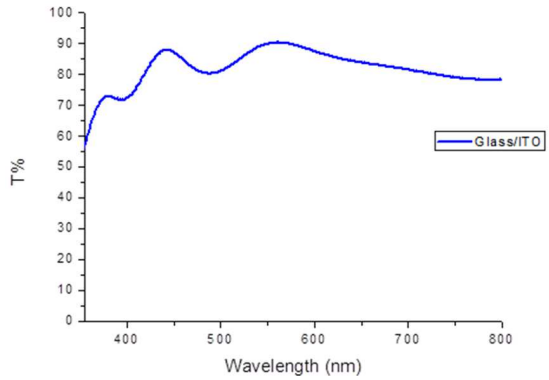

Figure 6.4 UV-vis transmittance in the 400-800 nm range for a typical ITO film over glass substrate.

The ITO electrodes were then employed as substrates for PLD (KrF excimer laser, wavelength of 248 nm, pulse duration of 25 ns, and repetition rate of 20 Hz), with an iron disk as the target in an O_2 atmosphere (4.5 Pa working pressure). Either 2000 (2K) pulses (for working electrodes) or 6000 (6K) pulses (for GIXD characterization) of Ed = 6.2 J/cm^2 (the choice of this value is motivated to obtain NPs)[11] were applied during the deposition process, leading to layers of respectively 15 ± 5 nm and 60 ± 5 nm thickness, as measured by SEM cross-sectional analysis (**Figure 6.5**, top). The substrate temperature during deposition (T_{dep}) was either 30 °C or 300 °C. Some of the electrodes were annealed at 500 °C in air for 2 hours to obtain hematite for the purpose of comparison. Iron is detected by XPS as iron(III) only (Fe(2p) peak; BE = 710.5 ± 0.5 eV; **Table 6.2**). SEM top-down imaging (**Figure 6.5**, bottom) reveals a structured surface, with ITO completely covered by 10-15 nm average diameter round-shaped features of homogeneous size distribution, present in all samples up to T_{dep} = 300 °C. This morphology is compatible with a NPs-assembled coating.

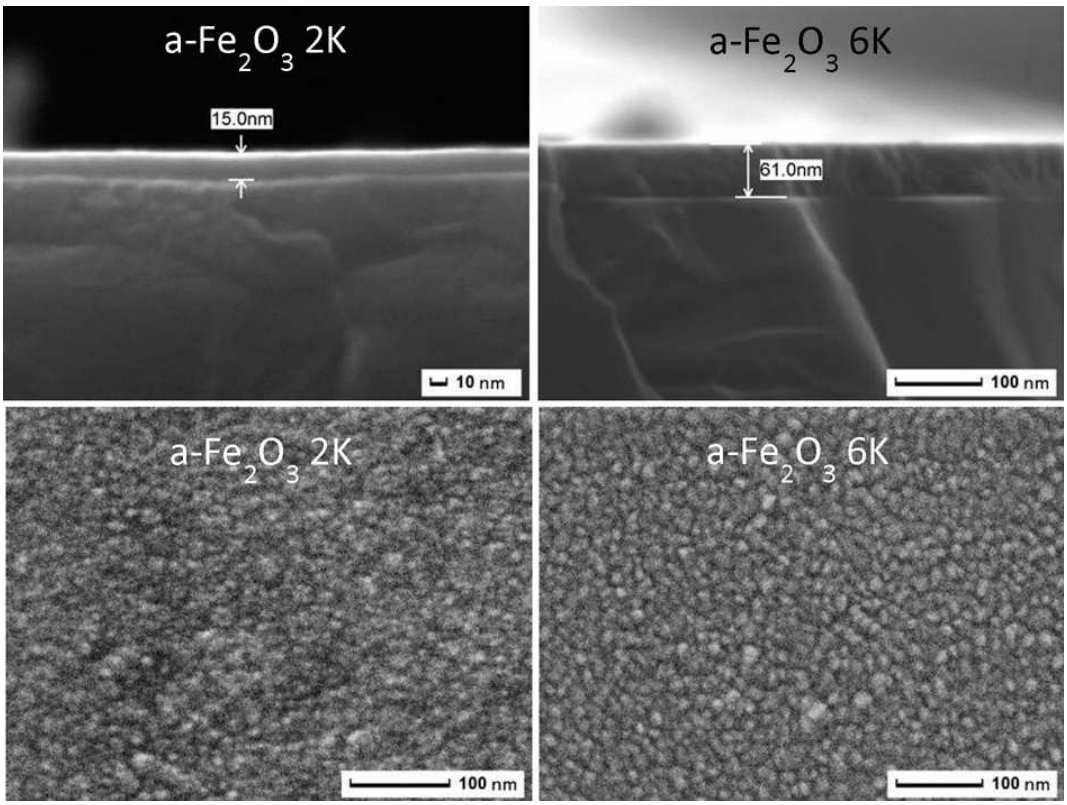

Figure 6.5 SEM images of a-Fe_2O_3-functionalized ITO electrode: cross section (top); top-down (bottom).

Table 6.2 XPS analysis of 2K a-Fe_2O_3 deposited over glass at various substrate temperatures. Si is included as a common contaminant and C is present both as an environmental contaminant and as adsorbed carbonate.

T_{dep} (°C)	*Fe(2p) (atomic %)* ***BE (eV)*** [a]	*O(1s) (atomic %)* ***BE (eV)*** [a]	*C(1s) (atomic %)* ***BE (eV)*** [a]	*Si(2p) (atomic %)* ***BE (eV)*** [a]
30 °C	16.9 710.5	43.5 532.5-529.5	38.0 284.5	1.6 102.5
100 °C	18.7 710.5	44.3 532.5-529.5	34.7 284.5	2.3 102.5
200 °C	11.4 710.5	38.3 532.5-529.5	50.3 284.5	--- 102.5
300 °C	15.7 710.5	36 532.5-529.5	48.3 284.5	--- 102.5

a) BE were measured with an approximation of 0.5 eV.

Transmittances for 2K pulses samples are between 40% and 70% (400-800 nm range; **Figure 6.6**). Micro-Raman spectroscopy of 6K pulse deposition over glass substrates (**Figure 6.7**) reveals mostly an amorphous material on samples up to T_{dep} = 300 °C, although a trend of increasing crystallinity with higher T_{dep} is clearly visible with this technique. Samples annealed at 500 °C in air for 2 hours appear to be completely crystalline. GIXD results (**Figure 6.2**) on samples up to T_{dep} = 300 °C are compatible with

those of a largely amorphous material, showing only a weak signal attributable to the presence of very small (6-11 nm) hematite scattering domains (hexagonal structure, unit-cell parameters a = 5.07 Å and c = 13.90 Å).

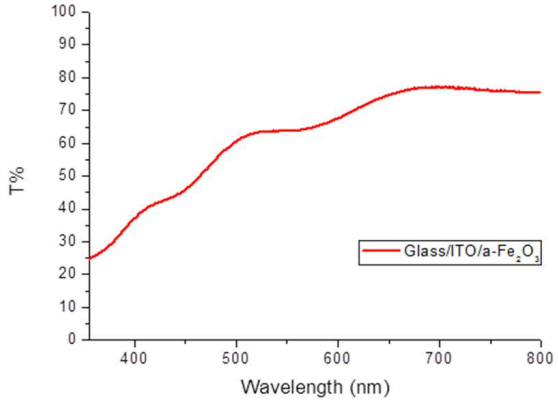

Figure 6.6 UV-vis transmittance in the 400-800 nm range for 2K a-Fe_2O_3 deposited over glass at substrate temperatures of 30 °C.

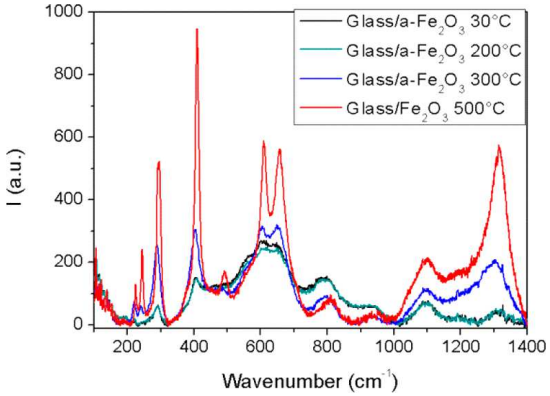

Figure 6.7 Micro-Raman spectra of 6K a-Fe_2O_3 deposited over glass at substrate temperatures of 30 °C, 200 °C, 300 °C and of hematite functionalized electrodes (glass/Fe_2O_3, 6K, 500 °C).

Electrochemical water oxidation tests were performed, as reported in **Section 6.3.9**, in a three-electrode configuration, with either 2K pulse a-Fe_2O_3 or hematite-functionalized ITO as the working electrode. Because Fe_2O_3 is stable at pH > 9,[8] a pH of 11.8 was maintained with a 0.5 M Na_2CO_3 buffer to ensure complete stability and thus well-defined electrochemistry.

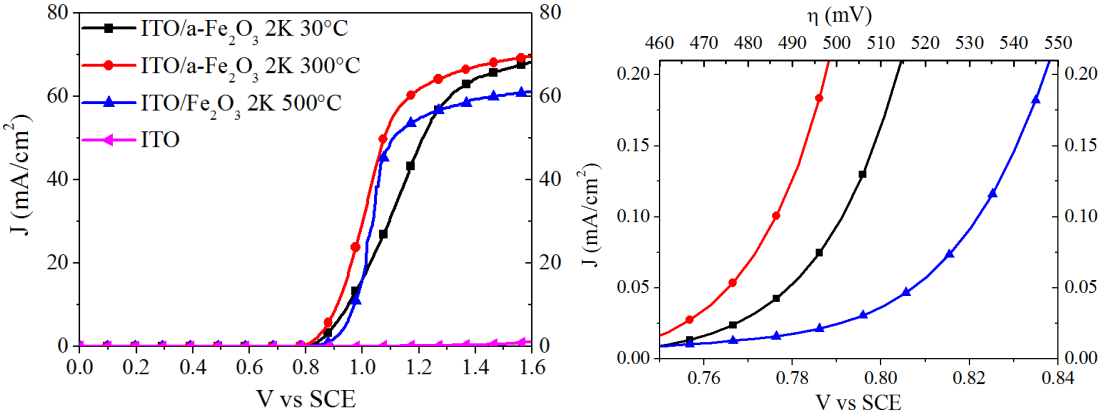

Figure 6.8 Linear sweep voltammetry (left) and its low overpotential magnification (right) of 2K a-Fe_2O_3 functionalized electrodes deposited at 30 °C (ITO/a-Fe_2O_3 2K 30 °C), at 300 °C (ITO/a-Fe_2O_3 2K 300 °C) and of hematite functionalized electrodes (ITO/Fe_2O_3 2K 500 °C). Bare ITO is reported as the reference. J-V characteristics are compensated for the iR-drop.

Oxygen evolution at this pH is expected at potential E_{OX} = 1.23 − (0.059×pH) = 0.53 V vs. reversible hydrogen electrode (RHE).[19] In **Figure 6.8** a comparison of the anodic responses of various functionalized electrodes against bare ITO is presented. Amorphous a-Fe_2O_3 shows considerable electroactivity toward water oxidation (**Table 6.3**) when deposited both at 30 °C (ITO/a-Fe_2O_3 2K 30 °C, black squares) and at 300 °C (ITO/a-Fe_2O_3 2K 300 °C, red circles) with onset overpotential η (taken at J = 0.2 mA/cm^2)

for anodic currents of 513 mV and 497 mV, respectively, while hematite (ITO/Fe_2O_3 2K 500 °C, blue triangles) is only slightly less active with η = 546 mV. Though not exceptional in terms of its onset overpotential, the amorphous catalyst has a remarkably low Tafel slope, thus being able to sustain considerable current densities at moderate η.

Table 6.3 Onset (J = 0.2 mA/cm^2) η and Tafel slope.

	η (mV)	***Tafel slope (mV/dec)***
ITO/a-Fe_2O_3 2K 30 °C	513 mV	39.7 mV/dec
ITO/a-Fe_2O_3 2K 300 °C	497 mV	35.6 mV/dec
ITO/Fe_2O_3 2K 500 °C	546 mV	57.3 mV/dec

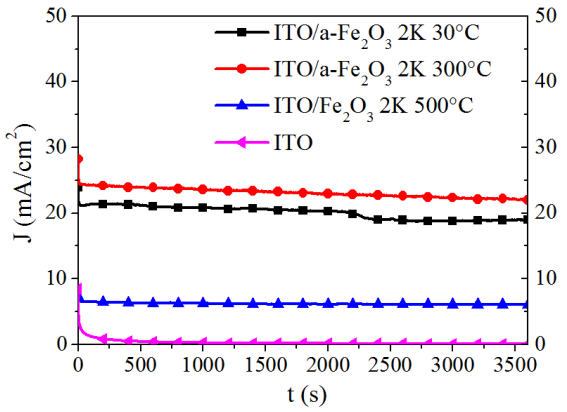

Figure 6.9 1 hour constant potential (1.40 V vs. SCE) chronoamperometry of 2K a-Fe_2O_3 electrodes deposited at 30 °C (ITO/a-Fe_2O_3 2K 30 °C), at 300 °C (ITO/a-Fe_2O_3 2K 300 °C) and of hematite functionalized electrodes (ITO/Fe_2O_3 2K 500 °C). Bare ITO is shown as the reference. Not compensate for the iR-drop.

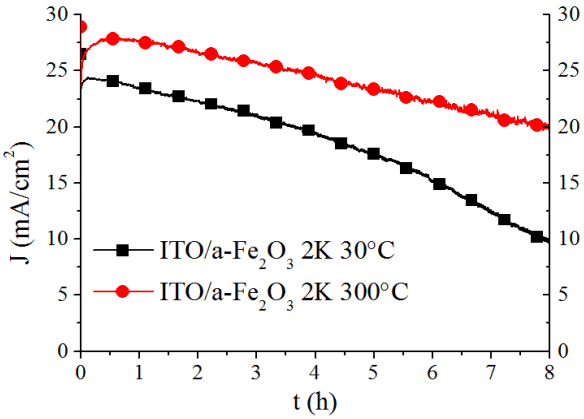

Figure 6.10 8 hours chronoamperometry, at 1.40 V vs. SCE, of 2K a-Fe_2O_3 functionalized electrodes, deposited at 30°C (ITO/a-Fe_2O_3 2K 30 °C) and 300 °C (ITO/a-Fe_2O_3 2K 300°C). Not compensated for iR-drop.

Indeed, where the amorphous material proves superior is in the constant potential electrolysis (V_{appl} = 1.40 V vs. SCE for 1 hour) reported in **Figure 6.9**: while hematite electrodes give current densities of about 6.5 mA/cm^2, the amorphous material can sustain currents of more than 20 mA/cm^2, with ITO/a-Fe_2O_3 2K 300 °C performing slightly better (24 mA/cm^2) than ITO/a-Fe_2O_3 2K 30 °C (21 mA/cm^2). These current levels could be sustained without significant loss for up to 8 hours (**Figure 6.10**) for ITO/a-Fe_2O_3 2K 300 °C, while a drop in the current density accompanied by bleaching of the surface was observed for ITO/a-Fe_2O_3 2K 30 °C. This could be due to the loss of catalyst from the electrode surface, indicating that higher T_{dep} improves adhesion.

It should be noted that a partial current drop, approximately 30%, could be observed also in the ITO/a-Fe_2O_3 2K 300 °C, electrode, at the end of the 8 hours constant potential (1.40 V vs. SCE) chronoamperometry. Such loss does not appear to be permanent because the initial

performance was re-observed on successive J-V and J-t scans (**Figure 6.11**) recorded on the following days, after rinsing and storing the electrode in air under dark conditions. Thus, the partial current decrease upon prolonged electrolysis may originate by adsorption of ions, of oxidation intermediates, and of molecular oxygen, limiting the active surface of the electrode, rather than by detachment of a-Fe_2O_3, leading to permanent loss of the catalytic performances of the electrode.

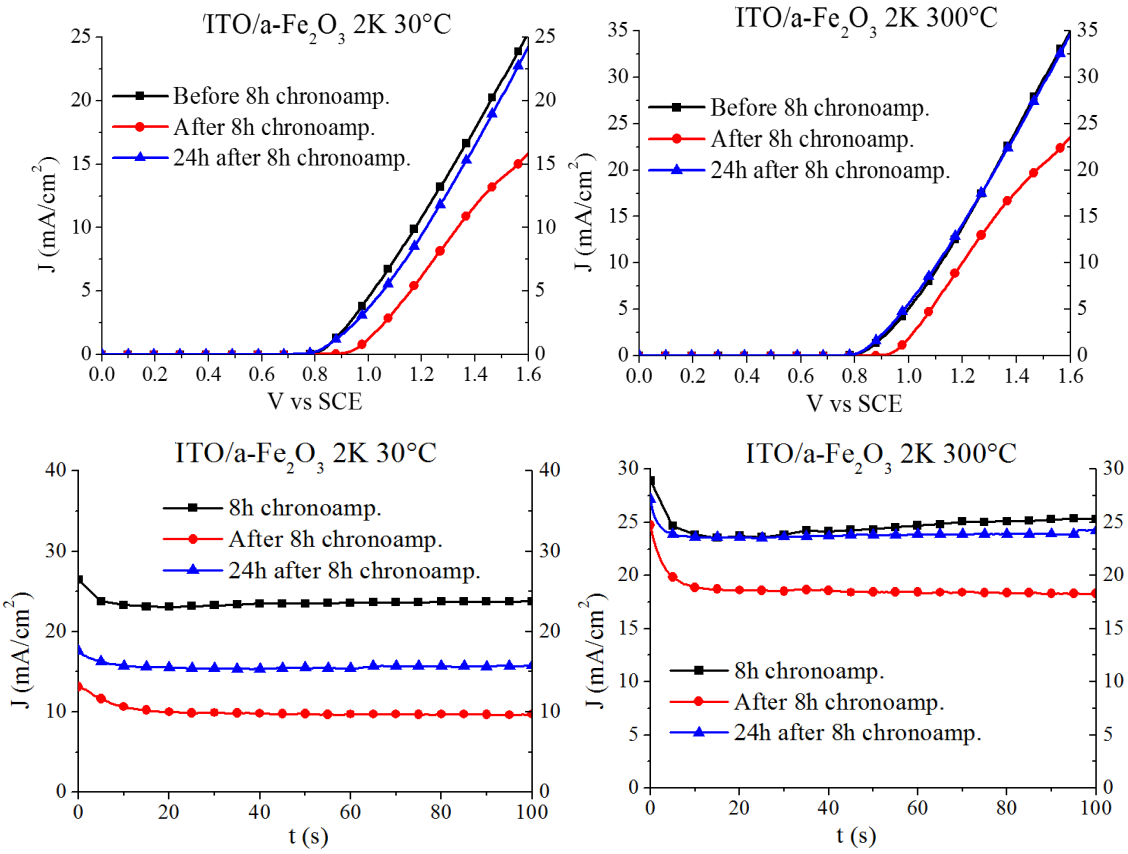

Figure 6.11 Linear sweep voltammetry of ITO/a-Fe_2O_3 2K 30 °C (top-left) and ITO/a-Fe_2O_3 2K 300 °C (top-right), and their respective chronoamperometry at 1.40 V vs. SCE (30 °C bottom-left and 300 °C bottom-right), before (black squares), immediately after (red circles) and after 24 hours (blue triangles) the 8 hours chronoamperometry. Not compensated for iR-drop.

Electrochemical impedance spectroscopy (**Section 6.3.9**) was used for evaluating the single resistive contributions arising from different interfaces and processes. Fitting of EIS was achieved with the two electric equivalents reported in **Figure 6.12B**,**C**, where the ohmic resistance (R_1) is followed by two parallel meshes accounting for the a-Fe_2O_3/ITO (R_2 - CPE_1) and the a-Fe_2O_3/electrolyte (R_3 - CPE_2) electrochemical interfaces. A warburg element (W_s1; **Figure 6.12C**) was introduced at voltages of ≥ 0.90 V vs. SCE to account for the appearance of a diffusional arc in the complex plane plots at higher overpotentials (**Figure 6.13** and **Figure 6.14**). This low frequency feature was not observed with ITO/Fe_2O_3 2K 500 °C (**Figure 6.15**), having a much slower charge transfer kinetic

compared to the amorphous material. For bare ITO (**Figure 6.12A** and **Figure 6.16**) only one parallel element was used, corresponding to the ITO/electrolyte interface.

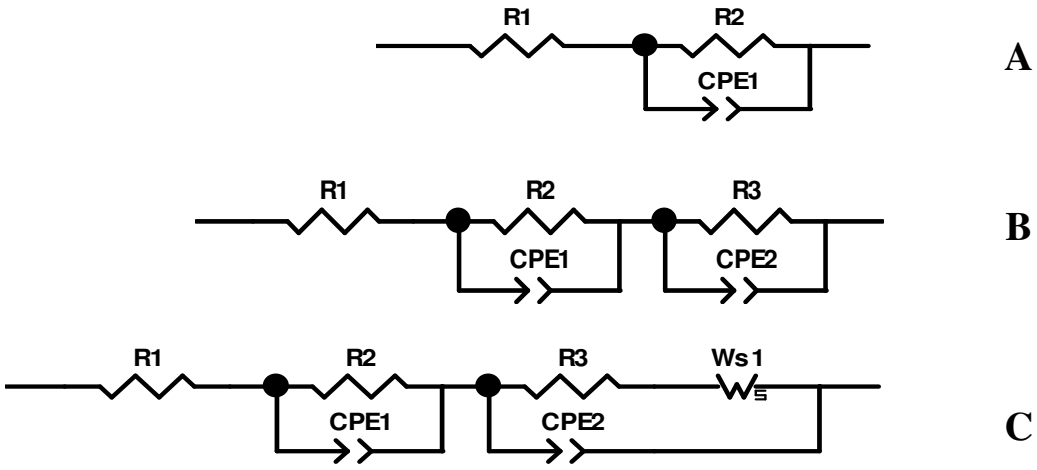

Figure 6.12 Electric equivalent used to describe ITO/a-Fe_2O_3 2K 30 °C and ITO/a-Fe_2O_3 2K 300 °C (B) in the voltage range 0.80 V - 0.85 V vs. SCE and (C) in the voltage range 0.90 V - 1.20 V vs. SCE. The electric equivalent used for bare ITO is (A) and for ITO/Fe_2O_3 2K 500 °C is (B), both within the whole explored voltage range.

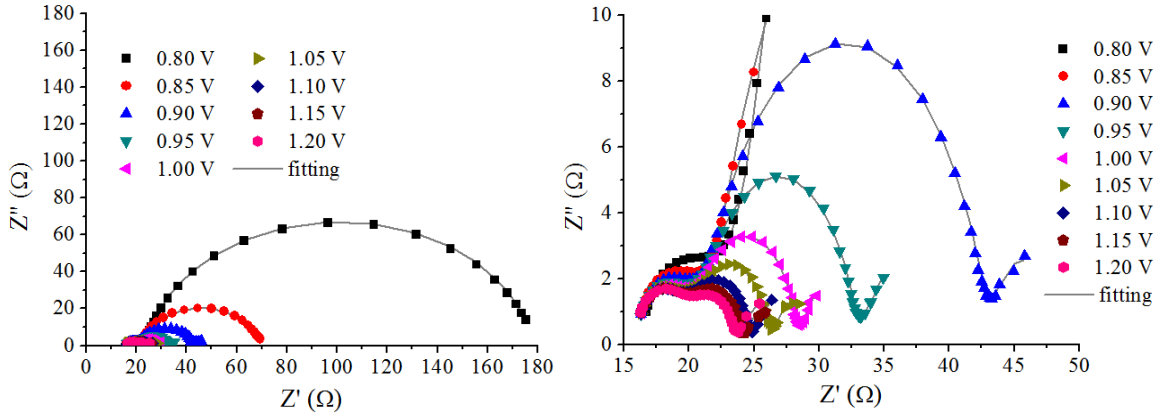

Figure 6.13 Nyquist plot of ITO/a-Fe_2O_3 2K 30 °C (left) and magnification of the plots recorded at potential ≥ 0.90 V vs. SCE (right). Symbols: experimental points; grey line: fitting according to the models reported in **Figure 6.12**.

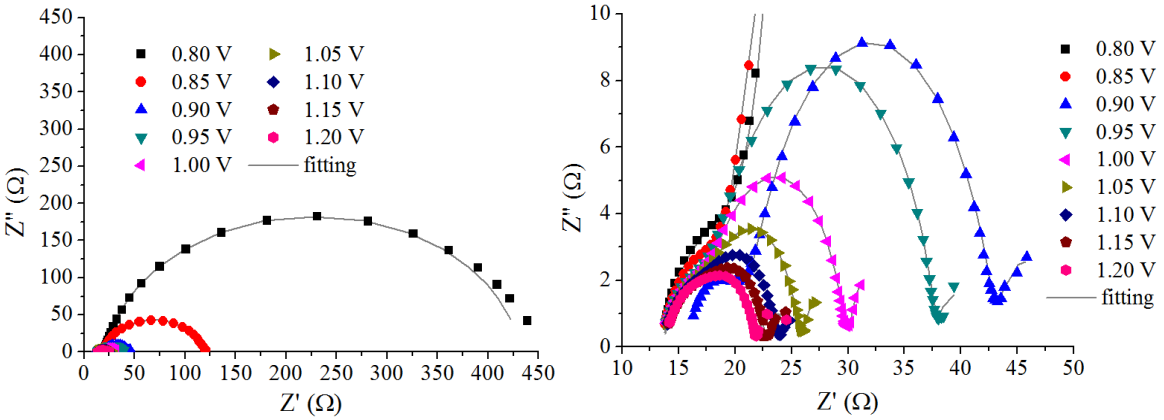

Figure 6.14 Nyquist plot of ITO/a-Fe_2O_3 2K 300 °C (left) and magnification of the plots recorded at potential ≥ 0.90 V vs. SCE (right). Symbols: experimental points; grey line: fitting according to the models reported in **Figure 6.12**.

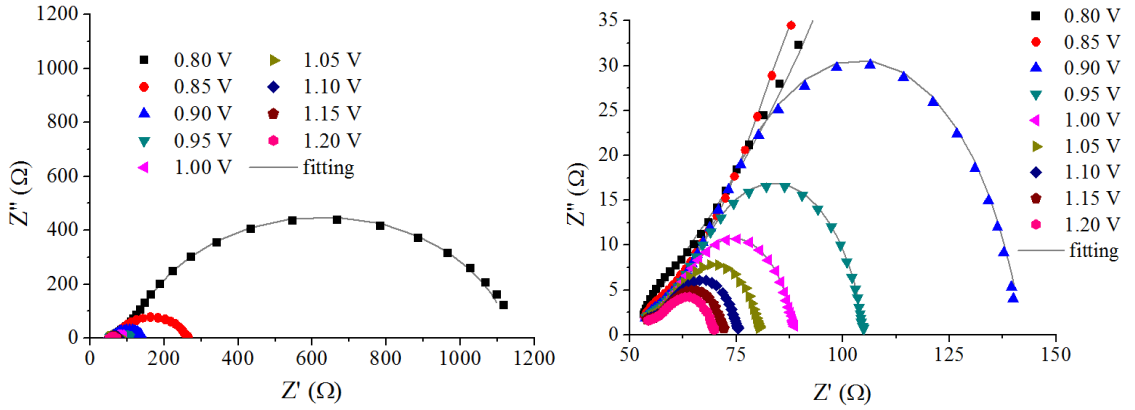

Figure 6.15 Nyquist plot of ITO/Fe_2O_3 2K 500 °C (left) and magnification of the plots recorded at potential ≥ 0.90 V vs. SCE (right). Symbols: experimental points; grey line: fitting according to the models reported in **Figure 6.12**.

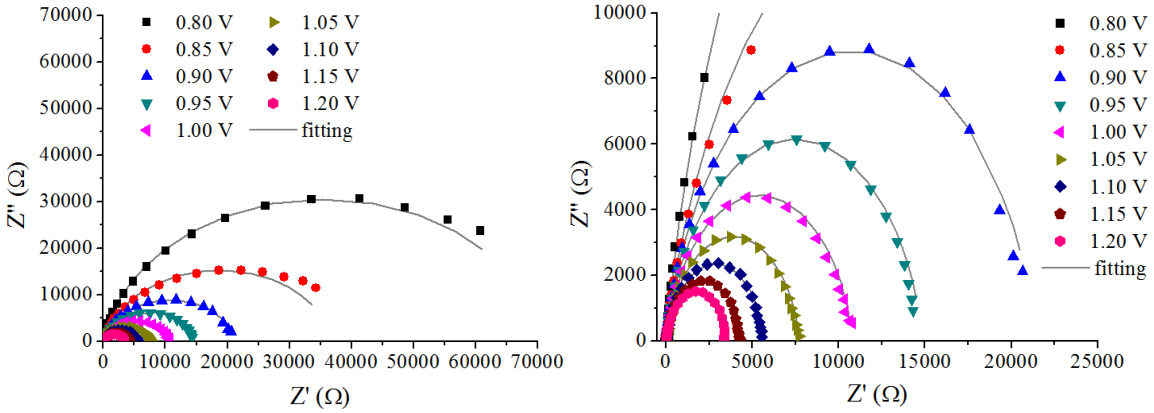

Figure 6.16 Nyquist plot of bare ITO (left) and magnification of the plots recorded at potential ≥ 0.90 V vs. SCE (right). Symbols: experimental points; grey line: fitting according to the models reported in **Figure 6.12**.

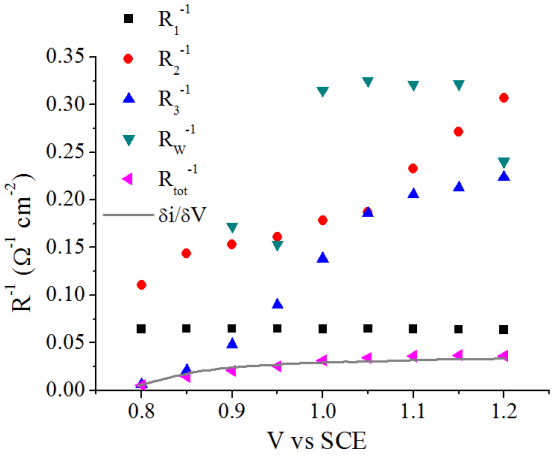

Figure 6.17 Reciprocal of the single resistive contributions and total reciprocal resistance R_{tot}^{-1} (magenta) compared to the derivative of the J-V curve (gray). ITO/a-Fe_2O_3 2K 30 °C in 0.5 M Na_2CO_3.

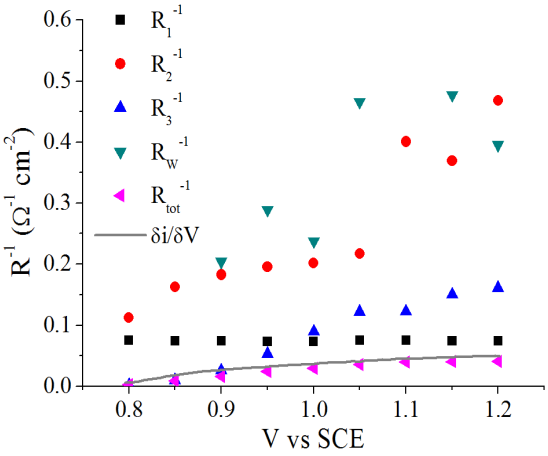

Figure 6.18 Reciprocal of the single resistive contributions and total reciprocal resistance R_{tot}^{-1} (magenta) compared to the derivative of the J-V curve (gray). ITO/a-Fe_2O_3 2K 300 °C in 0.5 M Na_2CO_3.

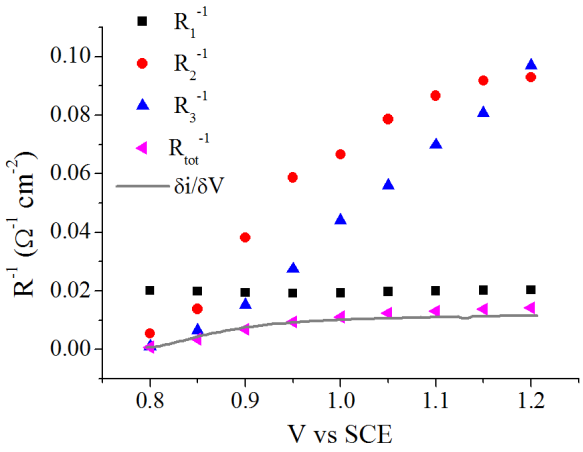

Figure 6.19 Reciprocal of the single resistive contributions and total reciprocal resistance R_{tot}^{-1} (magenta) compared to the derivative of the J-V curve (gray). ITO/a-Fe_2O_3 2K 500 °C in 0.5 M Na_2CO_3.

The model describes satisfactorily the impedance response of the electrode, as shown in all cases (a-Fe_2O_3 2K 30 °C, 300 °C, and 500 °C) by the excellent agreement of the reciprocal total resistance [$R_{tot}^{-1} = (R_1 + R_2 + R_3 + R_W)^{-1}$] with the slope of the J-V curve (**Figure 6.17**, **Figure 6.18** and **Figure 6.19**). The smallest charge-transfer resistance was observed for the 30 °C and 300 °C electrodes, showing in the core of anodic discharge (V ≥ 1.00 V vs. SCE) charge-transfer resistances on the order of few ohms, comparable to the a-Fe_2O_3/ITO interface resistance. In particular, it can be observed that, at potentials exceeding 1.05 V vs. SCE, the charge-transfer resistance (R_3) at the interface a-Fe_2O_3/electrolyte quickly becomes significantly smaller than the constant ohmic contribution (R_1; **Table 6.4**, **Table 6.5** and **Table 6.6**) arising from the electrolyte and ITO contact resistance; thus, after crossing the activation region, at ca. 0.76 V vs. SCE, the main limitation to the anodic current density arises simply from the limited ITO conductivity.

Table 6.4 Individual resistances of ITO/a-Fe_2O_3 2K 30 °C.

Potential (V vs. SCE)	R_1 (Ω)	R_2 (Ω)	R_3 (Ω)	R_W (Ω)	R_{tot} (Ω)
0.80	15	10	154	/	179
0.85	15	7	47	/	69
0.90	15	7	21	6	49
0.95	15	6	11	6	38
1.00	15	6	7	3	31
1.05	15	5	5	3	28
1.10	15	4	5	3	27
1.15	15	4	5	3	27
1.20	16	3	4	4	27

Table 6.5 Individual resistances of ITO/a-Fe_2O_3 2K 300 °C.

Potential (V vs. SCE)	R_1 (Ω)	R_2 (Ω)	R_3 (Ω)	R_W (Ω)	R_{tot} (Ω)
0.80	13	9	411	/	433
0.85	14	6	100	/	120
0.90	14	5	38	5	62
0.95	14	5	19	3	41
1.00	14	5	11	4	34
1.05	13	5	8	2	28
1.10	13	3	8	1	25
1.15	13	3	7	2	25
1.20	14	2	6	2	24

Table 6.6 Individual resistances of ITO/Fe_2O_3 2K 500 °C.

Potential (V vs. SCE)	R_1 (Ω)	R_2 (Ω)	R_3 (Ω)	R_{tot} (Ω)
0.80	50	184	920	1154
0.85	50	72	152	274
0.90	51	26	65	142
0.95	52	17	36	105
1.00	52	15	23	90
1.05	50	13	18	81
1.10	50	11	14	75
1.15	49	11	12	72
1.20	49	11	10	70

The preliminary study of the capacity of the 2K anodes (**Figure 6.20**), considering the potential range from 0.80 to 1.20 V vs. SCE, shows that the activity of the electrode cannot be straightforwardly related to its specific electroactive area, at least when considering the simplest model based on a parallel-plate capacitor (**Table 6.7** and **Table 6.8**). The sharp drop in capacitance resulting in an inflection point at ca. 1.1 V vs. SCE

could be related to the depolarization due to fast electron transfer. Indeed it is much less pronounced on electrodes having a relatively sluggish electron transfer kinetics, i.e. crystalline hematite and bare ITO.

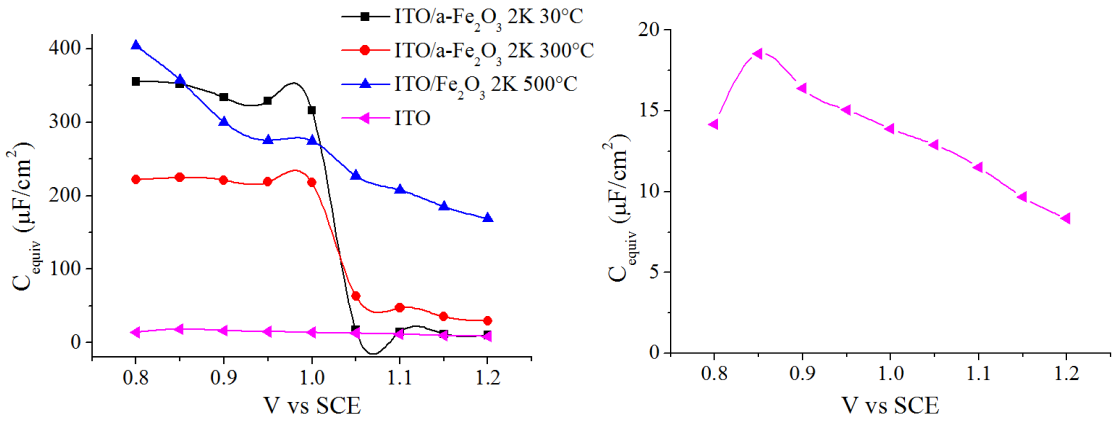

Figure 6.20 Comparison of 2K anodes equivalent capacities vs. potential (left), and a magnification of the bare ITO plot (right). The equivalent capacities were calculated in agreement with the **Equation 6.1**.

Table 6.7 Electrodes equivalent capacities at various potential.

Potential (V vs. SCE)	$C_{30\ °C}$ *(µF/cm²)*	$C_{300\ °C}$ *(µF/cm²)*	$C_{500\ °C}$ *(µF/cm²)*	C_{ITO} *(µF/cm²)*
0.80	355	221	404	14
0.85	352	224	357	19
0.90	334	221	300	16
0.95	329	219	275	15
1.00	316	218	275	14
1.05	17	64	227	13
1.10	15	48	208	12
1.15	12	35	185	10
1.20	10	30	169	8

Capacities are extrapolated from EIS, through the elements (**Table 2.1**) in the equivalent circuits, using **Equation 6.1**:

$$C = Y \cdot (j\omega)^{n-1} \qquad \textbf{Equation 6.1}$$

where Y is the constant phase element (CPE) admittance, ω is the angular frequency, evaluated at the maximum frequency of the interfacial charge transfer arc, and n is the CPE exponent ($0.8 < n < 1$). For an electrified interface in a concentrated solution (0.5 M

Na_2CO_3), which is dominated by the Helmholtz layer, the capacity can be approximated by a parallel plate condenser according to the **Equation 6.2**:

$$C = \varepsilon_0 \cdot \varepsilon_r \cdot \frac{S}{d} \qquad \textbf{Equation 6.2}$$

where ε_0 and ε_r are respectively the vacuum and relative permittivity, S is the electrode area and d is the thickness of the Helmholtz layer. All measurements were performed in the same electrolyte and concentration, so d and the dielectric constant can be assumed the same. Therefore from the ratio of the capacities (CR) with respect to that of the ITO, at the onset potential of the anodic discharge (0.80 V vs. SCE, **Table 6.8**), it is possible to evaluate the relative specific active area of the 2K ITO/Fe_2O_3 electrodes, that results ca. 20 times larger than that of bare ITO ($16 \leq CR \leq 29$).

Table 6.8 Ratio between capacities of the functionalized electrodes and the capacity of bare ITO.

Potential (V vs. SCE)	***$CR_{30\ °C}$ ($\mu F/cm^2$)***	***$CR_{300\ °C}$ ($\mu F/cm^2$)***	***$CR_{500\ °C}$ ($\mu F/cm^2$)***
0.80	25	16	29

6.5 Chapter 6 - Conclusions

Although the exact mechanism of oxygen evolution at a-Fe_2O_3 catalysts is unknown, a recent study,[20] on hematite photoelectrodes decorated by an amorphous iron(III) oxide catalyst, showed that the presence of the catalyst resulted in enhanced hole trapping in sites capable of undergoing favourable proton-coupled electron transfer reactions, leading to the formation of highly valent Fe^{IV}=O species,[21] which may undergo subsequent nucleophilic attack by the water molecule, finally resulting in the oxygen evolution reaction. Such a reaction pathway is probable also in a thin layer electrode, but the exact definition of the reaction intermediates remains a challenging task and requires determination of the coordination environment of the iron(III) and iron(IV) centres in the amorphous film. Such a study is currently underway.

In conclusion, we have demonstrated PLD as a valid method for functionalization of surfaces with a nanostructured a-Fe_2O_3 catalyst, obtaining electrodes that perform well toward water oxidation. With respect to other methods of preparation, PLD offers significant improvements in terms of material adhesion and control over critical parameters such as surface coverage and morphology. The methodology lends itself to the exploration of other metal oxide catalysts including mixed metal oxides and to functionalization of other surfaces including silicon-based photovoltaic cells or other photoactive materials for solar powered water splitting.

6.6 Chapter 6 - Figures index

6.7 Chapter 6 - References

(1) Eisenberg, R.; Nocera, D. G. *Inorganic Chemistry* **2005**, *44*, 6799.

(2) Rajeshwar, K.; McConnell, R.; Harrison, K.; Licht, S. In *Solar Hydrogen Generation*; Rajeshwar, K., McConnell, R., Licht, S., Eds.; Springer New York: **2008**, p 1.

(3) Rüttinger, W.; Dismukes, G. C. *Chemical Reviews* **1997**, *97*, 1.

(4) Lewis, N. S. *Nature* **2001**, *414*, 589.

(5) Gondal, M. A.; Hameed, A.; Yamani, Z. H.; Suwaiyan, A. *Applied Catalysis A: General* **2004**, *268*, 159.

(6) Mariana Balu, A.; Pineda, A.; Yoshida, K.; Manuel Campelo, J.; Gai, P. L.; Luque, R.; Angel Romero, A. *Chemical Communications* **2010**, *46*, 7825.

(7) Smith, R. D. L.; Prévot, M. S.; Fagan, R. D.; Zhang, Z.; Sedach, P. A.; Siu, M. K. J.; Trudel, S.; Berlinguette, C. P. *Science* **2013**, *340*, 60.

(8) Cristino, V.; Berardi, S.; Caramori, S.; Argazzi, R.; Carli, S.; Meda, L.; Tacca, A.; Bignozzi, C. A. *Physical Chemistry Chemical Physics* **2013**, *15*, 13083.

(9) Zotti, G.; Schiavon, G.; Zecchin, S.; Casellato, U. *Journal of The Electrochemical Society* **1998**, *145*, 385.

(10) Schrebler, R.; Bello, K.; Vera, F.; Cury, P.; Muñoz, E.; del Río, R.; Gómez Meier, H.; Córdova, R.; Dalchiele, E. A. *Electrochemical and Solid-State Letters* **2006**, *9*, C110.

(11) Warang, T.; Patel, N.; Santini, A.; Bazzanella, N.; Kale, A.; Miotello, A. *Applied Catalysis A: General* **2012**, *423–424*, 21.

(12) Shaheen, M. E.; Gagnon, J. E.; Fryer, B. J. *Journal of Applied Physics* **2013**, *114*, 083110.

(13) Guo, Q.; Shi, W.; Liu, F.; Arita, M.; Ikoma, Y.; Saito, K.; Tanaka, T.; Nishio, M. *Journal of Alloys and Compounds* **2013**, *552*, 1.

(14) Gower, M. C. *Optics Express* **2000**, *7*, 56.

(15) Kanan, M. W.; Nocera, D. G. *Science* **2008**, *321*, 1072.

(16) Lutterman, D. A.; Surendranath, Y.; Nocera, D. G. *Journal of the American Chemical Society* **2009**, *131*, 3838.

(17) Marco, B.; Claudio, C.; Antonio, M. *Measurement Science and Technology* **1999**, *10*, N27.

(18) Maissel, L., I. In *Mechanical properties of thin films*; Maissel, L., I., Glang, R., Eds.; McGraw-Hill: San Francisco, **1970**, pp. 13-1 to 13-33.

(19) van de Krol, R. In *Photoelectrochemical Hydrogen Production*; van de Krol, R., Grätzel, M., Eds.; Springer: New York, **2012**, Chapter 3, p 75.

(20) Dalle Carbonare, N.; Cristino, V.; Berardi, S.; Carli, S.; Argazzi, R.; Caramori, S.; Meda, L.; Tacca, A.; Bignozzi, C. A. *ChemPhysChem* **2014**, *15*, 1164.

(21) Klahr, B.; Gimenez, S.; Fabregat-Santiago, F.; Bisquert, J.; Hamann, T. W. *Energy & Environmental Science* **2012**, *5*, 7626.

THESIS CONCLUSIONS

In this Ph.D. thesis, photoelectroactive substrates, based on semiconductor electrodes, mainly applied in either photoelectrochemical or electrochemical water oxidation, were prepared. Several approaches were explored, and the resulting devices were fully characterized.

In **Chapter 3**, a new ruthenium sensitizer-catalyst assembly was synthesized and tested on TiO_2 electrodes. The two separate units having in principle the correct frontier levels for photoinduced water splitting, but when linked together, in the resulting dyad, become inefficient. The main problem was a substantial increase in the redox potential of the catalyst high-valent species (active toward water oxidation), energetically out of reach of the sensitizing unit. The difficulty of predicting changes in the redox potential of the catalyst, occurring upon interaction with the sensitizer, and the unsatisfactory results obtained with this binuclear complex, lead us to consider the co-adsorption, on the semiconductor surface, of independent sensitizing and catalytic species according to a simpler and more profitable approach.

In **Chapter 4**, this functionalization method was successfully applied in the modification of nanocrystalline WO_3 electrodes with perylene bisimide, a molecular organic sensitizer, and IrO_2 nanoparticles, as water oxidation catalyst, reaching very interesting results that show promise for future optimizations. The strong oxidizing power of perylene photogenerated holes can be employed to activate a wide array of catalysts, including other amorphous metal oxides or molecular species, to drive photo-oxidation reactions under visible illumination.

In order to obtain another efficient sensitizer, with the intention to improve the above discussed results, a new phosphonated Ru(II) polypyridine complex was designed, synthesized and characterized (**Chapter 5**). On modified SnO_2 photoanodes, the strongly oxidizing photogenerated Ru(III) state was demonstrated to activate co-adsorbed IrO_2, resulting in a significantly enhanced photoanodic response. Interestingly, the photocurrent on TiO_2 substrates were largely increased (four to six fold enhancement) in the presence of sodium ascorbate, due to a modification of the charge injection mechanism. This reductive quenching (anti-biomimetic pathway), was confirmed by transient differential absorption

spectra and in certain conditions, in the case of poorly reducing and short lived excited states, allows for a more efficient electron transfer from the dye reduced form to the TiO_2 conduction band.

Finally, in **Chapter 6**, an important study on pulsed-laser deposition (PLD), as valuable tool for the preparation of nanostructured amorphous Fe_2O_3 catalyst, for the functionalization of conductive surface, was considered. The resulting electrodes, based on earth-abundant and non-hazardous iron metal, was able to sustain high current densities (up to 20 mA/cm^2), at reasonably low applied potential bias, for more than 1 hour when employed as anodes for electrochemical water oxidation at pH 11.8. The good catalytic performance achieved proves the validity of PLD as a method to prepare nanostructured materials with good control over surface coverage and morphology. The methodology lends itself to the exploration of other metal oxide catalysts and to functionalization of other surfaces, among which the ohmic contact of multi-junction photovoltaic cells provide the most attractive example.

In conclusion, this Ph.D. has demonstrated some proof of principle that will be helpful to guide the development of molecular systems and semiconductor substrates, which could be usefully exploited in molecular level artificial photosynthesis. The work on amorphous iron oxides, as a cheap and environmentally friendly solution for water oxidation catalysts, is also finalized to the assembly water splitting cells ,which will couple the traditional photovoltaic devices with catalytic overlayers in integrated devices. While this approach could be less fascinating than a molecular systems, the stability an the efficiency of these amorphous oxides would lead to the fabrication of viable devices in the near future.

PUBLICATION LIST

M. Orlandi, **S. Caramori**, **F. Ronconi**, **C. A. Bignozzi**, **Z. El Koura**, **N. Bazzanella**, **L. Meda** and **A. Miotello**: "Pulsed-laser deposition of nanostructured iron oxide catalysts for efficient water oxidation".
ACS Applied Materials & Interfaces, **2014**, 6 (9), pp 6186-6190.
DOI: 10.1021/am501021e

F. Ronconi, **Z. Syrgiannis**, **A. Bonasera**, **M. Prato**, **R. Argazzi**, **S. Caramori**, **V. Cristino** and **C. A. Bignozzi**: "Modification of nanocrystalline WO_3 with a dicationic perylene bisimide: applications to molecular level solar water splitting".
Journal of the American Chemical Society, **2015**, 137 (14), pp 4630-4633.
DOI: 10.1021/jacs.5b01519

S. Caramori, **R. Argazzi**, **V. Cristino**, **N. Dalle Carbonare**, **F. Ronconi** and **C. A. Bignozzi**: "Molecular assemblies and nanostructured semiconductors for photoinduced water splitting".
La Chimica e l'Industria, **2015**, n. 4, pp 13-19.
DOI: http://www.soc.chim.it/riviste/chimica_industria/rivista/2015/4

S. Caramori, **F. Ronconi**, **R. Argazzi**, **S. Carli**, **R. Boaretto**, **E. Busatto** and **C. A. Bignozzi**: "Solar energy conversion in photoelectrochemical systems".
SPRINGER, *When Light Meet Molecules*, **2016**, Cap. 2.
In press

F. Ronconi, **M. P. Santoni**, **F. Nastasi**, **G. Bruno**, **S. Caramori**, **C. A. Bignozzi** and **S. Campagna**: "Charge injection into nanostructured TiO_2 electrodes from the photogenerated reduced form of a new Ru(II) polypyridine compound: the "anti-biomimetic" mechanism at work.
ACS Applied Materials & Interfaces, **2016**.
Manuscript submitted

F. Ronconi, **Z. Syrgiannis**, **F. Rigodanza**, **M. Prato**, **M. Bonchio**, **S. Caramori**, **C. A. Bignozzi** et al.: "Charge transfer dynamics on modified WO_3 photoanodes incorporating a perylene bisimide dye and tetra ruthenium polyoxometalate water oxidation catalyst".
Manuscript in preparation

ORAL COMMUNICATIONS AND POSTER PRESENTATIONS

Poster presentation at "XIII giornata di chimica dell'Emilia Romagna", **december 2013**, Bologna (BO), title "*Nanostructured electrocatalytic iron oxides for water splitting*".

Poster presentation at "Sigma-Aldrich Young Chemists Symposium", **october 2014**, Riccione (RN), title "*Pulsed-laser deposition of nanostructured iron oxide catalysts for efficient water oxidation*".

Poster presentation at the "Italian Photochemistry Meeting 2014", **november 2014**, Besate (MI), title "*Pulsed-laser deposition of nanostructured iron oxide catalysts for efficient water oxidation*".

Poster presentation at "XIV giornata di chimica dell'Emilia Romagna", **december 2014**, Parma (PR), title "*Pulsed-laser deposition of nanostructured iron oxide catalysts for efficient water oxidation*".

Oral communication at the "Italian Photochemistry Meeting 2015", **december 2015**, Bologna (BO), title "*Modification of nanocrystalline WO_3 with a dicationic perylene bisimide: applications to molecular level solar water splitting*".

ACKNOWLEDGMENTS

With the thesis written, also my Ph.D. experience ends, leaving to me good memories and frustrations, but overall a sense of maturity at both scientific and human levels. Many people have accompanied me in this journey, colleagues, friends and family, and for this reason I would like to express my sincere thanks. Also financial support from *FIRB Nanosolar project n.RBAP11C58Y* is gratefully acknowledged.